SSCL-SR-1239

The LEB Book

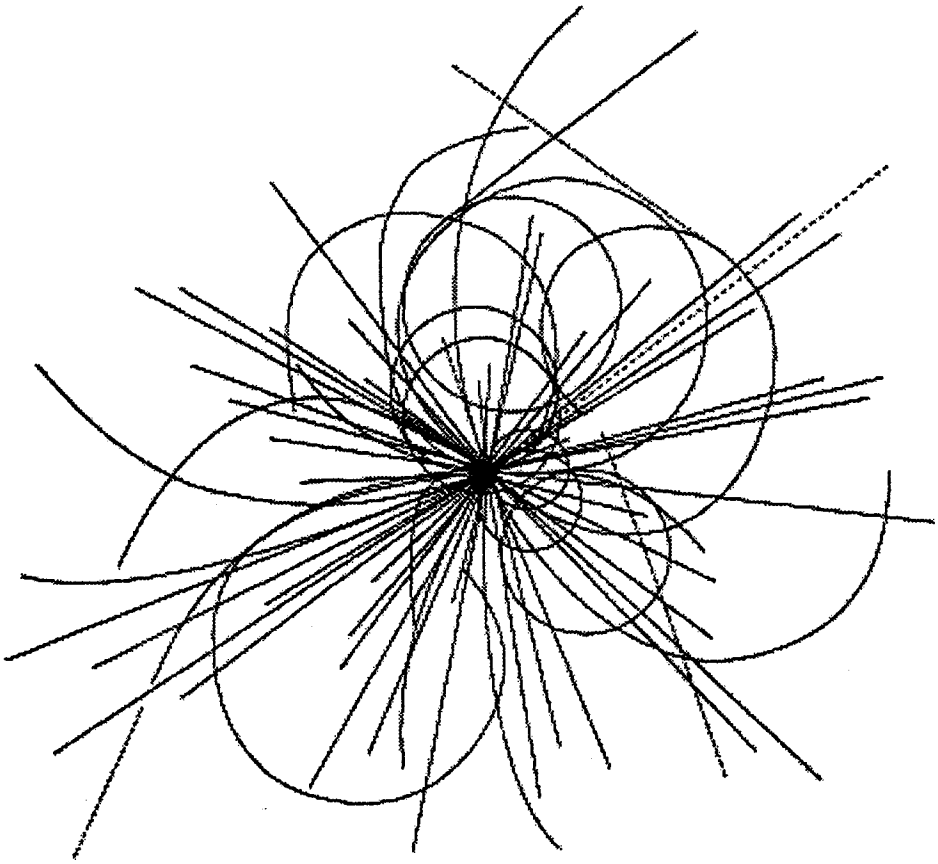

Superconducting Super Collider Laboratory

SSCL-SR-1239
October 1994
Distribution Category: 400

U. Wienands
N. K. Mahale
X. Wu
F. Knox-Seith
N. Li
M. Schulze
J. M. Wilson
W. Merz
J. A. Reimund
E. Tacconi
T. Treasure
P. D. Coleman
J. Ferrell
L. K. Mestha
J. Beach
R. Webber
R. Aiello
R. Bork
J. Bull
R. Parry
J. Jones
G. Bourianoff
J. Nonte
T. Webster

Disclaimer Notice

This report was prepared as an account of work sponsored by an agency of the United States Government. Neither the United States Government or any agency thereof, nor any of their employees, makes any warranty, express or implied, or assumes any legal liability or responsibility for the accuracy, completeness, or usefulness of any information, apparatus, product, or process disclosed, or represents that its use would not infringe privately owned rights. Reference herein to any specific commercial product, process, or service by trade name, trademark, manufacturer, or otherwise, does not necessarily constitute or imply its endorsement, recommendation, or favoring by the United States Government or any agency thereof. The views and opinions of authors expressed herein do not necessarily state or reflect those of the United States Government or any agency thereof.

Superconducting Super Collider Laboratory is an equal opportunity employer.

SSCL-SR-1239

The LEB Book

U. Wienands, N. K. Mahale, X. Wu, F. Knox-Seith, N. Li,
M. Schulze, J. M. Wilson, W. Merz, J. A. Reimund, E. Tacconi,
T. Treasure, P. D. Coleman, J. Ferrell, L. K. Mestha, J. Beach,
R. Webber, R. Aiello, R. Bork, J. Bull, R. Parry, J. Jones,
G. Bourianoff, J. Nonte, and T. Webster

Superconducting Super Collider Laboratory*
2275 N. Highway 77
Waxahachie, TX 75165

October 1994

*Operated by the Universities Research Association, Inc., for the U.S. Department of Energy under Contract No. DE-AC35-89ER40486.

Contents

1 Introduction **1**

1.1 History of the LEB Requirements 2

1.2 LEB Parameters 3

1.3 The LEB Systems 5

1.4 Acknowledgements 7

2 LEB Lattice and Beam Dynamics **9**

2.1 Optical Design of the Low Energy Booster
(U. Wienands) 9

2.1.1 Lattice Requirements 9

2.1.2 First-order Optical Design 10

2.2 Rf Program
(N.K. Mahale) 17

2.2.1 Overview 17

2.2.2 Injection Process 17

2.2.3 10-Hz Cycle 18

2.2.4 One-third Hz Operation 23

2.2.5 Conclusions 24

2.3 Beam Dynamics
(N.K. Mahale, U. Wienands, X. Wu) 26

2.3.1 Single-Particle Transverse Beam Dynamics
(U. Wienands, X. Wu) 26

2.3.2 Longitudinal Beam Dynamics
(N.K. Mahale) 39

2.3.3 Instabilities
(N.K. Mahale) 43

2.4 Beam Transfer
(X. Wu) 49

2.4.1 Injection 49
2.4.2 Extraction 54

3 The LEB Accelerator Systems **59**
3.1 Magnet System
(F. Knox-Seith, N. Li, M. Schulze, J.M. Wilson) . . . 59
3.1.1 Overview 59
3.1.2 Dipole
(F. Knox-Seith, N. Li) 63
3.1.3 Quadrupoles
(F. Knox-Seith, N. Li) 75
3.1.4 Corrector Magnets
(M. Schulze) 91
3.1.5 Extraction Kicker Magnet System
(J.M. Wilson) 112
3.1.6 Magnet Support and Alignment
(N. Li) 122
3.2 Power Systems
(W. Merz, J.A. Reimund, E. Tacconi, T. Treasure) . . 136
3.2.1 Ring Magnet Power Supply
(J.A. Reimund, E. Tacconi, T. Treasure) 136
3.2.2 Corrector Power Supply System
(W. Merz) 165
3.2.3 Injection Power Systems
(W. Merz) 184
3.3 LEB Rf System
(P.D. Coleman, J. Ferrell) 191
3.3.1 Overview 191
3.3.2 Rf Cavities 193
3.3.3 Rf Amplifiers 212
3.3.4 Power Supplies 213
3.3.5 Local Low-Level Rf Feedback Loops 214
3.3.6 Beam Synchronization and Low Level
Rf Feedback Loops
(L.K. Mestha) 218
3.3.7 Acknowledgements 231
3.4 Vacuum System
(J. Beach) 235
3.4.1 Overview 235

3.4.2 Vacuum Chambers 237
3.4.3 Vacuum Equipment 240
3.5 Beam Instrumentation and Diagnostics
(R. Webber and R. Aiello) 242
3.5.1 Background & Overview 242
3.5.2 Description of Measurements and Methods 246
3.5.3 Instrumentation Systems and Devices 248
3.6 The LEB Control System
(R. Bork) 265
3.6.1 Introduction 265
3.6.2 General Requirements 265
3.6.3 Design Approach 268
3.6.4 Infrastructure Design 269
3.6.5 Rf Supervisory Controls System 283
3.7 Radiation and Shielding
(J. Bull) 289
3.7.1 Beam Intensities and Source Terms 291
3.7.2 Shielding Calculations 293
3.7.3 Cover Requirements 293
3.7.4 Penetrations 294
3.7.5 Groundwater Activation 296
3.7.6 Radiation Concerns Associated with Beam Injection . 297
3.7.7 Radiation Concerns Associated with Beam Extraction 298
3.7.8 Summary 299
3.8 Personnel Access Safety System
(R. Parry) 300
3.8.1 Introduction 300
3.8.2 The Controller 301
3.8.3 Redundancy 301
3.8.4 Software 302
3.8.5 Fail-Safe Design 303
3.8.6 Miscellaneous Safety Requirements 304
3.8.7 Pass Access States 306
3.8.8 Conclusion 310
3.9 Civil Construction and Infrastructure
(J. Jones) 311
3.9.1 LEB Design and Construction 311
3.9.2 Site, Geotechnical, Earthwork and Infrastructure . . . 311
3.9.3 Architectural Systems 315

3.9.4 Structural Systems 315
3.9.5 Mechanical Systems 320
3.9.6 Electrical Systems 322
3.9.7 Fire Protection Design Analysis (FPDA) 323
3.9.8 Acknowledgements 323

4 Beam Commissioning **325**
4.1 Overview of Commissioning Task 325
4.1.1 Beam Commissioning Plan 326
4.2 The Beam Control Simulator 340
4.2.1 Application Software 340
4.2.2 High Level Beam Control Simulator
(G. Bourianoff) 341

A Tables and Technical Notes Index **353**
A.1 LEB Parameter Tables
(J. Nonte, T. Webster) 353
A.2 PMTN Technical Notes
(J. Nonte, T. Webster) 368

List of Figures

2.1 Layout of the LEB lattice. 11
2.2 Lattice functions of the LEB. 12
2.3 Layout of an arc-superperiod of the LEB. 14
2.4 Parameters of the LEB arc superperiod. 15
2.5 Capturing process. (a) The particles at injection; (b) the bunch just before the bucket is enlarged (30 μs). 19
2.6 Bucket area *vs.* time for the first 6 ms. 20
2.7 Rf amplitude *vs.* time. 21
2.8 Rf voltage program with a second harmonic rf system. . 23
2.9 Rf phase program with a second harmonic rf system. . . 24
2.10 Rf program for the one-third Hz cycle. 25
2.11 Chromatic variation of the LEB lattice functions. 27
2.12 Transverse phase space (a) and betatron resonance spectrum (b) of the "ideal" LEB lattice. 29
2.13 Typical closed orbit excursion with the field errors and misalignment of the magnetic elements before and after the closed orbit correction. 33
2.14 Transverse phase space (a) and betatron resonance spectrum (b) of the LEB lattice with magnetic errors, misalignment and closed orbit correction. 34
2.15 Transverse phase space (a) and betatron resonance spectrum (b) of the LEB lattice after the resonance corrections. 37
2.16 Dynamic aperture of the LEB lattice. 38
2.17 Longitudinal emittance and bucket area *vs.* time. 40
2.18 Laslett tuneshift *vs.* time. 41
2.19 Beam loss *vs.* synchronization error. 42
2.20 The LEB injection girder assembly. Vertical scale has been blown up for clarity. 50

2.21 Cross section at the exit ends of bump 1 and the septum magnets. 52
2.22 Schematic view of the stripper foil positioning mechanism. 53
2.23 Layout and optics of the extraction system. 55
2.24 Cross section at the entrance of the first septum magnet. 56

3.1 Isometric view of the dipole magnet. 63
3.2 Dipole cross section. 67
3.3 PE2D calculation of 2D dipole field. 68
3.4 Sketch of the dipole lamination punch and die. 70
3.5 Dipole stacking fixture. 71
3.6 Dipole lamination inspection results. 72
3.7 INP measurements of the dipole body field. 73
3.8 Measurements of the integrated dipole field uniformity. . 75
3.9 Field uniformity measurements. 76
3.10 Measurements of the dipole field strength. 77
3.11 Isometric view of the quadrupole magnet. 78
3.12 Quadrupole cross section. 82
3.13 PE2D calculation of the two-dimensional quadrupole field. 83
3.14 BINP design for LEB main quadrupole end-pack. 84
3.15 Quadrupole pole tip of the punched lamination (a) and the laser cut lamination (b). 85
3.16 Quadrupole lamination punch and die. 85
3.17 Quadrupole stacking fixture. 86
3.18 INP quadrupole prototype inspection result. 87
3.19 Body field harmonics in LBL prototype quadrupole. . . 89
3.20 Integral field harmonics in LBL prototype quadrupole. . 90
3.21 Field harmonics in the INP prototype quadrupole. . . . 91
3.22 Field on the midplane of the BINP prototype quadrupole. 92
3.23 Integrated gradient *vs.* current in the BINP prototype quadrupole. 93
3.24 Integrated gradient *vs.* excitation current in the LBL prototype quadrupole. 93
3.25 Saturation of main dipoles and quadrupoles. 94
3.26 Dependence of the temperature rise in the air-cooled LEB correctors as a function of the coil current density. 96
3.27 Cross section of the LEB dipole corrector magnet. 97
3.28 Integrated field uniformity of the LEB dipole corrector magnet. 99

3.29 Cross section of the LEB high field trim quadrupole. . . 103
3.30 Cross section of the LEB low field and skew quadrupole magnet. 104
3.31 Laser cut trim quadrupole lamination pole tip. 105
3.32 Orientation of poles for Table 3.13. 107
3.33 HFTQ field uniformity before chamfering. 108
3.34 HFTQ field uniformity after chamfering. 109
3.35 LFTQ field uniformity after chamfering. 110
3.36 Cross section of the chromaticity sextupole magnet. . . . 112
3.37 Chromaticity sextupole field uniformity. 113
3.38 LEB extraction kicker system block diagram. 115
3.39 LEB extraction kicker charging system schematic. 116
3.40 Prototype LEB extraction kicker modulator tank and charging system. 117
3.41 LEB extraction kicker charging waveforms. Note: current waveform not to scale. 118
3.42 Prototype LEB extraction kicker system data: (a) modulator output current, (b) integrated magnetic field. . . 119
3.43 Prototype LEB extraction kicker magnet, traveling wave version. 121
3.44 Prototype LEB extraction kicker magnet, solid core version. 121
3.45 Isometric view of the QF2 girder. 123
3.46 Socket for fiducial mark. 125
3.47 Transfer of horizontal position. 128
3.48 Transfer of vertical position. 129
3.49 Socket for tunnel monument. 130
3.50 Orientation survey. 130
3.51 Monopod. 132
3.52 General arrangement of ring magnet power system. . . . 137
3.53 LEB current operation modes. 138
3.54 ESI in a test stand at UETM. 140
3.55 Electrical diagram of the ESI. 141
3.56 Simplified mechanical design of the ESI. 142
3.57 Simulated magnet ripple current at injection. 143
3.58 LEB magnet simulation model. 143
3.59 Block diagram of LEB power supply regulation loops. . . 145
3.60 Block diagram of the voltage regulator. 146

3.61 Open loop gain/frequency response of the digital voltage loop. 147
3.62 Open loop phase/frequency response of the digital voltage loop. 147
3.63 Closed loop gain/frequency response of the digital voltage loop. 148
3.64 Rejection characteristics of the digital voltage loop. . . . 148
3.65 Block diagram of the current control loop for the linear ramp mode. 149
3.66 Magnitude frequency response of the load admittance including voltage loop and passive filter. 150
3.67 Open loop gain/frequency response of the digital current loop. 152
3.68 Open loop phase/frequency response of the digital current loop. 152
3.69 Closed loop gain/frequency response of the digital current loop. 153
3.70 Rejection characteristics of the digital current loop. . . . 153
3.71 Reference and magnet current. 154
3.72 Error between reference and magnet currents. 154
3.73 Block diagram of the current loop 10 Hz biased sinewave mode. 155
3.74 Magnitude and phase frequency response of the load admittance. 157
3.75 Block diagram representing the detection and modulation process. 158
3.76 Magnitude frequency response of the equivalent feedback regulator. 160
3.77 Magnitude frequency response of the total open-loop feedback regulation. 160
3.78 Difference between reference and magnet current by using feedforward compensator. 162
3.79 Difference between reference and magnet current by using feedback synchronous regulator. 162
3.80 Ac harmonic/power factor correction filter. 163
3.81 Power supply input power in ramp mode. 164
3.82 Power supply input power in 10 Hz resonant mode. . . . 164
3.83 General arrangement of the corrector magnet power system. 168

3.84 Dc offset sinewave. 170
3.85 1/3 Hz ramped waveform. 171
3.86 Graphical representation of TOD requirement. 173
3.87 LEB power supply load model. 177
3.88 LEB sextupole magnet impedance *vs.* frequency. 178
3.89 Block diagram—LEB corrector power supply system topology. 179
3.90 Typical LEB corrector power supply rack assembly. . . . 180
3.91 Output $V-I$ graph for 4 quadrant power supply operation. 181
3.92 Simplified load/switch arrangement. 182
3.93 LEB corrector P.S. controls. 184
3.94 Septum power supply RLC circuit. 186
3.95 Septum power supply output current simulation. 187
3.96 Bump power supply output current simulation. 188
3.97 LEB bump power supply circuit model. 189
3.98 Bump output current TOD definition (drawing not to scale). 190
3.99 LEB rf system block diagram. 192
3.100 Rf station block diagram. 193
3.101 LEB cavity diagram. 195
3.102 Calculated mode damper performance. 196
3.103 Conduction-cooled tuner geometry. 197
3.104 Liquid-cooled tuner geometry. 198
3.105 Liquid containment approach for liquid tuner. 200
3.106 Water-cooled ferrite carrier tuner geometry. 201
3.107 Cavity tuning range (conduction-cooled). 203
3.108 Conduction-cooled tuner frequency response. 204
3.109 Conduction-cooled cavity operating space. 205
3.110 Cavity tuning range (liquid-cooled). 207
3.111 Directly cooled tuner frequency response. 208
3.112 Swept frequency operation. 209
3.113 Cavity detuning due to non-linearity in ferrite. 210
3.114 Low-level rf simplified block diagram. 216
3.115 I & Q system block diagram. 217
3.116 Resonance loop block diagram. 218
3.117 Rf feedback and phase corrector diagram. 219
3.118 Rf beam control loops planned for the SSC Low Energy Booster. 220

3.119 Conceptual diagram showing the arrival time of a reference bunch in the LEB. 223
3.120 LEB trip plan. 224
3.121 Synchronization loop hardware used for bench testing the loop. 225
3.122 Basic timing diagram of the synchronization loop. 226
3.123 Synchronization loop "proof of principle" test results. . . 227
3.124 Schematic loop diagram of the experimental LLRF beam control system. 228
3.125 Trip measurement with time interval shown in seconds in FNAL booster synchrotron with beam. 229
3.126 Beam control experimental results in the FNAL booster synchrotron. 232
3.127 Oscillograms of the trip measurement on the CERN PS booster: (a) for a complete acceleration cycle, and (b) expanded view late in the cycle. 233
3.128 Cross section of the dipole vacuum chamber. 238
3.129 Location of beam instrumentation devices in LEB. . . . 245
3.130 BPM mechanical assembly. 250
3.131 Log-ratio position monitor electronics. 251
3.132 VXIbus beam position module. 252
3.133 BPM system dynamics: a) beam signal spectral amplitudes and b) BPM electronics resolution for first 50 turns after injection. 253
3.134 BPM electronics performance: a) measured *vs.* ideal position output signal; b) expected resolution *vs.* ideal case of noiseless electronics. 255
3.135 Block diagram of the log-ratio, AM/PM position test conducted at Fermilab. 256
3.136 Comparison of LEB and Fermilab BPM electronics performance: a) position output through one acceleration cycle. b) difference between outputs of the log-ratio circuit and the AM/PM module. 256
3.137 BLM electronics block diagram: BLM detector in LEB tunnel, electronics in VXI chassis in surface building. . . 259
3.138 Turn-by-turn profile at injection upstream of second orbit bump magnet. 261
3.139 Example of e^- catcher signal during 5 turn injection. . . 264
3.140 LEB control system communications infrastructure. . . . 271

3.141 LEB control system interconnections. 274
3.142 Block diagram of the RMPS supervisory control system. 279
3.143 Corrector magnet power supply controls. 281
3.144 Rf station control block diagram. 284
3.145 EPICS front-end processor internals. 285
3.146 Layout of the beam-instrumentation read-out system. . . 286
3.147 Dose equivalent per proton versus shielding thickness for a point loss. 295
3.148 System block diagram. 303
3.149 LEB service buildings and tunnel. 305
3.150 PASS state diagram. 307
3.151 Controlled access booth (CAB). 309
3.152 LEB site plan. 312
3.153 Typical tunnel cross section. 316

4.1 Schematic layout of the injection section. 327
4.2 Transmission and beam emittance in the LEB for different orbit excursion. 330
4.3 Effect of mismatch between quadrupole and dipole strength on straight-section dispersion and transition energy. . . . 331
4.4 Tune variation during the LEB cycle due to mistracking of quadrupoles and dipoles. 332
4.5 Emittance growth in the LEB cycle due to mistracking of quadrupoles and dipoles. 333
4.6 Emittance growth in the LEB cycle due to mistracking of quadrupoles and dipoles. 333
4.7 Momentum deviation *vs.* number of turns after injection for various deviations of the rf frequency from f_c. 335
4.8 Spatial phase deviation *vs.* number of turns after injection for various deviations of the rf frequency from f_c. . 335
4.9 Structure of high-level beam control simulator. 346
4.10 Typical screen for closed orbit correction. 352

List of Tables

1.1 Design parameters of the LEB and the FNAL booster. . 4

2.1 Lattice parameters of the LEB ring. 13
2.2 Lattice parameters for different superperiods. 16
2.3 Baseline rf parameters. 22
2.4 Mismatch results. 26
2.5 Alignment tolerances. 30
2.6 Uncorrected closed-orbit excursion. 31
2.7 Corrected closed-orbit excursion. 31
2.8 Maximum strength of orbit-correction dipoles. 32
2.9 Longitudinal beam dynamics parameters. 39
2.10 Impedance estimates and thresholds; the impedance estimates have been doubled for contingency. 45
2.11 General parameters of the septum magnets. 58

3.1 Magnet functions and quantities. 61
3.2 Parameters of the dipole magnet. 64
3.3 Field parameters of the dipole magnet. 66
3.4 Chemical analysis of AISI M-27 and Russian 2312 steel. 71
3.5 Quadrupole families. 79
3.6 Parameters of the quadrupole magnet. 80
3.7 Field parameters of the quadrupole magnet. 81
3.8 Quadrupole core inspection results. 88
3.9 LEB corrector magnets. 95
3.10 LEB orbit correction dipole magnet parameters. 98
3.11 LEB high field quadrupole magnet parameters. 101
3.12 LEB low field and skew quadrupole magnet parameters. 102
3.13 Dimensional conformance and mechanical inspection of the SSCL prototype HFTQ and LFTQ. 106

3.14 LEB chromaticity sextupole magnet parameters. 111
3.15 LEB extraction kicker system requirements. 114
3.16 Magnet design parameters. 144
3.17 LEB corrector magnet types. 165
3.18 LEB corrector power supply requirements. 167
3.19 Corrector load parameters. 176
3.20 Bulk power supply characteristics. 183
3.21 LEB injection power supply parameters. 185
3.22 LEB rf parameters. 191
3.23 Water-cooled ferrite carrier tuner expected performance. 202
3.24 Cavity Q for liquid-cooled tuner at 57 MHz. 207
3.25 High power summary for liquid-cooled tuner. 211
3.26 Nominal power supply ratings. 213
3.27 Design parameters of the LEB vacuum system. 236
3.28 Location of beam monitors and value of pertinent lattice parameters. 244
3.29 Beam loss monitor requirements. 258
3.30 Beam profile measurement requirements. 262
3.31 LEB discrete I/O channels (approx.). 267
3.32 LEBCS IOC by system and location. 278
3.33 Superconducting Super Collider radiation limits and design goals. 289
3.34 Shielding comparisons for different beam loss conditions. 292
3.35 Dose rates due to activated components. 298

4.1 Application packages: beam diagnostics. 341
4.2 Application packages: transverse beam dynamics. 342
4.3 Application packages: longitudinal beam dynamics. . . . 344

A.1 General LEB parameters. 353
A.2 Beam current parameters. 354
A.3 General lattice parameters. 354
A.4 Arc section lattice parameters. 355
A.5 Straight section lattice parameters. 356
A.6 Beam acceptance parameters. 356
A.7 Space allocation summary. 357
A.8 One-half standard (special) arc cell space allocation. . . 358
A.9 Straight section space allocations. 359
A.10 Magnet functions. 360

A.11 Magnet count. 360
A.12 Main dipole magnet parameters. 361
A.13 Main quadrupole magnet parameters. 361
A.14 Orbit correcting dipole magnet parameters. 361
A.15 Trim quadrupole magnet parameters. 362
A.16 Skew quadrupole magnet parameters. 362
A.17 Sextupole magnet parameters. 362
A.18 Skew sextupole magnet parameters. 363
A.19 Resonant mode cycle time parameters. 363
A.20 Non-resonant mode cycle time parameters. 364
A.21 Longitudinal parameters. 365
A.22 Impedance budget. 366
A.23 Tune shift and impedance parameters. 367

Chapter 1

Introduction

The Superconducting Super Collider—SSC for short—was to be the premier investigating tool for high energy physics research well into the 21st century. Expanding the reach at the "energy frontier" by more than an order of magnitude beyond that of the facilities available at this time (the FNAL Tevatron and, until recently, the CERN Sp$\bar{p}$S) with its 20-TeV beams and its projected luminosity of 10^{33} cm^{-2}s^{-1}, its goal was not only to find the so-called "Higgs Boson," thus validating the assumed mechanism responsible for the acquiring of mass by the hadronic matter, but also to recreate conditions thought to exist very shortly after the "Big Bang"— the creation of the Universe—and, thus, to provide humanity with a tantalizing glimpse at the early history of the world as we know it. The machine is no less daunting than the physics it has been designed to reach—83-km circumference for the collider tunnel housing two superconducting proton accelerator and storage rings, dwarfing the injector chain which itself has been designed to have the dimensions of the largest hadron collider in existence today, the Fermi National Accelerator Laboratory (FNAL) Tevatron.

The SSC has lost its funding and will not be built. As this book is being written, the facilities are being dismantled, the tunnel segments mothballed, and the staff of about 2000 technicians, engineers, scientists and managers is being laid off. Those of us who are still employed at the site are doing what they can to document and thus preserve as much as possible of the achievements during the short 5-year existence of the SSC Laboratory.

This book is entirely devoted to the description of one accelerator: the Low Energy Booster (LEB) synchrotron, the first of three synchrotrons and designed to boost the energy of the proton beam from 600 MeV—the final

energy of the Linac—to 11.1 GeV for transfer to the following synchrotron: the Medium Energy Booster or MEB. We believe that on one hand the LEB has sufficiently unique features to warrant distribution of this information. On the other hand, construction has advanced far enough for prototyping of most accelerator systems to have taken place so that some of the concepts we pursued already saw their first tests, albeit only in the laboratory. It is our wish that maybe publication of this work will help some of our colleagues to solve their own problems and issues.

1.1 History of the LEB Requirements

With its unprecedented energy and luminosity parameters, the SSC collider rings require a chain of injector accelerators equally complex to the largest existing high energy research facility. The luminosity can be reached essentially in two ways: either by acceleration of a very high beam current, or by using a low-intensity beam of very small emittance, thus providing a beam of very high brightness. The former approach is impractical as high beam currents cause problems with unavoidable beam losses and—this being a novel "feature" for proton machines—also with synchrotron radiation in the collider dipoles. This would create a heat load on the vacuum system that is difficult and expensive to remove by cooling. The approach therefore taken for the SSC is to limit the beam current in the accelerators but push beam brightness by reducing the emittance as far as possible. In this way, the normalized emittance of the proton beams in each of the the collider rings has been set at 1π mm-mr at a circulating beam current of about 100 mA.

In the very early days of the SSC design, a linac and two booster synchrotrons had been foreseen to prepare the proton beam for injection into the collider rings at 1-TeV injection energy. The LEB, was designed to accelerate the beam to 70 GeV at a slower cycling rate. At the fairly modest injection energy of 600-MeV space-charge forces become a major issue due to both the depression in betatron tune they cause, which can lead to the crossing of machine resonances, and the nonlinearity of the forces which gives rise to additional resonances. The large ratio of injection to extraction energy made the magnets difficult to design, esp. w.r.t. the field quality at injection. The net effect of all this is an increase in beam emittance and thus a reduction in beam brightness. In case of the SSC injectors the emittance budget is particularly tight as the beam emittance is very small to start with—about 0.4π mm-mrad—limiting any tolerable growth to an exceedingly small num-

ber of about 0.1π mm-mrad. It was therefore decided to reduce the demands on each injector machine by introducing a third booster synchrotron—the MEB—and reducing the LEB top energy. In the SSC Conceptual Design Report (CDR)[1] the LEB had a top energy of 8 GeV at correspondingly smaller size and a repetition rate of 10 Hz. This had several benefits: The LEB, becoming a smaller and faster cycling machine, operates at less circulating current, thus reducing the space charge tune shift and also the time for the beam emittance to grow. At the same time it was decided to avoid transition in the LEB and thereby the very tight bunching of the beam at transition that causes excessive peak currents with large space-charge forces. As a side effect the requirements for the LEB rf acceleration system could be relaxed, although they were still stringent. The increase of the injection energy into the collider rings from 1 TeV to 2 TeV led to an increase in the energy of the injector machines as well, thus raising the extraction energy of the LEB to 11.1 GeV (or 12 GeV/c momentum) and its circumference to 540 m.[2]

The detailed design of the LEB has been approached in earnest in the Fall of 1990. An injector workshop held in December 1990 further defined the requirements.[3] The final LEB lattice was first proposed during this workshop, further refined and evaluated in the following months and adopted in April 1991 after a slight increase in length in order to ensure sufficient space for the location of all hardware.[4,5] Construction has proceeded essentially on schedule until the funding uncertainty of the project in the summer of 1993 was beginning to show its impact.

1.2 LEB Parameters

Table 1.1 gives an overview of the most important LEB machine design parameters. It is instructive to compare these to its closest cousin, the 8.5-GeV FNAL Booster, the parameters of which are also listed in the table. The similarities are evident, but so are the differences. On the beam dynamics side, the LEB has about one-tenth the emittance of the FNAL Booster. The hardware differences are exemplified by the much higher rf voltage needed, and of course by the high transition energy (the FNAL Booster goes through transition). Dispersion-free straight sections in the LEB help not only the beam extraction system, but also avoid the excitation of synchro-betatron resonances that could blow up the emittance.

Beam intensity is achieved by accumulation of the H^- beam from the Linac over four turns. In this way, emittance is maintained and the high

Table 1.1: Design parameters of the LEB and the FNAL booster.

Parameter	LEB	FNAL Booster
T_{inj} (GeV)	0.6	0.2 (0.4)
T_{extr} (GeV)	11.1	8.5
ppp (10^{12})	1.14	2.5...3.5
f_{rep} (Hz)	10,1/3	15
Harmonic number	114	84
Rf frequency range (MHz)	47.5...59.8	30.3...52.8
Circumference (m)	570	474
long straight sections	3	0
Focusing	separated function FODO	combined function FODO
$\epsilon*_{rms}$ (πmm-mr)	0.4	4
γ_t	22	

brightness is achieved. At the same time, by increasing the number of turns accumulated a beam with increased intensity but reduced brightness can be accelerated to support the detector test facility.

While the demands on the transverse beam dynamics are stringent, the longitudinal emittance is restricted mainly by the economic considerations of keeping the maximum rf voltage as low as reasonable for a given acceleration cycle. In fact, a larger longitudinal emittance is required in the High Energy Booster (HEB) for stability reasons, but uneconomical to accelerate in the LEB. Therefore the LEB emittance has been chosen to be moderate, with the intention to blow up the emittance either in the MEB (possibly by injecting a mismatched beam) or in the HEB before acceleration.

The LEB is not required to run with a 100 % duty cycle to support collider operation. The MEB has almost 7 times the circumference of the LEB, therefore, 6 LEB pulses containing 110 bunches each are stored in the MEB in box-car fashion during the 0.7 s flat-bottom of the MEB cycle. The MEB accelerates in 3.4 s to 200 GeV kinetic energy with a 0.35 s flat-top (to allow cogging) and the same time taken for ramp-down. A 0.2 s flatbottom for stabilization complete the cycle for a total cycle period of 8.05 s. Four MEB pulses (2640 bunches) are stored in the HEB for acceler-

ation to 2 TeV; the HEB has a total cycle time of 515 s for a bipolar cycle (*i.e.* accelerating once clockwise and once counterclockwise). Finally, 15 HEB pulses (39600 bunches) are stored in each collider ring. Thus, one collider filling operation takes about 64 minutes, and it is expected to occur once every 24 hours. The 24-hour average duty factor of the LEB is no more than 0.05 %; averaged over 1 hr it is 1.1 %. This is of consequences for the rf cavity design (see Section 3.3).

1.3 The LEB Systems

In order to ensure tracking of both dipoles and quadrupoles all LEB main magnets are powered in series from a single bus. It has been recognized early on that beam commissioning at the 10-Hz repetition rate may be difficult, therefore a low-frequency linear ramped mode cycling at about 1/3 Hz is provided for testing and commissioning purposes. For 10-Hz operation the magnet excitation is provided by a resonant system, making the magnet inductance part of the resonant circuit and providing a biased sine wave current. Rather than providing two separate power supplies—one for the dc bias and one for the ac part—the FNAL modification of the "White" circuit is used whereby a single power source is used for both dc bias and the ac component.

The single-bus configuration prevents use of the main quadrupoles for trimming of the machine tune. Therefore trim quadrupoles have been added to the lattice that facilitate not only adjustment of the overall working point of the machine, but also matching of the sections and control of the half-integer betatron resonances, For this purpose each trim quadrupole is controlled individually. The control system has the ability to group the trim quadrupoles into families according to their functions and the machine symmetry. The same is true for the orbit correcting dipoles.

The rf system of the LEB provides the biggest challenge, mostly due to the fast cycling nature of the machine. The peak acceleration rate is 645 keV/turn, but in order to provide sufficient bucket height a peak voltage of 765 kV is required in the ring, while the frequency swing ($\Delta f/f$) is about 25 %. Providing such a voltage using the proven design of the FNAL Booster cavity (which operates at similar frequency swing and cycling rate) would require excessive space in the ring lattice—necessitating an increase the ring circumference. Therefore it has been decided to employ the approach Los Alamos had taken in the development of a cavity for their proposed AHF

machine, a $\lambda/4$ cavity with a perpendicularly biased ferrite tuner concentric about the beam line.[6] This design promises to deliver much higher rf voltages due to the reduced losses in the ferrite. However, such a cavity has never before used in any accelerator, although a development program at TRIUMF has demonstrated that an ac tuner for this cavity can be built.[7]

The fast cycling rate of the LEB requires special attention to the vacuum system as well, due to the eddy-current generated magnetic fields and the possible heat load on the beam pipe. Both effects are most severe in the dipoles. Of the three practical ways to handle this challenge, the AGS-Booster approach of using a vacuum chamber made of a high-resistivity material with an eddy-current compensation coil has been adopted. Alternatives include ceramic vacuum chambers with an inner rf shield a la Rutherford ISIS and dipoles that are *inside* of the vacuum chamber as used in the FNAL Booster. Both of these were perceived to be more complicated and costly than the chosen approach.

The LEB beam diagnostics design has to accommodate both the small beam sizes involved and the fast cycling rate of the machine. The former presents a challenge especially for the beam profile monitors (with beam sizes down to less than 0.5 mm the resolution of ionization profile monitors becomes an issue) while the latter requires fairly high bandwidth of the data acquisition system in order to keep up with the machine cycle. The challenges are being met by local front-end processors and crates where the analog data is digitized, pre-processed and stored. Read-out by the control system takes place at a rate suitable for both the bandwidth provided and also the "bandwidth" of the human operator/physicist. The communication between the control computers and the front-end processors is facilitated by a synchronous optical network (SONET), which provides a deterministic propagation time for the exchange of messages. The dynamic range in beam intensity required for the instrumentation system is about 1:100, driven by the desire to commission the ring at low intensity.

Injection into the LEB is facilitated by stripping injection of the H^- beam from the Linac and accumulation over 4 turns (collider operation) or 16 turns (for test beams). The beam is extracted in a single turn using fast kicker magnets, with a slower orbit bump to displace the adiabatically shrunk circulating beam close to the septum immediately before extraction. Both injection and extraction septum operate pulsed to allow higher current densities.

The LEB ring tunnel is located at the South end of the West Campus. At its size the tunneling method of choice is cut-and-cover; the cross section

of the tunnel shell is rectangular and measures 10-ft high by 12-ft wide (approximately 3 m × 3.66 m). Its depth in the ground is determined not only by radiation shielding considerations but also by the interface to the Linac and the MEB; as a result, a berm reaching 8.7 m in height at certain locations is to be provided where the depth in the ground is not sufficient for shielding. Six surface buildings house most of the support facilities of the LEB ring—one each per arc and per straight section—in addition, twelve concrete pads are foreseen around the arcs to provide mounting areas for the chokes and the capacitors that are part of the resonant magnet excitation circuit. Electrical power is to be provided by a substation feeding both the LEB and the HEB technical systems, with a separate transformer for the LEB main magnets and the other LEB technical systems.

The organization of this book does not follow the WBS structure in place during the construction phase. Rather, in the next chapter, the LEB beam-optical design will be presented in sufficient detail to give the reader an understanding of the reasoning behind the design, and at the same time to present sufficiently detailed results from the beam dynamics studies we have carried out to demonstrate that the design is sound and stable. The optics of the beam-transfer systems are part of this section. In Chapter 3 the LEB hardware is described; it is organized in an obvious manner by system. Within each section we will try to demonstrate how the design is driven by the beam physics requirements and what trade-offs have to be made to arrive at a reasonable, efficient design for each system. This chapter should be most intersting for the engineer and physicist "in the field" who has to make decisions on how to implement accelerator systems and functions. In Chapter 4 the beam commissioning studies that have been performed are described including the simulation facility.

1.4 Acknowledgements

Designing and building the LEB has required the collaboration and effort of many people: The LEB design group has been responsible for the machine design and defining the requirements (and in some cases the basic approach) to the accelerator systems. The departments and groups within the Accelerator Systems Division have been responsible for the design and construction of the LEB systems including the R&D needed to arrive at a working design where necessary. The Conventional Construction Division has had the responsibility for the civil construction of the LEB (which is managed by

PB/MK). The colleagues involved are acknowledged in a separate section following each major system description, but here we want to acknowledge those whose input has been critical to this project.

Of the LEB design group S. Machida, N.K. Mahale and X. Wu have been studying different aspects of beam dynamics in the LEB and developed requirements for the LEB systems. F. Knox-Seith and N. Li worked closely with the members of the Mechanical Engineering Dept. on magnet designs, the latter also served as liaison person to the manufacturer of the magnets, the Budker Institute for Nuclear Physics in Novosibirsk, Russia. T. Grimm worked closely with the Rf Dept. on the design and tests of the LEB cavity prototype. S. Tollefson and G. Tuttle coordinated the civil design and construction activities including installation planning. G. Tuttle and later T. Webster provided Systems Engineering support and managed budgets and schedule. At different times, S. Jernigan, M. McDonald and J. Handwork provided secretarial support to the LEB group.

The LEB Design Book has been the effort of many authors, most of these have been responsible for the construction of the systems they describe. It is a particular pleasure to acknowledge the diligent efforts of the SSC Technical Information and Publications group, especially Tom Coyne, Elbert Banzon, Wanda Rice, and Mary Ann Hill who created and polished many of the graphs in this book and Sylvia Lee, who took on the daunting task of converting the text from many different sources into LaTeX, assuring uniformity of style and combining everything into on complete document. Without their assistance this document could not have been created.

No acknowledgement would be complete, however, without mentioning Richard York, who, as the first LEB Machine Leader, built the LEB design group and, capably assisted by Gary Tuttle, energetically brought the LEB construction activities on their way. It has been a pleasure for the author to work with Richard on the LEB lattice design during the early phase of the project before taking the "driver's seat" himself.

Chapter 2

LEB Lattice and Beam Dynamics

2.1 Optical Design of the Low Energy Booster (U. Wienands)

2.1.1 Lattice Requirements

The magnet lattice of the LEB has to fulfill a number of requirements, both in terms of beam dynamics as well as hardware considerations. In particular, the following requirements are spelled out:

1. Avoid crossing of transition;
2. Peak η function no larger than 4 m;
3. Dispersion-free straight sections of sufficient length for beam injection and extraction, and for placement of the rf cavities;
4. Max. field in the dipoles about 1.3 T, on the quadrupole tips about 0.8 T;
5. Do not preclude the possibility of acceleration of polarized beams.

In practice, item 1 requires an value of > 20 for γ_t to (a) preserve some ability to match the LEB bunch shape to the MEB bucket shape and (b) use a cogging scheme for synchronization of the LEB to the MEB. The latter also sets an upper limit for the η function to be able to vary the LEB revolution

time by radial steering without exceeding the aperture necessary for the injected beam (see Section 3.3.6). Items 3 and 5 actually seem to be somewhat contradictory: Insertion of a long-straight section with zero dispersion (using dispersion suppressors) would lower the periodicity of the machine, while polarized-beam acceleration would be easier the higher the machine periodicity due to the reduction in the number of intrinsic depolarizing resonances. The upper limits for the magnetic fields chosen are a direct consequence from the 10 Hz repetition rate; too high a field would result in an increase in ac losses and also aggravate eddy-current induced field aberrations. Clearly, the values given are not "hard" limits.

In the SSC Conceptual Design Report (CDR)[1] a circular magnet lattice was proposed for the LEB with five-fold symmetry. Transition is pushed to about $\gamma_t \approx 15$ by employing the "harmonic" method, where the horizontal tune is set slightly below the machine superperiodicity thus creating an oscillating η function around the ring that has small or even negative values in the bending magnets. This has the effect of reducing the momentum compaction and thereby pushing up transition beyond its usual value of $\gamma_t \approx \nu$.[8,9] For the Site-Specific Conceptual Desing Report (SCDR)[2] the LEB energy and circumference were increased and a new lattice was presented with a tune of 16.7 which had a γ_t of ≈ 15 without recourse to a dispersion modulation. Neither of these had dispersion-free straight sections.

As $\gamma_t \approx 15$ was not sufficiently high an intense search for a new lattice fulfilling all or at least most of the above stated requirements was launched in 1990. Various lattices were investigated using both means to raise γ_t.[4] In April 1991 a threefold symmetric lattice with a γ_t of about 22 and a tune of about 11.6 was adopted that appears to meet the requirements. An important factor in the decision has been the apparent optical stability and flexibility of the lattice.

2.1.2 First-order Optical Design

The overall structure of the LEB lattice is shown in Figure 2.1. The lattice is three-fold symmetric, with a DOFO focusing structure throughout. Overall length is 570 m, mainly determined by hardware placement requirements. The optical properties of the lattice, in particular momentum compaction, are mostly determined by the arcs with the straight sections providing space for hardware and some additional phase advance. Located in the straight sections are H^- injection (S1), extraction (S2) and rf cavities (S3) as well as various beam diagnostic elements.

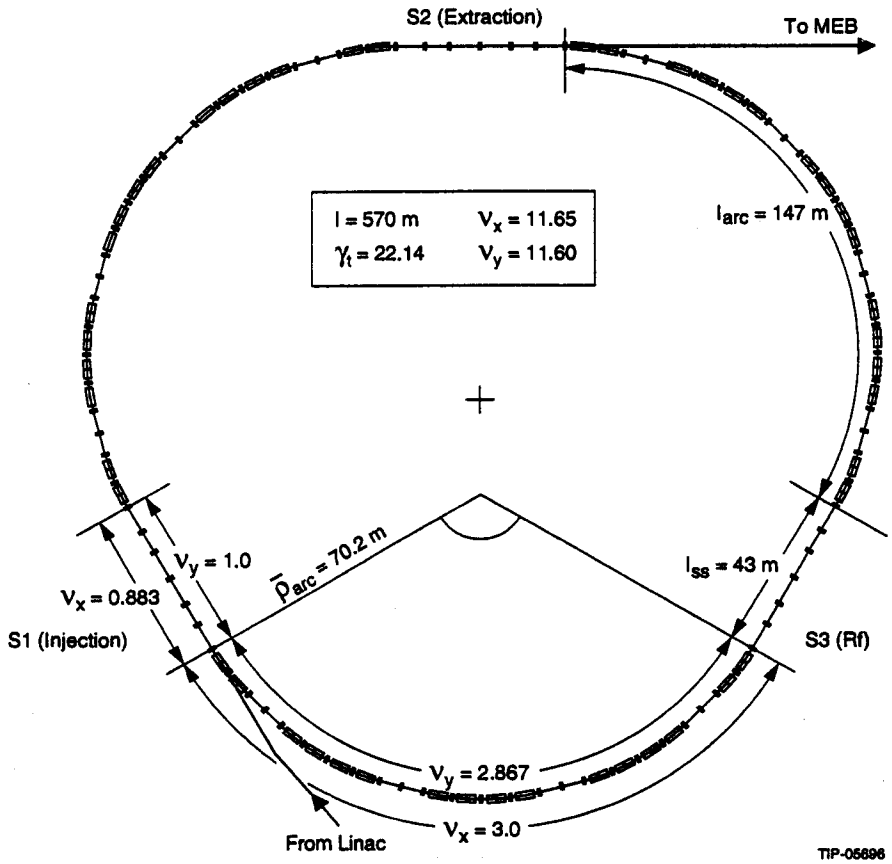

Figure 2.1: Layout of the LEB lattice.

Each arc has a horizontal phase advance of $\mu_x = 3 \times 2\pi$ and four superperiods with three DOFO cells each, the central one being devoid of bending magnets. Thus, the modulation of the bending radius is introduced that pushes up transition, in this case to $\gamma_t \approx 22$ for the whole machine. With an integer horizontal tune and symmetric structure the arcs are also unit sections in the horizontal plane, thus dispersion in the straight section vanishes. Each straight has a phase advance of $\mu_x = 0.883 \times 2\pi$ for a nominal tune of the ring of $\nu_x = 11.65$. In the vertical plane the tuning is the opposite: unit-section straights are inserted between arcs of fractional tune $\mu_y = 2.867 \times 2\pi$. In this way the straight sections become transparent to the vertical betatron motion and the apparent symmetry of the lattice is restored to 12. This

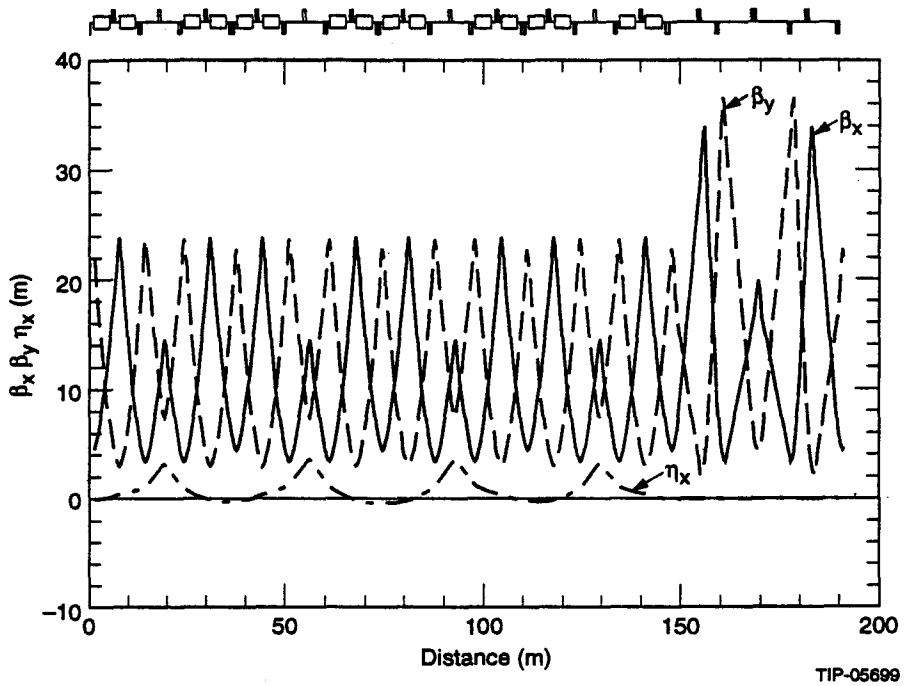

Figure 2.2: Lattice functions of the LEB.

serves to reduce the number of intrinsic depolarizing resonances to four in the acceleration range, making resonance-jumping a possibility as has been proposed for other similar rings.[10]

The lattice functions of the ring are shown in Figure 2.2. The straight cells in the arcs have been shortened by about 25 % compared to the bending cells in order to reduce the space taken up in the arcs; to recover γ_t a slight modulation is imposed on the quadrupoles.

The tuning range of the ring is $> \pm 0.5$ units in both planes independently. Tuning will be done using trim quadrupoles; three families are used to tune the arcs, while four additional families are used to match the straight sections to the arcs.

Table 2.1 summarizes the lattice parameters of the LEB ring. The length of the arc cells is determined by the dimensions of the magnetic elements including coil overhang, space for diagnostics and vacuum hardware *etc.* and space needed to access such items. All hardware in the lattice has been carefully itemized and its slot length determined and space allocated before

Table 2.1: Lattice parameters of the LEB ring.

	nominal	injection	extraction	unit
Kinetic Energy		0.6	11.1	GeV
Momentum		1.213	12.0	GeV/c
Circumference	570			m
Repetition rate	10 (sinusoidal)			Hz
	0.33 (linear)			Hz
Intensity (Collider)	1×10^{12}			ppp
(test beams)	5×10^{12}			ppp
Super Periodicity	3			
Arc Super Periodicity	4			
Focusing pattern	$D_1OF_1OD_2OF_2OD_2OF_1O$			
Bending pattern	BBOOBB			
L_{cell}	12.07			m
$L_{s.period}$	36.2			m
Horizontal tune, ν_x	11.65			
Vertical tune, ν_y	11.60			
$\hat{\beta}_x$ (arc)	21			m
$\hat{\beta}_y$ (arc)	21.2			m
$\hat{\eta}$(arc)	3.7			m
$\hat{\beta}_x$ (straight)	34.1			m
$\hat{\beta}_y$ (straight)	36.5			m
Transition energy γ_t	22.4			
Dipoles				
Number	96			
Magnetic length	2.00			m
Magnetic field		0.138	1.38	T
Bending radius, ρ	29.64			m
Quadrupoles				
Number	90			
Families	8			
Magnetic length	0.55–0.75			m
Magnetic gradient		1.55	15.36	T/m
Correction elements				
Orbit correctors				
Number	96			
Magnetic length	0.2			m
Magnetic field		0.017	0.17	T
Skew quadrupoles				
Number	4			
Magnetic length	0.55			m
Magnetic gradient		0.083	0.82	T/m
Sextupoles				
Number	48			
Magnetic length	0.2			m
Magnetic gradient		8.71	86.17	T/m^2
Skew sextupoles				
Number	2			
Magnetic length	0.3			m
Magnetic gradient		0.27	2.67	T/m^2

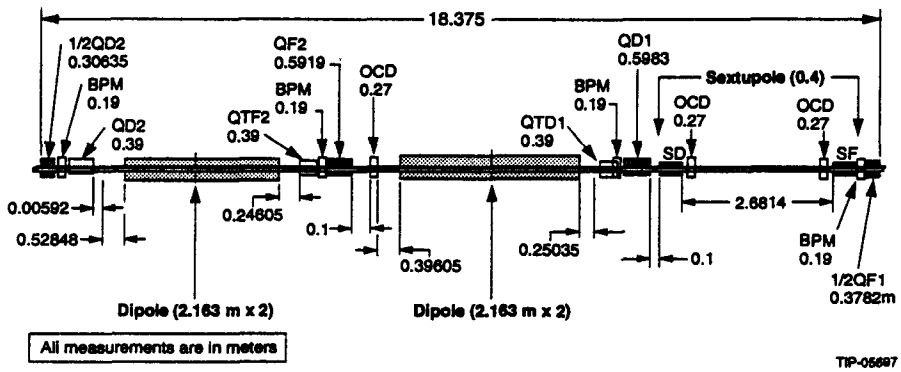

Figure 2.3: Layout of an arc-superperiod of the LEB.

the lattice geometry was finalized. Figure 2.3 shows the layout of a typical FODO cell in the arcs. Space has been allocated also for equipment needed for anticipated machine improvements like dampers, skew sextupoles, and pulsed quadrupoles for depolarizing-resonance jumping.

Analysis of the Arc Superperiod

To understand the properties of the lattice it is of interest to analyze the arc superperiod in detail. The main parameter of interest is the momentum compaction α, which is given by

$$\alpha = \frac{1}{\gamma_t^2} = \frac{dL/L}{dp/p} = \frac{1}{L}\left(\frac{\partial L}{\partial p/p} + \frac{\partial L}{\partial x}\eta_i + \frac{\partial L}{\partial x'}\eta_i'\right), \tag{2.1}$$

where L is the length of the superperiod and the dispersions η_i, η_i' are taken at the entrance of the superperiod. For the LEB arc superperiod $\eta_i' = 0$ due to symmetry, and α can be computed, using matrix optics, to be

$$\alpha = \frac{1}{3}\left[\phi^2\left(1 + \frac{4\eta_i}{\phi L_c}(1 - \sin(\mu/2))\right)\left(1 + \frac{\sin(\mu/2)}{2}\right) + \frac{4R_{56}}{L_c}\right], \tag{2.2}$$

where R_{56} is $\frac{\partial L}{\partial p/p}$ of one dipole and L_c, the length of a cell. The matched dispersion η_i is

$$\eta_i = \frac{\phi L_c}{2}\frac{(1 - 2\sin^2(\mu/2))(2 + \sin(\mu/2))}{(3 - 4\sin^2(\mu/2))\sin^2(\mu/2)} \tag{2.3}$$

for equal phase advance μ in empty and straight cells. These expressions are valid for both polarities of the quadrupoles by choosing positive values

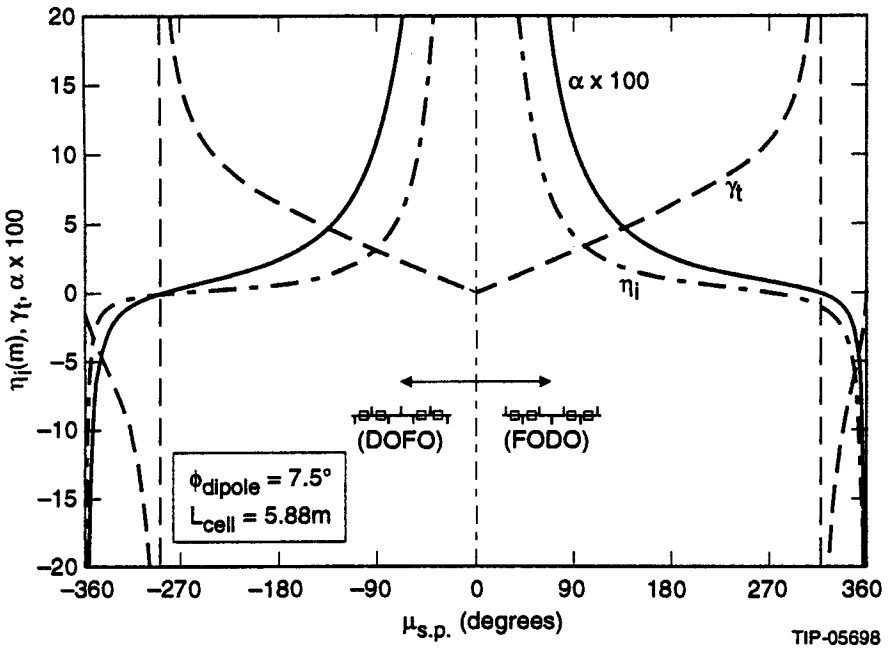

Figure 2.4: Parameters of the LEB arc superperiod.

for μ for the FODO cell and negative for the DOFO cell. In Figure 2.4 η, α and γ_t are plotted *vs.* μ using parameters suitable for the LEB. Comparing the values at either polarity for $\gamma_t = 20$, η_i is found to be significantly smaller in the DOFO case than in the FODO case. This is of advantage for matching of the dispersion-free straights as it reduces the sensitivity of the lattice against tuning errors in the arcs as well as higher-order dispersion in the straight sections. In addition, the dependencies of α and η_i on the phase advance are close to a minimum, thus further reducing the sensitivity of the lattice. Finally, for the DOFO lattice the phase advance across the superperiod is close to 270°, and the arc can easily be tuned to $\nu_x = 3$ with a small modulation on the quadrupole strength to keep γ_t at 20. The dispersion at the center is larger for this polarity but still within the 4-m limit.

Configurations of the superperiod with a different number of bending cells are conceivable. Lattices of this type have been investigated numerically; results are given in Table 2.2. Thin quadrupoles have been used for these runs, but thick dipoles in order to get accurate values for γ_t. It appears that

Table 2.2: Lattice parameters for different superperiods.

Parameter	2-cell s.p.	3-cell s.p.	4-cell s.p.
L_{cell} (m)	20.1	12.1	9.4
$L_{s.period}$ (m)	40.2	36.2	37.5
Θ_{dipole} (°)	15.0	7.5	5.0
γ_t	20	20	10
μ_x, μ_y [/cell] (°)	105, 102	93.6, 90	79, 79
ν_x, ν_y	0.582, 0.565	0.78, 0.75	0.876, 0.875
$\hat{\beta}_x, \hat{\beta}_y$ (m)	37.29, 36.29	20.78, 21.18	15.58, 15.62
$\hat{\eta}$ (m)	6.01	3.69	3.39
η_i (m)	−0.26	−0.15	−1.11
ξ_x, ξ_y	−1.40, −1.45	−1.28, −1.31	−1.19, −1.20

the three-cell superperiod is the only one giving the required value for γ_t at a phase advance close to 90° per cell, at the same time the length goes through a shallow minimum.

Acknowledgements

The LEB design has been the result of many individuals collaborating towards the same goal. E.D. Courant from Brookhaven National Laboratory, A. Garren from LBL, F. Botlo-Pilat, R. York and S. Machida all contributed significantly to the design.

2.2 Rf Program

(N.K. Mahale)

2.2.1 Overview

Since the LEB is the first synchrotron in the injector complex it has to capture the Linac bunches with a minimum beam loss. The injection energy and the beam brightness requirements make space charge effects rather important. It is necessary to keep the space charge tune spread, measure of which is the Laslett tune shift, small. Another requirement is matching the LEB bunch at extraction to the MEB (Medium Energy Booster) bucket; this, however, is not stringent since it is acceptable to blow up the longitudinal emittance in the MEB. Since a larger longitudinal emittance is required by the subsequent synchrotrons, it may be desirable to blow it up in the MEB if that does not increase the transverse emittance. Exact longitudinal matching requires too low an rf amplitude unless it is done dynamically by shaping the bunch by rf manipulations.[11] The cost of the rf system and therefore the maximum rf amplitude should be minimized with all the above criteria satisfied, requiring that the longitudinal emittance be small, while reduction of space charge effects favors the opposite approach.

The LEB can operate both at the 10-Hz sinusoidal magnet cycle and with a slow linear ramp. The latter operational mode, however, is not critical from an rf design point of view, and while rf programs for both modes are given, the emphasis is on the 10-Hz operation. A modified injection-timing scheme, which under ideal conditions could capture nearly 100 % of the beam in the 10 Hz mode, has been investigated and is discussed briefly.

2.2.2 Injection Process

The LEB rf system operates at a harmonic number of $h = 114$, therefore the bunch to bunch distance is 5 m. Since the Linac rf frequency is 1282.851 MHz, about 27 times the frequency of the LEB at injection, a 5-m Linac pulse has 27 buckets; however, only every third Linac bucket is filled. Multi-turn injection accumulates four turns during Collider operation and 20 turns for test beam operation to provide the specified beam intensity. Accumulation in the LEB is achieved by stripping the H^- beam from the Linac, thus being able to merge incoming with circulating beam.

Linac bunches are energy-compressed in the transfer line (with an rf cavity) to reduce the energy spread to 100 keV *rms* and the mean energy

jitter to 75 keV *rms*. Doing so reduces the rf voltage needed in the LEB to capture and accelerate the beam. The transverse emittance of the Linac beam is about 0.25 πmm-mr but is expected to increase to 0.4 πmm-mr during accumulation in the LEB due to scattering in the stripping foil.

The Linac rf frequency deviates slightly from the exact multiple of the LEB rf frequency so that the Linac bunches, referred as micro bunches, will be evenly spread along the circumference of the LEB during multiturn injection. In this way, high local current densities are avoided that may increase space charge tune shift. A slight tilt of the Linac bunches in the E-ϕ plane caused by the transfer line aids this spreading process. The injection process is the same for all operation modes; the pulse length, however, can be varied from 1 μs to about 40 μs.

2.2.3 10-Hz Cycle

The 10-Hz cycle is the fundamental LEB mode supporting Collider operation. The specified ("baseline") rf system consists of eight cavities operating at a single harmonic. Addition of a higher-harmonic rf system may reduce the space charge tuneshift and, thus, the emittance growth; this has been investigated and discussed later in Section 2.2.3.

Baseline Rf Program

The capture process used in the LEB differs somewhat from pure adiabatic capture.[12] In a resonant machine, in which the magnets are excited on a sinusoidal power supply, it is not possible to provide a flat bottom. The synchronous angle becomes non-zero almost immediately upon injection, not leaving sufficient time for adiabatic capture due to contraction of the bucket length (the bucket length is reduced by about three times the synchronous angle). This will give rise to considerable amount of beam loss. The process outlined below ameliorates this problem.[13]

The rf amplitude is set large enough at the onset of injection for there to be no particles outside the bucket near the center of the bucket (Figure 2.5a). Initially, a constant rf amplitude is maintained during which the particles near the unstable point move toward the center of the bucket (Figure 2.5b). Then the rf amplitude is increased rapidly, and the particles outside the bucket are captured. Capture efficiency is increased compared to pure adiabatic capture. The initial rf amplitude of 24 kV is set such that the losses are minimized.

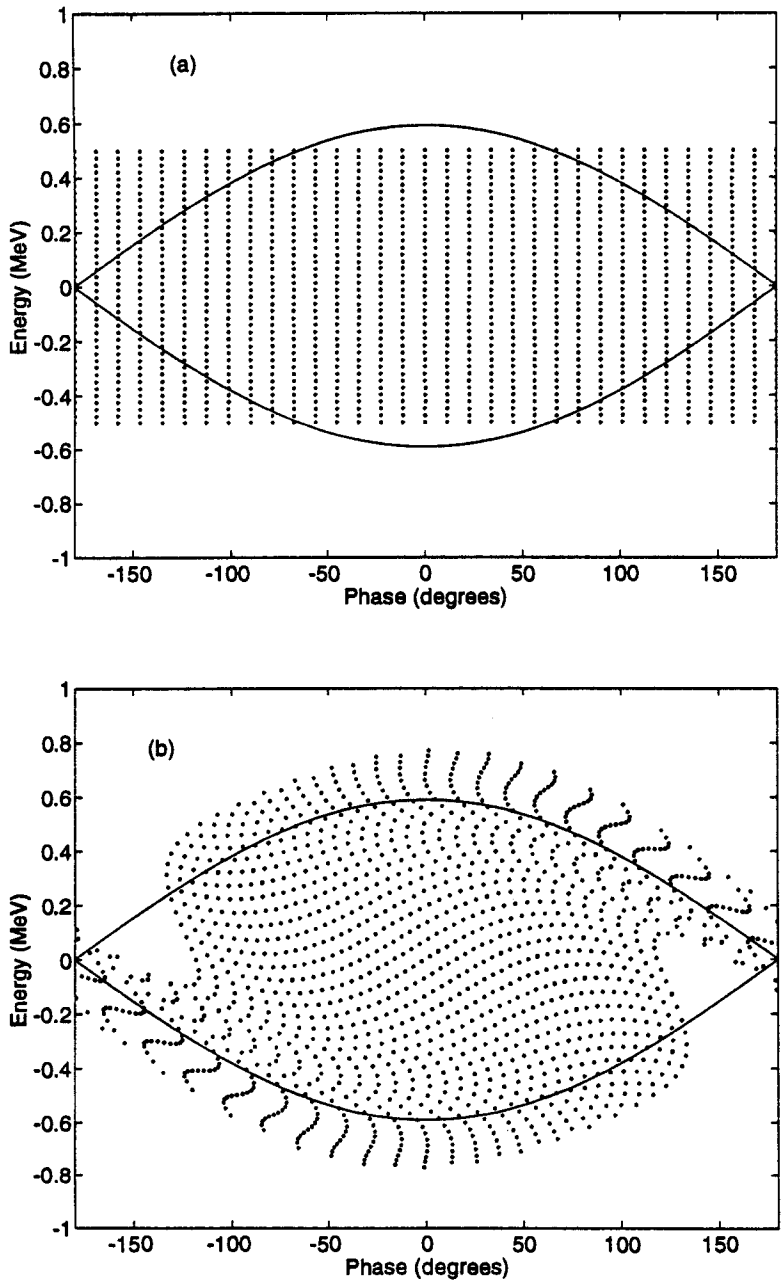

Figure 2.5: Capturing process. (a) The particles at injection; (b) the bunch just before the bucket is enlarged (30 μs).

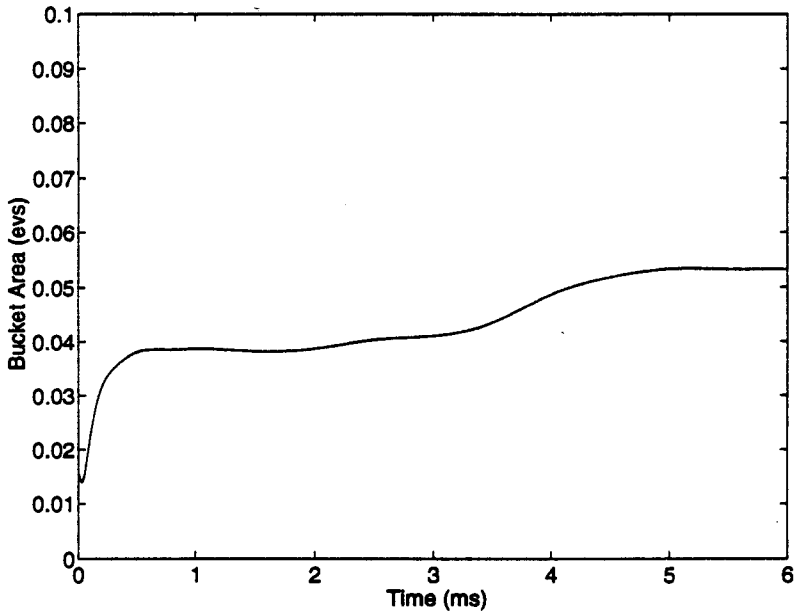

Figure 2.6: Bucket area *vs.* time for the first 6 ms.

Figure 2.6 shows the bucket area as a function of time for the first 6 ms. The capturing process lasts for about 2 ms. Between 2 ms and 4 ms the bucket area is kept small, 0.036 eVs; this keeps the particle density at the center and thus the tune shift low. The bucket area is increased to 0.054 eVs at 5 ms to prevent particle loss due to rf errors during the remainder of the cycle. The maximum demand for rf amplitude in order to maintain this bucket area, 765 kV, occurs at about 22 ms; this determines the voltage capability required of the rf system. It is necessary to keep the bucket area constant until that moment. If the bucket area is larger than 0.054 eVs before this time the bucket area would decrease during the cycle, giving rise to particle loss because of the large filling fraction. Later in the cycle γ increases and dE/dt decreases; to keep the bucket height small only a small rf amplitude is desired. This presents a difficulty due to the tightly bunched beam leading to greater beam loading towards the end of the cycle. Therefore the final amplitude has been chosen to be 80 kV, somewhat depending on the cavity characteristics. This value still being too large for matching the

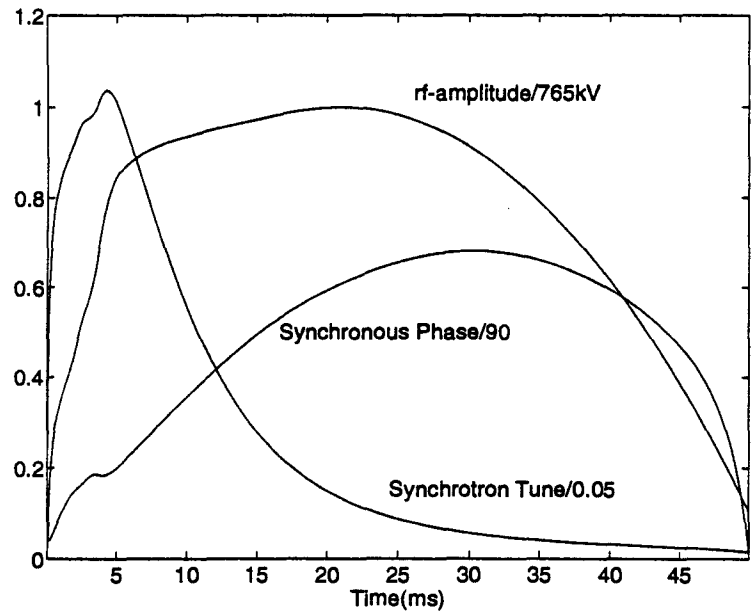

Figure 2.7: Rf amplitude *vs.* time.

bunch to the MEB bucket either rf manipulation will be used to dynamically match the beam or the longitudinal emittance will increase in the MEB. Figure 2.7 gives the rf amplitude, phase and synchrotron tune *vs.* time. The maximum amplitude is 765 kV and the maximum synchronous angle is 62.5°. In Table 2.3 additional parameters of the rf program are given.

Second Harmonic Rf

Space-charge induced tune shift (actually, a tune spread) is directly proportional to the peak current density. Thus it can be reduced by "flattening" the bunches, *i.e.* moving particles from the center of the bunch to either end. This can be accomplished by adding a properly phased higher harmonic rf system which flattens the rf waveform at the peak and, thus, reduces longitudinal focusing at the center of the bunch. The choice of the harmonic to be used is a trade-off between voltage requirement (less for higher harmonic to flat top the rf) and the width of the flat top to be achieved, avoidance

Table 2.3: Baseline rf parameters.

Parameter	Value
Injection momentum	1.219 GeV/c
Extraction momentum	12 GeV/c
Harmonic number	114
Injection rf frequency	47.514 MHz
Extraction rf frequency	59.776 MHz
Injection rf amplitude	24 kV
Extraction rf amplitude	80 kV
Max. energy gain per turn	0.645 MeV
Max. energy gain per second	336 GeV
Max. rf amplitude	765 kV
Max. rf phase	61.25°
Max. rf slew rate	1.05 GHz/s

of possible sub-bunching and ease of controls, all of which favor a lower harmonic of the fundamental frequency.

The use of a second-harmonic system for the LEB has been investigated, although it is not part of the baseline design and no hardware has been designed. It has been anticipated operation would take place with the second-harmonic system active all the time, although space charge is only an issue at injection. In this way, the second-harmonic rf could be used to facilitate matching of the LEB bunches to the MEB bucket, and no special precautions to prevent the turned-off system to be driven by the beam would have to be taken.

A possible rf program for both rf systems together is shown in Figures 2.8 and 2.9. At injection the second-harmonic rf would be counterphased to the fundamental system, thus flattening the bunches as desired. In fact, by varying the phase slightly the second harmonic would act also as a Landau damping cavity. After gaining sufficient energy to reduce space charge tune shift (5 ms), the second harmonic would be brought in phase with the fundamental rf. During this time it would actually reduce the fundamental rf voltage needed to accelerate the beam. Towards the end of the cycle, the system would shift back to counterphased operation, thus matching the LEB bunch shape more closely to that of the waiting MEB buckets. In the transition

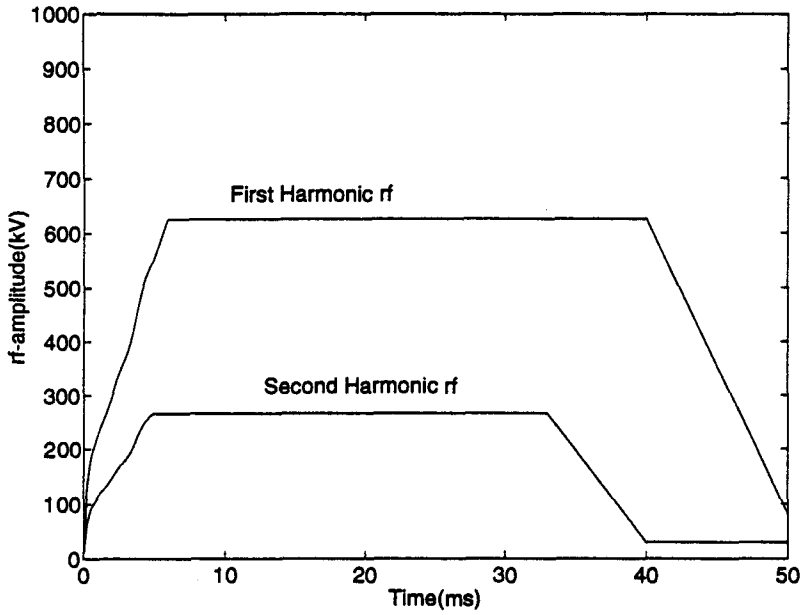

Figure 2.8: Rf voltage program with a second harmonic rf system.

regions the program parameters have been designed such as to minimize or avoid any beam loss.

Addition of a higher-harmonic rf system would complicate the low-level rf system and control of the rf. The rf and control systems designed for the LEB, however, have the flexibility to accommodate additions of this kind. Also, the lattice space exists in the ring to allow the addition of such cavities.

2.2.4 One-third Hz Operation

Slow ramped operation of the LEB is foreseen mostly for commissioning. The magnet ramp consists of 50-ms parabolic sections at the top and bottom and is linear in between. A 2-ms flat bottom at injection allows adiabatic capture of the beam without virtually any loss. Figure 2.10 shows the rf amplitude as a function of time. The initial amplitude is 24 kV, and the final amplitude is 80 kV as for 10-Hz operation, but the maximum required amplitude is reduced to 295 kV. Due to the slow increase in energy the emittance of

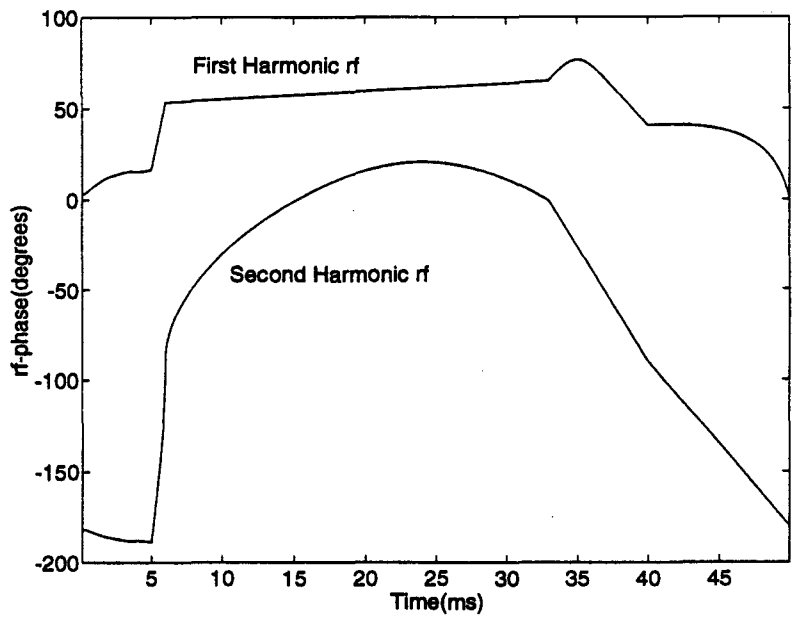

Figure 2.9: Rf phase program with a second harmonic rf system.

the beam will not meet the specifications for collider filling operation. The specifications for the test beam, however, are easily met.

2.2.5 Conclusions

In this section the rf program and design criteria are presented. One of the issues that will be faced during commissioning is synchronization of the rf program and the magnet ramp. The bottom of the ramp is rather difficult to detect. If injection occurs late on the ramp there may be considerable loss of beam since the synchronous angle is not zero. It would be advantageous to synchronize the rf with the beam injection; this can be done if the injection is before the bottom of the magnet curve.[13] Preliminary analysis shows significant improvement in the capture efficiency if injection occurs some 125 μs before the bottom of the ramp, while the sensitivity to injection errors appears reduced. Also, the optimum initial amplitude increases to 40 kV and capture is less sensitive to variation. This modification is

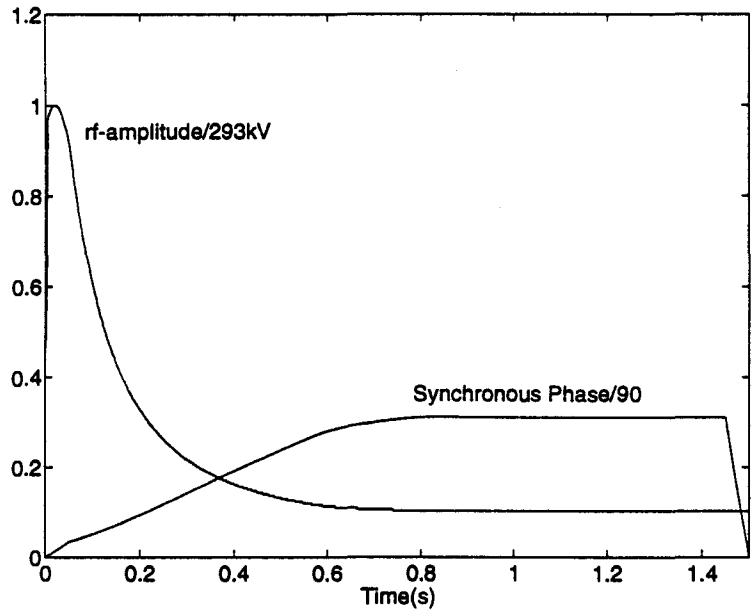

Figure 2.10: Rf program for the one-third Hz cycle.

described in Section 2.3.2 of this book. The effect of rf errors, however, has not been analyzed.

Acknowledgements

In the early days of the SSC, M. Furman of Lawrence Berkeley Laboratory collaborated to the design of the rf program.[14] The matching studies were done in collaboration with A. Maschke.[11] Use of a higher-harmonic rf system to reduce space charge forces has been suggested by W. Weng from Brookhaven National Laboratory during an injector review.

2.3 Beam Dynamics

(N.K. Mahale, U. Wienands, X. Wu)

2.3.1 Single-Particle Transverse Beam Dynamics (U. Wienands, X. Wu)

First-order Stability of the Lattice

An important consideration in any sectioned lattice—but especially in a fast-cycling machine—is the stability of the lattice under conditions of imperfect matching. Such conditions can arise from setting errors, eddy-current effects and space-charge and chromatic detuning and were studied in some detail. In Table 2.4 some results for different arc-straight mismatches are presented, where the quadrupoles in the arcs and straight sections were set different from their optimal values. It can be seen that differences up to 1 % are easily tolerable if both F and D quadrupoles err in the same direction; up to 0.5 % if F and D quadrupoles err in the opposite direction. In all these cases dispersion in the straight sections remains very well controlled.

Table 2.4: Mismatch results.

Arcs		Straights		Straights			
F quad	D quad	F quad	D quad	$\delta\hat{\beta}_x/\hat{\beta}_x$ (%)	$\delta\hat{\beta}_y/\hat{\beta}_y$ (%)	$\hat{\eta}$ (m)	γ_t
0.0 %	0.0 %	0.0 %	0.0 %	0.0	0.0	0.0	22.4
−1.0 %	−1.0 %	+2.3 %	+2.3 %	+18.2	+10.5	+0.10	19.8
+1.0 %	+1.0 %	−2.3 %	−2.3 %	− 2.0	− 5.4	−0.17	27.0
+0.5 %	−0.5 %	−1.05 %	+1.05 %	+ 0.5	+ 3.4	−0.12	25.4
−0.5 %	+0.5 %	+1.05 %	−1.05 %	+ 7.0	− 2.2	+0.07	20.2

Chromaticity Correction

The natural chromaticity of of the LEB lattice ($d\nu/d(\delta p/p)$) is about −15 in both the horizontal and the vertical plane. A total of 48 chromaticity sextupoles arranged in three families are positioned in the four straight cells in each arc to provide the chromaticity correction. Here they take advantage of the high momentum resolution $\eta/\sqrt{\beta}$, while at the same time

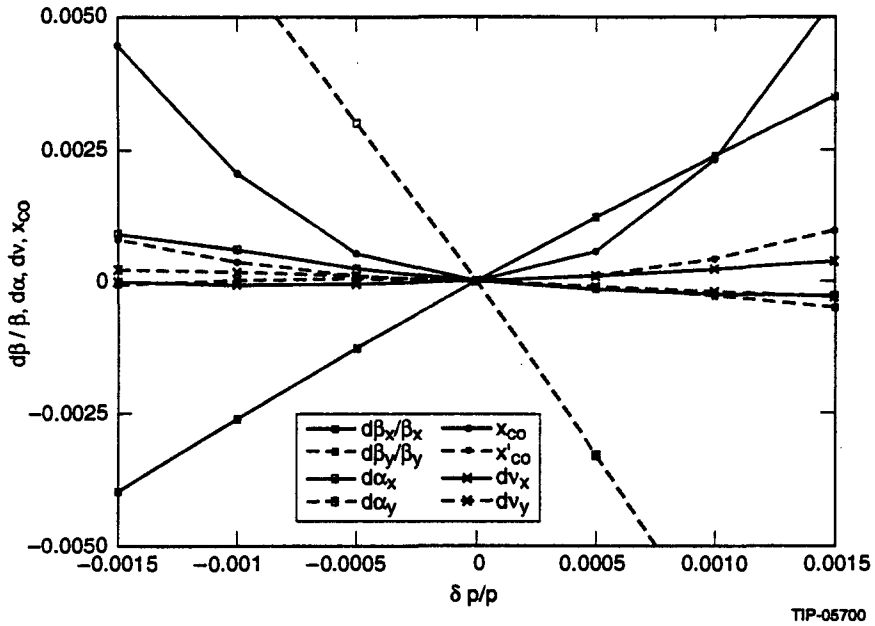

Figure 2.11: Chromatic variation of the LEB lattice functions.

requiring additional cell length. In the horizontal plane the arcs constitute second-order pseudo-achromats with no second-order geometric aberration terms. Figure 2.11 shows the chromaticities of various lattice functions for the chromaticity-corrected lattice.

Tracking Studies

Extensive beam dynamics studies[15] have been carried out to verify the optical stability and simulate the machine performance of the LEB lattice. The single-particle studies presented in this section include evaluation of the effects of misalignment and field errors, analysis of betatron resonances and their driving terms, and evaluation of correction schemes for closed-orbit excursions and betatron resonances. Most of these studies have been done with the orbit tracking and mapping modules of the beam optics and accelerator design codes DIMAD[16] and COSY INFINITY.[17] Additional ring lattice analysis tools and procedures have been developed in the process, these include tools to facilitate transfer of machine descriptor files and maps between DIMAD and COSY INFINITY.[18]

The LEB is space-charge dominated when delivering beam for Collider operation, therefore, the simulation of space-charge dominated beams has been a prime focus of the attention of the LEB simulation work. It is unfortunate that this activity cannot be documented here as the principal investigator of space-charge effects in the LEB has left the SSC Laboratory before writing of this document was begun.

The machine studies have followed a path of successive refinement. Analysis of the performance of the "perfect" lattice is a good indicator for the soundness of the basic lattice design. Misalignment and correction of the resulting closed-orbit excursions are studied to assess various correction schemes and derive the corrector strength needed. Inclusion of the field errors of the magnetic elements is then used in parallel with the magnet design effort to specify the field uniformity requirement for the magnets. At the same time these studies give important insight into the non-linear behavior of the lattice. Once the magnet designs have been sufficiently advanced resonance-correction studies have demonstrated how the machine acceptance can be extended by suppressing the driving terms of those resonances that will be crossed by the beam. It should be noted, though, that the LEB design does not depend on the presence of a correction system to meet its specifications.

The tracking studies have in general been carried out as 1000-turn runs of "protons" in the computer code DIMAD under static conditions (*i.e.* no acceleration). Since at injection the beam is largest and thus nonlinear effects are strongest most runs have been performed at injection conditions. In all cases the operating margins under extraction conditions were found to be more relaxed—*i.e.* less smear, larger acceptance relative to beam emittance, *etc.*

The "Perfect" Lattice Protons with different initial amplitudes are tracked through the "perfect" LEB lattice (*i.e.* no misalignments or field errors) where the major sources of nonlinearity are the chromaticity sextupoles.

Figure 2.12 shows the transverse phase space plot and the betatron resonance spectrum of the tracking result of a proton at $\epsilon^* = 36\pi$ mm-mrad. The 1000-turn dynamic aperture is larger than 800 π mm-mrad. The horizontal and vertical "smear" (*rms*) for the proton beam, $\sigma_{\epsilon_x}/\epsilon_x$ and $\sigma_{\epsilon_y}/\epsilon_y$, which indicate the degree of nonlinearity of the betatron motion, are 2.0 % and 3.7 % at $\epsilon^* = 5.4\pi$ mm-mrad (3 σ collider beam), and 6.3 % and 9.5 %

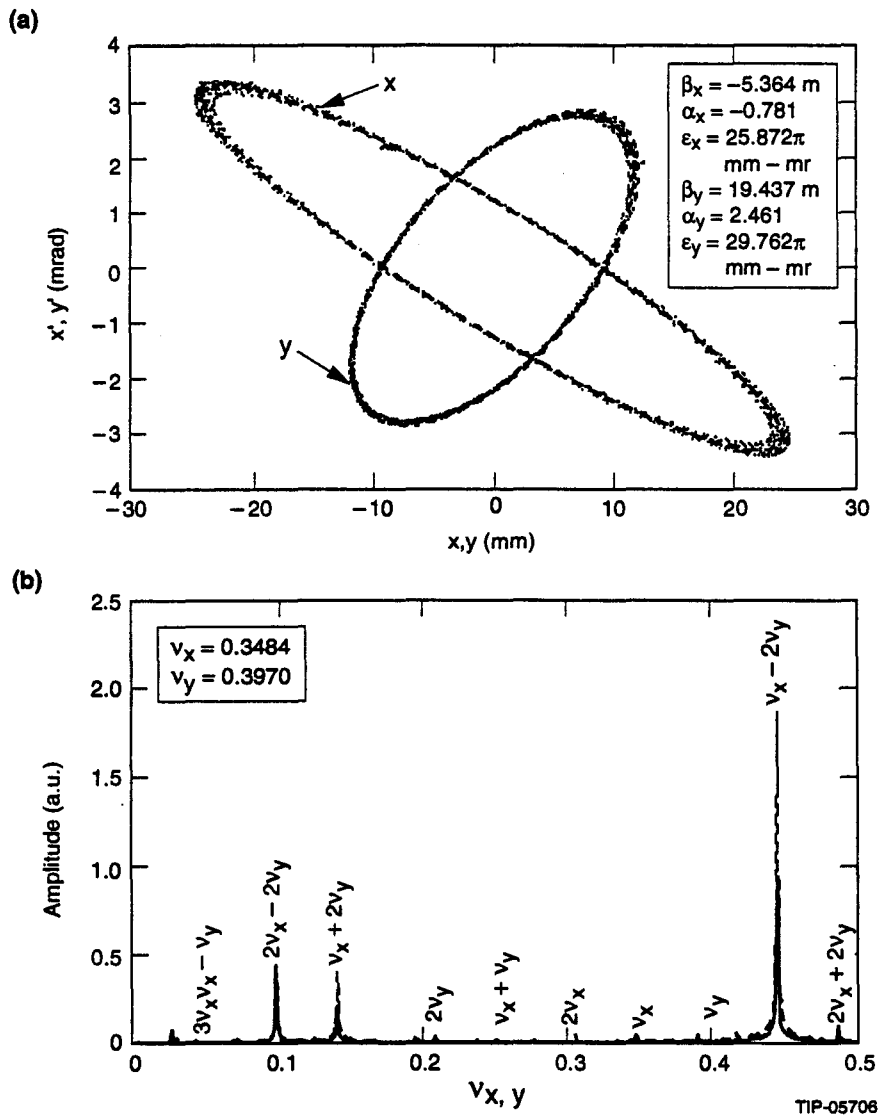

Figure 2.12: Transverse phase space (a) and betatron resonance spectrum (b) of the "ideal" LEB lattice.

Table 2.5: Alignment tolerances.

Parameter	Main dipole	Main quadrupole	Corrector
σ_x	1.0 mm	0.4 mm	1.0 mm
σ'_x	1.0 mrad	1.0 mrad	2.0 mrad
σ_y	1.0 mm	0.4 mm	1.0 mm
σ'_y	1.0 mrad	1.0 mrad	2.0 mrad
σ_z	5.0 mm	5.0 mm	5.0 mm
σ'_z	1.0 mrad	1.0 mrad	1.0 mrad

at $\epsilon^* = 36\pi$ mm-mrad (3 σ test beam), respectively. The Fourier transform (FFT) of the tracking coordinates produces the betatron resonance spectrum in Figure 2.12. The dominant resonance causing most of the "smear" is the third-order structural resonance at $\nu_x - 2\nu_y = -12$, which arises due to the deviation of the vertical phase advance in the arcs from $3 \times 2\pi$. It has been demonstrated by Machida[19] that the lattice can be retuned to suppress this resonance; however, once all lattice imperfections and space-charge effects are taken into account, the improvement of optical performance at this working point has been found to be insignificant.

Misalignment and Correction of the Closed Orbit Alignment errors are a fact of life in accelerator construction and their effects have been carefully studied to set alignment tolerances that are neither overly strict and expensive, nor overly relaxed impacting the optical properties of the machine. The orbit-correction system uses dedicated orbit-correction dipoles in both planes rather than back-leg windings on the main magnets in order to achieve the fast response necessary to dynamically adjust the orbit should this become necessary.

Misalignment and orbit-correction studies have been carried out using DIMAD. Gaussian-distributed misalignments are randomly imposed on each element in the lattice. Ninety beam position monitors (BPM), which are adjacent to the main quadrupoles, are used to read the transverse beam positions. Each main quadrupole also has an associated orbit-correction dipole (OCD) acting in its focusing plane, which is used to minimize the beam position monitor readings at the next BPM active in that plane. Each orbit corrector is individually controlled.

Table 2.5 shows the alignment tolerance specified for the LEB magnets. Orbit correction then proceeds in DIMAD by tracking a particle launched on

the central orbit (all coordinates 0) and using 90° corrector-monitor pairs to minimize the read-out value of the monitor in a least-squares procedure. The impact of a given set of misalignments on machine dynamic aperture, emittance growth, residual closed-orbit excursion and correction dipole strength have been evaluated and used to establish the alignment tolerance for the LEB lattice elements given in Table 2.5. The closed-orbit excursions in the LEB lattice with these misalignments are given in Table 2.6 for five different seeds of the random-number generator.

Table 2.7 shows the closed-orbit excursions of the lattice after orbit correction, for the same five random seeds. The required maximum strength of the corrector dipoles is given in Table 2.8. Figure 2.13 shows a typical closed-orbit distribution in the LEB lattice before and after correction.

Table 2.6: Uncorrected closed-orbit excursion.

Seed	x_{rms} (mm)	y_{rms} (mm)	x_{peak} (mm)	y_{peak} (mm)
1	3.91	3.82	12.75	11.34
2	4.30	4.98	15.75	11.56
3	5.10	4.92	17.76	12.58
4	3.17	3.15	14.54	9.30
5	4.12	3.43	14.58	10.88

Table 2.7: Corrected closed-orbit excursion.

Seed	x_{rms} (mm)	y_{rms} (mm)	x_{peak} (mm)	y_{peak} (mm)
1	0.87	1.06	4.48	5.28
2	0.95	1.02	3.55	4.48
3	0.89	0.86	4.42	3.83
4	0.87	1.06	4.08	5.06
5	1.11	0.90	4.86	4.24

The magnetic field parameters of the lattice elements determine the transverse machine acceptance but can also lead to transverse emittance growth and possibly beam loss. The effects of magnetic field errors have been studied and specifications for the magnet design developed. Iterating back and forth between magnet design using the codes POISSON and PE2D,[20–24] and particle tracking using DIMAD at injection and extraction energies using the field distributions, magnet polefaces and iron yoke are optimized. This iteration is continued until both linear and non-linear machine acceptance are sufficient, *i.e.* the acceptance is outside the beam pipe

Table 2.8: Maximum strength of orbit-correction dipoles.

Seed	Max. strength
1	1.41 kG
2	0.93 kG
3	0.85 kG
4	1.35 kG
5	1.38 kG

and the linear acceptance is outside of the 3 σ Collider beam envelope. As prototype magnets have become available and their magnetic field distributions and harmonics are measured these are used in the tracking models. The measurements also give an indication of the non-allowed field harmonics present in the magnets that are caused by mechanical imperfections. Details of the magnet measurements are given in Section 3.1 in this book.

Figure 2.14 shows the transverse phase space plot and the betatron resonance spectrum of the tracking result for a particle at an amplitude corresponding to $\epsilon^* = 36\ \pi$ mm-mrad. The tracking model includes magnetic field errors, misalignment and closed-orbit correction. The field errors have been parametrized as thin lenses which are placed at the beginning, center and the end of each magnet. The central multipole has four times the strength than the outer multipoles, for a Simpson-like arrangement believed to improve the accuracy of the model. The sum of these multipole strength equals the integrated strength of the measured (or designed) field harmonic.

Increased rms "smear" is evident for particles at large amplitude, resulting in significant transverse emittance growth. The dynamic aperture of the lattice is reduced from about 800 π mm-mrad to 60 π mm-mrad; however, this is still well beyond the vacuum system admittance of 40 π mm-mrad. Studies of multiple seeds for the random component of the magnetic field errors and for the alignment errors indicate little dependence of the dynamic behavior on the specific setup. The "smear" is caused by the increase of the amplitude of the dominant third-order structural resonance as well as strong linear coupling resonances at $\nu_x + \nu_y = 23$ and $\nu_x - \nu_y = 0$, driven by the misalignment and magnetic field error multipoles.

Resonance Correction Third order resonances are excited not only by the chromaticity sextupoles in the arc sections but also by the magnetic field harmonics and by alignment errors due to symmetry breaking. While

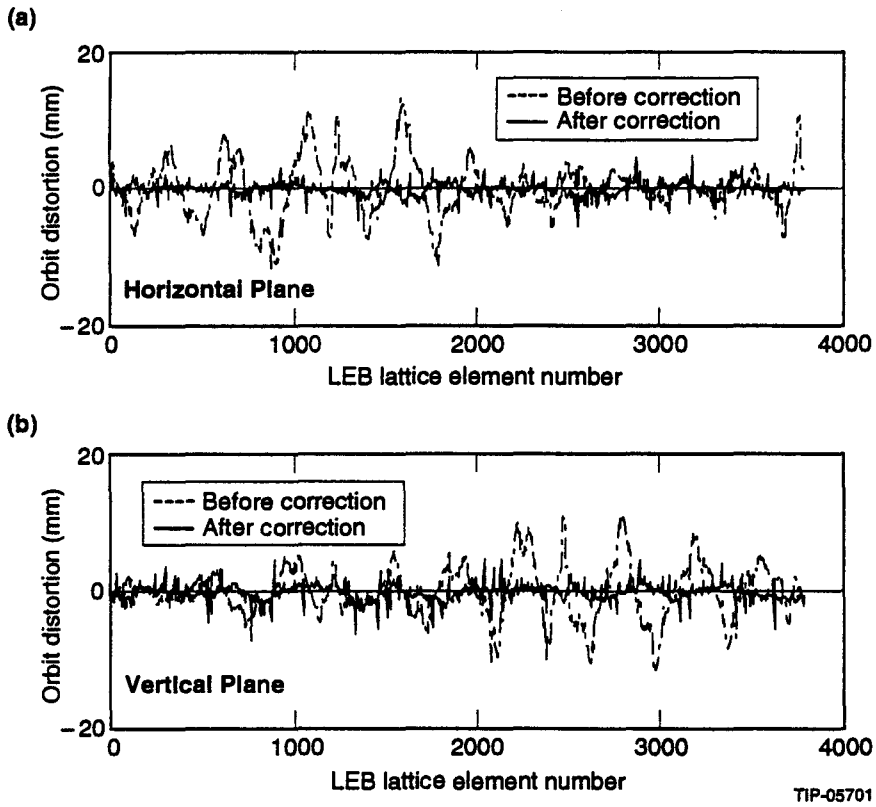

Figure 2.13: Typical closed orbit excursion with the field errors and misalignment of the magnetic elements before and after the closed orbit correction.

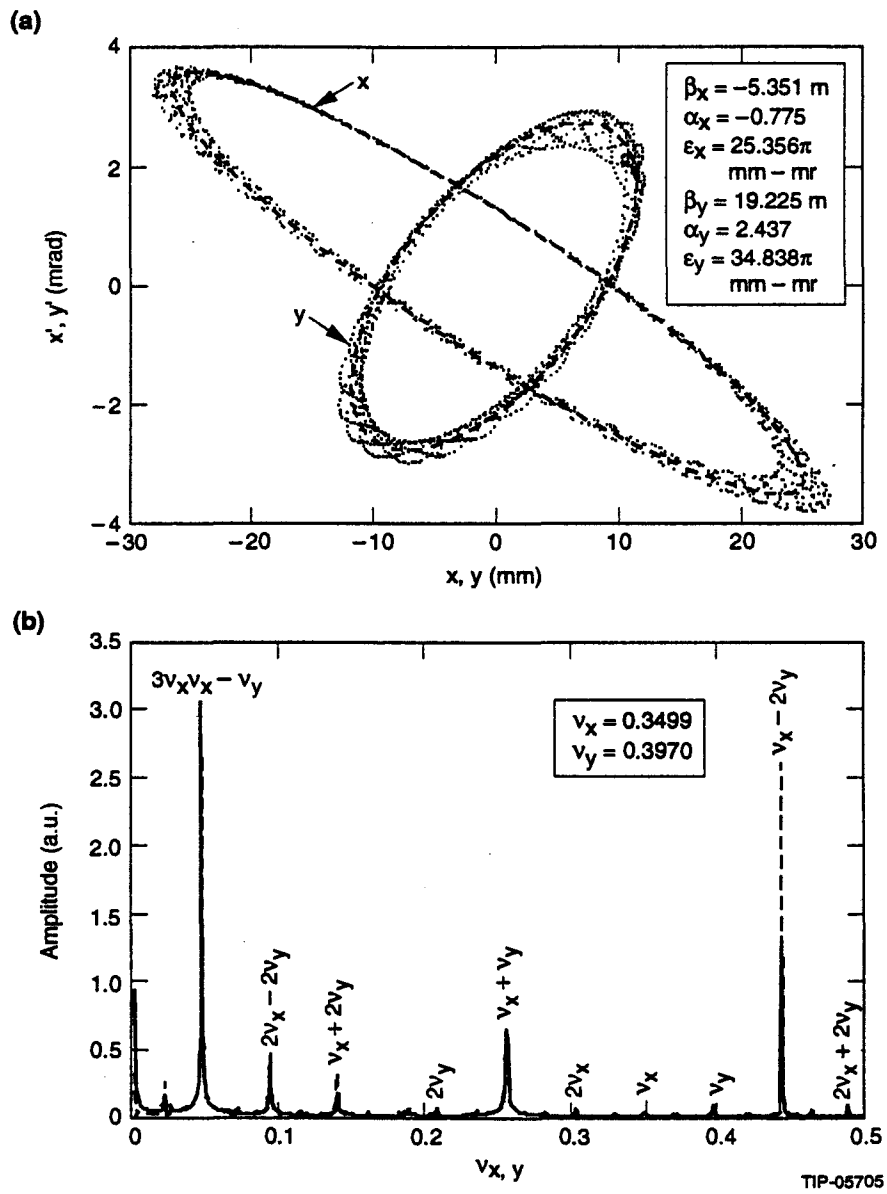

Figure 2.14: Transverse phase space (a) and betatron resonance spectrum (b) of the LEB lattice with magnetic errors, misalignment and closed orbit correction.

our tracking studies indicate that these resonance strengths are quite tolerable, they do generate significant "smear" for the particles at large betatron amplitudes and therefore might conceivably lead to unwanted transverse emittance growth.

A resonance correction procedure has been developed at SSCL using DIMAD and the differential-algebra (DA) code COSY INFINITY. To facilitate systematic resonance analysis and correction, new features have been introduced into DIMAD to allow transfer of a complete lattice description, including imperfections, like field and alignment errors and orbit corrector settings, to COSY INFINITY, which is used to produce Taylor series maps of the lattice to any given order. The DA tools available in COSY INFINITY are then used to analyze the map, evaluate non-linear resonance phase and strength coefficients and to perform the resonance correction systematically using available correctors. Since the number of different correctors used is always small (< 10), their settings can easily be transferred back to DIMAD manually for verification of the correction.

The third-order structural resonance driving terms can be corrected by adding new sextupoles in either the arcs or the straight sections. Extensive studies have been carried out using either option. Although reasonable resonance correction has been achieved with either scheme, the requirement for additional sextupoles is somewhat difficult to satisfy due to the tight space allocation. The adopted correction scheme employs the chromaticity sextupoles already in the lattice, superimposing a strength modulation to reduce the resonance-driving geometric terms. The superimposed strength is adjusted in 8 families rather than 3. To avoid coupling of the resonance correction with the chromaticity setting the 8 families are grouped into 4 family pairs with the same modulation strength but with opposite polarities. Since each pair occupies symmetric positions in each arc, its influence on the chromaticity is cancelled. Although only four independent parameters ("knobs") exist—plus the three chromaticity knobs—better resonance correction is achieved than by using separate sextupoles in the straight sections.

The degree of correction is limited by the correction system driving other resonances, mostly of the same order. The penalty function used in the fitting of corrector strength therefore takes into account the strength of all third-order resonances to find an overall optimum.

The linear coupling resonances $\nu_x + \nu_y = 23$ and $\nu_x - \nu_y = 0$ are mainly caused by the skew quadrupole terms of the field error multipoles and feed-down from the sextupole terms by element misalignment. Four skew quadrupoles have been added in the injection straight section to globally decouple

the lattice. The complex coefficients of the contributions by these skew quadrupoles to the coupling resonances have been calculated using the resonance analysis code RES,[25] which implements the formulae of Guignard.[26] Four orthogonal parameters are defined which are linear combinations of the four skew-quadrupole strengths. Each parameter can be used independently to compensate the real or imaginary coefficient of a certain coupling resonance excited by the existing lattice. The correction procedure again consists of iterating back and forth between skew-quadrupole strength adjustment and FFT analysis of the resultant tracking results, but by having orthogonal parameters the procedure converges fast enough for manual iteration, an important point for operation of the machine. Multiple seeds for magnetic field and alignment error generation and different LEB working points have been investigated. The 6-dimensional tracking code SIMPSONS[27] has been used to compare and validate the tracking results.

Figure 2.15 shows the transverse phase space plot and the betatron resonance spectrum of the tracking result for a particle at $\epsilon^* = 36\pi$ mm-mrad after second- and third-order resonance correction. The improvement of linearity is evident by comparison with Figure 2.14. The dominant third-order structural and linear coupling resonances have been almost eliminated. For a specific random seed, the horizontal and vertical "smear" (rms) of the emittance are 2.9 % and 2.5 % at $\epsilon^* = 5.4\pi$ mm-mrad and 5.6 % and 4.1 % at $\epsilon^* = 36\pi$ mm-mrad, respectively; to be compared to about 30 % in the uncorrected case. Similar results were obtained for different seeds for magnetic field and alignment errors and at different LEB working points such as $(\nu_x, \nu_y) = (11.85, 11.80)$.

Dynamic Aperture Figure 2.16 shows the average dynamic aperture as a function of $\delta p/p$ for the LEB lattice, before resonance correction. The acceptance is well beyond the LEB vacuum system aperture of 40π mm-mrad for $\delta p/p$ between $\pm 5 \times 10^{-3}$. Also shown is the linear aperture after resonance correction for a specific random seed of misalignment and field errors. Here the linear aperture is defined as the initial amplitude of particles for which the smear $d\epsilon/\epsilon < 10$ %, expressed in terms of the normalized emittance ϵ^*. For this specific case, the resonance correction has increased the dynamic aperture by about 20 % and extended the linear aperture well beyond the LEB vacuum chamber aperture within $\delta p/p$ of $\pm 5 \times 10^{-3}$. Similar results have been obtained for different seeds for magnetic field and alignment errors.

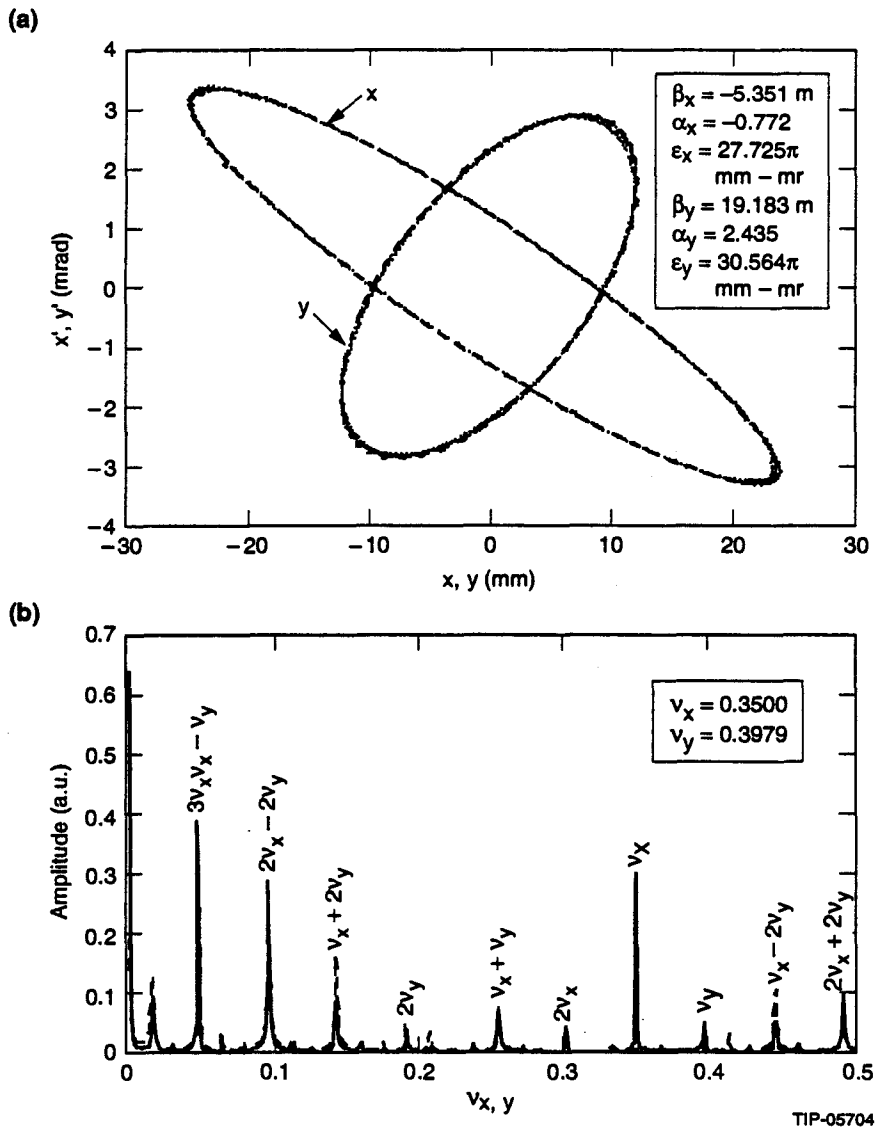

Figure 2.15: Transverse phase space (a) and betatron resonance spectrum (b) of the LEB lattice after the resonance corrections.

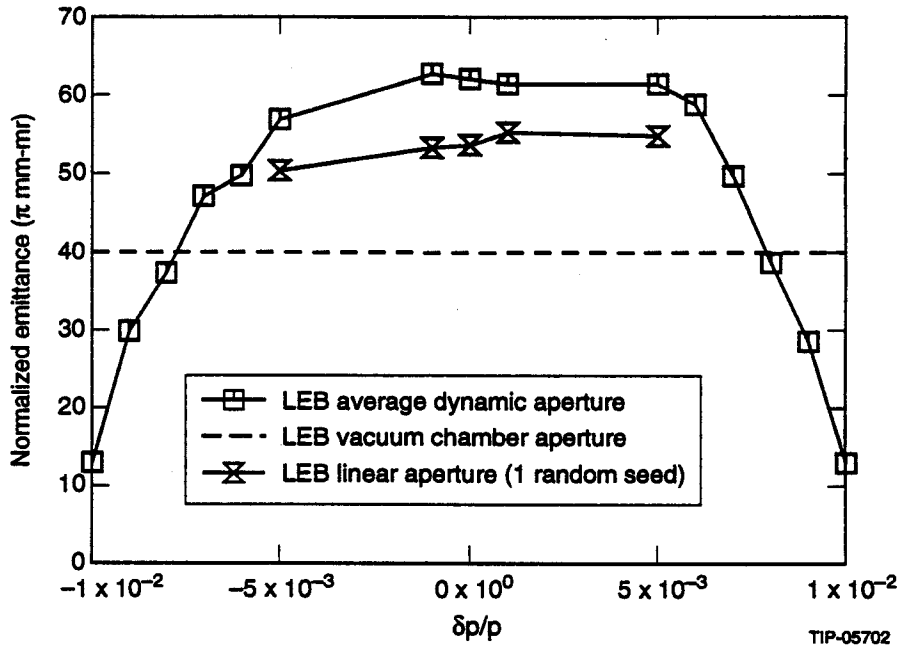

Figure 2.16: Dynamic aperture of the LEB lattice.

Table 2.9: Longitudinal beam dynamics parameters.

Parameter	Value
Capture efficiency(no errors)	99.8 %
Bunch area at injection (95 %)	0.011 eVs
Bunch area at extraction (95 %)	0.025 eVs
Bunch length at injection (*rms*)	1.43 m
Bunch length at extraction (*rms*)	0.14 m
Bucket area at injection	0.016 eVs
Bucket area at extraction	0.760 eVs
$\delta p/p$ at injection (*rms*)	0.107×10^{-3}
$\delta p/p$ at extraction (*rms*)	0.25×10^{-3}

2.3.2 Longitudinal Beam Dynamics (N.K. Mahale)

Longitudinal beam dynamic simulation has been done using the code ESME.[28] The beam is assumed to be round, in a round beam pipe; one bunch is filled and 114 fold superperiodicity is imposed. 43,200 macro particles are used in the simulation. Space charge effects are incorporated as described the literature.[29] 1024 bins are used for estimating the longitudinal distribution of particles in the bunch. Fourier modes are cutoff above a frequency given by[30]

$$\omega_{cut} = 1.841\frac{c}{r}, \tag{2.4}$$

where c is the velocity of light and r is the radius of the beam pipe. This equation holds true only approximately because the LEB beam pipe is circular in the quadrupoles and elliptical and curved in the dipoles. The geometric mean of the two semi axes of the elliptical cross section, which is about same as the radius of the beam pipe at the quadrupoles, is used in Eq. (2.4). Six space charge kicks are applied per turn. Various machine configurations have been simulated,[31] but only the baseline system is covered in this section. Beam dynamics parameters are given in Table 2.9.

For an idealized case, without errors, Figure 2.17 shows the longitudinal emittance (95 %) of the beam across the acceleration cycle. The spike in the curve is due to a small number particles, about 0.2 %, moving away from the bucket; when these particles are lost, the emittance, which is calculated only for the surviving particles, drops back. A particle is considered lost if

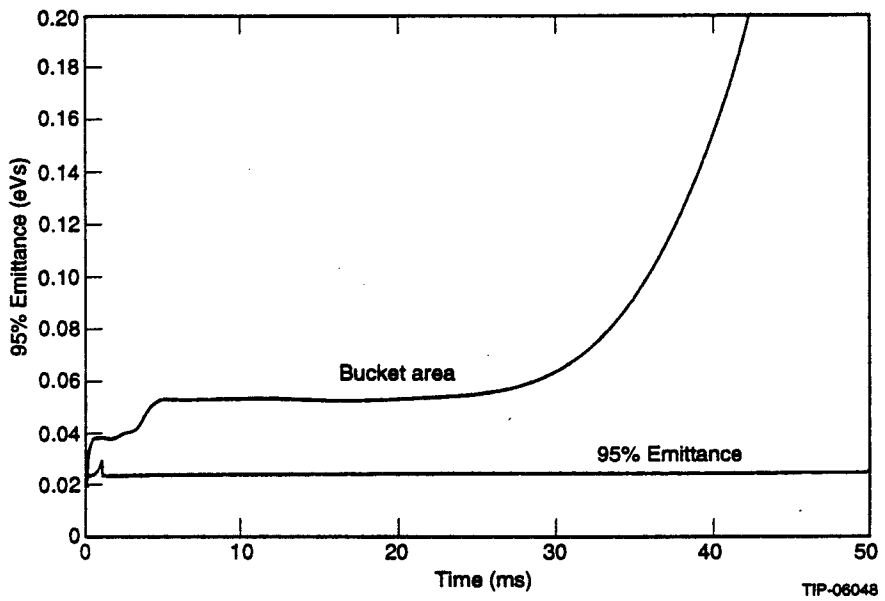

Figure 2.17: Longitudinal emittance and bucket area *vs.* time.

its mean closed orbit moves 1 cm—corresponding to $\delta p/p \approx 5 \times 10^{-2}$—away from the synchronous closed orbit. Figure 2.18 shows the maximum Laslett tune shift, with and without a second-harmonic rf system. The benefit of the second harmonic system manifests itself in the reduced tune shift evident in the figure. It has been found in a fully six-dimensional tracking study that the second-harmonic system reduces the increase in the transverse emittance by up to a factor of two.[32]

Several injection errors have been considered. Energy offset at injection can be compensated by tuning the magnetic field. The energy compressor has a considerable amount of control over the energy spread; it is assumed that a total momentum spread covers this uncertainty. Timing error of the injection increases losses, especially if injection occurs after the bottom of the magnetic field. Since the synchronous phase angle is non zero the beam loss will increase rapidly. Injecting early in the cycle, by about the uncertainty in the detection of the bottom of the magnet cycle, this can be avoided. An error in the synchronization of the rf program and the magnetic field, however, is most detrimental. Figure 2.19 shows the loss of particles as function of this synchronization error. Evidently it is of advantage to start the rf program early such that the sensitivity to this error is minimized. It

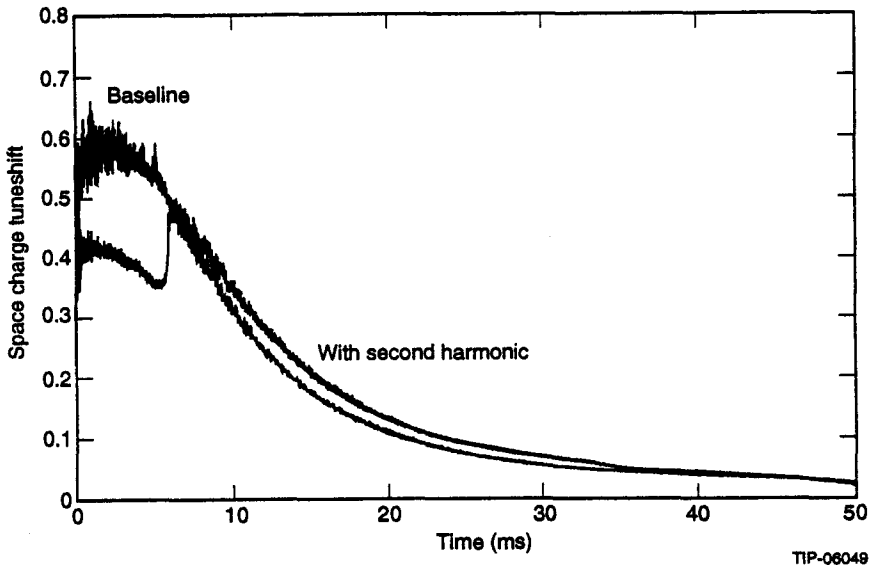

Figure 2.18: Laslett tuneshift *vs.* time.

is also preferable to synchronize the injection and rf program and choose an injection time before the bottom of the magnetic field.

Simulation of phase and amplitude noise in the rf system has been carried out in order to assess the sensitivity of the system and to set specifications for the low-level rf system. These calculations are not straightforward since the noise is not uniformly distributed due to the large time constant of the high-Q cavity. Realistic error analysis must also simulate the rf feed back loops; the design of which depends on the tolerance specification. Simulations have been done using errors generated with an exponential autocorrelation; *i.e.* the correlation function is assumed to be exponentially decaying. Phase errors and amplitude errors are assumed to be uncorrelated. Gaussian random errors with various correlation time have been investigated.[31] Not surprisingly, setting the correlation time equal to one synchrotron period results in a maximum increase in the longitudinal emittance and in largest particle loss. Limiting the beam loss in the simulations to 2 % the tolerances on the phase and amplitude control have been set at 10 kV *rms* for the rf amplitude and 1° *rms* for the phase. These errors are used for the preliminary design of the control system. Addition of a second-harmonic rf system would introduce an additional parameter: the error in the relative phase between the two harmonics. This has not been studied at the time of project termination.

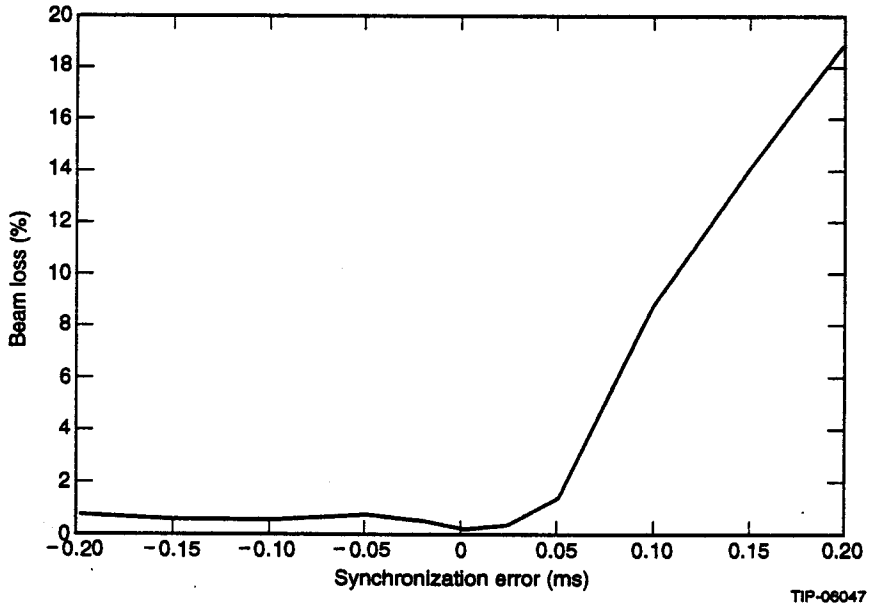

Figure 2.19: Beam loss *vs.* synchronization error.

2.3.3 Instabilities (N.K. Mahale)

Overview

Instabilities in the LEB are not expected to limit the Collider luminosity since the beam intensity is low. For test-beam operation at circulating current up to 0.5 A the situation is different, and while a certain amount of emittance growth can be tolerated in this case, beam loss has to be avoided. Instabilities that have been investigated in some details are:[33]

- Single-bunch longitudinal and transverse instability,
- Longitudinal coupled-bunch instability,
- Longitudinal bunch-by-bunch feedback requirements,
- Transverse coupled-bunch instability,
- Resistive wall instability,
- Trapped rf modes due to beam pipe discontinuities,

- Head tail instability,
- Beam loading (Robinson) instability.

Of these, the coupled-bunch instability and Robinson instability are most likely to limit the beam intensity, but active damping by feed back and feed forward can effectively limit growth times to where they no longer of concern.

Single Bunch Mode

Single-bunch instability is caused by the longitudinal or transverse impedance of the vacuum system. The threshold for the longitudinal impedance, for microwave instability, is given by,

$$\left|\frac{Z_{\|}}{n}\right| = \frac{2\pi \mid \eta \mid}{I_p}\frac{E}{e}\left(\frac{\sigma_E}{E}\right)^2 \tag{2.5}$$

where η is the slip factor, I_p is the peak current, E is the energy, e is the electron charge and σ_E is the energy spread of the bunch. The threshold for the transverse impedance causing mode-coupling instability is,

$$\mid Im(Z_{\perp}) \mid = \frac{2\nu_s}{I_{av}}\frac{E}{e}\frac{4\sigma_z}{\beta R} \tag{2.6}$$

where ν_s is the synchrotron tune, I_{av} the average current, σ_z is the bunch length, R is the radius of the machine and $\beta = v/c$.

Table 2.10 gives an estimate of the impedance in the ring and the threshold for the instabilities; the LEB is well below the threshold even at test-beam intensity.

Longitudinal Coupled-bunch Instability

The coupled-bunch instability is caused by higher-order modes (HOM) in the rf cavities. The growth time, τ, for the coupled-bunch instability can be estimated roughly by the formula,

$$\tau = \frac{2V_{rf}\cos\phi_s}{I_{av}Z\omega_s} \tag{2.7}$$

where V_{rf} is the rf amplitude, ϕ_s is the synchronous phase, h is harmonic number, ω_s is synchrotron frequency and Z is the shunt impedance of the higher order mode under consideration.

Table 2.10: Impedance estimates and thresholds; the impedance estimates have been doubled for contingency.

Parameter	Collider mode	Test beam
Laslett tune shift(maximum)	−0.6	−0.6
Longitudinal impedance budget	3.6 Ω	3.6 Ω
Z Longitudinal threshold		
Injection	380 Ω	76 Ω
Extraction	24 Ω	4.8 Ω
Transverse impedance budget	1.2 MΩ/m	1.2 MΩ/m
Z Transverse threshold		
Injection	83 MΩ/m	16.6 MΩ/m
Extraction	16 MΩ/m	3.2 MΩ/m

The rf frequency in the LEB sweeps from 47.5 MHz to 59.8 MHz while the synchrotron frequency varies from about 25 kHz to 500 Hz. Hence it is necessary to estimate the growth time at various points in the cycle, *i.e.* at injection (t = 0.1 ms), at maximum synchrotron frequency (t = 4.25 ms) and at extraction (t = 50 ms). It is assumed that the HOM under consideration coincides with the first synchrotron sideband to the bunch frequency. Besides the undamped case, damping of the HOM by a factor of 10, 50 and 100, using a passive HOM damper is considered. The HOM shunt impedance for the undamped cavity is assumed to be 100 $k\Omega$.

The most critical mode is $m = 1$ at the moment of injection. In the absence of damping the growth time is 0.40 ms and Landau damping in the beam is not sufficient. In the presence of HOM dampers the growth times are 11.2 ms, 239 ms and 594 ms, corresponding to damping factors of 10, 50 and 100, respectively. Based on these results, a HOM damper for the cavity has been designed[34] (see Section 3.3).

Longitudinal Bunch-by-Bunch Feedback Requirements

The LEB acceleration time is 50 ms; however in ramped operation the LEB may take up to 1.5 s to accelerate the beam to 11.1 GeV. The LEB has a large filling factor, close to one. Therefore longitudinal emittance growth will give rise to beam loss and it is desirable to have rf feed back in addition to the mode dampers.

For a single damping cavity with $R/Q = 40\ \Omega$ and a beam current of 500 mA the voltage and power requirements on the cavity are 60 kV and 14 MW in the absence of passive HOM dampers. If HOM dampers on the cavity are present, power requirements for the active damper are reduced to 4 kV and 62 kW for a passive damping factor of 10, 440 V and 0.8 kW for passive damping by a factor of 50 and 150 V and 0.1 kW for passive damping by a factor of 100.

Transverse Coupled-bunch Instability

Transverse coupled-bunch modes are driven by higher-order modes in the rf cavities and by the resistivity of the vacuum chamber. First we consider transverse multibunch instability driven by higher-order modes in the rf cavities. The contribution to this from the resistive wall will be considered in the next section.

The tune spread in the beam arinsing from various nonlinearities in the magnet lattice is on the order of magnitude of 10^{-3}. This will be sufficient for Landau damping of all modes. In addition there will be space charge tune spread of about 0.6. However, the dipole mode will not be Landau damped and dampers for the dipole mode may be required. Here, we consider bunch shape modes, $m = 0$ and 1, at injection and and extraction. At an impedance of 2 MΩ without the dampers, for the $m = 0$ mode, the growth times are 16 ms at injection and 20 ms at extraction; for the $m = 1$ mode these values are 12 ms and 499 ms. This requires dampers; damping by a factor of 10 is sufficient. At this damping rate the growth time for $m = 0$ mode is 244 ms at injection and 289 ms at extraction; for the $m = 1$ mode, 164 ms and 6864 ms. If this can be achieved then there is no need for transverse feed back system to damp the coupled-bunch instability.

Resistive Wall Instability

The resistivity of the vacuum chamber may cause transverse multibunch instability. To estimate the effect of the broadband impedance due to the wall the beam pipe is considered to be of circular cross-section and entirely made of Inconel 625 with a resistivity of $\rho = 12.5 \times 10^{-7}\ \Omega/\mathrm{m}$.

The growth time for the instability is given by,

$$\frac{1}{\tau} = \frac{c r_p}{2\pi\gamma} \frac{N_{total}}{\nu_\beta b^3} \delta \tag{2.8}$$

where c is speed of light, r_p is the classical radius of the proton, $\gamma = E/m$, N_{total} is the number of particles in the machine, ν_β is the betatron tune b is the pipe radius and δ is the skin depth.

At injection the growth times are 5.3 ms for Collider beam and 1.1 ms for test beam operation; at extraction these numbers are 46 ms and 9.3 ms. However, Landau damping due to the betatron tune spread will suppress the instability.

Trapped Rf Modes

The beam pipe, at quadrupoles, is circular with 80-mm inside diameter; the while in the dipoles it is elliptical with 62-mm major axis and 52-mm minor axis. There are 48 transitions of 4-cm length between elliptical and circular cross sections.

The transitions trap high frequency modes and behave as parasitic cavities. The Q factor for these is estimated to be about 2000 at about 1 GHz. This would couple 30–40 bunches. Extensive numerical study of this phenomenon has been carried out for the Collider.[35] For the Collider the growth time is about 100 s. All the parameters of the LEB in comparison to the parameters of the Collider will increase the growth time. Therefore the growth time will be very large compared to the cycle time of the LEB. Thus the trapped high frequency field is insignificant.

Head-tail Instability

A study of transverse head-tail instability has been done for earlier versions of the LEB lattice.[36] The conclusions of the study are that, while dipole modes have been found to be stable, the higher-order modes are in general unstable. On the basis of this result the sextuples are provided to control the chromaticity, stabilizing the machine against higher order modes. The slip factor and chromaticity for the lattice as adopted are of the same sign and similar magnitude as the values used in the study, therefore the conclusions would not differ significantly for the final lattice discussed in this book.

Beam Loading: Robinson Instability

The LEB prototype cavity has been found to multipactor below 10 kV. Since there are to be eight cavities in the LEB, reaching voltages below 80 kV will be achieved by counterphasing cavities in pairs. This can lead to the Robinson type of instability. Fortunately a cure exists in the form of fast rf

feedback, which increases the threshold by about the loop gain. With fast feedback the Robinson criterion takes the form,

$$\frac{(1+H)V_t \sin(\phi)}{R_s I_b \sin(2\psi)} \geq 1 \ , \tag{2.9}$$

where R_s is shunt resistance, H is the feed back gain, I_b is beam current, V_t is the cavity voltage, ϕ is the cavity phase and ψ is the detuning angle.

If cavities are counter phased, then, while half the cavities will give power to beam the other half will extract energy from the beam. The required feedback gain is about 6.3. The accelerating cavity requires 20 kW of power while the decelerating cavity absorbs 5 kW of power. This is to be compared with open loop power requirement of 450 kW for the accelerating cavity and 170 kW for the decelerating cavity. The feedback requires sweep of $0.3°/\mu s$ for the counter phase angle. The rate of detuning is $0.1°/\mu s$.[37] These rates can easily be achieved in the LEB.

Acknowledgements

F. Botlo-Pilat and S. Machida contributed greatly to the transverse beam-dynamics work done for the LEB. R. Servranckx, U. of Saskatoon and TRIUMF, Vancouver, BC, were instrumental in providing guidance and maintaining and adapting DIMAD and developing the interface to COSY INFINITY. The instability calculations have been done chiefly by W. Chou. The Robinson instability with feedback has been investigated by Y. Goren and T. Wang. The HOM damper for the rf cavities has been designed by L. Walling using ideas originally published by R. Smythe, U. of Colorado.

2.4 Beam Transfer

(X. Wu)

Beam transfer into and out of the LEB takes place using space in two of the three dispersion-free straight sections: injection the first half-cell in S1 and extraction the last cell in S2. Each one of the straight sections has a vertical tune of 1.0 regardless of the working point of the machine. The horizontal tune across each straight section is adjusted to achieve the overall non-integer tune in that plane and thus varies with the working point. The beam-transfer systems therefore have to cope with β-function values ranging from about 25 m to about 40 m. No dispersion exists in the straight section regardless of the LEB working point.

2.4.1 Injection

The 600-MeV Linac[38] delivers an H^- beam of 25 mA average intensity during the pulse time of up to 50 μs. Injection is done via charge-exchange, stripping the H^- ions to H^+ ions (*i.e.* naked protons). Since Collider operation requires about 100 mA current in the LEB the Linac beam is accumulated over four turns before acceleration; this requires a Linac pulse length of just under 10 μs (2.4 μs per LEB turn). For test beam operation 500 mA current in the LEB is specified, which can be achieved with 20-turn accumulation.

The transfer line[39,40] to the LEB consists of a FODO transport line, momentum compressor, emittance scraper section, spectrometer, emittance measurement section and matching into the LEB lattice. Beam simulation studies show that the Linac beam emittance will be $\epsilon^*_{rms} \approx 0.23\pi$ mm-mrad in both transverse planes. The emittance is allowed to grow to 0.4π mm-mr right after completion of the injection process; larger growth would jeopardize the goal of $\epsilon^*_{rms} \leq 1\pi$ mm-mr in the Collider rings. The momentum spread of the beam at the Linac exit is about 1.25 MeV/c. Since such a large spread would require very high rf voltage in the LEB (to provide for sufficient bucket height) the momentum compressor and the spectrometer have been included in the transfer line to reduce the momentum spread injected into the LEB to $\leq$ 125 keV/c (100 keV energy spread). The matching section has sufficient flexibility to match the Linac beam to the LEB acceptance for all working points.

The H^- injection elements consist of a pulsed septum magnet and four bump magnets, supported by two stands. Figure 2.20 shows the injection girder assembly.[41] Quadrupoles QD2S2 and QFS1 are regular LEB lattice

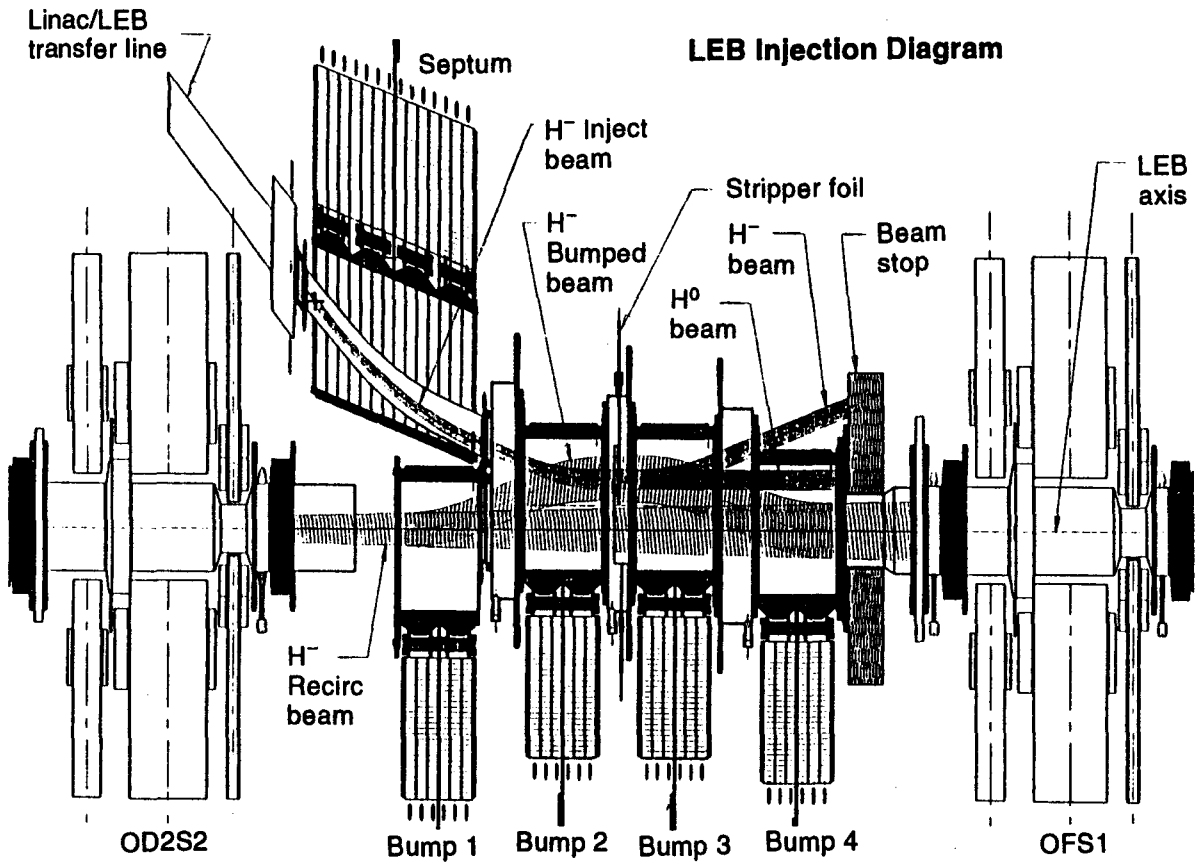

Figure 2.20: The LEB injection girder assembly. Vertical scale has been blown up for clarity.

quadrupoles. Two wire scanners between bumps 1 & 2 and bumps 3 & 4 will scan both injected and circulating beams. Four identical bump magnets, excited by one power supply in series, will bump the circulating beam by 47.2 mm from the LEB axis during the injection. Each bump has a magnetic length of 0.6 m and a flattop time of 35 μsec. While the rise time is not critical, the fall time of the field has to be short to quickly move the circulating beam off the foil and is about 11 μs. The bump magnets have ceramic vacuum chambers to eliminate eddy current effects. The 1.4-m long septum magnet, excited by a 1.5-ms half-sine current waveform, guides the H^- beam into the second bump magnet. Figure 2.21 shows cross sections of the first bump and the septum magnets at their exit ends, and relative positions of the injected, bumped and circulating beams. An iron shield between the two magnets minimizes the magnetic field interaction. The magnets will be made using thin (0.05 mm) laminations in form of a tape wound core, as shown in Figure 2.20. All these magnets have been designed to operate at 4-kG peak field at 1 GeV and are described in more detail in Section 3.1.5 of this book.

The H^- beam will be stripped to H^+, with 95 % efficiency, using a 200–250 $\mu g/cm^2$ thick foil placed midway between bump 2 and 3. Over 4 % of the incoming H^- beam will be converted to H^0 and the remaining 1 % emerges as H^-. The H^0 beam travels undeflected to a beam stop at the exit of bump 4. The H^- beam, bent to the left by bump 3, comes out into the air through a thin window to fall on the same beam stop. Intensity of this beam will be monitored, and its unusual rise will indicate stripping foil rupture. Two position monitors in the ring, downstream of bump 4, will be used to align the injected beam. A foil positioning mechanism as shown in Figure 2.22 holds spare foils on a carousel with six positions, which can be exchanged without breaking the vacuum. It has been planned to allow one position to be fitted with a viewer screen and to provide a viewing port for a TV camera to aid the commissioning of the injection system.

Emittance Preservation

Magnetic field instabilities, phase space and dispersion mismatches and scattering in the stripper foil are the major sources of emittance growth. Sypher's formalism[42] has been used to estimate the emittance growth due to the first two sources. In this formalism, the time-averaged distribution under the effect of errors is calculated. Comparison with the initial distribution yields the emittance dilution factor.

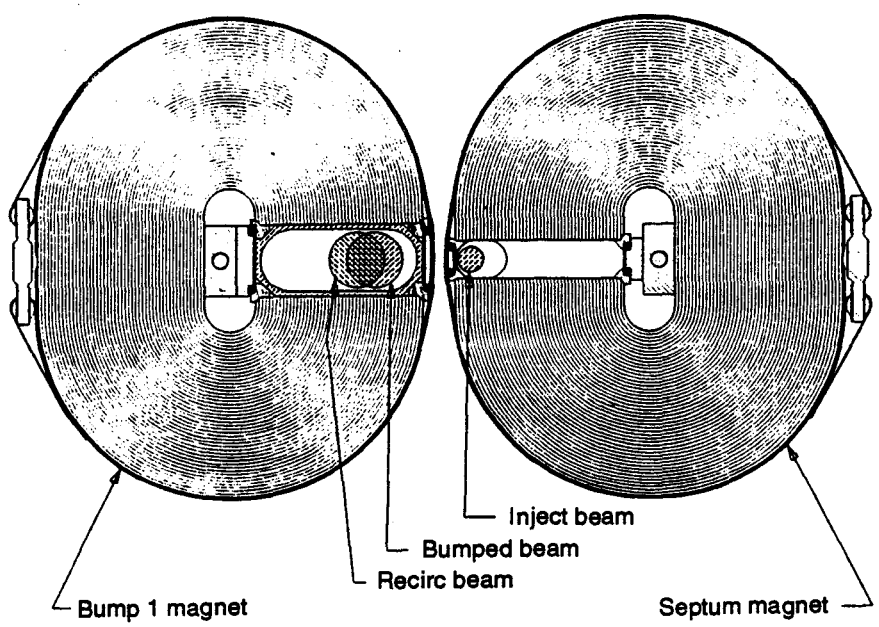

Figure 2.21: Cross section at the exit ends of bump 1 and the septum magnets.

The emittance growth (*rms*, normalized) caused by field variations in the bump or septum magnets is given by:

$$\Delta\epsilon* = 0.5\pi\beta_1(\Delta\alpha)^2(\beta\gamma)_{Lorentz}, \tag{2.10}$$

where β_1 is the lattice function at the magnet and $\Delta\alpha$ is the relative variation in the bending angle due to field change. For LEB parameters we obtain for the growth of the normalized *rms*-emittance:

Bump Magnet (Stability 0.1 %): 0.0153π mm-mrad;

Septum Magnet (Stability 0.04%): 0.0082π mm-mrad.

Since all four bump magnets are excited in series by one power supply partial cancellation occurs and the above emittance growth is an upper limit.

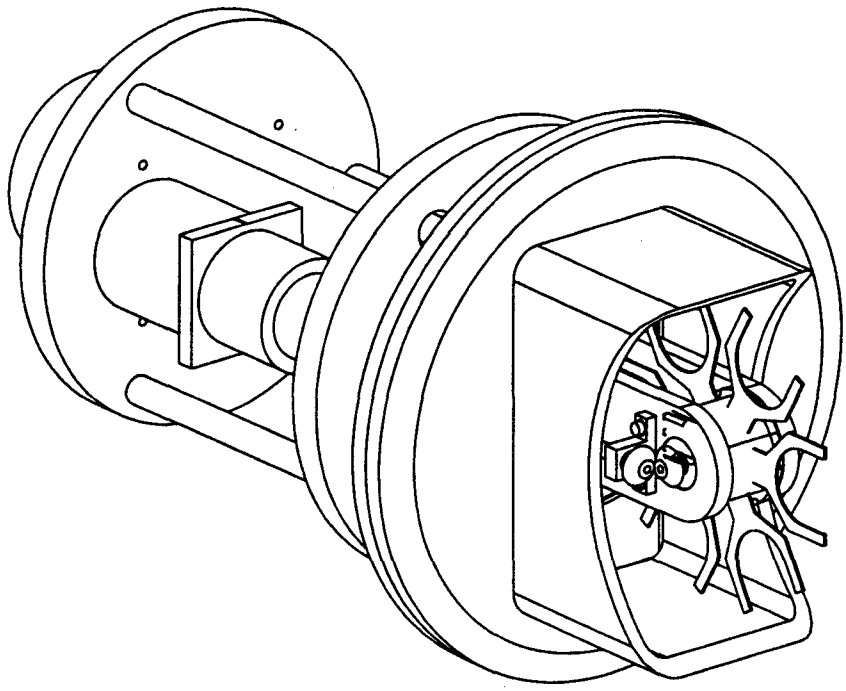

Figure 2.22: Schematic view of the stripper foil positioning mechanism.

Emittance growth due to dispersion mismatch at injection is proportional to $(\delta p/p)^2$. It is negligible for the LEB injection because of the small momentum spread of the injecting beam ($\delta p/p \approx 10^{-4}$). Nominal values of η and η' are zero at injection straight section.

The stripper foil is the single largest source of emittance growth as the foil has to have sufficient thickness for high stripping efficiency and each proton has to traverse the foil several times, depending on the timing of the orbit bump magnets. For the LEB, foil thickness is 200–250 μg/cm^2. Emittance growth can be calculated from the *rms* scattering angle for each foil traversal and *rms* addition over the number of such traversals. One uncertainty in these calculations is the scattering model to be used: foils of the thickness contemplated here typically cause a few scattering processes per proton traversal which falls in between the extremes of single scattering and

multiple scattering and is often referred to as "plural" scattering. No good approximations exist for the scattering-angle distribution in this regime.

The average number of traversals for each proton depends on the orbit bump fall time which is a compromise between cost and performance. A value of $11\mu s$ has been chosen for just above seven traversals/proton during Collider-fill operation and an expected emittance growth of 0.06π mm-mrad. The emittance growth has been calculated using the multiple scattering model and an average β-function of 14.7 m at the foil.

Extensive simulations of the injection process using the code ACCSIM[43,44] have been planned, but not carried out at the time of project termination. ACCSIM is a six-dimensional tracking code with foil scattering and multi-turn injection as well as space charge detuning being modeled to first order. Acceleration can be included in the simulation. The code has been used extensively for simulations of the multi-turn beam accumulation in the TRIUMF KAON Accumulator[45,43] ring as well as for the CERN PS Booster.[46] While serious work with the code for the LEB has not been done, some preliminary runs indicate that the basic assumptions made in the injection design are correct, *i.e.* the average number of foil traversals (≈ 7) and the amount of scattering in the stripper foil, and have yielded an emittance growth consistent with the analytic predictions.

2.4.2 Extraction

The LEB extraction system[47] has been designed to extract a 12 GeV/c proton beam from the LEB in both the Collider fill mode and for test beam operation with the normalized transverse beam emittance (*rms*) being 0.6π mm-mrad and 4.0π mm-mrad, respectively. It is a single-turn, vertical extraction system that provides the same extracted central orbit at the septum magnets for all possible working points of the LEB.

Beam Optics

Figure 2.23 shows the layout of the extraction system in the LEB S2 straight section. It also shows the bumped orbits (dashed curves) and the extracted orbits (solid curves) in the vertical plane at several different LEB working points, of which (11.65,11.60) and (11.85,11.80) are the nominal LEB operating tune points and the other four are the corners of the rectangular boundary of all possible LEB operating tune points. The system consists of a fast kicker, 2 septum magnets and 5 bump magnets. The kicker mag-

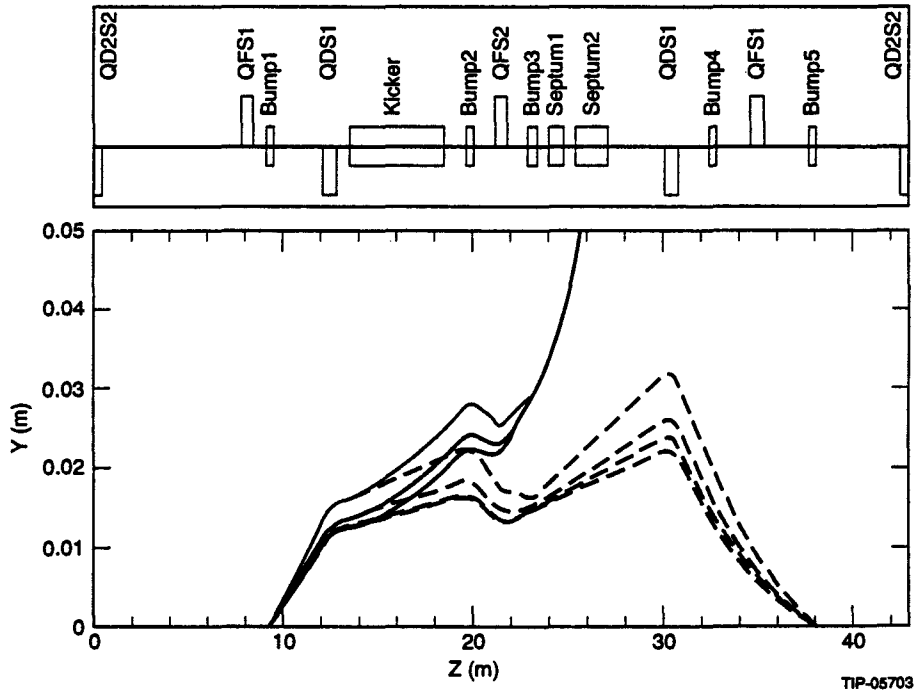

Figure 2.23: Layout and optics of the extraction system.

net follows the vertical focusing quadrupole QDS1, and 2 septum magnets are located one cell downstream. Once the beam approaches the extraction momentum, five bump magnets are excited to steer the circulating beam towards the septum several milliseconds before the kick. The fast kicker deflects the beam across the septum where it receives additional deflection to leave the machine.

Each of the five bump magnets has its own independent power supply so their magnetic field can be independently adjusted in order to generate an adequate vertical displacement and angle at the septum for all possible working points. Thus the same extracted orbit will be achieved regardless of the LEB working point. Bumps 1 and 2 are positioned before and after the kicker and deflect the orbit by about 15 mm towards the septum. Located right in front of the first septum magnet, bump 3 is used to adjust the angle of the proton beam. Bumps 4 and 5 bring the bumped orbit back onto the median axis within the extraction section; no orbit distortion exists in any

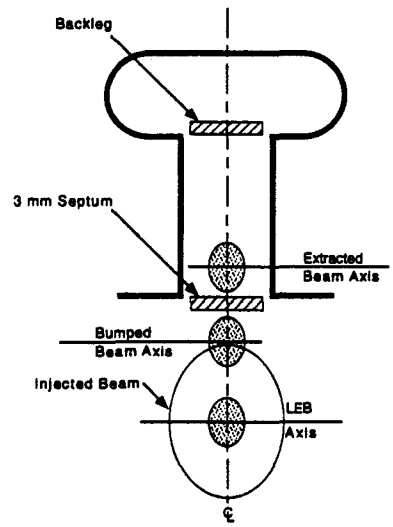

Figure 2.24: Cross section at the entrance of the first septum magnet.

other section in the LEB. The maximum deflection angle required for the bump magnets is about 5.0 mrad.

In order to minimize the kicker strength and achieve the bending required to extract the 12-GeV/c proton beam, two septum magnets are used in this system. The first has a thin septum of 3 mm total width and provides a moderate deflection angle of 5 mrad; the second has a 7-mm septum and deflects the proton beam by 50 mrad. The orbit displacement, Δ, generated by a kick δ at the septum is given by:

$$\Delta = \delta\sqrt{\beta_1\beta_2}\sin(\phi_2 - \phi_1), \tag{2.11}$$

where β_1, β_2 are the β functions and ϕ_1, ϕ_2 are the betatron phases at the kicker and septum, respectively. For a kicker with length L, Δ is given by:

$$\Delta = \frac{\delta}{L}\sqrt{\beta_2}\int_0^L \sqrt{\beta_1(s)}\sin(\phi_2 - \phi_1(s))ds\ . \tag{2.12}$$

The required orbit displacement is about 15 mm. This takes into account the maximum extracted beam envelope (4.7 mm for 3 σ test beam), maximum beta function and 3-mm thickness for the first septum, and about 5 mm for the closed orbit excursion. Figure 2.24 shows proton beam sizes and vertical

locations at the entrance of the first septum magnet. The kicker strength, δ, is then given by:

$$\delta = \frac{\Delta L}{\sqrt{\beta_2}\int_0^L \sqrt{\beta_1(s)}\sin(\phi_2 - \phi_1(s))ds}. \tag{2.13}$$

A kicker strength δ of 1.5 mrad will be adequate for the LEB beam extraction.

The LEB Extraction System Components

The extraction kicker magnet[48,49] has an integrated strength of 600 Gm, and is made up of eight modules to achieve a risetime of 80 ns. With total magnetic length of 5.3 m, it has a maximum field of 115 G. With this risetime, two to three beam bunches (spaced 16.68 ns apart at 12 GeV/c) are lost due to partial kicker deflection with the head and tail bunches of the extracted beam being sheared somewhat. The aperture of the kicker magnet is 50 mm by 70 mm to accommodate the maximum proton beam size at injection. The magnetic field variation $\delta B/B$ is no more than ± 1.0 % across the good field region of 20 mm by 40 mm to limit the transverse beam emittance growth. A prototype traveling-wave kicker magnet has been designed, built and tested as described in Section 3.1.5.[49] Bump and septum magnets will be made using thin (0.05 mm) laminations.[47] The required maximum integrated strength for the five bump magnets is 0.18 Tm. With a magnetic length of 0.45 m, the maximum magnetic field will be 4.0 kG. A laminated, H-shaped, 8 turn/pole dipole magnet design, with a pole gap of 80 mm, has been used for these bump magnets. A stainless steel vacuum chamber of 75 mm in diameter is placed into the aperture of the bump magnet. The magnetic field $\delta B/B$ is allowed to change no more than ± 0.1 % within a good field region of 30 mm by 50 mm, which is determined by the transverse proton beam sizes at the extraction energy, in order to limit the transverse beam emittance growth as well. The bump magnets are pulsed by power supplies with 2 msec half-sine wave and peak current of 1600 A.

Single turn current sheet septa are used in both short and long septum magnet designs with thicknesses of 3 mm and 7 mm, respectively. The required design parameters are listed in Table 2.11. The magnets are placed in vacuum tanks, and vacuum tight feedthroughs provide power and cooling water. Special shielding is required for both magnets to prevent leakage of the magnetic field outside the septa that otherwise could cause transverse beam emittance growth on the last few hundreds turns prior to powering the

Table 2.11: General parameters of the septum magnets.

Parameter	Short septum	Long septum
$\int Bdl$ (T-m)	0.2	2.0
Magnetic length (m)	0.8	1.6
Maximum field (T)	0.25	1.25
Field uniformity (%)	0.24	0.1
Peak current (A)	4780	20400
Pulse Duration (msec)	1.0	1.5

kicker. This shielding is accomplished by a U-shaped low-carbon steel shell which is brazed to the conductor assembly and is a part of the conductor support structure.

Acknowledgements

S. Penner, NIST, designed the H^- injection section. In the earlier days of the SSC Laboratory, the beam-transfer systems have been the responsibility of a separate group under the leadership of J. McGill. R. Bhandari later took on responsibility for the injection girder layout and hardware.

Chapter 3

The LEB Accelerator Systems

3.1 Magnet System

(F. Knox-Seith, N. Li, M. Schulze, J.M. Wilson)

3.1.1 Overview

The main challenge for the LEB magnets (as for several other LEB systems) arises from the fast 10-Hz cycling rate. Relatively high voltages are necessary to generate the excitation current necessary in the magnet coils, and the fast change of magnetic field generates non-negligible eddy currents wherever a closed current path exists. The short ramping time also makes correction of dynamic ill-effects in the magnets more difficult; this leads to increased considerations given to tracking between the different magnet families.

The challenges are addressed in several ways: Peak magnetic fields are moderate to avoid saturation effects and limit eddy-current generation. Thin (0.5 mm) laminations of 2 % silicon steel are used throughout. This steel provides a compromise between high saturation and low ac-effects, having a slightly lower saturation than low carbon steel but high resistivity and a narrow hysteresis curve. All materials in regions of significant field strength (like mounting brackets *etc.*) have been examined for either replacement with non-conductive material or mitigating measures like slotting to break eddy-current loops. Special considerations have been given to the vacuum system in the magnets as described in Section 3.4.

The LEB magnet system can be divided functionally into three groups: main dipoles and quadrupoles, corrector magnets and pulsed magnets.

The main dipoles and quadrupoles bend and confine the proton beam inside the vacuum system. All dipoles are identical. Eight distinct quadrupole families are used—four in the arcs and four in the straight sections—which differ in length but have identical lamination cut. One common current loop excites all magnets to reduce tracking errors between families to a minimum.

The corrector magnets are used to compensate for setting and alignment errors of the main magnets and also for cancellation of betatron-resonance driving forces. Orbit-correcting dipoles are C-shaped magnets with air-cooled coils; all are of identical design but oriented differently about the beam axis depending on their horizontal or vertical action. Two different designs are used for the trim quadrupoles which provide the tuning capability of the machine. They differ in the coil configuration: The low-field quadrupoles and the skew quadrupoles have air cooled coils while the high-field quadrupoles have water cooled coils. Lamination cut is the same as for the main quadrupoles. Air-cooled chromaticity sextupoles are used in the arcs to provide focusing dependent on the particles' momentum, thus cancelling the tune shift with momentum. The skew sextupoles are air-core magnets because of their very low strength. All corrector magnets use the same lamination thickness and steel type as the main magnets.

Pulsed magnets are used during beam injection and extraction; orbit bumps which operate on a ms time scale deflect the closed orbit while kickers with a rise time under 100 ns guide the extracted beam into the extraction channel. While the orbit bumps use tape-wound cores with thin layers of grain-oriented steel the fast kickers have ferrite cores. Table 3.1 lists the various magnet types used in the LEB and their most important parameters.

All LEB magnets—with the exception of the pulsed magnets and the skew sextupoles—are to be manufactured by the Budker Institute for Nuclear Physics (BINP) in Novosibirsk, Russia. Administratively, an umbrella agreement between BINP and SSCL (Interlaboratory Agreement) provides the framework for the contracts; the magnets are to be manufactured according to Attachment 4 to the Agreement. In the Attachment delivery and payment schedule are spelled out as well as a Statement of Work and the magnet specifications. Each Laboratory designated a technical representative to facilitate communication and coordination. Measurements of prototype and production magnets are to be performed by BINP as well, under Attachment 25 to the Agreement.

Table 3.1: Magnet functions and quantities.

Type	Field Strength	Length	Families	Magnets
Dipole	1.38 T	2.1 m	1	96
Quadrupole	15.355 T/m	0.5...0.8 m	8	90
Orbit-corr. dipoles	0.17 T	0.15 m	1	90
Trim quadrupoles	2...6 T/m	0.3 m	2	90
Chroma. sextupoles	120 T/m^2	0.3 m	1	48
Skew quadrupoles	0.82 T/m	0.3 m	1	4
Skew sextupoles	2.67 T/m^2	0.3 m	1	12

Under this collaboration the SSCL has developed the design and produced one or more prototypes to test and prove the design. The designs are then reviewed with scientists and engineers from BINP and changes made where appropriate to take full advantage of the manufacturing techniques and materials that are available at BINP. As a result of this procedure, it has been agreed that the magnet laminations would use standard Russian electrical grade steel (0.5 mm) which has been verified at SSCL to be equivalent or superior to the M36 steel in terms of lower coercivity and reduced saturation at high fields. The conductor cross section used on the SSCL prototypes is generally slightly different from what is readily available to BINP. All LEB corrector magnets will use Russian M1R copper conductor. The turn-to-turn insulation on the SSCL prototypes has been found to be marginal, and typically a slightly reduced cross section (< 5 %) has been accepted in favor of increased insulation.

Studies have been performed at BINP to examine the effect of radiation on materials that are used in magnet fabrication. The standard coil insulation materials available in Russia have been found to be acceptable as a result of these studies. Mylar and Lavsan, the Russian equivalent, have been found to maintain their mechanical and electrical integrity at radiation levels up to 300 Mrad. Kapton and fiberglass samples show no significant deterioration at radiation levels of higher than 1000 Mrad. These studies and other comparisons between different materials used to manufacture the LEB corrector magnets are presented in a technical note.[50]

Magnet apertures are determined by the beam emittance and the lattice functions. For a certain type of magnets, such as dipole, the maximum half

size of the beam envelope of a beam with normalized *rms* emittance $\varepsilon^*_{x,y}$ and *rms* momentum spread $(\frac{\sigma_\rho}{\rho})_{x,y}$ is given by

$$\Delta_{x,y} = 3\sqrt{\frac{\varepsilon^*_{x,y}\beta^{max}_{x,y}}{\pi(\beta\gamma)_{Lorentz}} + \eta^{max}_{x,y}\left(\frac{\sigma_\rho}{\rho}\right)^2_{x,y}}, \tag{3.1}$$

where $\beta^{max}_{x,y}$ and $\eta^{max}_{x,y}$ are the maxima of the lattice functions in all magnets of this type. Taking into account closed orbit distortion, vacuum chamber thickness, mechanical and other tolerances, the half-aperture of the magnets is chosen to be $A_{x,y} \geq \Delta_{x,y} + 5$ mm.

To avoid uncontrolled tune swings during the acceleration cycle, the dipole and quadrupole field strengths must remain proportional during the entire cycle. Tracking studies have shown that if the ratio remains constant to within a part in 10^3, no tune correction is necessary. Field strength tracking at the 10^{-3} level between the dipole and quadrupole has been adopted as a design goal. In addition, because the quadrupoles come in several lengths, any saturation in the end packs changes the effective length and, thus, the relative strengths of the magnets. This imposes constraints on the end-pack shape.

Two methods have been used to reduce errors in tracking due to variations in material properties. The magnet efficiencies are high, greater than 98 % to keep the material out of saturation. In this way the details of the saturation curve become less important. The yoke is designed so that the magnetic flux density (B) in the back leg is the same in both dipole and quadrupole magnets, and the flux return through the yoke has a path length proportional to the ampere-turns enclosed in the loop (*i.e.*, dipole coil has twice as many turns, so its flux return path is twice as long). The $B - H$ curves for the two magnets should be fairly well matched as they are built from the same steel. This results in matched magnetic field (H) in the back legs. The resultant designs should track regardless of the details of the actual $B - H$ curve as magnet strength is proportional to $1 - \int_{\text{Iron}} H\,\text{dl}/NI$. We have $\int_{\text{Dipole-Iron}} H\,\text{dl} \approx 2\int_{\text{Quadrupole-Iron}} H\,\text{dl}$.

Prototypes of each magnet have been built to test the physics and mechanical designs. Field measurements of the prototypes have been used to adjust the 3D field to arrive at an acceptable final design, as discussed in Sections 3.1.2 and 3.1.3. Extensive measurements have been planned for the prototype at BINP, including ac testing—to test the adequacy of the design. During production, all LEB magnets were to be measured before installa-

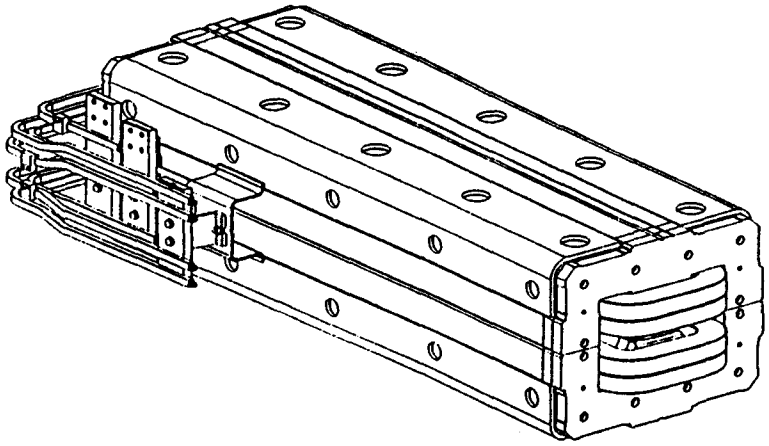

Figure 3.1: Isometric view of the dipole magnet.

tion. This would provide a check for manufacturing problems, and a data base on the individual magnet's variations from the prototype.

3.1.2 Dipole
(F. Knox-Seith, N. Li)

The main dipole is a straight laminated H magnet of 1.94 m effective length, to be installed in pairs. This design has been chosen in favor of the curved four meter long dipoles originally envisaged and has been developed in collaboration with the manufacturer, BINP in Novosibirsk, Russia. An isometric sketch of the magnet is shown in Figure 3.1, its parameters are given in Table 3.2

Table 3.2: Parameters of the dipole magnet.

Magnet Parameter	Value
Peak Central Field	1.35 T
Peak Integrated Field	2.62 T-m
Effective Length	1.94 m
Good Field Region (Injection)	±32.5/±25 mm horizontal/vertical
Good Field Region (Extraction)	±14/±14 mm horizontal/vertical
Field Uniformity ($\Delta BL/BL$)	$\leq 10^{-4}$
$\Delta BL/BL$ Magnet-Magnet	5×10^{-3}
Bending Radius	29.64 m
Gap Height	57.2 mm
Pole Half-Width	73 mm
Slot Length	2.163 m
Lamination Height	517 mm
Lamination Width	660 mm
Lamination Thickness	0.5 mm
Weight	4240 kg
Max Cooling Water Flow	11.4 gpm
Conductor Size	18 mm × 21 mm
Conductor Area	312 mm^2
Peak Amp-Turns/Pole	32 kA
Turns per Pole	8
Peak Current	4000 Amps
RMS Current	3473 Amps
Excitation Frequency	10 Hz
Inductance	2.35 mH
Resistance	4.2 mΩ
Average Power	61.5 kW
Peak Stored Energy	17.8 kJ
Number of Magnets	96

Mechanical Design

Each lamination is a single piece providing excellent dimensional consistency and avoiding the potential offset between upper and lower halves often found in laminated magnet cores separated at the horizontal midplane. The H design also simplifies core assembly. To provide the necessary rigidity of the assembly, angle-plates are welded to the core along its entire length.

Initially, end packs have been designed to be glued-together laminations; however, concerns about the radiation resistance of the glue have prompted investigation of alternative designs. Studies carried out by BINP using a short model of the dipole magnet have led to an improved design using steel frames at either end of the magnet. The frames, which would be welded to the angle plates, would stabilize the end packs by means of G10 blocks (or its Russian equivalent, STEF) which are pushed towards the end packs. The blocks are attached to the frames using insulated stainless bolts. This design is to be tested on the second prototype and expected to be used for production.

The coils consist of four pancakes with four windings each. Each coil is wound starting from the midpoint in two layers, with terminal leads exiting tangentially to the coil end at each layer. Full length of the copper conductor has been specified to avoid joints within a winding (which historically lead to magnet coil failures). A rectangular hollow conductor of 21 mm$\times$18 mm outer dimension, with a 9-mm inside diameter coolant channel is specified.

Coil insulation consists of Kapton or Mylar film providing ground insulation up to 7.5 kV. BINP has studied radiation effects on these materials as well as the Russian equivalent to Mylar, Lavsan, providing evidence that their radiation resistance is sufficient for the LEB magnets.[50] The conductor is wrapped in fiber glass insulation and pressure impregnated with epoxy for mechanical stability. Expected lifetime of the coils is more than 25 years.

Stainless steel compression fittings are brazed onto the copper conductors of the coils to connect to the hoses carrying the LCW for cooling because brass fittings are known, over time, to lose zinc content and become porous. The hoses will have a useful life in the expected radiation environment of greater than 5 years. They will be replaced in the normal course of maintenance activities. Fittings attached to hose ends are made of brass and push-on style because of the low pressure of the water system. Inexpensive stainless steel clamps are used with the push-on fittings to provide redundant safety.

Each coolant circuit is equipped with a thermal switch (Klixon) to interrupt power when overheating is sensed. These switches protect the magnets, coils and insulation materials, by opening at 66°C—above the anticipated hot water temperature but below the heat distortion temperature of the epoxy coil insulation.

Magnetic Design

The magnetic field requirements for the dipoles are determined by the beam dynamics calculations outlined in Section 2.3 and are given in Table 3.3. Note that the good-field region shrinks significantly at higher excitation due to adiabatic shrinking of the beam; this allows for a significant reduction in pole-face width and, thus, cost savings in the construction and operation (due to the smaller stored energy) of the magnets. Due to the length of the magnets, field uniformity requirements are to be met for both the body field and the field integrated over the length of the magnet including fringe fields.

Table 3.3: Field parameters of the dipole magnet.

	Injection	Extraction
$\int B d\ell$	0.262 T-m	2.62 T-m
Good-field region (horizontal/vertical)	±32.5/±25 mm	±14/±14 mm
Uniformity tolerance	10^{-4}	10^{-4}
Magnet-to-magnet tolerance	5×10^{-3}	5×10^{-3}

A quarter of the dipole cross section is shown in Figure 3.2. Magnet types and considerations have been discussed in the literature by Fisher[51] and Halbach.[52] The dipole is designed for a peak field of 1.35 T in the gap and of 1.5 T in the return yokes. The shape of the pole face has been determined using the computer codes POISSON and MIRT[22,23] for pole-face shimming to meet the specified field uniformity tolerance at both injection and extraction fields. The computer code PE2D[24,53] has been used to confirm the the field calculation results from POISSON. Using the saturation tables for the steel to be used (ARMCO M-27 or its Russian equivalent)

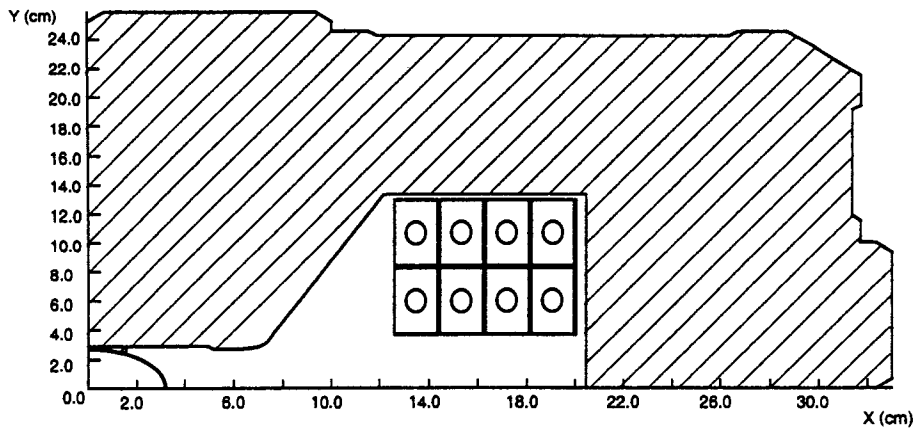

Figure 3.2: Dipole cross section.

the PE2D model has also been used to predict saturation behavior of the magnet, which is important in assessing the tracking between dipoles and quadrupoles and can be varied to a certain extent by varying the thickness of the return yokes. To minimize the cost of the magnet, about 2 % saturation at extraction field was allowed; this reduces significantly the yoke thickness and thus the weight and cost of the magnet.

Figure 3.3 shows a plot of the dipole field as given by PE2D after optimization was completed. The design of both the dipole and quadrupole magnets has been performed in collaboration with LBL and SLAC and is documented in detail in various reports and papers.[20,21]

The magnet excitation circuit is divided into 12 separate resonant cells, each consisting of 8 dipoles and 7 or 9 quadrupoles. The voltage across the string of magnets in a cell is limited to avoid excessive insulation requirements, this limits the inductance of the magnets in each cell. Each dipole coil has two pancakes with four turns each, connected electrically in series with both coils connected in parallel; resulting in an inductance of 2.3 mH. This value has been specified in close coordination with the power supply requirements.

Requirements for the three-dimensional design are the same as for the two-dimensional design. A large effective length at high current is favored as it will allow a lower peak current at the required extraction strength. Tracking would be improved by an increase in saturation at high currents. The process of three-dimensional measurement and design was similar to

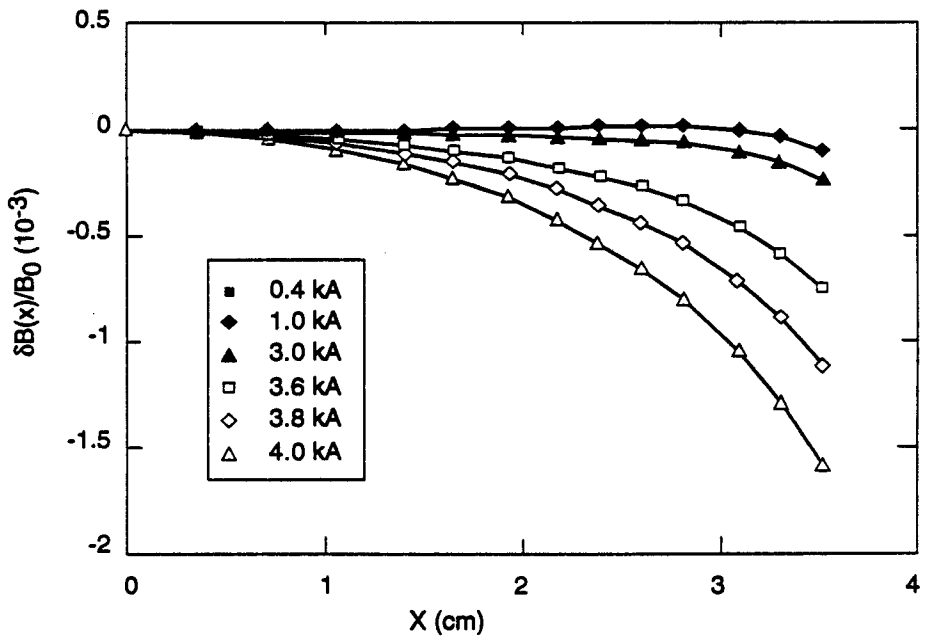

Figure 3.3: PE2D calculation of 2D dipole field.

that used for the quadrupole, Section 3.1.3, concentrating on attaining the required field uniformity.

The field was measured with a 38.1-mm-thick end pack. Slight modifications were made yielding an acceptable field quality. The final end pack has two planar cuts across the pole tip, 8.78 mm at 44° and 8.89 mm at 64°; modified by removal of a 4-cm wide strip 0.5 mm deep from the center of the pole tip.

Ac Related Issues Primary ac effects are power loss and field quality degradation. Predicted power loss is roughly 1 kW in the iron core of each dipole during 10-Hz operation. Similarly calculated losses in the coils are approximately 10 kW, compared to resistive losses of approximately 51 kW. Ac coil losses can be reduced by reducing the conductor size, but the price paid is an increase in the number of turns and, thus, the inductance which is unattractive. The power level also does not warrant the use of expensive stranded cable for the magnet conductor.

While degradation of the magnetic field within the magnet gap is not expected, eddy currents at the magnet ends could lead to variation of the effective length of the magnet and also to spurious field harmonics. The end-pack chamfer has been designed with this in mind and should reduce eddy currents to tolerable levels. Due to the difficulties associated with fully three-dimensional field calculations only ac measurements on the prototype can provide a definite answer on this issue (see Section 3.1.2).

Eddy currents in the vacuum chamber have a significant effect on field quality. The effects and mitigating efforts are discussed in detail in Section 3.4. In addition to the field harmonics generated, the vacuum system will lead to a field retardation on the dipole axis different from that in the quadrupole, thus producing a phase shift between dipole and quadrupole field. The effect has been estimated to cause a tune shift of up to $\Delta\nu \approx 0.18$ but can be mitigated by external resistors to match the time constants of both quadrupole and dipole magnets.[54]

Fabrication

Tolerances Based on experience at other accelerator laboratories a tolerance of 0.025 mm has been specified for all critical dimensions of the lamination.

Field uniformity variations due to mechanical tolerances have been studied extensively.[55] Tolerances are broken down into ten types of lamination stamping and assembly errors. For the worst case (within tolerance) of each error the field change is calculated and the field-uniformity errors are added in quadrature to find the largest possible error. In this way the quadrupole and sextupole terms are each found to possibly exceed the field-error tolerance by a factor of two. However, it is felt that this is acceptable since probability for such a scenario is low and correction is possible by means of end-pack shaping. The relevant mechanical tolerances can not be tightened further without unacceptable cost increase. Measurement results for the prototype corrector quadrupoles indicate that exceeding the tolerance by a large amount (≈ 4) can indeed lead to unacceptable non-uniformity of the field, see Section 3.1.4.

The quadrupole term is caused by a stamping error which is cancelled by the planned lamination flipping during stacking. The sextupole term is caused by a symmetric stamping error, which cannot be cancelled through lamination flipping. The probability of the die having a large error of this type is low, but should the die exhibit this flaw, it would have been detected

during the field measurements of the prototype allowing for corrective action. The magnet measurements performed at SSCL and at BINP do not indicate presence of any flaw of this kind.

Tooling

Punch and Die The iron core of about 2-m length consists of stacked laminations. The packing factor is specified to be no less than 97 %, which is required both for mechanical rigidity and for the magnetic field properties (tracking with the quadrupole) of the magnet. To meet this specification, the lamination burr should be less than 0.04 mm. Therefore, the clearance between punch and die has to be less than 0.02 mm. Compared to the dimension of the lamination of 660 mm×515 mm, this tolerance is extremely difficult to reach and maintain, requiring a stamping press of high precision and small stroke distance. Since such a machine was not available for the LEB contract at the contractor fabricating the laminations (ZVI in Moscow, Russia), a novel die has been designed by ZVI, shown in Figure 3.4. Contrary to common practice the punch is floating, guided by pins, and has a very short stroke, rather than being mounted rigidly to the press plate. The quality of the lamination for the prototypes indicates that this approach is successful.

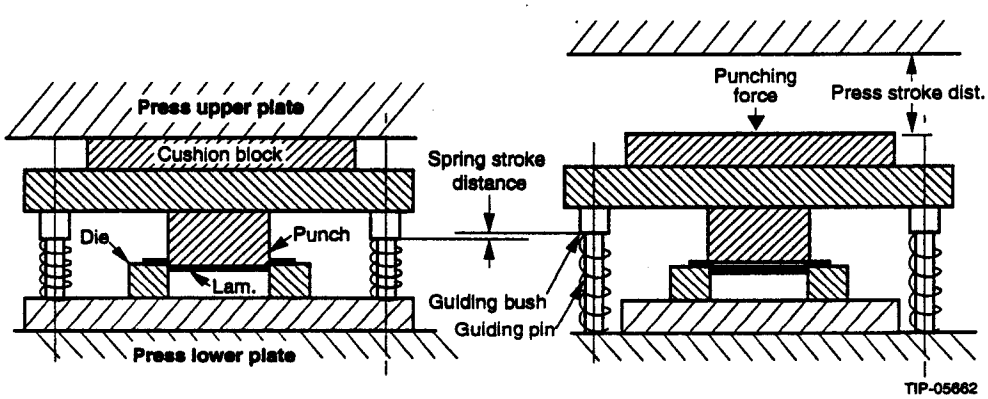

Figure 3.4: Sketch of the dipole lamination punch and die.

Stacking Fixture Figure 3.5 shows the principle of the dipole stacking fixture. Because of the length of the iron core, using the magnet gap as the

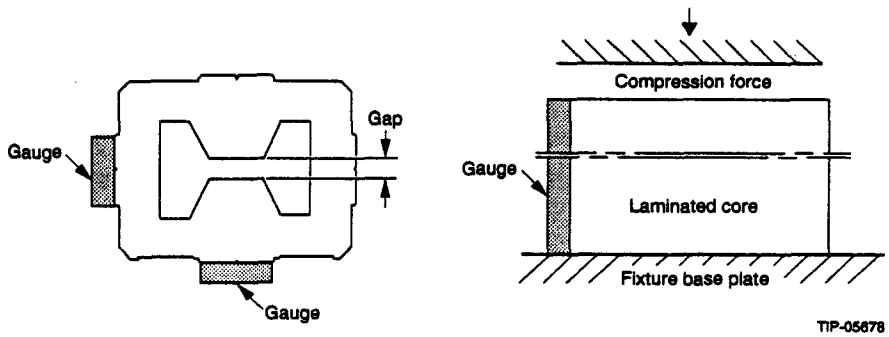

Figure 3.5: Dipole stacking fixture.

stacking reference is not adequate to maintain tolerance and two sides of the lamination are used as reference surfaces. The hydraulic stacking fixture is upright; this configuration simplifies welding of the core since all four sides can be welded at the same time and in the same core position.

Prototypes

Lamination Material Prototypes have been built both at SLAC and at BINP, Russia. The core of the SLAC prototype is made from AISI M-27 steel while the BINP prototype core is made using its closest Russian equivalent, 2312 isotropic electrotechnical steel. Several samples of both steel types have been blind-tested in order to ensure equivalence of both materials in chemical composition as well as electromagnetic properties.[56] Chemical composition of both steels is given in Table 3.4 Comparing the magnetic field measurement results of two samples, the Russian steel shows a somewhat higher default $B - H$ curve. Based on these results the Russian 2312 steel was approved for the LEB magnet production.

Table 3.4: Chemical analysis of AISI M-27 and Russian 2312 steel.

	Si	C	Mn	P	S (%)
M-27	2.0	0.01	0.15	0.01	0.05
2312	2.0	<0.02	0.2-0.3	<0.015	<0.01

Mechanical Inspection Results Laminations of both the SLAC and the first BINP prototype have been inspected for mechanical tolerances. Figure 3.6 shows the lamination profile together with the tolerance region; deviations from the design shape are magnified by a factor of 10. The SLAC prototype uses laser-cut laminations while the BINP prototype uses punched laminations using the production die. As expected the quality of the laser-cut lamination is relatively poor, the pole segments exceed the tolerance by as much as a factor of 10. The punched lamination on the other hand is of excellent quality, more than 90 % of the measurement points on the pole segments stay within the tolerance belt. For each lamination three samples have been measured; variations from sample-to-sample are small compared to the measured deviations.

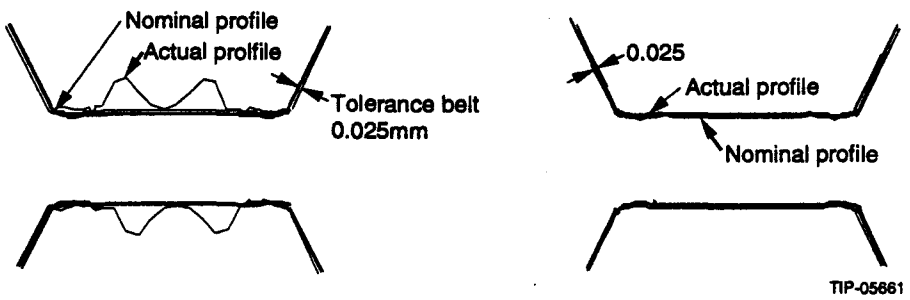

Figure 3.6: Dipole lamination inspection results.

The assembled BINP dipole prototype has been measured before shipment to the SSC Laboratory. Some inspection results are

- Packing factor: 99.2 %;
- Flatness of outside surfaces of the core: 0.05 mm;
- Pole gap (nominally 57.20 mm): Max. 57.22 mm, Min. 57.14 mm;
- Deflection (core supported by 3 points, one at each end and one halfway in between, laterally offset): 0.17 mm.

These results demonstrate good rigidity of the INP dipole prototype. The pole gap has rather good quality as well but quality control will be improved to meet the requirement of less than 0.05 mm.

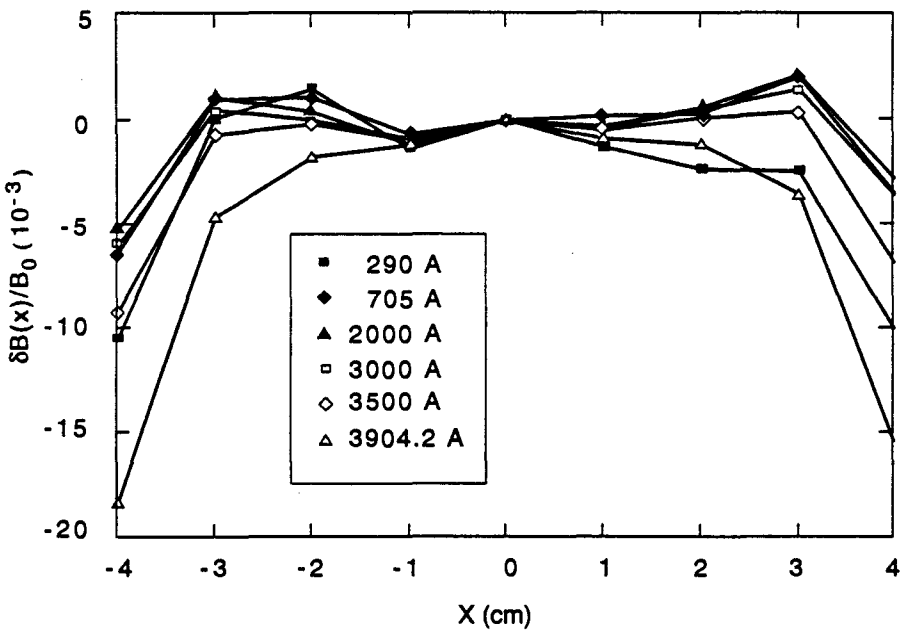

Figure 3.7: INP measurements of the dipole body field.

Shuffling In order to reduce magnet-to-magnet variations, lamination shuffling is specified for the LEB magnets. This is practical as the steel rolls are warehoused at the manufacturer of the laminations. Each roll will be categorized into one of at least four groups based on the measured coercivity. Each magnet will have an identical number of laminations from each coercivity group, thus ensuring minimum variation in the magnetic properties.

Magnetic Measurements BINP has made extensive dc measurements of the dipole prototype using an array of temperature compensated Hall probes. The array consists of 11 probes displaced horizontally by one centimeter, for a total width of ±5 cm. The array can be stepped through the magnet to map out the field in one plane at a time. Given the nature of Hall probes, only the vertical field component is measured in this way.

Results of the 2-dimensional (body) field measurement are shown in Figure 3.7 for several excitation currents, normalized to the field at the center of the magnet. The data show the body field to be somewhat out of the specified tolerance of $\pm 1 \times 10^{-4}$ at 3.25 cm and injection current. However, a relatively small signal-to-noise ratio as indicated by the spread of

the data points makes interpretation of the results on such a scale difficult. The data do indicate the absence of any gross error possibly arising from the lamination cut or the magnet stacking procedure.

While the lamination does not appear to completely meet the field uniformity specifications, the drop-off of the field towards the boundary of the good-field region is sufficiently small to make compensation by end-pack chamfering practical and acceptable. Thus this deficiency by itself does not warrant rejection of the lamination.

The integrated dipole field uniformity has been measured by both INP and SSC. The BINP measurement data have been generated by point-wise integration of the Hall probe data along the magnet axis. At the SSCL multiple measurements with a long rotating coil at several transverse positions have been taken, yielding a direct measurement of the integrated strength. Field uniformity data from these measurements are shown in Figure 3.8. The data have been taken using a double chamfer of the endpacks. The first section (closest to the core) has an angle of 44° against the horizontal plane and is 8.78-mm long, while the second part is 8.89-mm long at an angle of 64°. The end packs have a thickness of 38.1 mm.

At high current the measurements agree to within about 10^{-4}, considering the SSC measurement is at 2.5 % higher current this is acceptable. However, field drop-off is too strong by a factor of 2–3 at extraction, the specification is $\leq 10^{-4}$ at ± 14 mm.

At low current the disagreement between the two measurements is significantly larger than the specified field tolerance. The data taken at the SSCL appear smoother than the BINP data, suggesting a higher signal-to-noise ratio. But neither set of measurement data fulfills the uniformity requirement of 1×10^{-4} at ± 3.25 cm transverse position. Given the relative adequacy of the lamination this can be attributed to end-effects and, therefore, can be compensated by modification of the end-pack shape.

The dipole end-pack was modified by cutting out a 0.5-mm deep strip along the center of the pole tip. This strip is 4-cm wide, and extends 20.43 mm along the horizontal plane and across both of the angled plane of the end-pack. SSCL measurements of the resultant field uniformity are shown in Figure 3.9.

The measurement appears to have random errors, which would require improvements to the measurement technique at low currents if the project were continuing. At low current, 400 A, the measured field errors are less than $\pm 10^{-4}$ to just over ± 30 mm. The 2000 A measurement shows a slightly wider good field region of approximately ± 32 mm. At extraction, 4000 A,

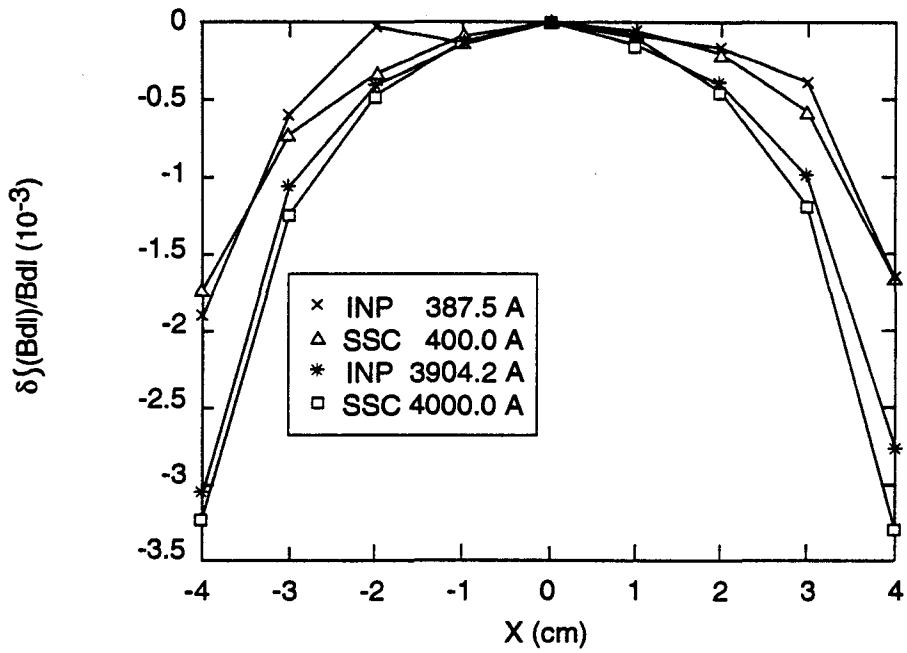

Figure 3.8: Measurements of the integrated dipole field uniformity.

the good field region has shrunk to ±16 mm. Thus the good field region is just under the specified ±32 mm at injection and exceeds the specified ±14 mm at extraction. At the time of project termination it was decided that this is an acceptable field uniformity.

Measurements of the dipole transfer function are shown in Figure 3.10. The integrated field strength of the dipole is slightly less than anticipated. In order to achieve the required 2.62 T-m, the magnet current would have to be increased to 4000 A from the original 3904.2 A; alternatively, the magnet core would need to be lengthened somewhat by adding laminations. Fine tuning of the core length has been expected to be necessary, but has not been done at the time of project termination.

3.1.3 Quadrupoles
(F. Knox-Seith, N. Li)

The main quadrupole is a laminated four-quadrant design. Eight different families, with an effective length varying from 0.5552 m to 0.7564 m, are used

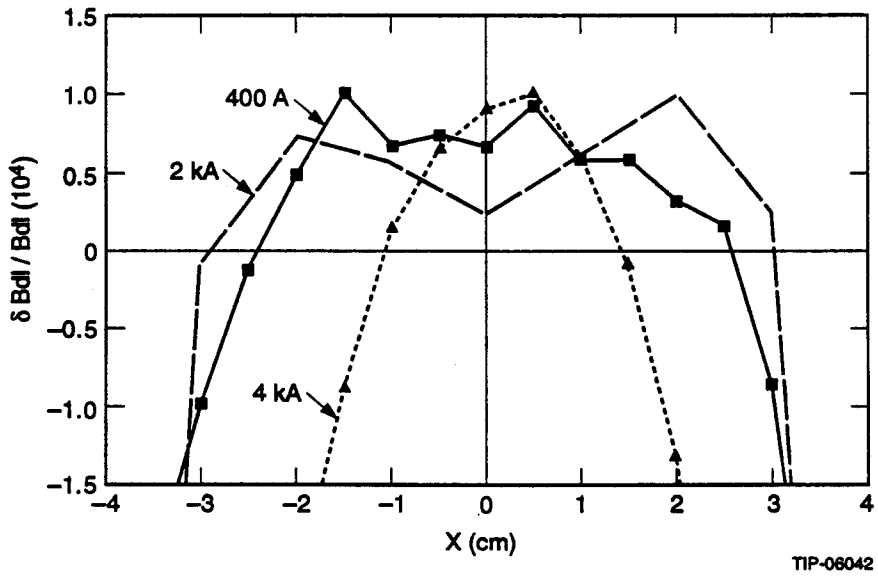

Figure 3.9: Field uniformity measurements.

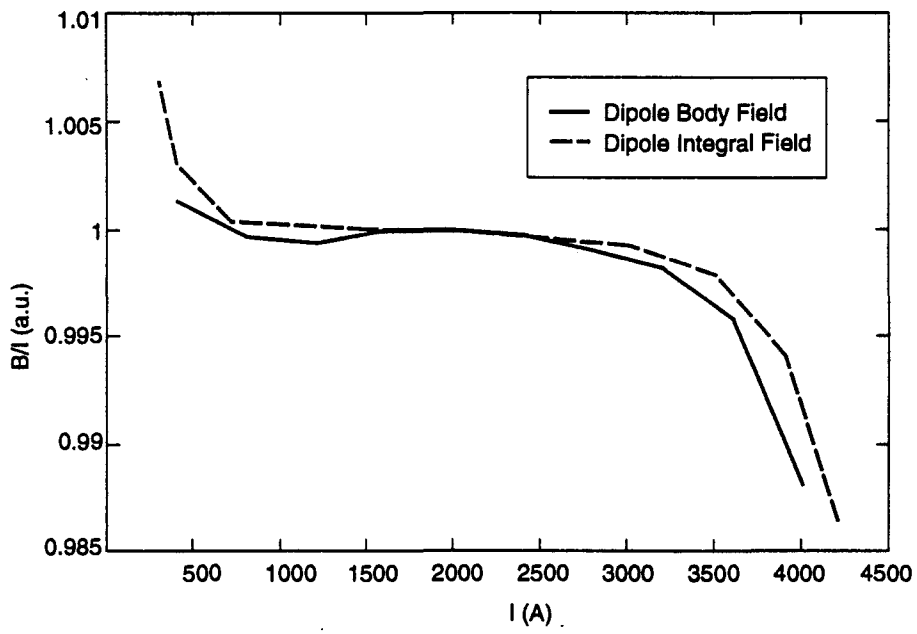

Figure 3.10: Measurements of the dipole field strength.

in the LEB; however, all use the same lamination cut with 5-cm aperture radius. Three different coil configurations are used. An isometric sketch of the magnet is shown in Figure 3.11, its parameters are given in Tables 3.5 and 3.6.

Mechanical Design

To simplify lamination production and coil assembly, the quadrupole body is designed for fourfold symmetry. The laminations are symmetric about the pole axis, with the exception of the quadrant to quadrant assembly lugs. Laminations will be flipped in groups during quadrant stacking to minimize effects of small differences in steel thickness and any dimensional asymmetry of the pole shape.

The laminations of each quadrant are not glued together except in the end packs, which are glued, welded and machined to achieve the 3D requirements. The core quadrants are fusion welded at regular intervals at the outer periphery and along the entire length to a tie bar which is recessed in a notch in the back leg. To prevent delamination during 10-Hz operation, an

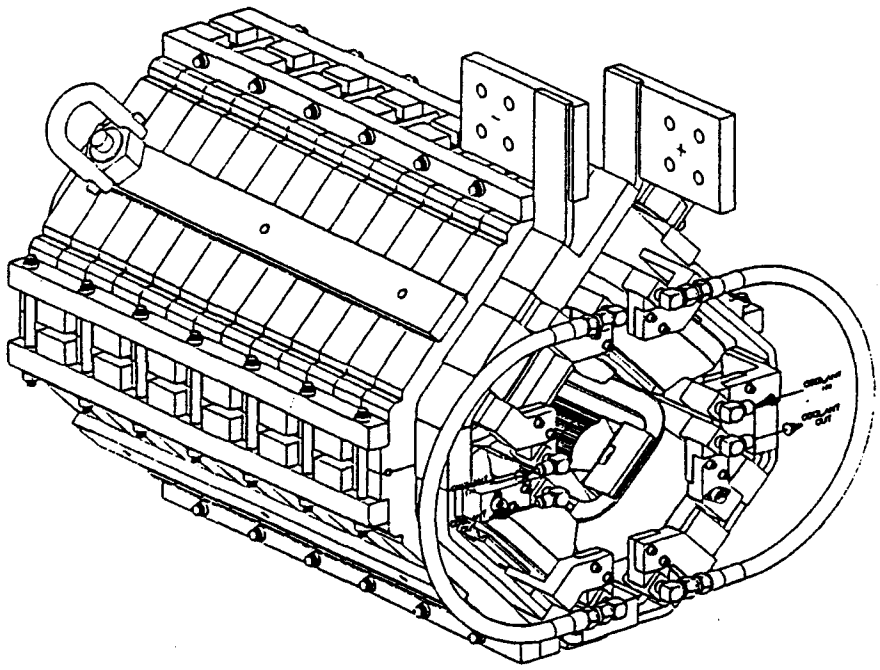

Figure 3.11: Isometric view of the quadrupole magnet.

insulated stainless steel rod goes through a hole in each pole tip, clamping G10 blocks against the end packs. The blocks will be wedged to follow the chamfer of the end pack.

Conductor size has been determined during magnetic design. The choice of four turns per pole is determined by the magnet field strength and the aperture in combination with power supply considerations of inductance and peak current. To reduce the operating costs a conservative current density (<5.6 A/mm^2 *rms* and <8.2 A/mm^2 peak) is maintained by choice of the conductor size, 23 mm×21.9 mm with a 6.5-mm inside diameter. The shape of the pole tip and of the coil requires that the core be constructed in quadrants with the coil attached to each quarter core before assembly of the entire core.

The coils are held in place on each quarter core by mounting brackets. The original design is felt to be prone to eddy current problems and alterna-

Table 3.5: Quadrupole families.

Quadrupole Name	Number Required	Effective Length (m)	Slot Length (m)
QF1	12	0.7564	0.9964
QF2	24	0.5919	0.8319
QD1	24	0.5983	0.8383
QD2	9	0.6127	0.8527
QFS1	6	0.6568	0.9179
QFS2	3	0.5552	0.8326
QDS1	6	0.6980	0.9380
QD2S2	6	0.6858	0.9258

tives have been under investigation at the time of project termination. No final decision has been reached, but it is likely that the brackets would be slotted.

Magnetic Design

The magnetic field requirements for the quadrupoles are determined by the beam dynamics calculations outlined in Chapter 2.3 and are given in Table 3.7. Unlike the dipole, the good-field region shrinks very little at extraction field, due to the beam size at the largest quadrupole aperture requirement being dominated by dispersion. Also, from a beam dynamics point of view only the integrated field uniformity has to meet the requirements, because the magnets are rather short. However, since the goal is to use one end-pack shape for all eight families it is still important that the two-dimensional field meets the requirements as well in order to minimize variations between the families. Compared to the dipole, the specification is relaxed by an order of magnitude, this results from the much lower fields of the quadrupoles when integrated over the whole ring.

The cross section of a lamination octant is shown in Figure 3.12. The quadrupole is designed for a peak gradient of 15.355 T/m in the gap, pole tip field of 0.768 T and a field of roughly 1.3 T in the return yokes. After adjusting the size of the return yokes to optimize tracking, the return yoke fields are quite different in the dipole and quadrupole.

Table 3.6: Parameters of the quadrupole magnet.

Magnet Parameter	Value
Peak Central Gradient	15.355 T-m
Peak Pole Tip Field	0.768 T
Good Field Region Radius (Injection)	42.5 mm
Good Field Region Radius (Extraction)	40 mm
Field Uniformity (ΔBL/BL)	$\leq 10^{-3}$
ΔGL/GL Magnet-Magnet	5×10^{-3}
Aperture Radius	50 mm
Core Height	486 mm
Core Width	486 mm
Lamination Thickness	0.5 mm
Weight	130–184 kg
Max Cooling Water Flow	4.2 gpm
Conductor Size	23 mm $\times$ 21.9 mm
Conductor Area	469 mm^2
Peak Amp-Turns/Pole	16 kA
Turns per Pole	4
Peak Current	4000 A
RMS Current	3473 A
Excitation Frequency	10 Hz
Inductance	0.52 mH/m
Resistance	0.54 mΩ + 1.1 mΩ/m
Average Power	6.5 kW + 22.5 kW/m
Peak Stored Energy	4 kJ/m
Number of Magnets	90

Table 3.7: Field parameters of the quadrupole magnet.

	Injection	Extraction
$\int B d\ell$ 8 families	0.853...1.16 T/m-m	8.53...11.6 T/m-m
Good-field region (radius)	42.5 mm	40 mm
Uniformity tolerance	10^{-3}	10^{-3}
magnet-to-magnet tolerance	5×10^{-3}	5×10^{-3}

To reduce stored energy, the minimum pole width which can maintain adequate field quality has been chosen. The pole-side angle has been adjusted to maximize magnetic efficiency at extraction while leaving sufficient space for the coil. The back-leg width is kept just large enough to maintain magnetic efficiency.

The shape of the pole face has been determined again using the computer codes POISSON and MIRT[22,23] for pole-face shimming to meet the specified field uniformity tolerance at both injection and extraction fields. As for the dipole design, the computer code PE2D[24,53] has been used to confirm the the field calculation results from POISSON. Figure 3.13 shows a plot of the quadrupole field as given by PE2D, after completed optimization.

Saturation of the quadrupole has been calculated for various yoke thicknesses. The final yoke thickness has been chosen just above a point where saturation increases dramatically with decreasing yoke thickness. This yields about 2 % saturation at extraction field. The dipole yoke has then been adjusted to optimize tracking with the quadrupole.

Requirements for the three-dimensional design are the same as for the two-dimensional design. Tracking of the different quadrupole families with each other and with the dipoles requires minimization of the change of quadrupole effective length over the full excitation range. The three dimensional measurement and design process are discussed in some detail in a technical note.[57]

Two different end packs have been designed. At SSCL, a 24-mm thick endpack has been designed with a straight chamfer extending 23.4 mm towards the magnet core and a length of 23.8 mm. BINP has proposed a

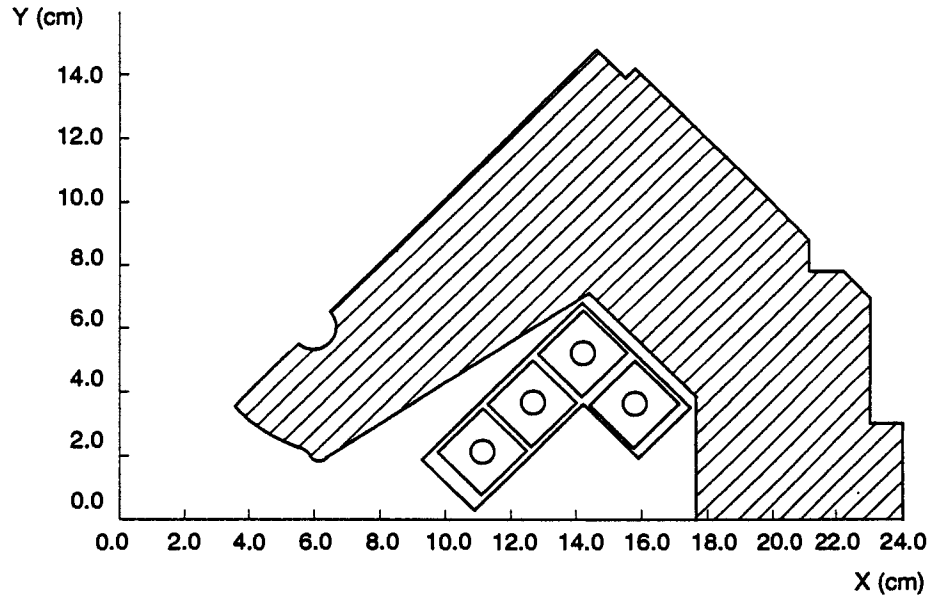

Figure 3.12: Quadrupole cross section.

50-mm thick end pack with three chamfers as shown in Figure 3.14, designed by numerical modeling and measurements on a test magnet. The sides of each end pack are chamfered to allow clearance for the excitation coil.

Both end pack configurations have been measured at SSCL. The chamfer of the SSC designed endpack has been varied to improve field uniformity across the good field region. Results of this work are discussed in Section 3.1.3.

Ac issues in the quadrupole are the same as in the dipole, but mitigated by the lower fields and power levels involved. The power loss to the core of a quadrupole is roughly 260 W/m. Calculated losses in the coils due to eddy currents are quite high at 8960 W/m. Compared to resistive losses in the coil of approximately 13.27 kW/m. While these losses affect the power supply requirements, there is no significant effect on field uniformity.

The field distortion caused by eddy currents in the vacuum chamber is sufficiently small that no correction coils are necessary.

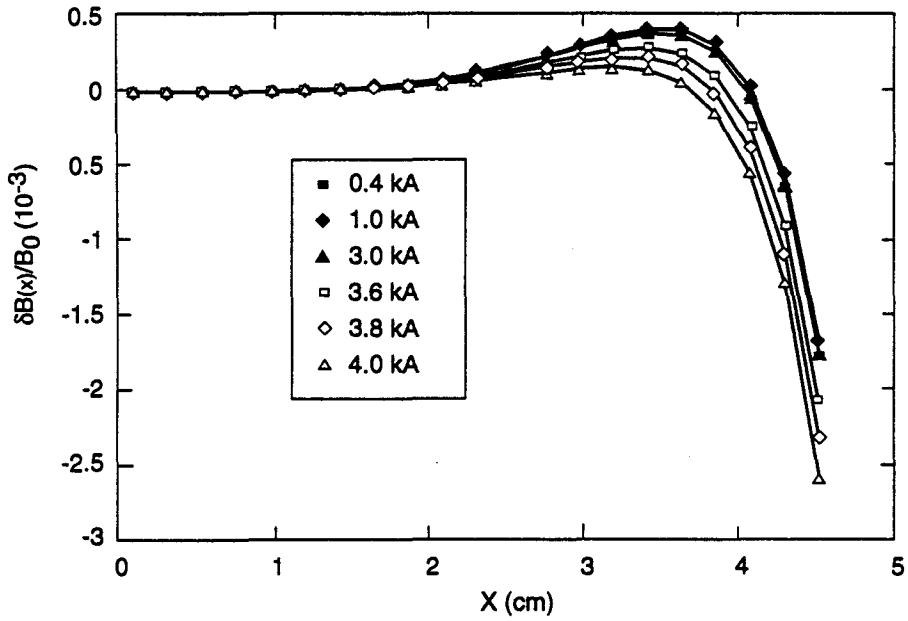

Figure 3.13: PE2D calculation of the two-dimensional quadrupole field.

Fabrication

Tolerance The prototype built in the LBL uses laser cut laminations and the prototype fabricated in the INP was used die punched laminations for iron cores. The laser cut laminations have reached the ±0.0125 mm design tolerance requirements for the critical segments. The die punched laminations have very good quality as well. Figure 3.15 shows sketches of the pole-tip regions of both laminations together with their error-envelope.

Tooling

Punch and Die The principle of the die design is similar to the dipole lamination die. The difference is that the quadrupole punch and die are built in one solid piece each, which is quite unusual (see Figure 3.16). ZVI has chosen this design based on the complicated pole shape of the quadrupole lamination, which consists of more than 50 tiny broken lines. The one-piece design is the key to reaching the high quality die required, see Figure 3.15. The disadvantage of the solid die is that, in the event of a die failure, the

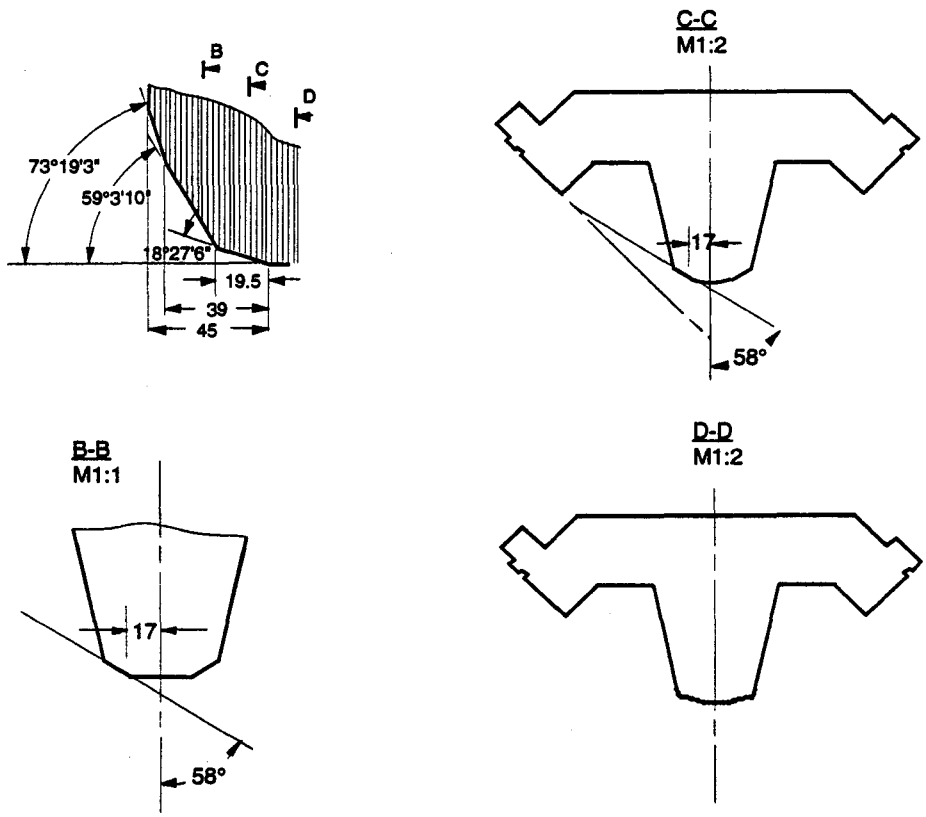

Figure 3.14: BINP design for LEB main quadrupole end-pack.

complete die has to be replaced, whereas with a composite die only the damaged part requires replacement.

Punch and die have been cut on an EDM machine made in Switzerland. The finish of the die is $\nabla 8$–$\nabla 9$, the hardness of the punch and die is HRC 57-59, and the precision is up to 0.005 mm. The die has been continuously cut in 4 shifts, 32 hours. All sharp corners are rounded to 0.25-mm radius increasing ZVI's estimate of the die life from 330 000 to 500 000 pieces. Clearance of the die is 0.017mm–0.022mm, which is a factor of 10 less than the regular design. The press used for quadrupole laminations production is a 350-ton auto-machine made in Germany with a very small stroke distance.

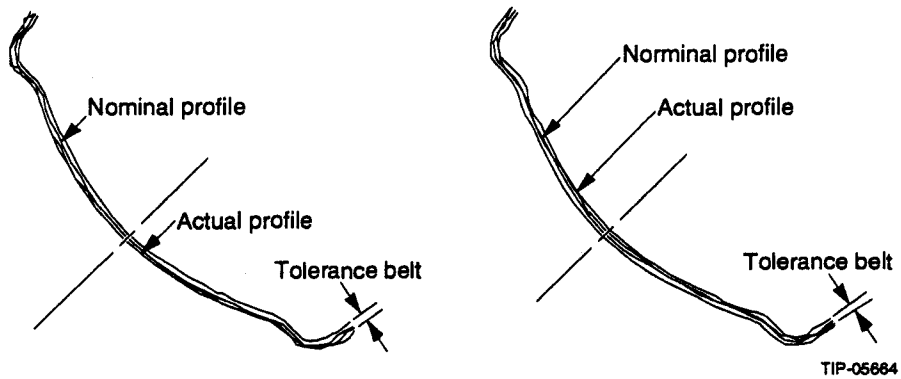

Figure 3.15: Quadrupole pole tip of the punched lamination (a) and the laser cut lamination (b).

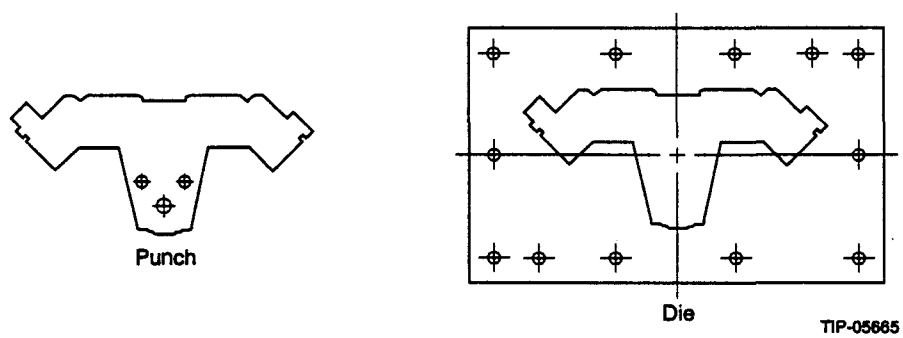

Figure 3.16: Quadrupole lamination punch and die.

Stacking Fixture Figure 3.17 shows a sketch of the quadrupole stacking fixture. Because the iron cores have rather short length and the fusion welding occurs on the back of the lamination only, the stacking fixture is horizontal.

Prototypes

One prototype has been built under contract by LBL using laser cut laminations. This magnet has been measured both at LBL and at SSCL. BINP has built three prototypes, using punched laminations, one of which has been shipped to SSCL for measurement while the others have remained at BINP for dc and ac measurements.

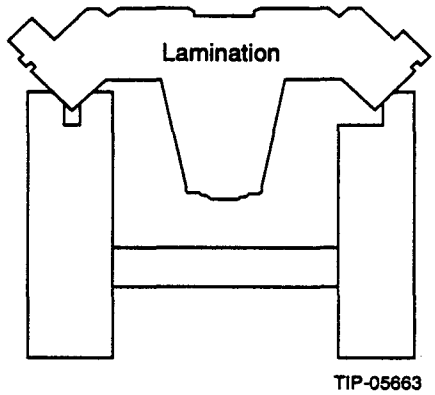

Figure 3.17: Quadrupole stacking fixture.

Mechanical Inspection Results Figure 3.18 shows the mechanical inspection results of the INP prototype. The pole diameter measurements taken at two ends and the mid-part of the core show that the aperture is within tolerance. This indicates that the convexity of the yoke caused by welding is eliminated after assembling. The gap tolerance varies across the eleven lamination packs and from gap to gap, between 0.08 mm and 0.18 mm. These inspection results indicate that the reproducibility of core assembly is not sufficient.

In addition to the above results, four yokes show that the non-flatness of the mating surfaces with lugs ranges from 0.05 to 0.10 mm, while mating surfaces without lugs range from 0.05 to 0.12 mm and pole surfaces range from 0.05 to 0.27 mm. Such large deviations demonstrate rather poor reproducibility of yoke stacking and that the procedure for quadrupole stacking and welding is not yet mature. Tight mechanical tolerances not only ensure magnetic field quality but also reproducibility during production, which is important for magnet to magnet uniformity.

The prototype quadrupole built at LBL has been measured at SSCL. The magnet has had very good mechanical quality when inspected at LBL, however, after shipping to the SSC site its dimensions have been found to have changed significantly. Table 3.8 shows the inspection results from three measurements. The deviations of the gaps range from −0.0654 mm to 0.1632 mm, exceeding the specified tolerances and affecting the field quality. It is planned to improve the rigidity of the quadrupole either by increasing the diameter and/or the quantity of the bolts which clamp the quadrants to-

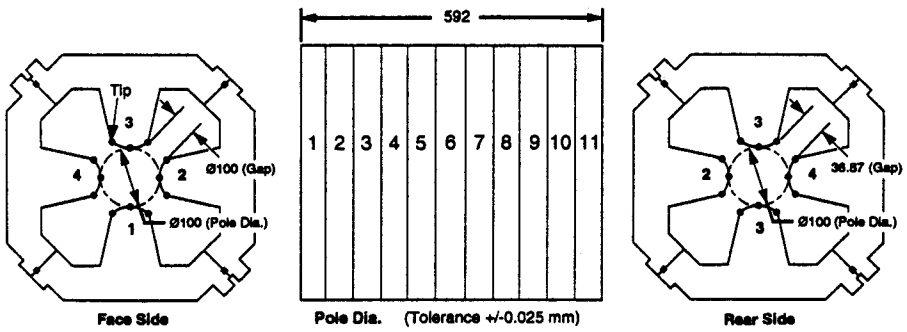

Tip to Tip

Position \ Item	Nominal Dia.	1	2	3	4	5	6	7	8	9	10	11	Average
1 - 3	100.00	-0.01				0					0.01		
2 - 4	100.00	0.01				-0.01					0		

Gap Dim. (Tolerance +/- 0.025 mm)
Tip to Tip

Position \ Item	Nominal Gap	1	2	3	4	5	6	7	8	9	10	11	Average
1 - 2	36.87	36.82	36.86	36.85	36.84	36.88	36.89	36.85	36.84	36.81	36.85	36.83	0.08
2 - 3	36.87	36.91	36.84	36.86	36.85	36.83	36.83	36.85	36.81	36.85	36.83	36.91	0.10
3 - 4	36.87	36.77	36.95	36.89	36.83	36.81	36.81	36.87	36.84	36.83	36.87	36.81	0.18
4 - 1	36.87	36.90	36.82	36.82	36.88	36.87	36.87	36.83	36.87	36.87	36.87	36.84	0.08

TIP05666

Figure 3.18: INP quadrupole prototype inspection result.

gether or by adding angle plates to reinforce each quadrant. A final decision has not been made at the time of project termination.

Magnetic Measurements Both prototype quadrupoles have been measured at the SSCL. Measurements of integral and body field harmonics have been used to evaluate the magnets. Integral measurements have been used to evaluate various end pack chamfers. A cost saving option of using three coil lengths for all eight quadrupole families has been approved following measurements of field harmonics with a modified core length.

The LBL prototype has been measured at both LBL and SSCL. The body field harmonics near injection and extraction field as measured at both labs are shown in Figure 3.19. Both measurements yield consistent data for the allowed field harmonics (n = 6, 10 and 16) and most non-allowed harmonics. The $n = 6$ harmonic has the opposite sign of $n = 10$ and $n = 14$, thus partially cancelling on the midplane. There is however a dramatic difference between the two measured values for the skew sextupole ($n = 3$) component.

Table 3.8: Quadrupole core inspection results.

†	Gap*	Deviation		
		1. measurement	2. measurement	3. measurement
l	1	0.0235	0.0362	0.0235
e	2	0.0616	0.0235	0.0616
a	3	−0.0654	0.0108	−0.0273
d	4	0.0870	0.0997	0.0616
m	1	0.0870	0.0870	0.1251
i	2	0.1378	0.1632	0.1505
d	3	−0.0400	−0.0273	−0.0146
	4	−0.0019	0.1632	0.1505
r	1	−0.0146	0.0362	0.0108
e	2	0.0870	0.0997	0.1124
a	3	−0.0654	−0.0146	−0.0146
r	4	0.0870	0.0870	0.0997

† lead/mid/rear: indicates position of measurement
* Nominal value 36.87 mm

Additional body field measurements taken at different longitudinal positions have demonstrated that the skew sextupole component is a localized phenomenon. The observed consistency between LBL and SSCL data for all other harmonics supports the validity of both measurements; therefore the skew-sextupole component has to be accepted as being actually present.

As discussed in the "Mechanical Inspection Results" section the original mechanical design is not rigid enough and allows parts of the magnet to shift. The cause of the skew-sextupole component in the body field has been attributed to stretched bolts in the mechanical assembly, impairing the dimensional stability of the magnet. Particle tracking studies show that the other harmonics are acceptable. As this error is an unallowed harmonic, it is still possible to certify the basic lamination design and to continue with 3D measurement and chamfer development.

Figure 3.20 shows measurement results of the integrated field harmonics in the LBL prototype quadrupole, taken at the SSCL with the originally designed chamfer (end pack #0) and with the chamfer empirically optimized at SSCL (end pack #3). Measurements have been taken at the excitation current near its injection and its extraction value. LBL has made similar

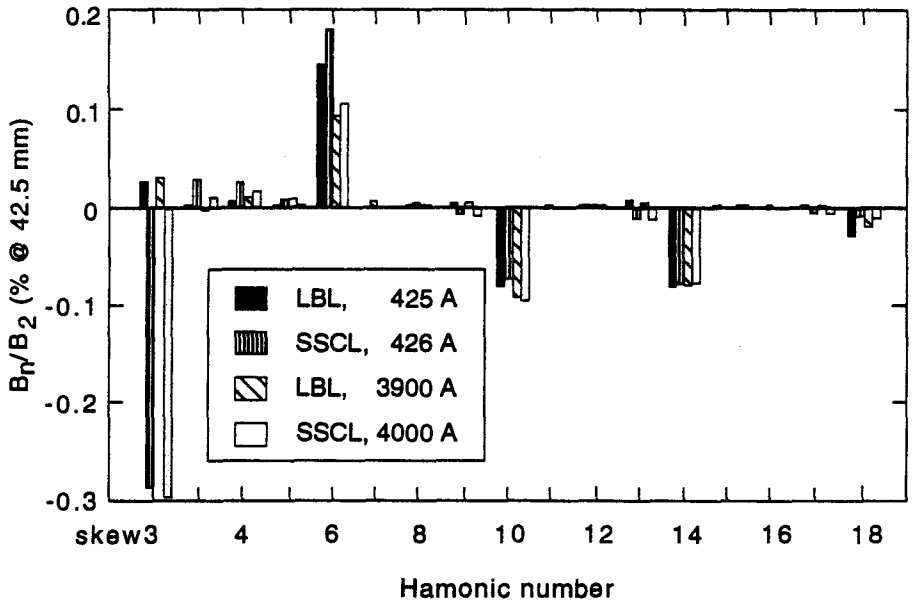

Figure 3.19: Body field harmonics in LBL prototype quadrupole.

measurements with the same end pack which are in agreement with SSCL's measurements except for the skew sextupole component discussed above.

The chamfer on end pack #3 has then been modified to improve the transverse uniformity of the integrated field. End pack #0 gives $n = 6$, 10 and 14 harmonics which are all negative (*i.e.* in phase), and therefore reinforce one another on the midplane. The goal for end pack #3 is to move all of the harmonics toward more positive values. The result has the $n = 6$ harmonic changing it sign (phase flip by 180°), thus partially offsetting the negative $n = 10$ and 14 and reducing the field drop-off towards the limits of the good-field region. This has been achieved by lengthening the chamfer from 20.6 mm to 23.4 mm and maintaining the same approximate chamfer angle in order to remove more material from the center of the pole tip. The uniformity of the integrated gradient across the good field region meets the specifications.

Results of the SSCL measurements of the BINP prototype integrated field harmonics are shown in Figure 3.21. There is good agreement with the LBL quadrupole data for body field harmonics (not shown) and also for the integrated harmonics with end pack #3, which has been mounted to the

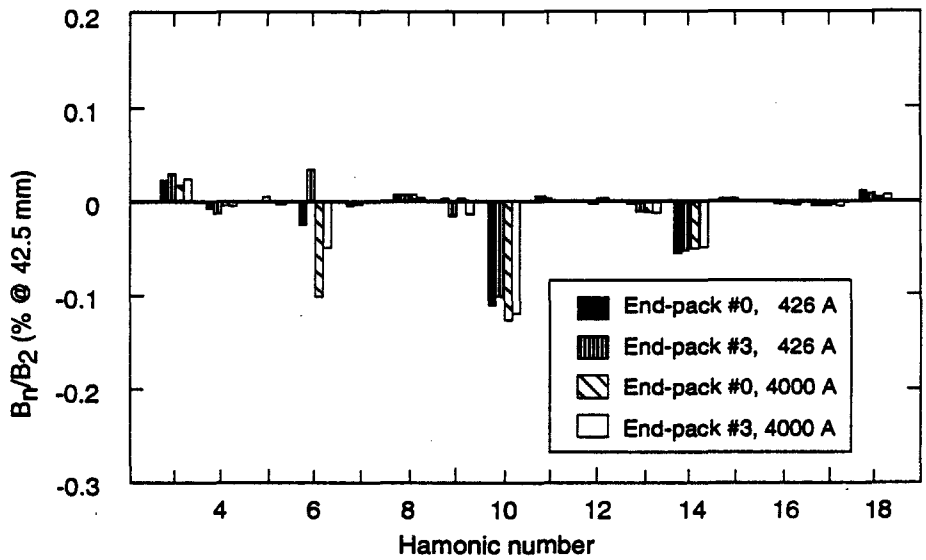

Figure 3.20: Integral field harmonics in LBL prototype quadrupole.

BINP prototype for this measurement. End pack #4 is the BINP designed end pack. Integrated gradient uniformity of this configuration is not quite as good as for end pack #3, but particle tracking has shown this configuration to be acceptable as well. The integrated field gradient uniformity on the midplane of the BINP prototype is displayed in Figure 3.22, taken at the same currents as in Figure 3.21.

The excitation function of the BINP prototype is shown in Figure 3.23 and of the LBL prototype in Figure 3.24. The effect of hysteresis on the injection field strength is the same for both magnets. Differences in the steel characteristics and a higher packing factor of the BINP prototype result in approximately 1 % less saturation at extraction field of this prototype as compared to the LBL magnet. The BINP designed chamfer, end pack #4, reduces the effective-length change by another 0.5 % compared to the SSC designed end pack.

Figure 3.25 shows the relative strength of the dipoles and quadrupoles over the excitation range for the INP prototype magnets in the configuration closest to the anticipated final one. The dipole has the original end pack and the quadrupole has end pack #4. It appears that the tracking error reaches approximately 1 % at either extreme end of the excitation current. The

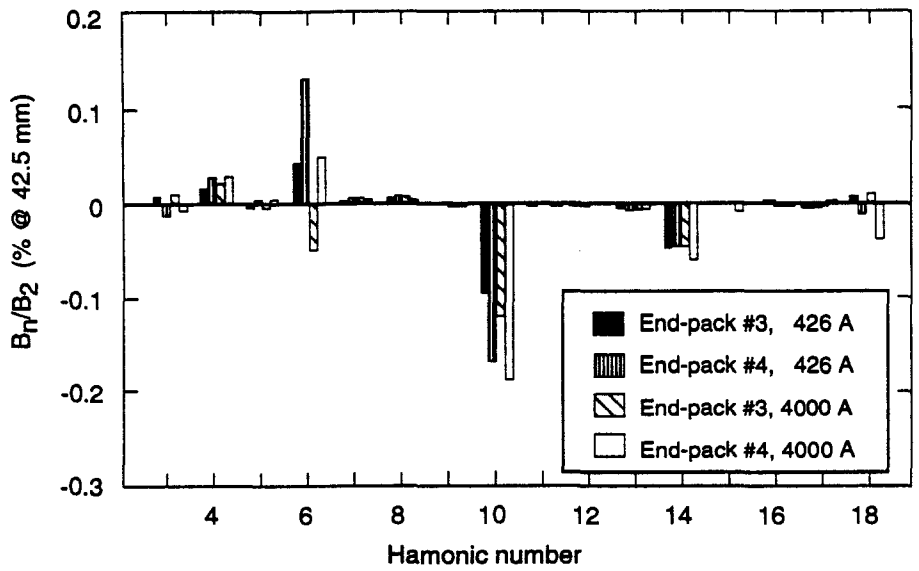

Figure 3.21: Field harmonics in the INP prototype quadrupole.

situation may improve with the redesigned dipole end pack, however, it is unlikely that the specification of 0.5 % max. tracking error will be met. As the tuning capabilities of the LEB are more than sufficient to compensate for this error no performance degradation is expected, however, machine commissioning may require additional time to setup and tune the tracking compensation.

A final decision on the quadrupole end pack configuration has not been made before project termination. The SSCL design (#3) has slightly better field quality, but the BINP design (#4) is favored for its smaller effective length change and better tracking with the dipole in light of the fact that field harmonics are acceptable as well for this configuration.

3.1.4 Corrector Magnets (M. Schulze)

Overview

The LEB corrector magnets provide for a wide variety of tune adjustment, orbit correction and matching between the cells, supercells, and superperiods which comprise the LEB ring. Six magnet groups, grouped by functionality,

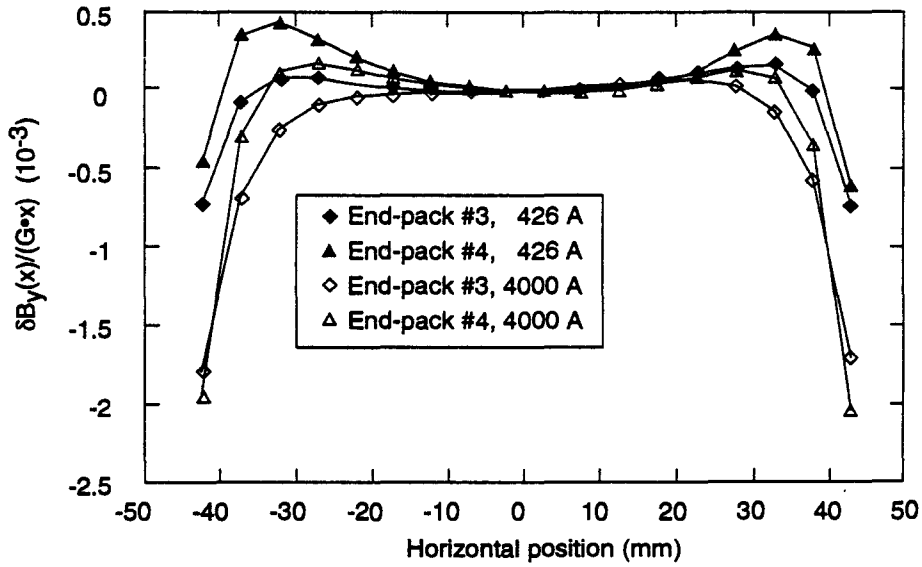

Figure 3.22: Field on the midplane of the BINP prototype quadrupole.

make up the LEB corrector magnet systems. Within each group, the magnets may be further classified according to whether the magnet is focusing or defocusing and in terms of orientation. This is summarized in Table 3.9.

The similarity between the skew quadrupoles and low-field trim quadrupoles is such that a single magnet design with provision for mounting on a support stand in different orientation will suffice. Thus, five independent magnet designs are needed for the LEB corrector magnets.

With the exception of the skew sextupoles, each of these magnets is made of 0.5 mm laminations coated with electrical insulation sandwiched between thick end plates to form the magnet yoke. The shape of the laminations is defined by the main multipole of the magnet, the good field region, and other constraints related to accessibility and ease of fabrication. The magnetic circuit is formed by attaching coils of copper wire to the yoke with the appropriate polarity and orientation to achieve the required magnetic field when energized. The skew sextupoles are intended to facilitate crossing skew resonances, they require only nominal field strength allowing for an air core design.

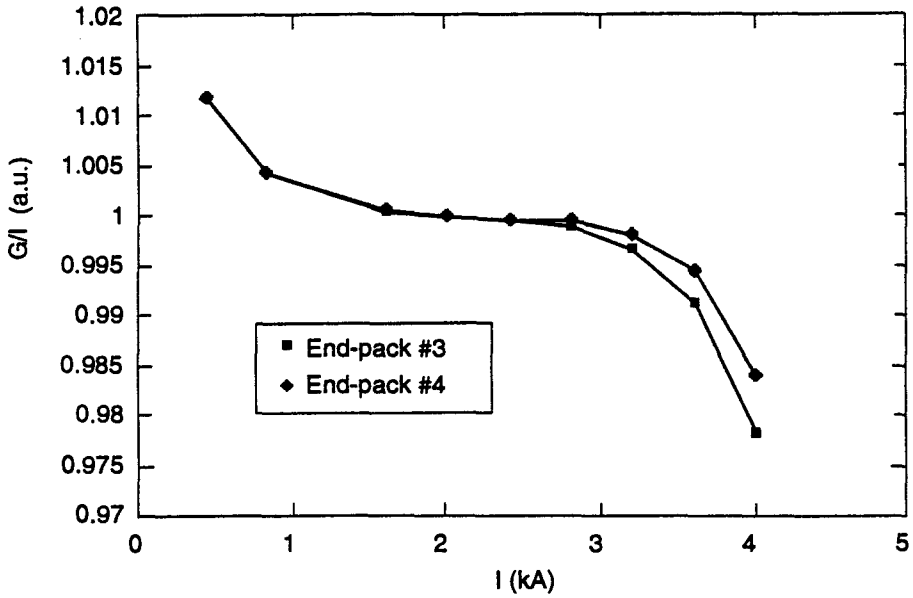

Figure 3.23: Integrated gradient *vs.* current in the BINP prototype quadrupole.

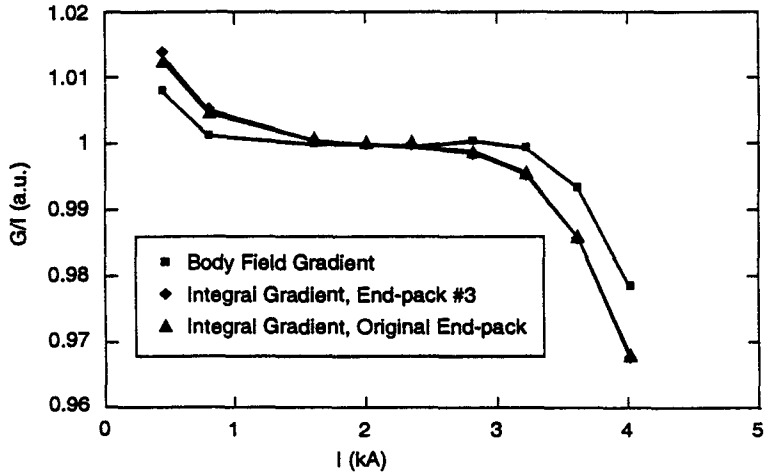

Figure 3.24: Integrated gradient *vs.* excitation current in the LBL prototype quadrupole.

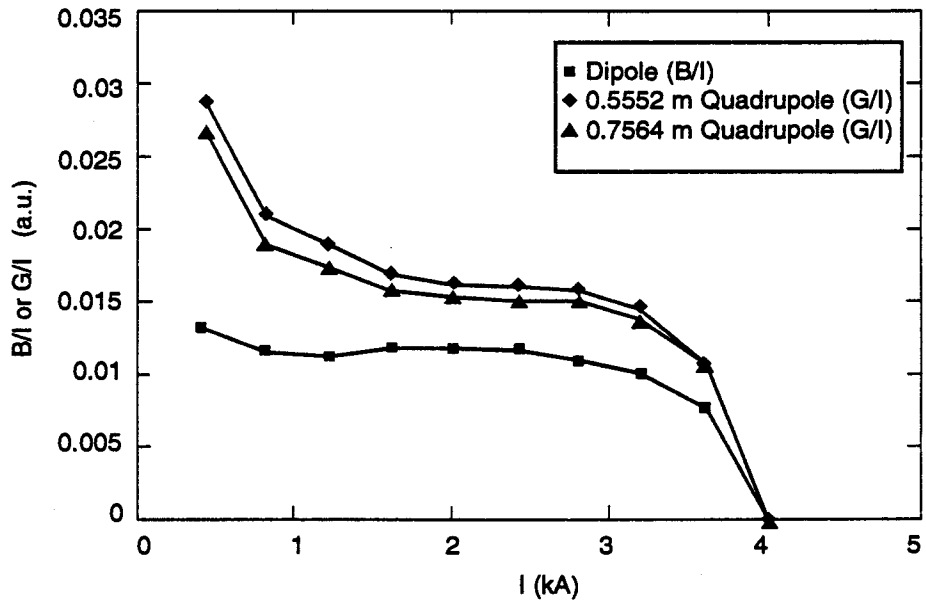

Figure 3.25: Saturation of main dipoles and quadrupoles.

All of the LEB corrector magnets except for the skew sextupoles are to be fabricated as part of an international collaboration with Budker Institute for Nuclear Physics (BINP) in Novosibirsk, Russia.

Many of the LEB correctors that have been designed and fabricated at the SSCL are not actively cooled; that is, they are cooled by ambient air convection. As a result of this design, it is important to understand the safe limit for the magnet excitation. An experimental and analytical study has been performed to quantify and understand this issue.[58] The results of this study show that the current or power density is the critical factor is determining the temperature rise, as expected. The results for the three air-cooled LEB correctors are presented in Figure 3.26.

At the time of termination, BINP has fabricated three prototypes each of the orbit correcting dipole (OCD), high-field trim quadrupole (HFTQ), low-field trim quadrupole (LFTQ), and chromaticity sextupole. One each of the OCD, HFTQ, and LFTQ along with two chromaticity sextupoles have been fabricated by the Resistive-Corrector Magnet Group at the SSCL. Electromechanical and magnetic measurements have been made on all of the above prototype magnets.

Table 3.9: LEB corrector magnets.

Design	Type	Quantity	Integrated Strength (*)	Effective Length (m)
Orbit Correcting Dipoles	Horizontal	45	0.0255	0.15
	Vertical	45	0.0255	
High Field Trim Quadrupoles (HFTQ)	QTFS1	6	0.92	0.24
	QTFS2	6	1.44	
	QTDS2	6	0.56	
Low Field Trim Quadrupoles (LFTQ)	QTF2	24	0.12	0.24
	QTD2	18	0.31	
	QTD1	24	0.26	
	QTDS1	6	0.14	
Skew Quadrupoles		4	0.30	0.24
Chromaticity Sextupoles	SF	24	13.4	0.30
	SD	12	24.0	
	SD1	12	25.8	
Skew Sextupoles		12	3.60	0.30

(*) Dipoles (T-m), Quadrupoles (T-m/m), Sextupoles (T-m/m2)
[these strengths are the maximum integrated field]

Orbit-Correcting Dipole Magnets

The orbit correcting dipole magnets for the LEB are designed as small C-magnets for easy placement and removal in the ring. The magnetic circuit consists of precision punched laminations held together between two thick stainless steel end plates (8.0 mm) and assembled with its electrical wiring. The electrical circuit consists of four pancake coils, two coils per pole, connected in series. The height of each coil is 41 mm to facilitate installation into the 50-mm gap. Each coil is made of two layers which are connected (brazed) in series electrically. The conductor is solid copper wrapped with fiberglass tape prior to winding. Each individual coil is wrapped with fiberglass tape after winding to provide a layer of ground insulation. The coils are then vacuum impregnated and cured.

A sketch of the LEB dipole correction magnet lamination and coil geometry along with the good field area is shown in Figure 3.27. Mounting bars are attached to the endplates on the side or the bottom to facilitate installation as a horizontal or vertical dipole corrector. The end plates also hold the

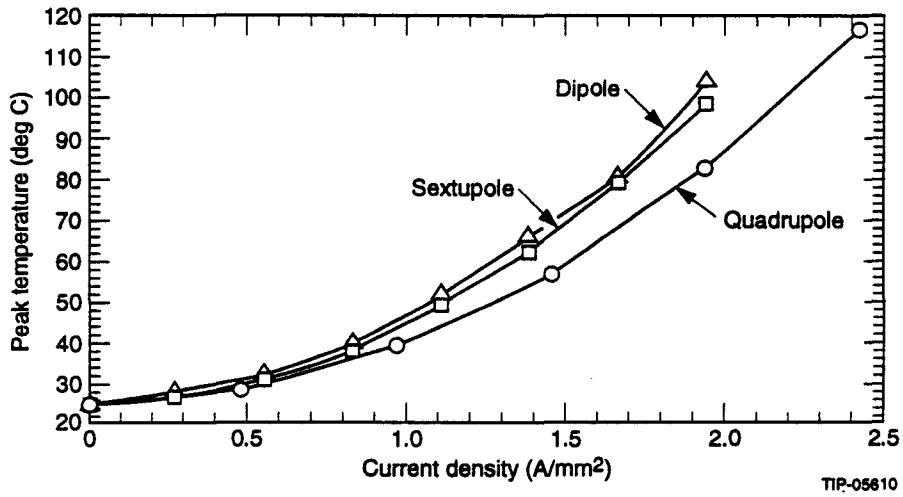

Figure 3.26: Dependence of the temperature rise in the air-cooled LEB correctors as a function of the coil current density.

electrical leads and provide rigidity to the lamination pack. The lamination packs for the prototypes built at BINP have been glued, stacked and cured, whereas the SSCL prototype does not use an adhesive. The magnet core is held together by four studs located at the four corners and used to compress the end plates and laminations. This design does not require any welding and avoids shorts between adjacent laminations. The effect of eddy currents have been considered in the design and the surface area of the end plates in the higher field region near the gap is minimized.

The die punched laminations produced and inspected at the ZVI site in Russia have also been inspected at SSCL. In both inspections the region of the pole tip and magnet gap have been found to be within the specified tolerances of ± 0.015 mm and ± 0.0125 mm respectively. There are some small discrepancies between the inspections of the external edge of the laminations. Some areas have been observed to be outside the specified tolerances, but they do not affect magnet performance and the laminations have been accepted.

Four prototype magnets have been fabricated, three of these at BINP. Table 3.10 gives the design requirements and measured values for the electromechanical and magnetic parameters which describe the dipole correctors.

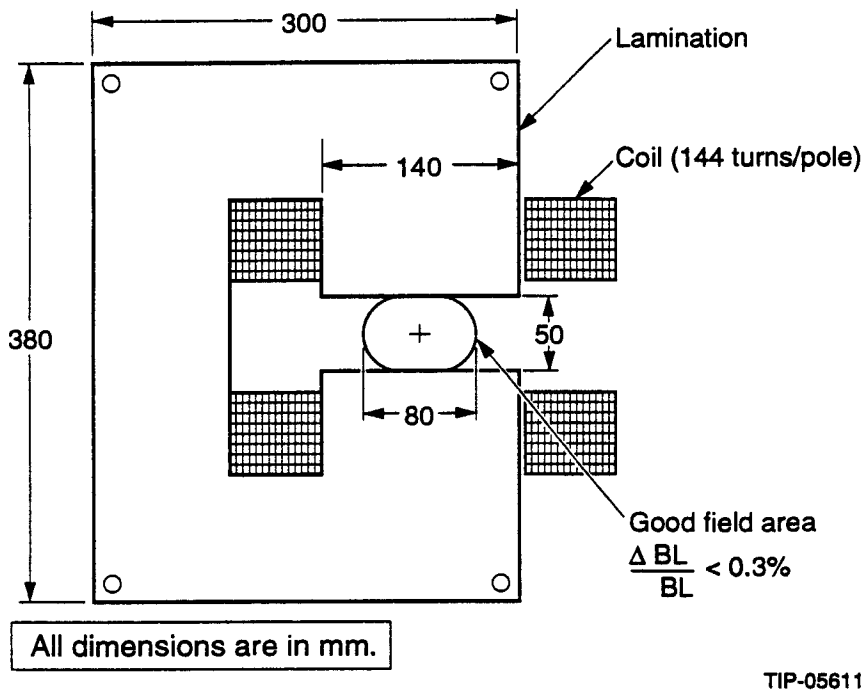

Figure 3.27: Cross section of the LEB dipole corrector magnet.

The values presented in Table 3.10 represent the parameters which describe the BINP prototypes in those cases where a difference exists.

The ratio of the iron length to the magnetic field gap is less than two. As a result, there is no true central field region where the magnetic field is uniform; the magnet is entirely fringe field. This feature makes achieving the integrated field uniformity requirement very difficult.

A great deal of effort has been expended to achieve the field uniformity requirement. The 2D model and measurements of the central field show the magnetic field to be lower in the center compared to the edges of the good field region as desired. However, it has proved extremely difficult to achieve the integral field uniformity both with 3D model predictions with TOSCA and by experiment and measurements. In hindsight, two changes would have improved the situation. These are (1) an increase of the pole width and (2) an increase of the shim at the edge of the pole tip. The fringe field at the edge of the magnet falls off much more rapidly due to the relatively narrow pole. This causes the integrated field in the center of the magnet

Table 3.10: LEB orbit correction dipole magnet parameters.

Magnetic Parameter	Design	Actual/Measured
Peak Integrated Field (T/m)	0.0255	0.02563
Peak Central Field (T)	0.17	0.1706
Good Field Region	±40 mm/ ± 25 mm long/short dimension	SAME
Field Uniformity ($\Delta BL_{eff}/BL_{eff}$)	< 0.30 %	±0.18 %
Effective Length (mm)		150.
Gap Height at Pole Center (mm)		52.5
Minimum Gap Height (mm)	50.0	50.0
Excitation Frequency (Hz)		10.
Total Ampere Turns		7200
Magnetic Efficiency	0	.995
Turns per Pole		144
Peak Current (A)	±25.	±25.
RMS Current (A)		15.86
Conductor Size (mm × mm)		2.8 × 6.3
Conductor Cross Section (mm^2)		17.64
Peak Current Density (A/mm^2)		1.42
RMS Current Density (A/mm^2)		0.90
Average Length per Turn (m)		0.71
Inductance (mH)	53.0	53.0
Resistance (mΩ)	200.	197.
Peak Voltage Drop (V)		57.9
Peak Power (W)		1448.
Average Power (W)		58.4
Stored Energy (J)		16.6
Cooling	Air	Air
Lamination Thickness (mm)	0.5	0.5
Core Length (mm)		90.
Core Width (mm)		300.
Core Height (mm)		380.
Total Length (mm)	270.	268.
Total Width (mm)		364.
Total Height (mm)		380.
Copper Weight (kg)		31.
Steel Weight (kg)		66.
Total Weight (kg)		97.

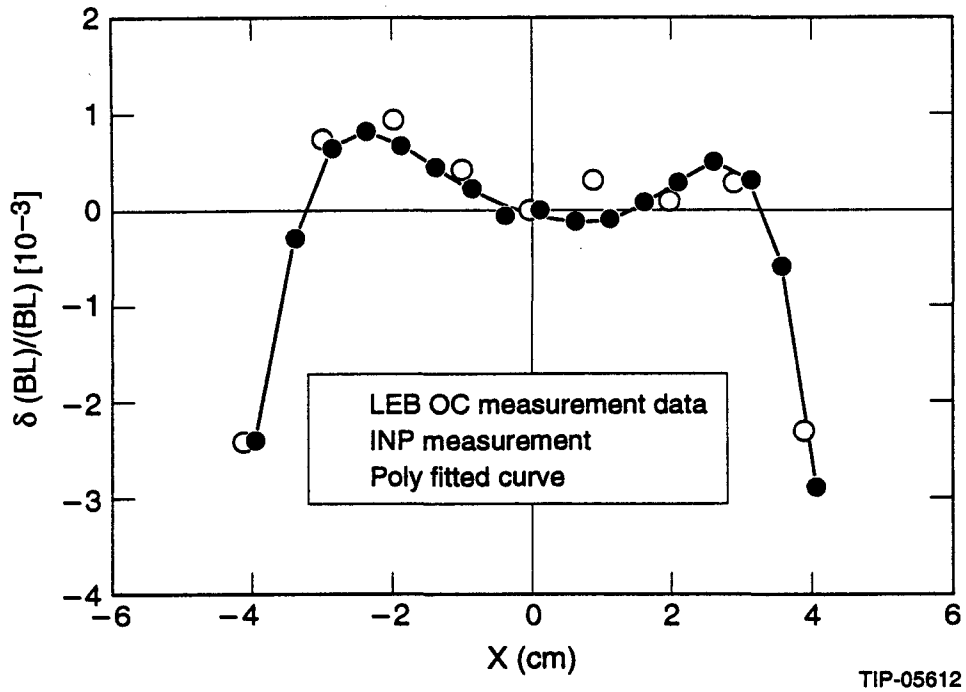

Figure 3.28: Integrated field uniformity of the LEB dipole corrector magnet.

to be a few percent higher than at the edges of the good field area in the absence of chamfering.

Approximately 40 iterations have been performed on the shape and chamfer of the pole tip, and studied with TOSCA. Great care has to be taken when using TOSCA for 3D prediction on a magnet that is entirely fringe field. After many iterations and a careful comparison with the measurement results from both SSCL and LBL, the use of "nibbled" laminations at the ends of the magnet have been adopted instead of the chamfered pole. Once a reasonably close solution has been found small iterations have been made to improve the field quality. The SSCL prototype has been modified about 10 times before an acceptable solution was found. Three of these iterations have been fabricated and measured at BINP in verification of our results.

Figure 3.28 shows a plot of the integrated field uniformity measured at SSCL and BINP using different measurement systems. The SSCL and BINP measurements have been made using a rotating coil and an Hall probe array

respectively. The plotted results for the final iteration of the pole are in excellent agreement with each other and show a field uniformity of ± 0.18 %. Because of the difficulties outlined above the field specifications for the OCD have been re-examined and, based on tracking studies using all data available at the time, relaxed from the original value of 0.1 % to the present 0.3 %.

Trim and Skew Quadrupole Magnets

Although two different trim quadrupole designs are used in the LEB, the magnets differ only in the design of the coils. They use the same iron length and lamination design. The laminations are the same as used in the main LEB quadrupoles described in Section 3.1.3. This choice avoids the need for additional lamination dies as the aperture requirements are basically the same. The high-field trim quadrupole (HFTQ) and low-field trim quadrupole (LFTQ) are designed for pole-tip fields of 0.3 Tesla and 0.1 Tesla respectively. The LEB lattice design requires 18 HFTQ and 76 LFTQ (including the 4 skew quadrupoles) as presented in Table 3.9. The HFTQ design requires water cooling because of the larger number of ampere turns necessary to achieve the specified pole tip field. Due to the smaller quantity of HFTQ and the complexity imposed by water cooling, an air-cooled coil design has been adopted for the LFTQ. The design requirements and measured results for these two magnets are summarized in Tables 3.11 and 3.12.

The magnetic circuit of the HFTQ consists of four identical quadrants which are assembled so that adjacent poles are of opposite magnetic polarity. Each quadrant is composed of precision punched laminations and assembled with its electrical wiring. The quadrants are assembled in six stacks with a precision-built stacking fixture. A thick steel bar is welded along the return yoke, after the pole alignment is fixed with a rod which passes through a hole in the laminations near the pole tip. Four fuse welds located on the outside of the quadrant on each side of the bar near the mating surfaces are used to secure the individual lamination stacks together. This assembly technique works well for the corrector quadrupoles due to their short iron length. The quadrants are assembled into half cores using a key way for transverse alignment. The half cores are then assembled to form the complete magnet.

The electrical circuit of the HFTQ consists of four identical coils with 70 turns per pole. The conductor is hollow with dimensions as given in Table 3.11 to allow for water cooling. Each coil includes two independent

Table 3.11: LEB high field quadrupole magnet parameters.

Magnetic Parameter	Design	Actual/ Measured
Peak Integrated Gradient (Tm/m)	1.44	1.764
Pole Tip Field (T)	0.30	0.30
Magnetic Field Gradient (T/m)	6.0	6.0
Good Field Region	40 mm Radius	
Field Quality in Good Field Region ($\delta \int B(x)dl / \int g \cdot x\, dl$)	0.10 %	0.07 %
Effective Length (mm)	240	294
Radius of Inscribed Circle (mm)	50.	52.5
Excitation Frequency (Hz)		10.
Ampere Turns per Pole		6000
Magnetic Efficiency		0.995
Turns per Pole		70
Peak Current (A)	100.	85.71
RMS Current (A)		54.86
Conductor Size (mm × mm)		5 × 5 (3 mm dia)
Conductor Cross Section (mm^2)		18.0
Peak Current Density (A/mm^2)		4.90
RMS Current Density (A/mm^2)		3.133
Average Length per Turn (m)		0.90
Inductance (mH)	52.0	53.0
Resistance (mΩ)	250.	286.
Peak Voltage Drop (V)		140.3
Peak Power (kW)		2.20
Average Power (kW)		0.88
Lamination Thickness (mm)	0.5	0.5
Core Length (mm)		250.
Core Width (mm)		486.
Core Height (mm)		486.
Total Length (mm)	390.	375.
Total Width (mm)		486.
Total Height (mm)		486.
Copper Weight (kg)		38.
Steel Weight (kg)		209.
Total Weight (kg)		247.
Water Pressure Drop (kg/cm^2 - psi)		5.6–80
Number of Water Parallel Circuits		8
Total Water Flow (m^3/hr)		0.576
Temperature Rise (°C)		1.31

Table 3.12: LEB low field and skew quadrupole magnet parameters.

Magnetic Parameter	Design	Actual/ Measured
Peak Integrated Gradient (T-m/m)	0.31	0.588
Pole Tip Field (T)	0.10	0.10
Magnetic Field Gradient (T/m)	2.0	2.0
Good Field Region	40 mm Radius	
Field Quality in Good Field Region ($\delta \int B(x)dl / \int g \cdot x\, dl$)	0.20 %	0.07 %
Effective Length (mm)	155.	294.
Radius of Inscribed Circle (mm)	50.	52.5
Excitation Frequency (Hz)		10.
Ampere Turns per Pole		2000
Magnetic Efficiency		0.997
Turns per Pole		144.
Peak Current (A)	±15.0	±13.89
RMS Current (A)		8.89
Conductor Size (mm × mm)		2.54 × 4.064
Conductor Cross Section (mm^2)		9.95
Peak Current Density (A/mm^2)		1.40
RMS Current Density (A/mm^2)		0.89
Average Length per Turn (m)		0.85
Inductance (mH)	22.0	22.0
Resistance (mOhm)	840.	920.
Peak Voltage Drop (V)		94.2
Peak Power (kW)		0.198
Average Power (kW)		0.079
Lamination Thickness (mm)	0.5	0.5
Core Length (mm)		250.
Core Width (mm)		486.
Core Height (mm)		486.
Total Length (mm)	390.	337.
Total Width (mm)		486.
Total Height (mm)		486.
Copper Weight (kg)		42.
Steel Weight (kg)		209.
Total Weight (kg)		251.
Cooling	Air	Air

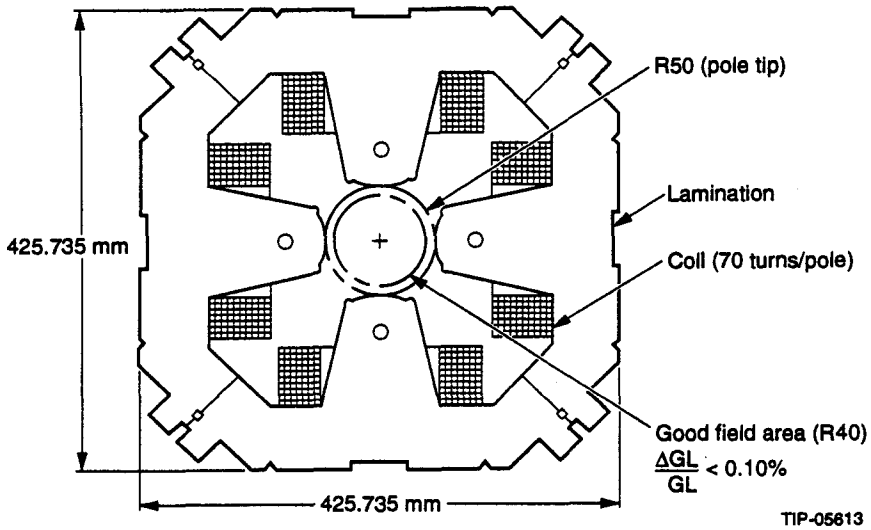

Figure 3.29: Cross section of the LEB high field trim quadrupole.

hydraulic circuits in parallel so that the complete magnet includes a total of eight parallel water circuits.

The magnetic circuit of the LFTQ and skew quadrupoles is essentially the same as the HFTQ except for the lack of water cooling and the number of turns per pole. The LFTQ contains 144 turns per pole. Figures 3.29 and 3.30 present a cross sectional view of the magnets which shows the coils, good field area and the laminations.

The laminations used on the prototypes built at BINP are described in Section 3.1.3 of this chapter. The laminations used on the SSCL-built prototypes have been fabricated with programmable laser cutting tools. These laminations show significant deviations from the specified dimensions in the region of the pole tip as shown in Figure 3.31. It should be noted that the laser cut laminations used on the main quadrupoles have been manufactured by a different vendor than those used for the corrector magnets and have a slightly smaller pole tip radius.

One prototype of each LEB corrector quadrupole has been built at the SSCL. The LFTQ has been measured extensively at both LBL and SSCL The HFTQ has been measured only at SSCL. These initial measurement results have indicated that the field uniformity of both magnet types re-

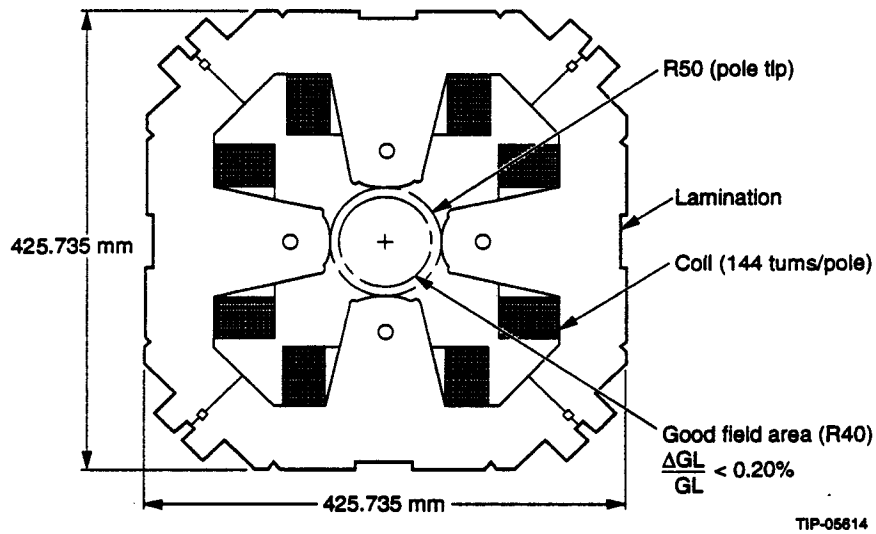

Figure 3.30: Cross section of the LEB low field and skew quadrupole magnet.

quire modifications. The measured field uniformity is typically 0.4 % or worse at a radius of 40 mm. In addition, the LFTQ shows a significant sextupole component. This sextupole component is believed to be introduced by assembly errors in both the quadrants and the magnet assembly. The dimensional conformance and mechanical inspection results for the two SSCL trim quadrupoles are summarized in Table 3.13. These inspections clearly show an asymmetry in the LFTQ prototype that is out of tolerance while the HFTQ is within tolerance. These asymmetries will result is the sextupole field content and other field non-uniformities. The LFTQ prototype has been disassembled and carefully reassembled in an attempt to understand the reason for the asymmetry. At that time, a significant distortion in one of the iron quadrants has been observed.

A single modification has been made to achieve the field uniformity requirements on the basis of detailed analysis of the magnetic field data. Each pole tip is chamfered at an angle of 45° to a depth of 5.0 mm. Subsequent measurements of both the HFTQ and LFTQ prototypes at SSCL show a significant improvement in the field uniformity. Figures 3.33 and 3.34 show the results for the HFTQ before and after chamfering, respectively. The variation in the integrated field gradient, [ΔGL/GL], is plotted for the horizontal, vertical and total field as a function of the transverse axes. As seen

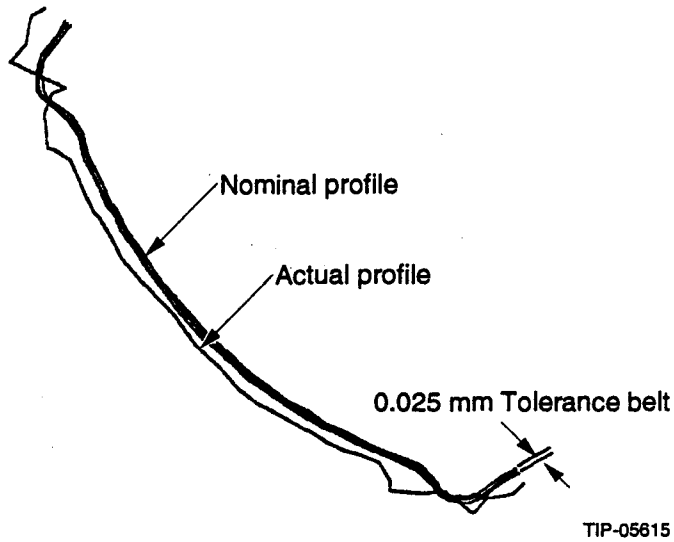

Figure 3.31: Laser cut trim quadrupole lamination pole tip.

in these figures, significant improvement is achieved by this chamfer, such that the magnetic field uniformity is within the specified requirements. Figure 3.35 shows the results after chamfering for the LFTQ. Here the magnet meets the field uniformity requirements even with the sextupole component present. It should be noted that this measurement has been made after careful reassembly, and the dimensional conformance is better than that presented in Table 3.13.

The SSCL measurements have been performed on a bench that has been designed specifically for the LEB quadrupoles.* This system uses a rotating radial measurement coil and is described above. INP has performed measurements of their quadrupole prototypes using a Hall probe array that they developed. The Hall probe array shows results that are similar to the SSCL results although the accuracy and repeatability the data is not as good as that achieved with the rotating coil.

Sextupoles

The requirements for the LEB chromaticity sextupole are presented in Table 3.14 along with the resulting values for the electromechanical and mag-

*Manufactured by Field Effects, Inc.

Table 3.13: Dimensional conformance and mechanical inspection of the SSCL prototype HFTQ and LFTQ.

Quantity (*)	HFTQ		LFTQ	
	Average Value	Tolerance/ Difference	Average Value	Tolerance/ Difference
Diameter				
Nominal	100.00	±0.05	100.00	±0.05
1-3	99.953	−0.021	100.060	0.140
2-4	99.974		99.920	
Pole-to-Pole Separation				
Nominal	37.00	±0.025	37.00	±0.025
1-2	36.754	0.028	36.90	0.290
2-3	36.729		36.66	
3-4	36.755		36.89	
4-1	36.727		36.61	

(*) Please reference Figure 3.32 for the corresponding pole orientation.

netic parameters which have been measured and/or derived. Five prototype sextupole magnets have been fabricated, two at SSCL and three at BINP. The electromechanical parameters for the BINP prototypes are somewhat different because 85 turns per pole with a smaller cross section wire are used on these magnets. The magnetic circuit consists of two symmetric half-cores built from precision punched laminations and held together between two thick end packs and assembled with its electrical winding. The electrical circuit consists of six coils, one coil per pole, connected in series such that adjacent poles have opposite polarity. The coils for the chromaticity sextupoles are fabricated in much the same way as the LEB dipole correctors. A cross sectional view of the magnet showing the laminations, coils and good field area is shown in Figure 3.36.

Figure 3.36 shows the hole pattern in the laminations used to align and assemble the individual lamination packs and the half-cores. The half-cores consist of seven segments with two end packs. The laminations in the end pack are nibbled in order to achieve an approximate Rogowsky pole tip and improve the field uniformity. Each segment is assembled using a tight-fitting tube in each of the three smaller holes in the pole centerline and fuse welding between lamination along the outside of the segment. The tube is also fuse welded to the outside laminations. The larger holes provide alignment on

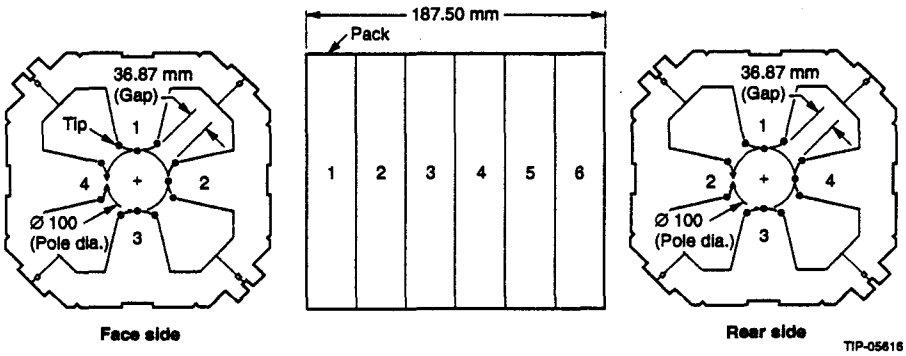

Figure 3.32: Orientation of poles for Table 3.13.

the stacking fixture. A second tube is fitted in these holes for the half core assembly. The tubes are made from undersized stainless steel that is wrapped with impregnated fiberglass tape, cured and precisely ground to the specified diameter. This technique provides a means for fastening the laminations without introducing shorts between the laminations. A similar technique has been used in the other LEB corrector magnets.

One feature of these sextupole magnets is the relatively unique clamping system that has been designed for these magnets and the lack of a key-way in the mating surface between the poles. This system has minor advantages over more conventional clamping systems such as that used in the LEB quadrupoles.

The main disadvantages in practice are:

- the need to precisely maintain tight tolerances on the laminations in the region of the clamp as well as the clamping bars.
- difficulties arising from multiple points of contact for the clamping bar on different surfaces, resulting in asymmetries between the upper and lower half-cores.

These disadvantages as well as the increase in complexity have been the subject of much debate, and in hindsight a more conventional clamping system with a key-way should have been used. The laminations fabricated at BINP include a key-way as a fallback.

The SSCL measurement results for the LEB chromaticity sextupole are shown in Figure 3.37. The magnet as designed meets the specified requirements. The measurements from BINP show significantly worse field unifor-

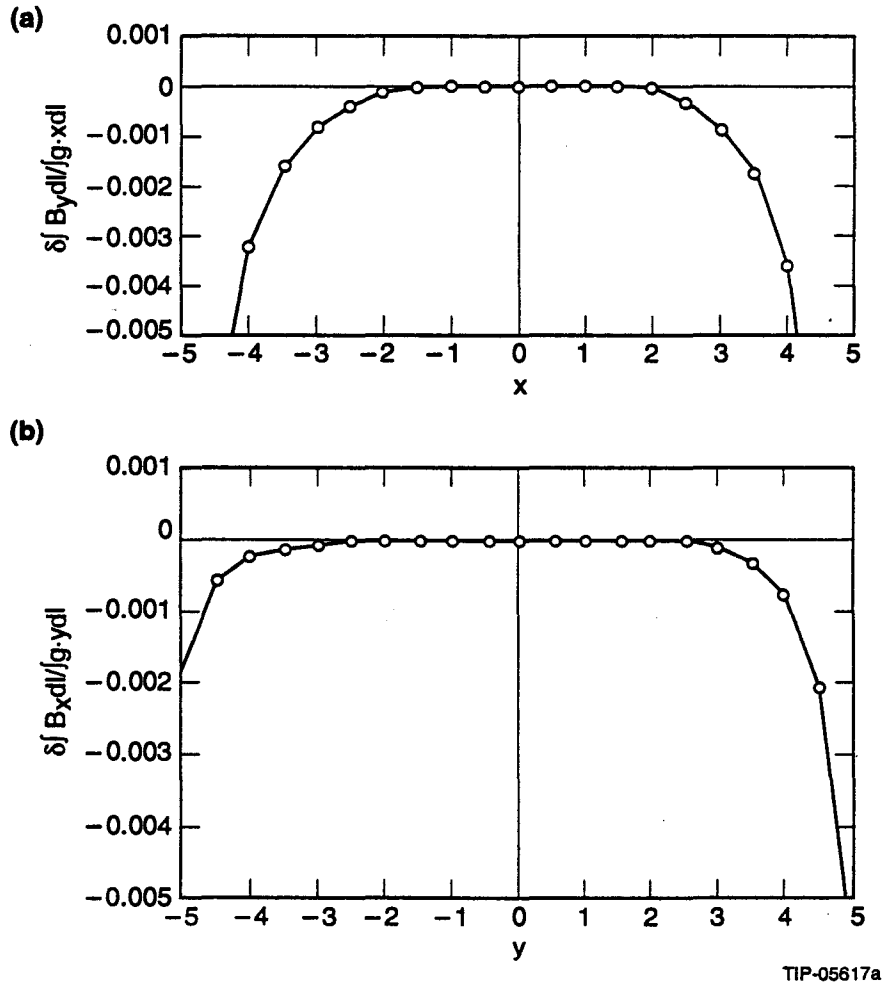

Figure 3.33: HFTQ field uniformity before chamfering.

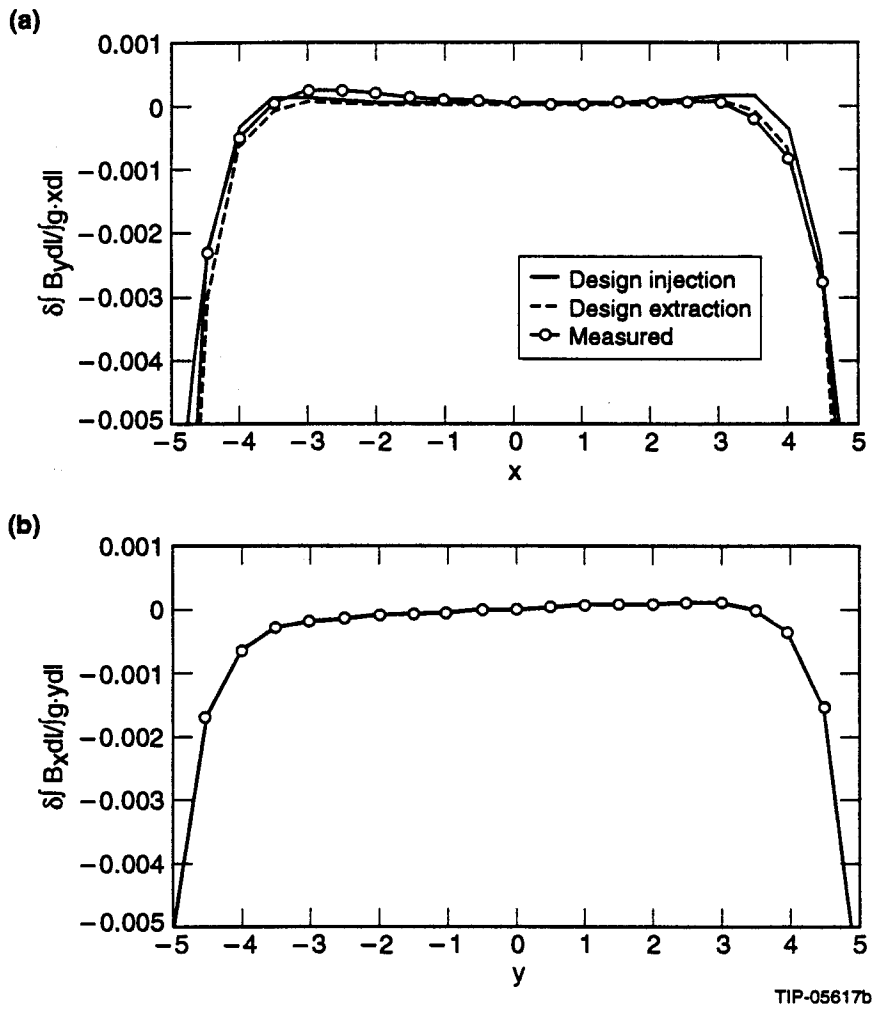

Figure 3.34: HFTQ field uniformity after chamfering.

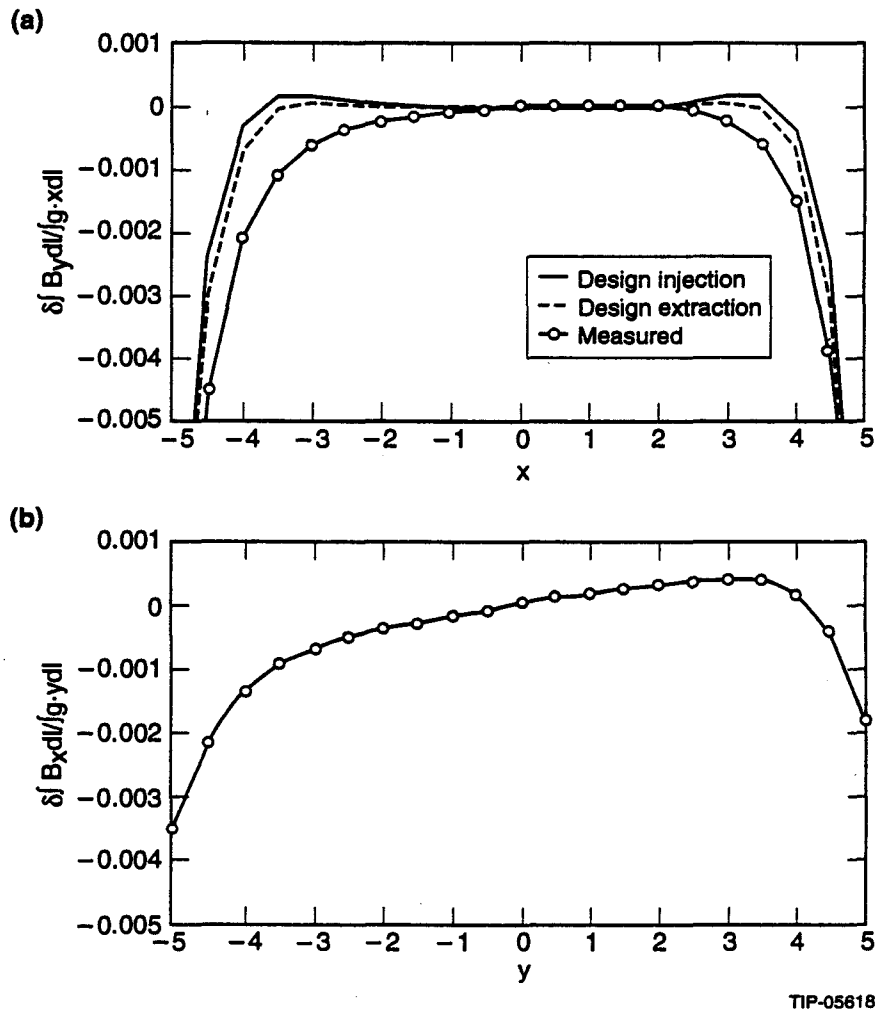

Figure 3.35: LFTQ field uniformity after chamfering.

Table 3.14: LEB chromaticity sextupole magnet parameters.

Magnetic Parameter	Design Requirement	Actual/ Measured
Peak Integrated Gradient (T-m/m^2)	25.8	25.8
Pole Tip Field (T)	0.15	0.15
Sextupole Strength, S [$B = 0.5Sx^2$] (T/m^2)	120.	120.
Good Field Region	40 mm Radius	
Field Quality in Good Field Region ($\delta \int B(x)dl / \int S \cdot x^2\, dl$)	1.0 %	0.70 %
Effective Length (mm)	215.	300.
Radius of Inscribed Circle (mm)	50.	50.
Excitation Frequency (Hz)		10.
Ampere Turns per Pole		2125
Magnetic Efficiency		0.995
Turns per Pole		80
Peak Current (A)	±25.0	±25.
RMS Current (A)		16.
Conductor Size (mm × mm)		6.35 × 2.84
Conductor Cross Section (mm^2)		17.613
Peak Current Density (A/mm^2)		1.42
RMS Current Density (A/mm^2)		0.91
Average Length per Turn (m)		0.74
Inductance (mH)	120.	128.
Resistance (mΩ)	410.	416.
Peak Voltage Drop (V)		96.32
Peak Power (kW)		0.26
Average Power (kW)		0.107
Lamination Thickness (mm)	0.5	0.5
Core Length (mm)		270.
Core Width (mm)		440.
Core Height (mm)		440.
Total Length (mm)	400.	351.
Total Width (mm)		440.
Total Height (mm)		440.
Copper Weight (kg)		55.
Steel Weight (kg)		191.
Total Weight (kg)		246.
Cooling	Air	Air

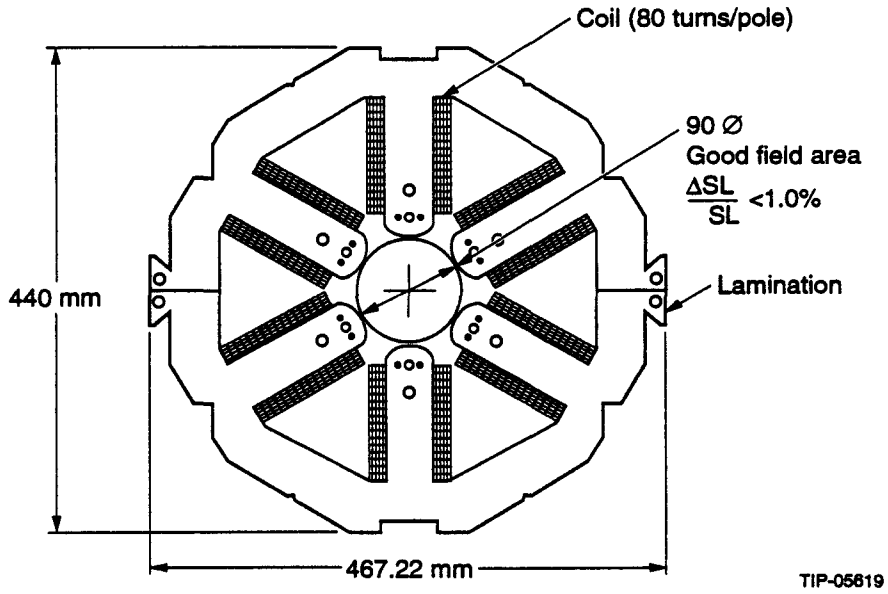

Figure 3.36: Cross section of the chromaticity sextupole magnet.

mity ($\Delta SL/SL > 2.5$ %). The reasons for this discrepancy are not understood and have not been investigated at the time of the SSC termination.

3.1.5 Extraction Kicker Magnet System (J.M. Wilson)

Requirements

The requirements for the Low Energy Booster (LEB) extraction kicker system[59] are summarized in Table 3.15. The 600 G-m field is required to deflect 12 GeV/c LEB beam 1.5 mrad vertically onto the extraction channel. The 80 ns risetime requirement translates into partial deflection of four LEB batches at extraction momentum.[60] The extraction system will be placed in the S2/Extraction Straight (see Figure 2.1, Section 2.1), and the nearest surface building is directly above this straight section of tunnel. An additional ES&H requirement to eliminate flammables in the tunnel forces such selections as halogen-free insulators and cable jackets, and ceramic or potted-epoxy insulation systems instead of simpler oil-insulated systems.

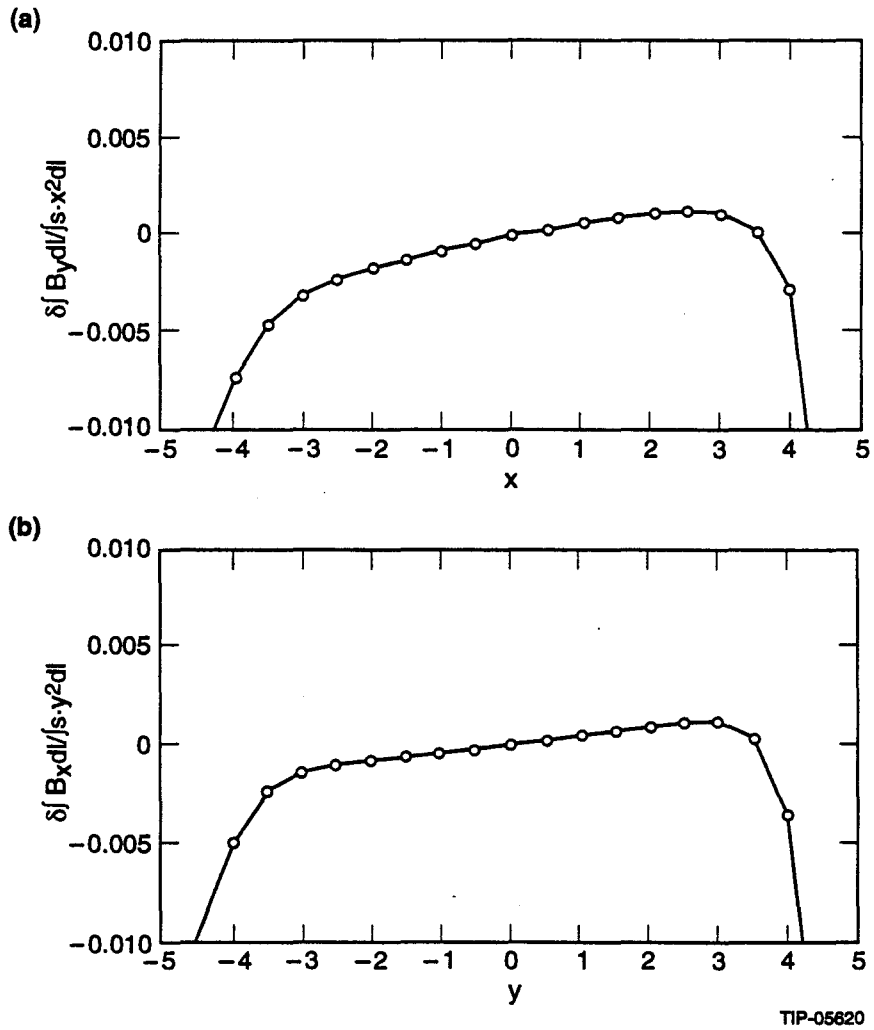

Figure 3.37: Chromaticity sextupole field uniformity.

Table 3.15: LEB extraction kicker system requirements.

Parameters	Value
Total integrated field	600 G-m (vertical deflection)
Available slot length	5.932 m
Field risetime (1–99 %)	80 ns
Field pulsewidth	2.4 μs
Field falltime	n/a
$\Delta B/B$	± 1 %
Repetition rate	10 Hz
Aperture	5×7 cm $(X \times Y)$
Good field region	2×4 cm $(X \times Y)$

System Approach

The available magnetic length within the 6-m slot is expected to be no more than 5 m in the final configuration, after allowances for vacuum flanges, bellows, and interconnections between magnets. This implies a nominal field for the magnets of 120 G, and, assuming a 10 % margin for actual operations, a 132 G design field. Using a minimum gap length of 6 cm (in the event an internal beampipe is inserted between the polefaces), the necessary current through the magnet is 630 A. In order to use standard 50 Ω RG220 coaxial cables as a Pulse Forming Network (PFN) and to use a commercial single-gap thyratron in a matched modulator, a maximum modulator charge voltage of 30–35 kV has been imposed on the design. This leads to a PFN/magnet/load system of 25 ohms, or two RG220 cables in parallel feeding each magnet.

To first order, the minimum risetime for the modulator, assuming no pulse-sharpening, is an L/Z effect, where L is the modulator's thyratron/feedthrough assembly inductance and Z is the PFN impedance. The modulator inductance is approximately equal to the electrical length of the modulator's thyratron housing and feedthroughs (approximately 0.5 m or 2.5 ns of time in oil) times the average thyratron/housing impedance of 40–50 Ω, or 100–125 nH. Assuming a 25 Ω impedance, the 10–90 % risetime is 2.2 L/Z or 10 ns. Using a single 12.5 Ω modulator to drive two magnets in parallel results in an L/Z time of approximately 8–10 ns, and a 10–90 % current risetime of approximately 20 ns.

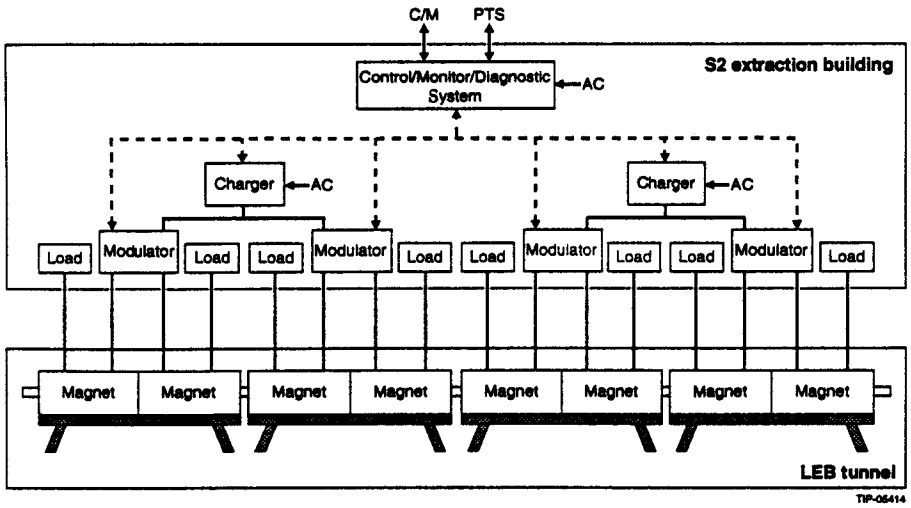

Figure 3.38: LEB extraction kicker system block diagram.

Studies of the CERN PS systems,[61,62] simulations and laboratory experiments[49] indicate that, with an input risetime of 20 ns (10–90 %), the maximum electrical length of the magnet can be no more than 60 ns if an 80 ns (1–99 %) magnetic field risetime is required. The magnet inductance, driven by aperture size, is approximately 1.8–2.2 μh/m; a 25 Ω impedance implies an electrical length (L/Z) of 80 ns per meter of magnet length, and a maximum length per magnet of 0.75 m. The number of magnets required to fill the 5 m of magnetic length is, then, six to eight.

The baseline design, depicted in Figure 3.38, includes eight magnets 0.6–0.65 m in length, driven by four 12.5 Ω modulators. Also included in the system are the charging subsystem, matching load assemblies, and a control/monitor/diagnostic system for interfacing to the accelerator control system.

System Configuration

The eight magnets are packaged in four independently-aligned vacuum vessels; packaging the magnets within four tanks allows a "hot spare" of two prefabricated magnets in an extra vessel ready for installation as a method of reducing downtime. Solid-core magnets require a vacuum vessel approximately 0.35 m in diameter, with an input port for the two RG220 cables per magnet. An air-insulated matched load, mounted to the vacuum vessel at

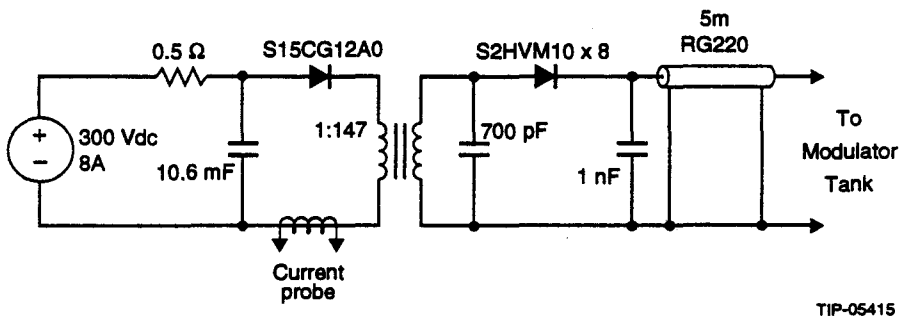

Figure 3.39: LEB extraction kicker charging system schematic.

the output end of the magnet, will also contain the primary current monitor for each of the eight magnets. Details of aligning magnets to the vessel(s), aligning the vessels to the stands, and specific requirements of the vacuum system have not been completed at the time of project cancellation.

RG220 cables, routed in conduits that run from the surface building to the tunnel, must be cut to length and terminated after pulling; special jigs and cable-preparation tools have been designed and prototyped for this task. The PFN cable spools, modulator and charging tanks, low-voltage charging racks, control system racks, and a hot spare for each major subassembly, fit easily within the allotted surface building floorspace.

Prototype Experiments

Many of the proposed kicker system components and subsystems have been successfully prototyped in the laboratory. The charging system, modulator, and two different magnet types were fabricated and tested at full voltage and shown to meet specifications.[49,63] Items not prototyped include the control/monitor/diagnostic system and a precision, oil-filled load that may be necessary in the final system.

A critical part of the kicker system is the cable feedthrough for RG220 cable; commercially available feedthroughs were identified, costed, and quickly eliminated as options due to their cost ($400–1000 per connection). A simple, custom feedthrough has been designed and tested off-site for dc withstand and corona inception voltage; this feedthrough is qualified for LEB system duty and can be fabricated for less than $150 per cable connection.

As shown in Figure 3.39, the prototype charging system consists of a low-voltage (300 V) dc power supply, an electrolytic capacitor bank, an SCR as

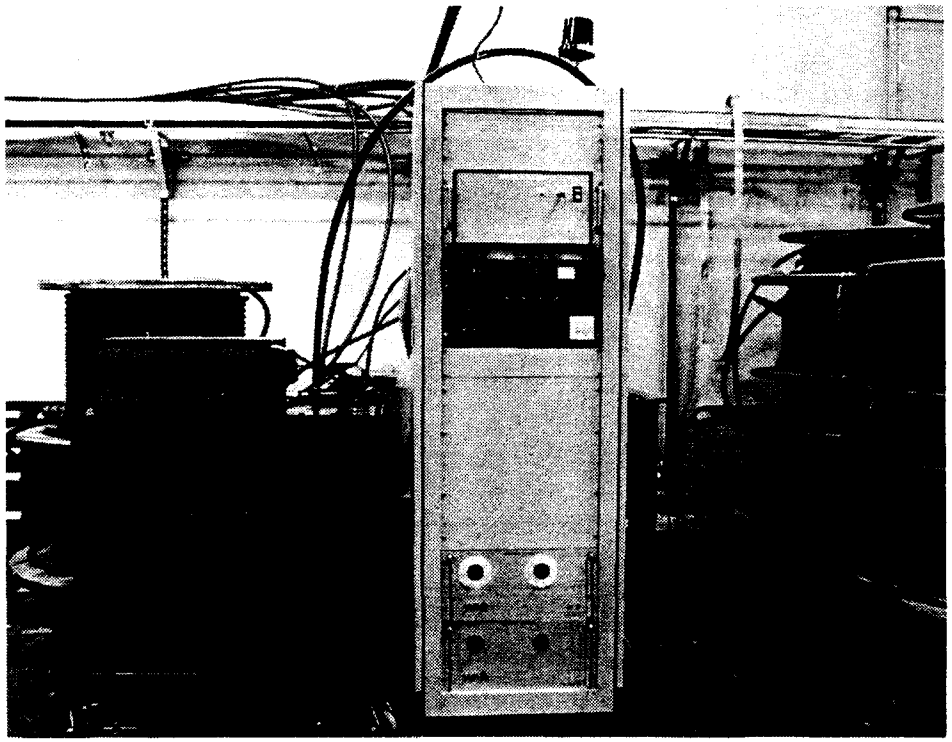

Figure 3.40: Prototype LEB extraction kicker modulator tank and charging system.

the primary switch, a step-up pulse transformer, along with dividers, filters and trigger and SCR-commutation circuitry. This system is rack-mounted with the exception of the step-up transformer, output filter, and HV diagnostics, which are enclosed in an oil-filled tank (see Figure 3.40). The low-voltage power supply, capacitor bank, and charging resistor are sized to allow continuous 10-Hz operation. The capacitor bank and transformer parameters are chosen to charge four 50 Ω PFN cables to 35 kV in approximately 2.0 ms (see Figure 3.41). During initial testing of the charging system, inconsistent turn-off of the primary SCR resulted in the addition of forced-commutation circuitry within the charger. The charger has been successfully operated into both simulated and real PFN loads at nominal 35-kV output for several million shots at a 10-Hz rate, and the design has essentially been qualified as sound. A prototype modulator has been fabricated for testing both LEB extraction and Medium Energy Booster (MEB)

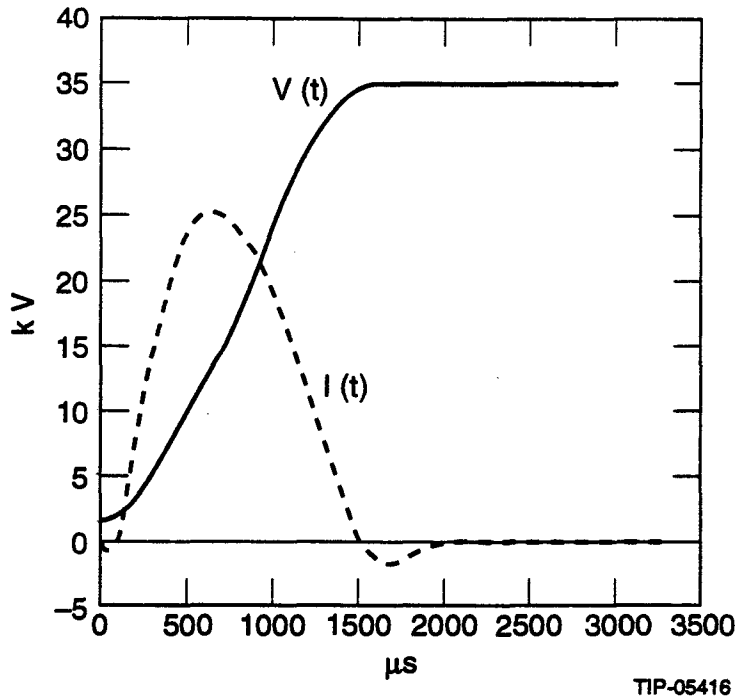

Figure 3.41: LEB extraction kicker charging waveforms. Note: current waveform not to scale.

injection system applications. The oil-filled modulator tank contains two ceramic thyratrons, floating decks for the tubes' support electronics, and the HV triggering and isolation circuits. Custom feedthroughs are used on either end of the tank for connecting the PFN and output RG220 cables. The 254-m long PFN cables are connected between the anodes of the two tubes. Firing the primary tube, which is enclosed within a wrap-around shroud to minimize inductance, delivers a 2.5-μs pulse to the output load (or magnet) through four 50-m lengths of RG220 cable. A 12.5 Ω resistor is connected between ground and the cathode of the second "tail-biter" tube; this tube can be fired to vary the modulator's output pulse width (for conditioning vacuum-insulated magnets and feedthroughs, and demonstration of the required falltime for the MEB injection system), or protect the primary tube in the event of a short-circuit within the system. Test results with CX1573CG

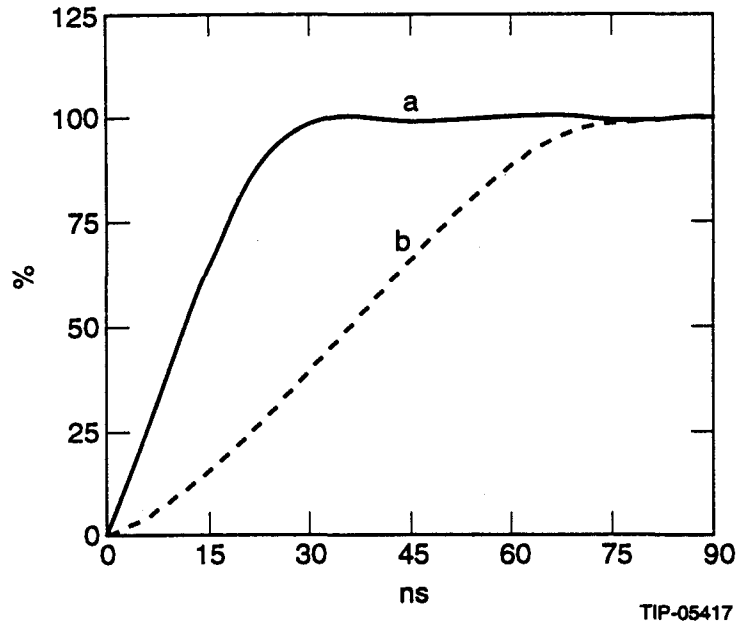

Figure 3.42: Prototype LEB extraction kicker system data: (a) modulator output current, (b) integrated magnetic field.

hollow-anode tubes† indicate shot-to-shot jitter of less than 2 ns (1σ), as well as flat-top ripple, droop, and shot-to-shot repeatability within specifications; testing of other candidate switches has not been completed. The modulator output current risetime, shown in Figure 3.42(a), is sufficiently fast to allow the field within the kicker magnets to reach its peak value within the system specification of 80 ns.

Two candidate kicker magnets have been prototyped and tested in the laboratory. 25 Ω versions of a traveling-wave magnet of the CERN design[61] and a 3-cell "solid-core" magnet similar to those used at DESY[64] and elsewhere, have been designed for the LEB aperture. The prototype traveling-wave magnet, shown in Figure 3.43, consists of 25 ferrite cells of 25.1-mm length. After characterization at low voltage, full voltage operation with the prototype modulator has successfully been demonstrated within a prototype 0.6-m diameter vacuum vessel. Compensation networks, consisting of discrete resistors and/or capacitors, are added at the modulator switch,

†English Electric Valve Co.

at the input and output of the magnet tank, and across the matching load, to optimize the magnetic field risetime. The demonstrated risetime of the integrated B-field, as shown in Figure 3.42(b), is less than the 80-ns requirement. The prototype solid-core magnet, shown in Figure 3.44, has been similarly bench tested, and, with proper selection of the three capacitors between the HV conductor and ground (*i.e.*, 100, 200, and 440 pF capacitors between cells of 180, 160, and 160 mm ferrite length), is shown to produce rise times equal to the traveling-wave prototype of the same length. High voltage testing of this magnet has not been completed at the time of project termination.

Extraction Kicker Power System

The LEB extraction kicker power system, per Figure 3.38, consists of a control/monitor/diagnostic rack, two charging systems, and four modulators. The control/monitor system, besides providing the interface between operators in the main control room and the kicker system, also is specified to make minor shot-to-shot or burst-to-burst timing corrections to keep the overall system within specification.

Due to the success of the prototype charger, only minimal modifications are required to upgrade the design for final installation—splitting the output to charge two modulators, eliminating some of the diagnostics included in the prototype, and respecifying some of the transformer parameters. Similarly, the modulator prototype has successfully demonstrated the validity of the basic circuit and topology. Simplifying the modulator—by removing the tailbiter tube and its support circuitry, eliminating some of the specialty diagnostics of the prototype, and some reconfiguration of the hardware to ease maintenance—are desirable before committing to final design.

Acknowledgements

The contributions of the following are acknowledged: D.E. Anderson, G.C. Pappas, P.R. Dumitriu, L.X. Schneider, and K.R. Rust as principle design engineers and experimenters on the prototype hardware. D.E. Askew, J.J. Jaeger, and C.A. Wilson as technicians responsible for fabrication of the system and assisting in the experiments. L.L. Reginato, D.L. Fiander, and many others for their insights and opinions into the workings of fast kicker systems.

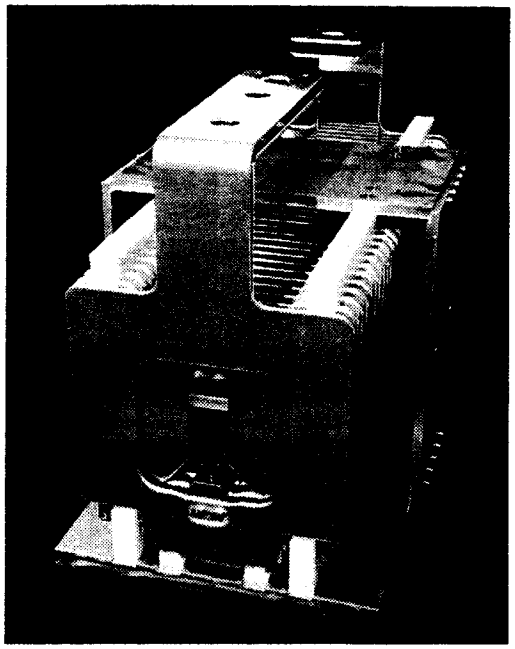

Figure 3.43: Prototype LEB extraction kicker magnet, traveling wave version.

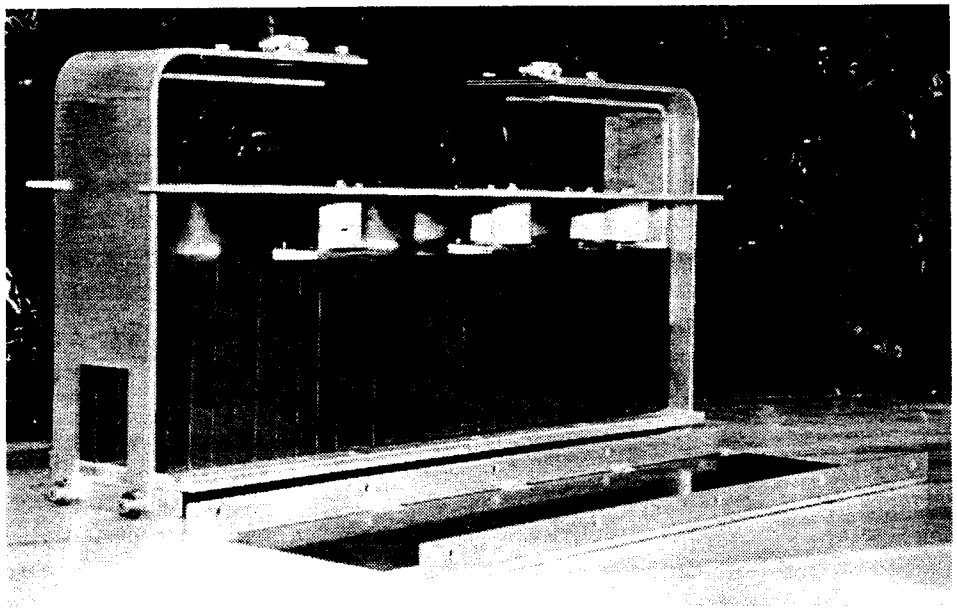

Figure 3.44: Prototype LEB extraction kicker magnet, solid core version.

3.1.6 Magnet Support and Alignment (N. Li)

Magnet support stands

There are 186 magnet support stands (extraction girders not included) in LEB ring with eleven different designs based on the magnet package supported. For each main quadrupole a support girder has been designed supporting the magnet itself plus the associated trim quadrupole and orbit corrector dipole. Supports for the main dipole magnets are simpler, supporting only the magnet itself. All support stands are to be fabricated from steel. The QF2 support, a girder supporting the QF2 main quadrupole and the associated trim quadrupole and orbit corrector dipole, has been prototyped in order to assess its mechanical properties, in particular its resonance spectrum, and to assess the alignment system used.

Mechanical Design For the LEB magnet support stand a six-strut system with spherical-head struts has been adopted, which provides six dimensional adjustability. The advantage of the six-strut system is that alignment is relatively easy to perform and the tolerance requirements are easily met. Then required adjustments for each of the struts to obtain alignment can be computed directly and independently of each other and displayed to the operator. Tests on prototypes have shown this to be a very efficient alignment method.

The girder design is shown in Figure 3.45 using the QF2 girder as an example. The main quadrupole, QF2, is located approximately at the center of the girder, supported by three columns sliding inside their respective posts. Coarse alignment of the magnet relative to the girder is achieved using excentric cams on the columns adjusting their height. These would be spot-welded to the post after alignment. The trim quadrupole is mounted to the girder on two beveled aluminum rails, which in turn are mounted to the girder using a six-strut system to facilitate alignment. The orbit corrector dipole is doweled and bolted to an aluminum plate, which again is mounted on a six-strut system After prealignment of the magnets on the surface, the assembled girder will be mounted in the tunnel where alignment of the assembly will take place using the alignment datum on the main magnet. The vacuum chamber is supported by a post on the orbit corrector dipole side of the main quadrupole. A beam position monitor (BPM) is keyed to

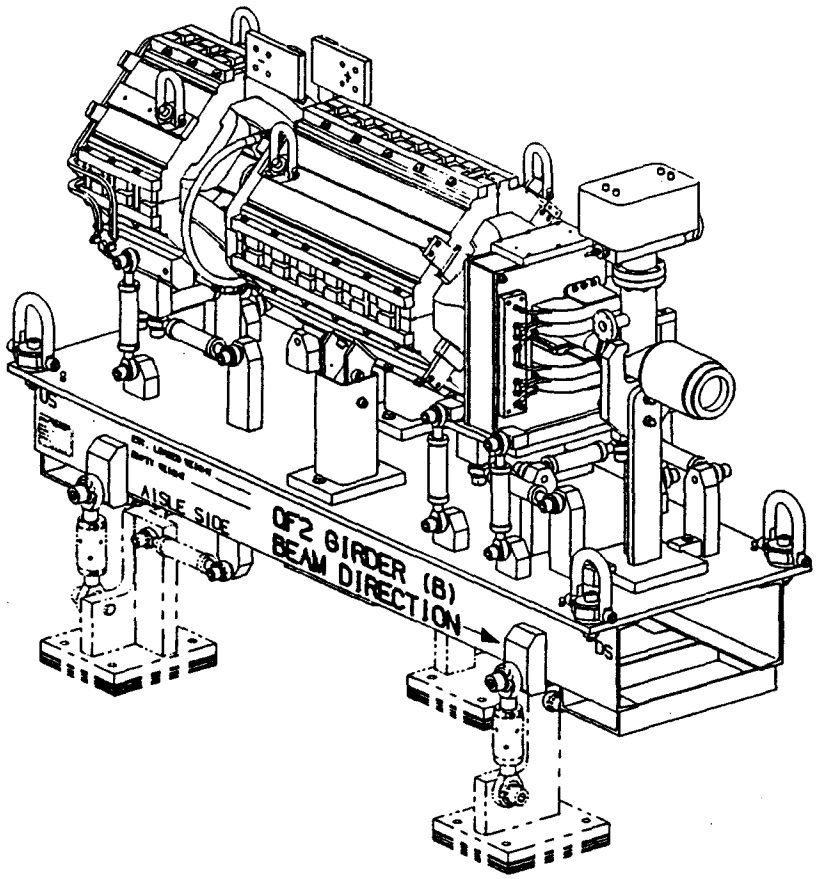

Figure 3.45: Isometric view of the QF2 girder.

the main quadrupole through a G10 collar which has a compression fit with the BPM and a sliding fit with the quadrupole lens aperture.

Prototype The QF2 girder assembly has been fabricated by a local vendor and has been assembled at the SSCL. Tests performed include

- Alignment time: It has been found to take about 10 minutes each to align the trim quadrupole and the trim dipole relative to the main quadrupole.
- Resonant modes: Using a transducer, the girder is excited at varying frequencies. The lowest-frequency modes found are:

- 71.5 Hz in the X direction (transverse horizontal);
- 43.25 Hz in the Y direction (longitudinal); and
- 15.75 Hz in the Z direction (vertical).

It is concluded that the girder structure should not cause amplification of vibration at the LEB cycling frequency of 10 Hz. While the longitudinal mode appears to be close to the cycling frequency, the resonance is actually quite weak and thus not significant.

Following prototype construction—and in light of a re-evaluation of the alignment specifications—the quadrupole girder design has been reviewed, especially with respect to the use of the six-strut alignment system for the corrector magnets. No final conclusion has been reached by the time of project termination, but it appears likely that a somewhat simpler approach—possibly similar to the mounting of the main quadrupole—would have been adopted in order to save hardware costs.

Alignment

Due to the large quantities of components requiring alignment, an efficient, easy to use and precise automated approach has been sought that minimizes set-up time and the number of iterations required. The SSC Machine-Alignment Group has planned to establish a universal alignment system making use of a laser tracker measuring device that tracks the 3D location of a 38.1-mm diameter spherical target. The need for this (comparatively expensive) approach is driven by the requirements of the Collider, however, in this context the advantages of this system make it cost-efficient to use it for all machines including the LEB. The LEB alignment task breaks down into the following five categories:

- Fiducialization;
- Girder pre-alignment;
- Tunnel reference network;
- Component installation and alignment, and
- Beam path smoothing.

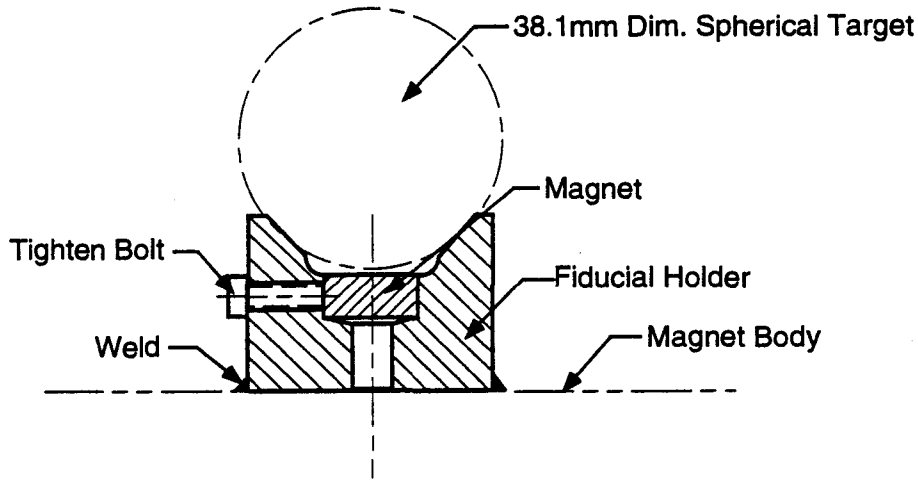

Figure 3.46: Socket for fiducial mark.

Fiducialization For using the laser tracker, a repeatable reference surface needs to exist on each of the LEB components. The surface should be located such as to easily allow resolution of the six degrees of freedom. An economical fiducial fixture with a conical reference surface and a permanent magnet to hold the target for the tracking laser has been designed for this purpose (see Figure 3.46). The fiducial holder will be welded to the magnet body without a tight tolerance. The conical surface ensures very good accuracy and high repeatability of the target position. Four fixtures of this kind are placed on the aisle side of the magnets.

Girder Pre-alignment Girder pre-alignment consists of the following steps:

- Find the magnetic center of the main quadrupole magnet. The measuring coil is fixed on the flange and has a certain fixed position (x, y). As the coil is rotated, the magnet is repositioned until the magnetic center coincides with the flange center, *i.e.* the coil center.

- Transfer the magnetic center to the mechanical dimension, *i.e.* measure the distance between the fiducial target center and the flange center along both transverse directions and record the data in the computer database.

- Position the main quadrupole horizontally on the girder using the three eccentric cams indicated in Figure 3.45.
- Using the fiducial targets placed on the orbit corrector dipole and the trim quadrupole respectively (which are referenced to the mechanical center of these magnets) align both of these to the quadrupole magnet using the six-strut systems.

After prealignment the girder is ready for transfer to the tunnel.

Tunnel Reference Network A precision reference network is required in the tunnel to support installation and alignment of the machine component. This tunnel reference network is a sequential series of monuments whose positional interrelationships are determined in a common coordinate system prior to component installation and alignment. Once in place, the tunnel reference network provides the framework necessary to align and/or accurately define the position of machine components and other supporting hardware that is location dependent. It also supplies the infrastructure required for the FIS (Facility Information System). Establishment of the tunnel reference network can be divided into the following three tasks: densification of surface network, coordinate transfer from the surface to the tunnel level and tunnel reference network survey.

Densification of Surface Network On the terrain of the SSC project, a site-wide primary survey reference frame called the Primary Surface Reference Network (PSRN) will be established for both the horizontal and vertical survey and physically represented by a set of concrete monuments. Densification of the surface network adds secondary monuments at each sight pipe and surveys them with respect to the PSRN. For the LEB, the additional monumentation (*i.e.*, transfer stations) at the service area will take the form of vertical sight pipes strategically located over the tunnel. The densification procedure will be performed prior to the coordinate transfer to the tunnel level. Horizontal and vertical densification require different methodologies.

Horizontal densification utilizes the Global Positioning System (GPS) satellite survey system to assign coordinates to each sight pipe. The basic measurement of GPS is a three-dimensional vector (baseline) between a pair of simultaneously observing satellite receivers. The location of the survey reference on each sight pipe must be chosen to allow an unobstructed true vertical line of sight (along the gravity vector) between the sight pipe reference and the tunnel below. A minimum of five primary monuments (three

with inverted pendula) with strong geometric interrelationships will be utilized in each densification survey. As part of each densification, a deformation analysis using the University of New Brunswick Generalized Approach will be performed to verify that the original datum depicted by the fiducial monuments is stable. The inclusion of five fiducial monuments with strong geometric relationship in each densification insures a rigorous solution to obtain this stability information. In addition, direct measurement of the horizontal displacement of the three fiducial monuments equipped with inverted pendula will facilitate removal of GPS-datum induced effects from actual monument displacements.

Vertical densification will be accomplished using spirit leveling. The measurement obtained from spirit leveling is an accumulated height difference between end points of each leveling line. The vertical reference for the densification needs only to be located within single measurement range of the sight pipe, which for vertical measurements serves the sole purpose of direct vertical access to the tunnel. A minimum of two fiducial benchmarks (BM) at each service area will be utilized in each densification to allow verification of the vertical stability of the vertical fiducial BM.

Coordinate Transfer from the Surface to the Tunnel After the densification surveys have been completed, the resulting coordinates in all three dimensions must be transferred to the tunnel through the sight pipes. These transfers supply the beginning and the end point coordinates that are required to control the tunnel surveys between service areas. The transfer includes both horizontal and vertical coordinates, and they require different methodologies.

Horizontal The horizontal transfer will be performed using both optical and mechanical means as each measurement type is adversely affected by different systematic errors. Consistency of the results of each method will generate a high degree of confidence that the systematic errors in the transfers have been properly modeled.

Figure 3.47a illustrates the concept of the optical transfer of the horizontal position. The transfer will be accomplished using an automatic nadir plummet. It uses a free swinging pendulum to reference the direction of gravity (plumbline). A laser attachment is attached to the optics of the plummet to allow automatic creation of the required downward reference line of sight through the sight pipe from the surface. A photo detector mounted on a

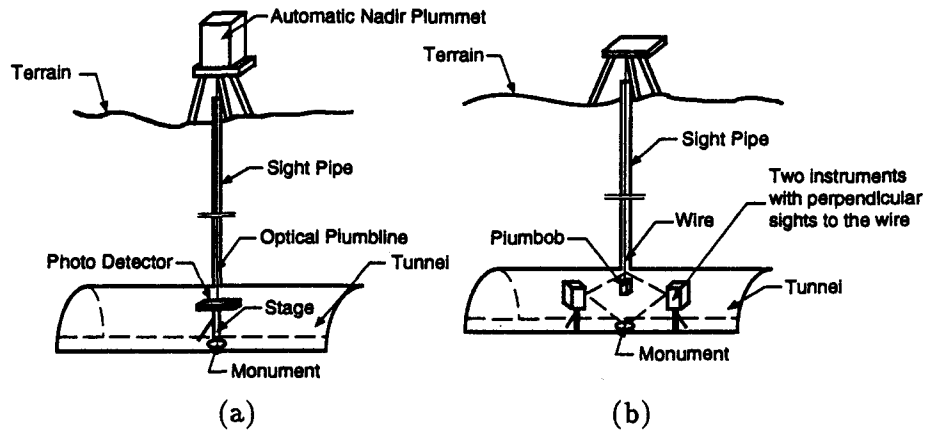

Figure 3.47: Transfer of horizontal position.

two-dimensional translation stage is employed below the sight pipe in the tunnel to register the location of the generated visible plumbline.

Figure 3.47b illustrates the mechanical transfer of the horizontal position. The transfer will make use of the well proven mining practice of suspending a wire plumbline down through the sight pipe. In essence, it is the same as using a traditional survey plumb bob except the wire is much longer and the weight required is much larger. The position of the wire can easily be transferred to a tunnel reference by intersecting perpendicular lines of sight with the wire in the tunnel.

The goal of the above process is to allow the transfer of position from the sight pipe reference to the tunnel with a standard error of ≤ 1 mm.

Vertical Vertical transfer will also be performed using both optical and mechanical means of measurement to obtain two independent, redundant measurements.

For the optical measurement an electro-optical distance meter (EODM) will be used to measure the distance from the tunnel to the top of the sight pipe at the surface. The ME 5000 EODM[‡] chosen uses a laser carrier for the distance measurement. Figure 3.48a illustrates the optical transfer of elevation.

The mechanical transfer method for the vertical coordinate is very similar to that used for horizontal transfer, with a graduated tape replacing the wire. The tape can be suspended down the sight pipe and vertical measurements

[‡]Manufactured by Leica Co., St. Gallen, CH.

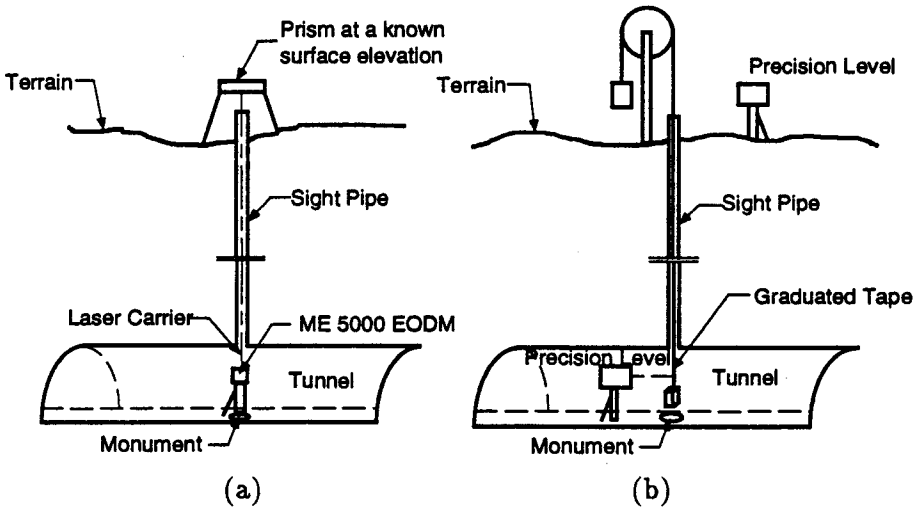

Figure 3.48: Transfer of vertical position.

with a spirit level can be made between the references in the tunnel and on the surface with respect to the suspended tape. Figure 3.48b illustrates the mechanical transfer of elevation.

The coordinate transfer must be performed at two adjacent sight pipes to allow for tunnel survey closure.

Tunnel Reference Network Survey The LEB tunnel reference network has 72 monuments. The reference network survey will be done before installation of accelerator components and requires uninterrupted continuous access to the entire LEB tunnel. The survey procedure is subdivided into the types of observations required: orientation, distance, and height.

Figure 3.49 illustrates the design of a tunnel monument that fulfills the following requirements:

- A distinct and highly repeatable three-dimensional point of reference for survey instrumentation and forced centering of survey targets and reflectors to avoid time consuming manual centering of targets.
- Resistance to corrosion that is expected in a tunnel environment (*i.e.* stainless steel).
- Easy installation in the tunnel.

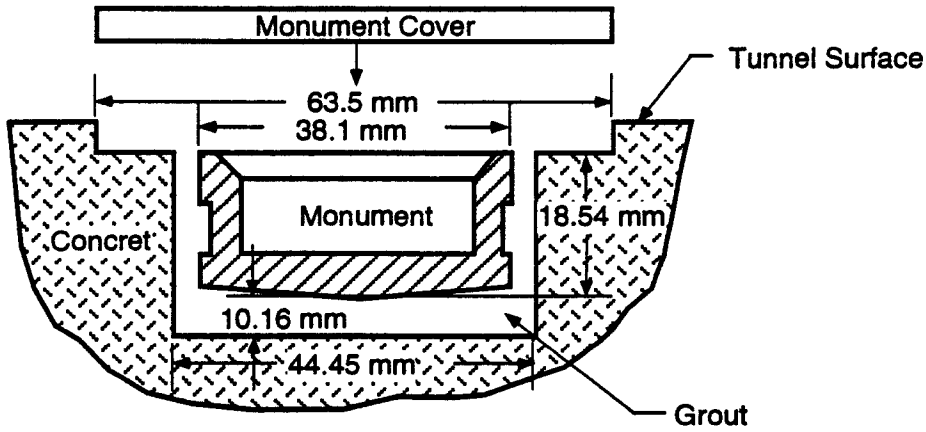

Figure 3.49: Socket for tunnel monument.

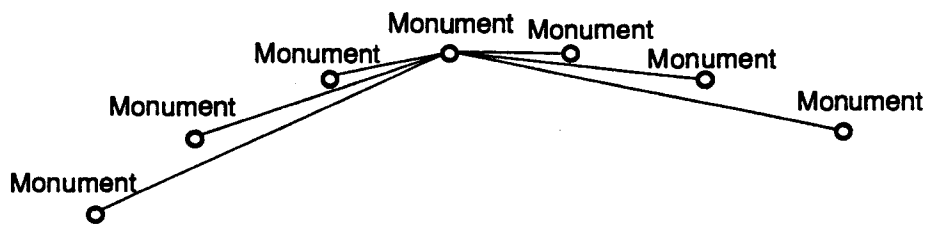

Figure 3.50: Orientation survey.

The tunnel location of a monument will be nominally coincident with the center of a main quadrupole (the girder alignment datum) with 0.9 m offset into the aisle. The monument stationing begins at the LEB injection point and increases in the beam direction with a spacing between 6.52 m to 12.47 m, preserving the line of sight between monuments and accessibility throughout the life of the project. The monuments will be set below the tunnel floor surface so they can be covered and protected from any other tunnel activities.

The primary orientation survey which determines the transverse coordinate of the monument is a set of measurements of small angles, shown in Figure 3.50, with the majority of the redundancy created by overlapping angles in both directions. Each monument will be measured against the next two monuments on either side, for 4 angles, and this pattern will be repeated through the entire network with each monument in turn providing the start-

ing position. The LEB tunnel reference network will require measurement of 288 small angles.

The primary distance survey which determines the horizontal longitudinal coordinate of the monument will be performed using the ME 5000, and again redundancy will be created by measuring overlapping distances. The procedure to be used for the distance measurement is similar to the one described above, but only one direction, *i.e.* three distances, will be surveyed on each monument toward the adjacent monuments. The LEB tunnel reference network, therefore, consists of 216 distance measurements.

A monopod system has been designed to allow for quick and very precise forced centering of the orientation and distance measuring instruments above the monument. As shown in Figure 3.51, the length of 2 perpendicular struts is adjusted until the Kern base adapter is horizontal, the center line of the monopod and hence the instrument will then be vertical above the monument reference point.

The height difference between monuments will be measured using geodetic leveling. The required redundancy will be created by overlapping height differences. The measurement procedure is the same as for the distance survey. There are 216 height measurements necessary for the LEB tunnel reference network.

Component Installation and Alignment Installation of the LEB magnets involves bolting the support to the tunnel floor such that the component is installed in its designated location. The bolt holes, support base, *etc.* that are required for installation will be marked on the tunnel floor using a footprint template. Since each magnet family will have a different footprint, it will require its own template. The template is equipped with two fiducials, one at either end, that have predetermined relationships to the support footprint; therefore, the positioning coordinates of the components supported by the stand can be computed. The survey for positioning the templates will be performed using the tunnel reference network with the laser tracker pointing to the fiducial targets on the template.

The alignment concept developed for the components employs a minimum of one laser tracker, two in the case of the quadrupole girders. The trackers are interfaced, possibly with electronic tiltmeters, to a control computer that guides the entire process. The location of the trackers can be determined in three dimensions by resection from the tunnel reference network. Once positioned in the system, measurements can be made quickly

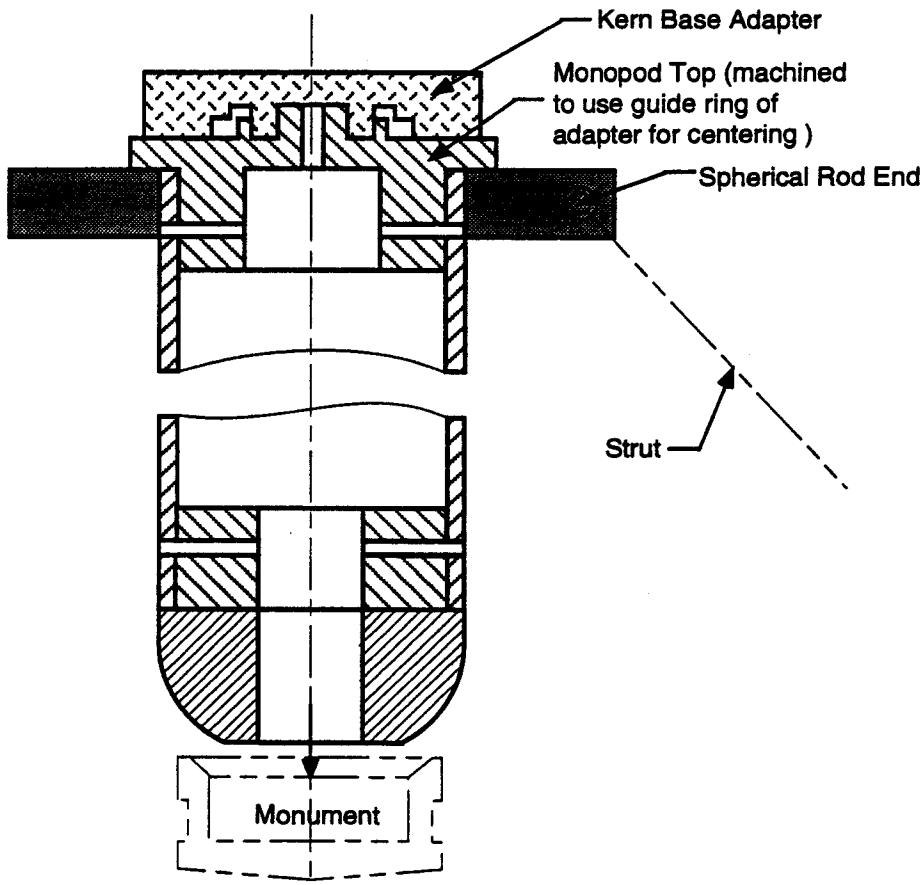

Figure 3.51: Monopod.

to the fiducials on the components to determine the amount of adjustment required to bring the component into position. The adjustment will be easily performed by using the six strut system. Since the magnets on each girder are prealigned, no realignment of these is expected. Spot checks will be made to ensure alignment of the components on a girder relative to each other is maintained throughout the installation process.

To evaluate capabilities and robustness of the laser tracker in daily operation the SSCL tested two trackers from different manufacturers. Preliminary results of the evaluation indicated that only one of the trackers[§] is *a priori* suitable for the SSC alignment task.

Beam Path Smoothing As outlined above, the survey for locating all LEB components will be performed using the tunnel reference network. An important consideration is that, when making successive surveys of long and flexible figures, absolute comparisons would be a nonsense. In fact, magnets are positioned around an unknown mean trend curve (one among an infinity) contained within the envelope of errors. Before commissioning, a last activity called as the final beam path "smoothing," which makes directly survey from component to component, will bring the trend curve into the envelope of specified errors.

The components elected for beam path "smoothing" survey will be equipped with an "active (or called secondary) fiducial" (a fiducial that allows the precision mounting of an instrument) to undertake the direct measurement. A network with a reasonable amount of redundancy will be used for the measurement to determine relative locations between components to each other. The relative alignments computed from these measurements will be analyzed to determine which components require adjustment in the radial direction to achieve the local component to component smoothness requirements, *i.e.*, ensure the trend curves contained within the envelope of specified errors. The principle behind the network measurements is that systematic errors still bias the measurements, but as long as the systematic effects are reasonably consistent then they can be removed from the final computation results. This is accomplished by fitting smooth curves to the measured component locations and analyzing the discrepancies between the curve and the computed position to determine the amount of misalignment. The analysis and designs of how the network will be measured and the type of curve fitting was not addressed before SSC shutdown.

[§]Manufactured by CHESAPEAKE, Kenneth Square, PE.

Alignment Error Sources Four error sources contribute to the total uncertainty of the alignment. Therefore, the budget of 0.4 mm *rms* alignment uncertainty for the LEB is distributed in the following way:

- Fiducialization uncertainty **0.2 mm**. This reflects the accuracy by which the relationship between fiducials and the true center of a component is know.
- Uncertainty because reference is adjacent component center line **0.2 mm**.
- Component alignment uncertainty **0.10 mm** This is the accuracy of transferring position from tunnel network to components fiducials.
- Network uncertainty **0.25 mm** This is the uncertainty arising from the surveying accuracy of the local monument relative to adjacent monuments.

The total uncertainty is obtained by adding these contributions in quadrature:

$$\sqrt{0.2^2 + 0.2^2 + 0.10^2 + 0.25^2} = 0.39[\text{mm}]. \tag{3.2}$$

Acknowledgements

Besides the rf system the magnets are the most important hardware elements in any circular accelerator, consequently, a large number of individuals has contributed to the LEB magnets.

The magnetic design of the main magnets has been done by V. Thiagarajan in collaboration with X. Wu, R. York, W. Heilbrunn and F. Knox-Seith. The advise and collaboration of K. Halbach and R. Schlueter from LBL greatly contributed to the design effort. R. Bell and the late G. Fisher of SLAC assisted in determination of the lamination materials and sizing. The collaboration with members of BINP, in particular E. Trachtenberg and G. Tumaikin, has led to further refinement and improvement of the design. Responsible for the mechanical design has been W. Heilbrunn; he has been capably assisted by R. Stegman and G. Li. Corrector magnets have been the responsibility of J. Skaritka.

At different times, R. Clerihew, W. Heilbrunn, T. Hunter, F. Knox-Seith, M. Schulze and J. Skaritka all have contributed to the magnet measurements at SSCL. In this context the advise and help of M. Green of LBL is also acknowledged.

The magnet support structures have been designed by J. Slessor and J. Huang. The alignment system is the result of the work done by P. Smith, J. Wilkinson and D. Veal; the latter has also been of great help in writing this particular section of this work.

The LEB magnet program has drawn heavily on other laboratories for fabrication of the magnets. LBL has built and measured a prototype quadrupole; at SLAC a dipole has been manufactured and BINP has built several prototypes of each magnet in anticipation of the mass production of the LEB magnets.

3.2 Power Systems

(W. Merz, J.A. Reimund, E. Tacconi, T. Treasure)

3.2.1 Ring Magnet Power Supply

(J.A. Reimund, E. Tacconi, T. Treasure)

General Requirements

The LEB can operate in two distinct cycling modes, fast and slow. Fast cycling operation uses a biased sine wave magnet current at 10-Hz frequency. Slow cycling is a linear ramp and hold mode, and is used for test purposes and implemented as a resonant system. Figure 3.53 shows the current waveforms for both operating modes.

The Ring Magnet Power System provides current and driving voltage to the LEB main dipole and quadrupole magnets. An overview of the ring magnet power system is shown in Figure 3.52. The dipoles and quadrupoles are connected in series to a common bus to ensure current tracking. Three power supplies spaced equally around the ring provide the current drive requirements. These power supplies are fed from a three-phase 4.7-kV bus which has a harmonic/power factor correction filter shunt connected to ground. The dc output from the power supply is filtered for differential and common mode ripple arising from the power supply. Twelve LC resonant circuits are spaced around the ring and are switched into a series configuration with the magnet ring for 10-Hz operation.

Slow-Cycling Operation In this mode the injection-level current starts at about 10 % of flat top current (375 A) and goes through a 50 ms parabolic transition region before the ramp starts. The current then ramps at a rate of up to 5600 A/s until it reaches the parabola region prior to reaching the flat top which corresponds to the MEB injection level beam energy. The current remains in this flat top region for about 100 ms and then ramps down in the same manner. This whole cycle is repetitive and has a cycle time of 1.6 s or larger.

Fast-Cycling Operation A resonant system has been chosen primarily to reduce the size and cost of the power supplies required to meet the 10-Hz cycling requirement. If a non-resonant system had been chosen for the 10-Hz cycling, the power supply would have to provide 480 MVA of peak power *vs.* the 8-MVA peak power required by the resonant system. The ad-

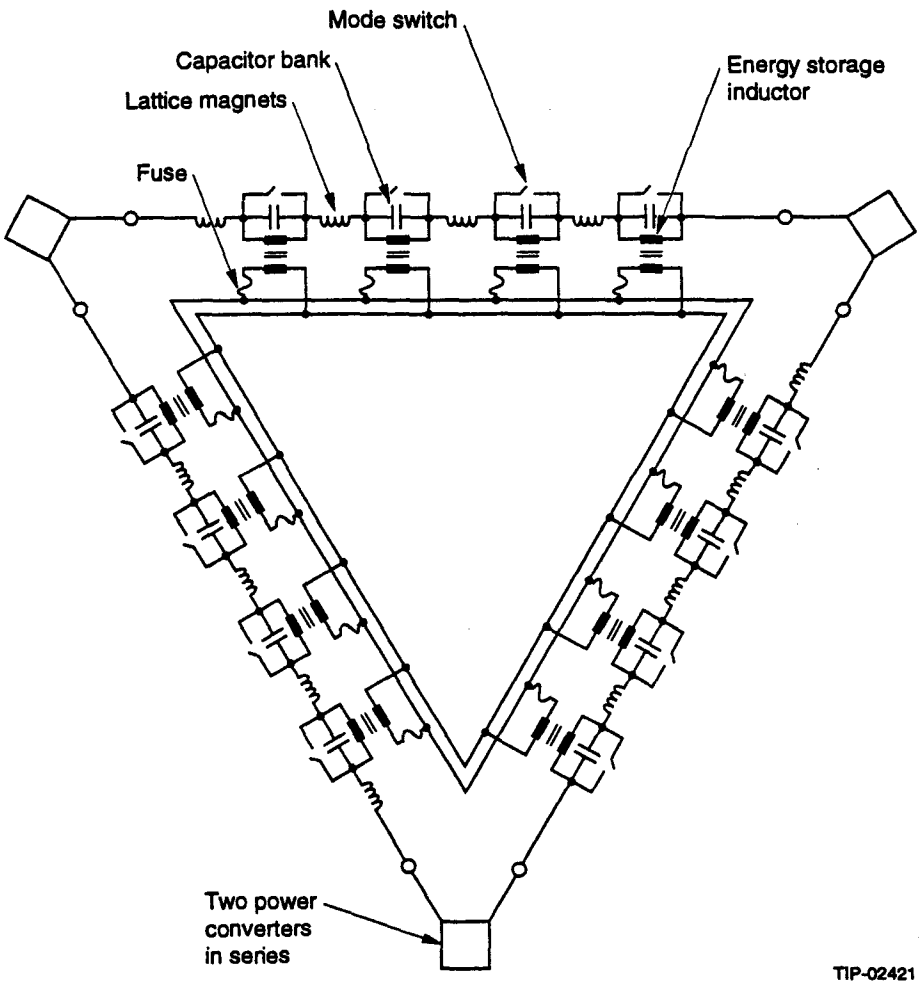

Figure 3.52: General arrangement of ring magnet power system.

ditional cost of the 12 resonant circuits is significantly less than the cost of a 480-MVA power supply system.

In this mode of magnet excitation, a current sine wave is biased at 2000 amps. The peak current is 3750 amps and the minimum current is 375 amps. The current waveforms are shown in Figure 3.53.

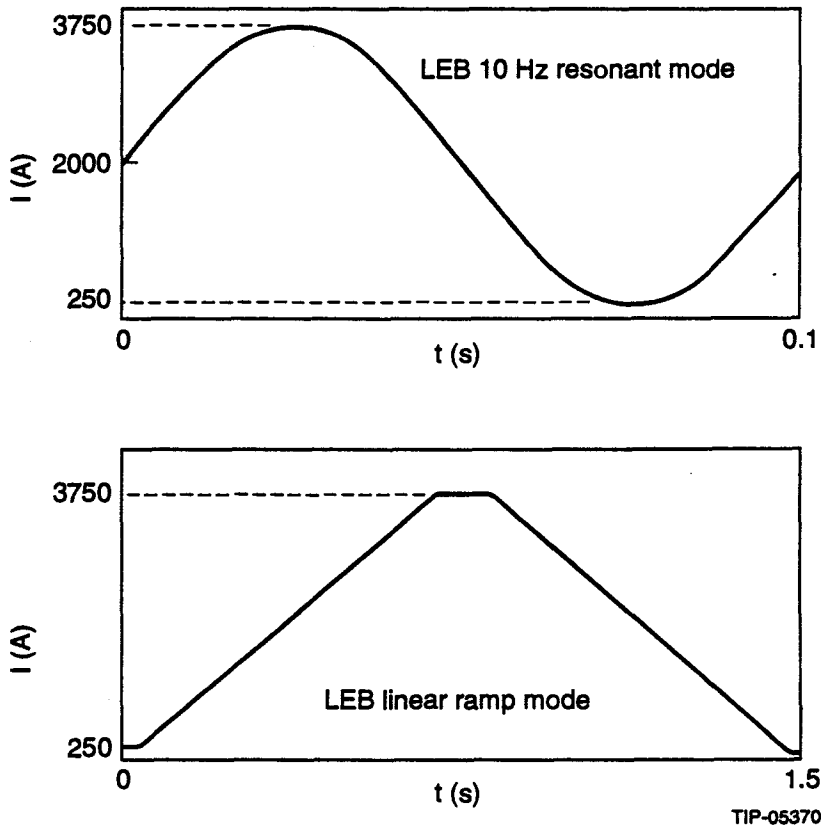

Figure 3.53: LEB current operation modes.

Resonant System Twelve inductors (Energy Storage Inductors, ESI) of 40 mH each are connected in parallel with 16.5-mF capacitor banks. This parallel L/C circuit combined with the LEB magnet inductance produces a 10-Hz resonance condition.

The inductors have a low current secondary winding which is connected in parallel with all the other inductor windings to enhance frequency stability in the steady state resonance condition. The capacitor banks are manually adjustable over a few percent range in order to account for seasonal temperature changes.

The photograph in Figure 3.54 shows one of the inductors in a test bay at the factory, Uralelektrotazmashash (UETM) in Ekterinburg, Russia.

The energy storage inductor is a 40-mH steel-cored inductor designed to carry currents between 1700 and 3400 A with less than 1 % change of inductance. The high linearity of inductance is achieved by providing air gaps in the core and limiting the magnetic flux in the core to 1.6 T. The electrical diagram is shown in Figure 3.55.

The inductor is oil cooled with passive oil circulation in radiators attached to the containment tank. The passive cooling design has been selected over a lower cost active cooling design because reliability is a prime concern. The core configuration shown in Figure 3.56 is known as a two-legged picture frame with two coil sets connected in parallel. This design has been selected for its low construction costs and low energy losses. The core is made from Type 3408 anisotropic silicon transformer steel with 0.3-mm thick laminations. The "air gap" consists of a stack of non-magnetic material gaps in the core which add up to the equivalent of 475 mm of air gap. The two main coils have copper windings of 140 turns each.

Internal shock absorbers are provided between core and containment tank to control vibrations and prevent fatigue stress to radiators and other items mounted on the containment tank. The ESI weighs 55 000 kg when fully assembled.

LEB Ring Current Ripple Requirements The ripple current requirement for the LEB ring magnet system is specified to be no greater than 100 ppm. For design purposes, this figure is divided in half with 50 ppm allotted to current regulation variance and 50 ppm allotted to harmonic ripple associated with the power supplies. To achieve 50 ppm or less harmonic current ripple, a Praeg filter is used to attenuate both differential and common mode ripple. This filter has been designed to have a differential low pass frequency roll off of 40 dB per decade starting at 120 Hz, and a 20 dB per decade roll off at about 4 kHz. The filter attenuation combined with the natural low pass characteristics of the LEB main magnets provide an acceptable current ripple as observed in the simulations.[65] Simulated LEB

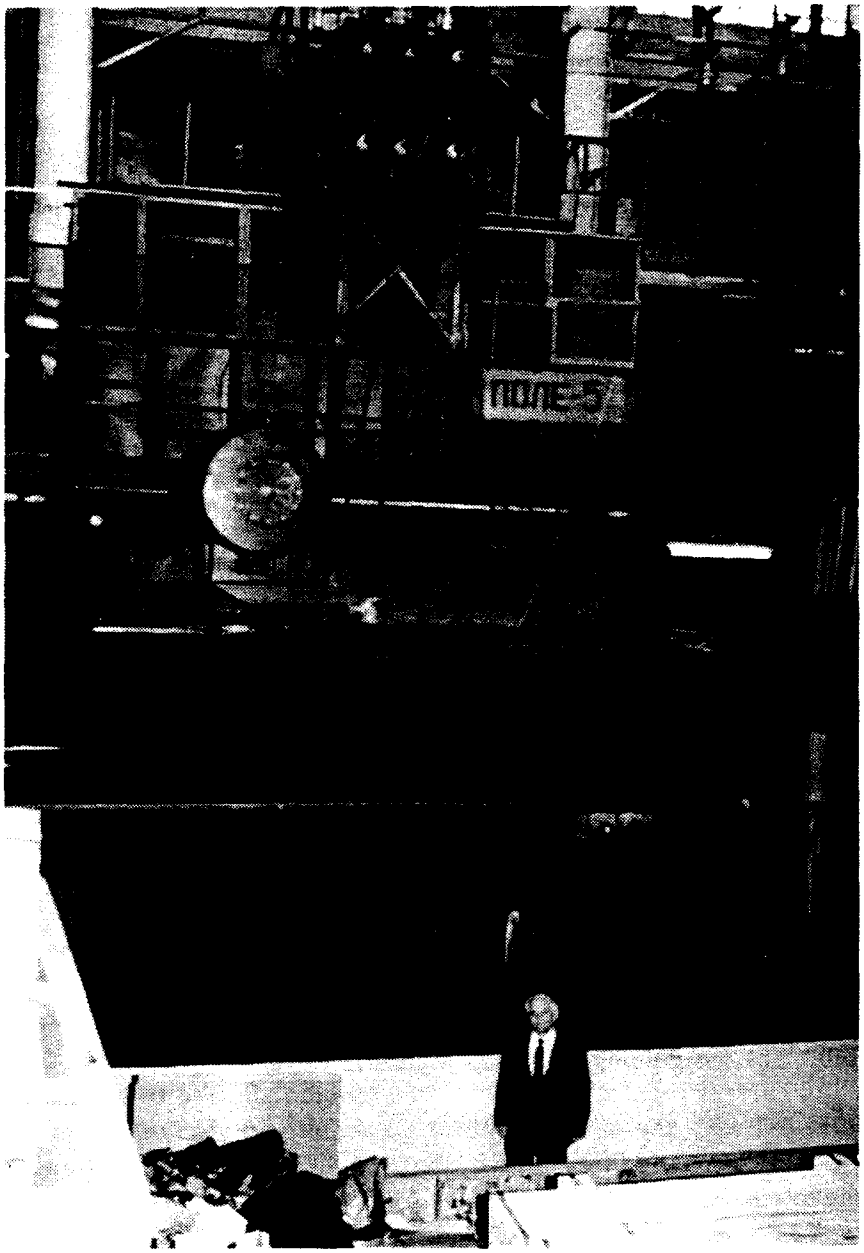

Figure 3.54: ESI in a test stand at UETM.

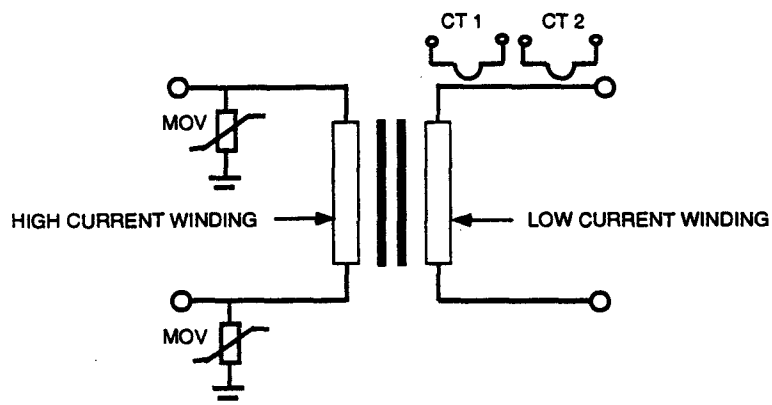

Figure 3.55: Electrical diagram of the ESI.

main magnet current ripple can be seen in Figure 3.57. This ripple amounts to about 20 ppm at 375 amps (injection).

Since LEB magnets have not been available in time for testing, modeling parameters could not be derived from measurements. The information used to make the simulation models is based on the magnet design parameters for both the dipole and quadrupole magnets. The model used for the simulation is shown in Figure 3.58, and the data used for the simulation is summarized in Table 3.16.

Current Regulation

A digital implementation of the current control system has been chosen over analog implementation because of the case of interfacing to the global control system, the digital firing circuits for the power converters, and the digital DCCT. The digital approach also allows easy implementation of remote control of system parameter adjustments during on-line machine tuning.

Voltage and Current Control Strategy The current regulation strategy has been published in the literature.[66–68] The regulation system consists of two major loops; an internal loop controlling the output voltage of each power supply and an external loop controlling the current in the magnets. The voltage control loop is designed to have fast response to regulate the voltage applied to the magnets. It must follow a predetermined voltage reference related to the current reference, reject line voltage changes, and correct

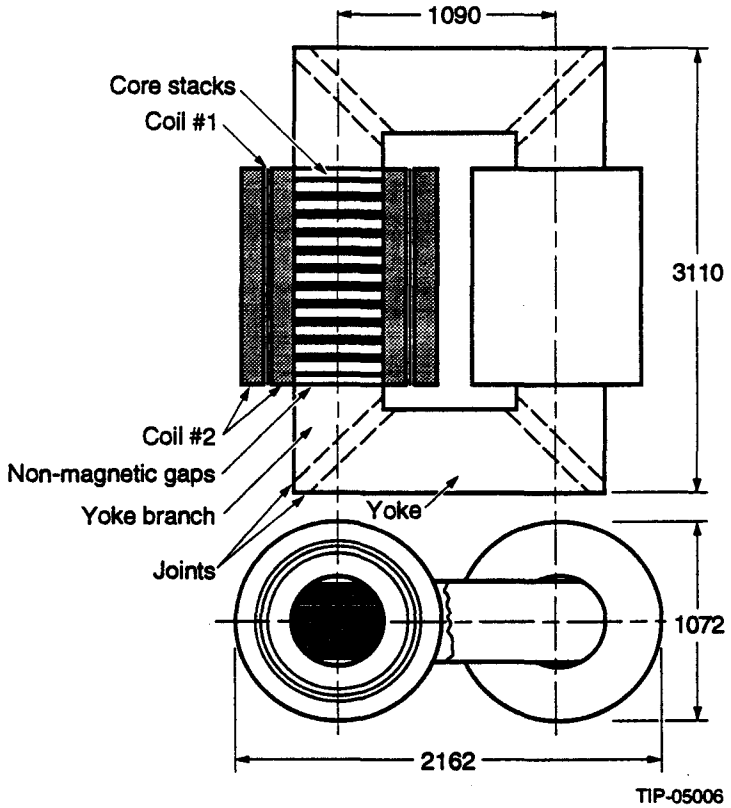

Figure 3.56: Simplified mechanical design of the ESI.

offset errors and other voltage perturbations. Each power supply has its own voltage loop and output filter. The external current regulator loop has a slow response and very high gain to meet the dc accuracy requirements. A block diagram of the regulation system is shown in Figure 3.59.

The same voltage loop is used for both ramp and resonant modes of operation, but different current regulation designs are required for each operating mode.

Voltage Regulation Control Loop Design The voltage loop is designed to have a fast response and its main function is to regulate the voltage applied to the magnets. It must follow a predetermined voltage reference related to the current reference, rejecting line voltage changes, offset errors and other voltage perturbations. Due to bandwidth limitations, the voltage loop only

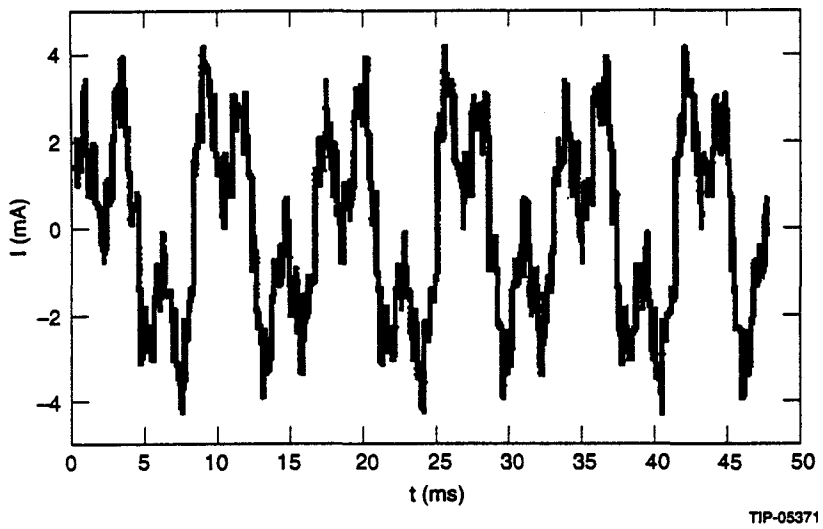

Figure 3.57: Simulated magnet ripple current at injection.

rejects voltage perturbations up to 120 Hz while the output filter rejects the ripple at 360 Hz and other higher frequency perturbations. The block diagram of the digital voltage loop is shown in Figure 3.60.

The voltage sensing is composed of a transmitter unit located in the passive output filter and a receiver unit located in the regulation rack. The transmitter unit has a 12 and a 16 bit analog to digital converter operating at a sampling rate of $f_s \geq 40$ kHz. A serial digital voltage signal is transmitted via a fiber optic link to the receiver unit. The receiver unit has a serial to

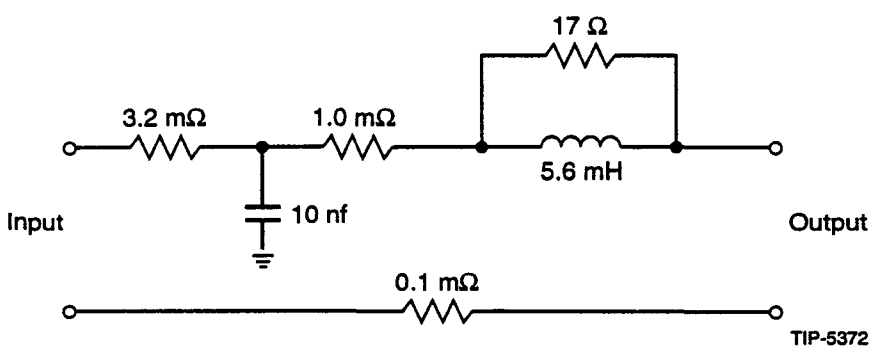

Figure 3.58: LEB magnet simulation model.

Table 3.16: Magnet design parameters.

	Dipole	Quadrupole	ESI	Capacitor bank	Dc bus
Peak Current	3750 A	3750 A	3750 A		4000 A
Average Current			2000 A		2600 A
Shrt Ckt. Current					75 kA/167 ms
Inductance	5.6 mH	0.3 mH	40 mH		
Dc Resistance	4.1 mΩ	1.3 mΩ			
Ac Resistance	7.0 mΩ	0.5 mΩ			
Capacitance				16.5 mF	

16 bit parallel converter and a 12 bit D/A converter for monitoring purposes. The voltage compensator operates at a frequency rate $f_o = 1440$ Hz while the sampling frequency of the voltage sensing is $f_s \geq 40$ kHz. Both frequencies are synchronized with $N = f_o/f_s$. The digital filter provides the mean value of the power supply output voltage to complete the feedback loop.

The voltage compensator is made up of three blocks connected in parallel. These blocks have Z transforms C_i, C_{60} and, C_{120} which provide the integral action and the additional gain at 60 Hz and 120 Hz respectively. The summed output of these three blocks drives the digital linearizer. The voltage compensator has been designed in the Z domain with a one-step prediction providing minimum phase frequency rotation. The voltage compensator transfer functions are given by:

$$C_i = \frac{0.4375 \cdot Z}{Z - 1} \tag{3.3}$$

$$C_{60} = \frac{0.0292 \cdot Z \cdot [Z - 0.7674]}{Z^2 - 1.9277 \cdot Z + 0.9956} \tag{3.4}$$

$$C_{120} = \frac{0.06314 \cdot Z \cdot [Z - 0.5775]}{Z^2 - 1.7245 \cdot Z + 0.9913}. \tag{3.5}$$

The integral action C_i is dominant at low and high frequencies. The bandpass amplifiers at 60 and 120 Hz, presenting an equivalent Q of 60, and only modify the frequency response at these particular frequencies. This

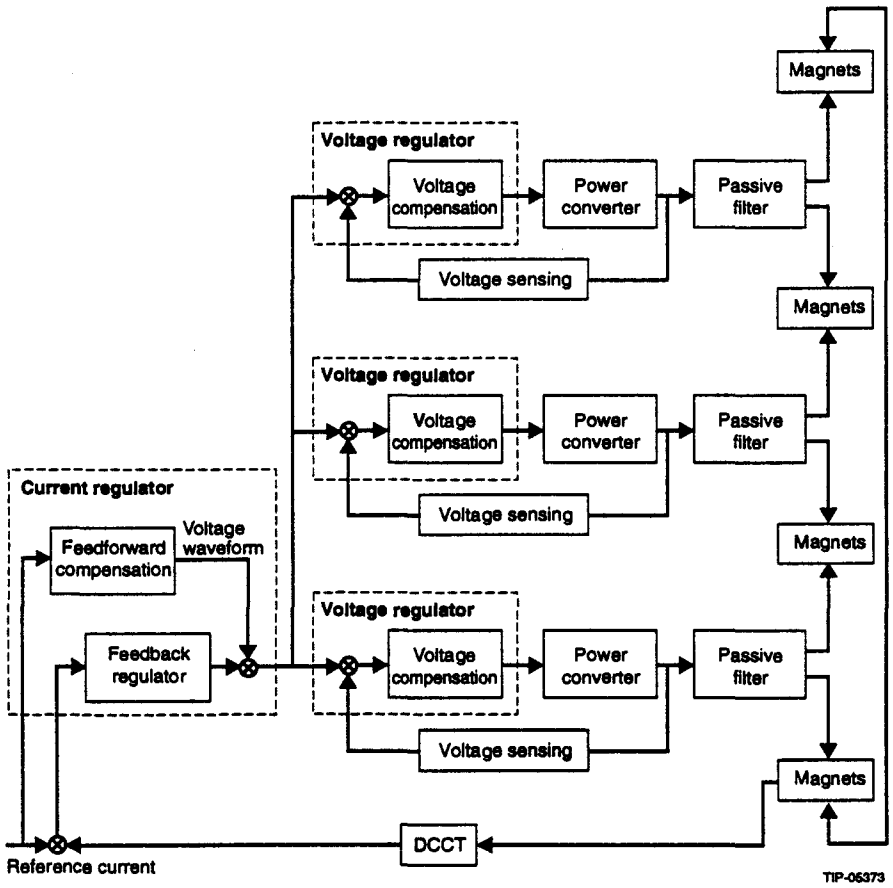

Figure 3.59: Block diagram of LEB power supply regulation loops.

means that they can be inserted or removed at any time without affecting the system stability.

In Figures 3.61, 3.62, and 3.63, the firing circuits and power converters are modeled with a constant gain without phase delay. The open loop gain and phase frequency response of the digital voltage loop with and without the bandpass filters are shown in Figures 3.61 to 3.62. The closed loop gain and frequency response of the digital voltage loop with, and without the bandpass filters are shown in Figure 3.63.

The rejection characteristics versus frequency of the digital voltage loop are plotted in Figure 3.64.

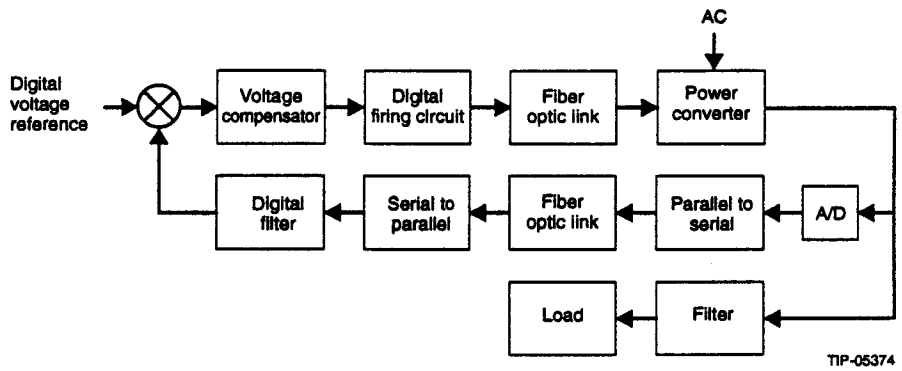

Figure 3.60: Block diagram of the voltage regulator.

Current Regulation Control Loop Design The main function of the current control loop is to regulate the magnet current by following the reference waveform provided by the control system. The current control loop must also reject dc voltage perturbations from the power converters and reject dc current perturbations due to changes in the load resistance.

The magnet current is measured with a Zero-Flux dc current transducer (DCCT) with an accuracy of 50 ppm. An analog differential amplifier with a gain of 30 amplifies the difference between the current reference and the magnet current. An 18 bit D/A converter provides the digital reference current while a 16 bit A/D converter digitizes the differential amplifier output. The D/A converter, A/D converter and the differential amplifier are located inside the DCCT in a temperature regulated chamber with a precision of 0.01° C.

Current Regulator Design for the Linear Ramp Mode The current control loop must have sufficient dc gain (80 dB) to satisfy the tolerance requirements and have a frequency response fast enough to follow the reference current waveform with a small error.

The block diagram of the current control loop for the linear ramp mode is shown in Figure 3.65.

The digital current regulator operates at a frequency rate of 1440 Hz. It is made up of a feedforward compensator, a feedback regulator and an adaptive feedforward compensator. The voltage reference signal for the voltage regulators is generated by adding the outputs of the feedforward and

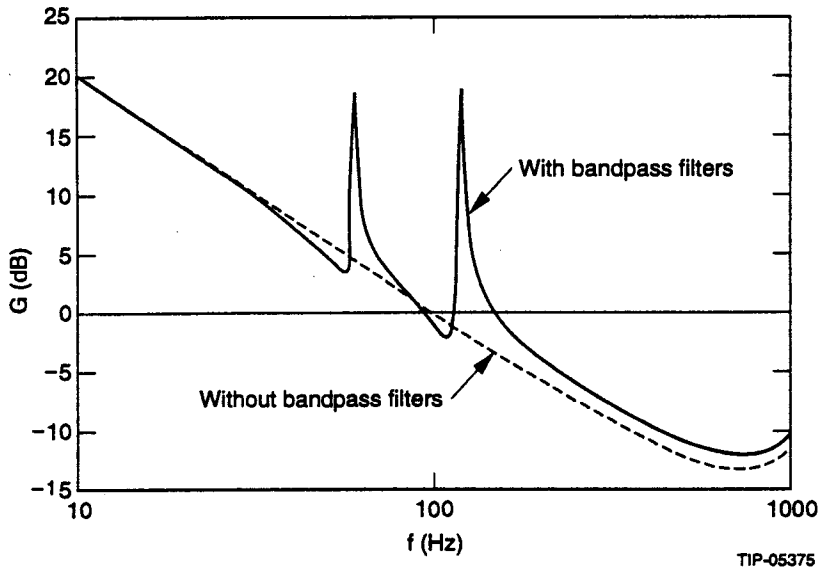

Figure 3.61: Open loop gain/frequency response of the digital voltage loop.

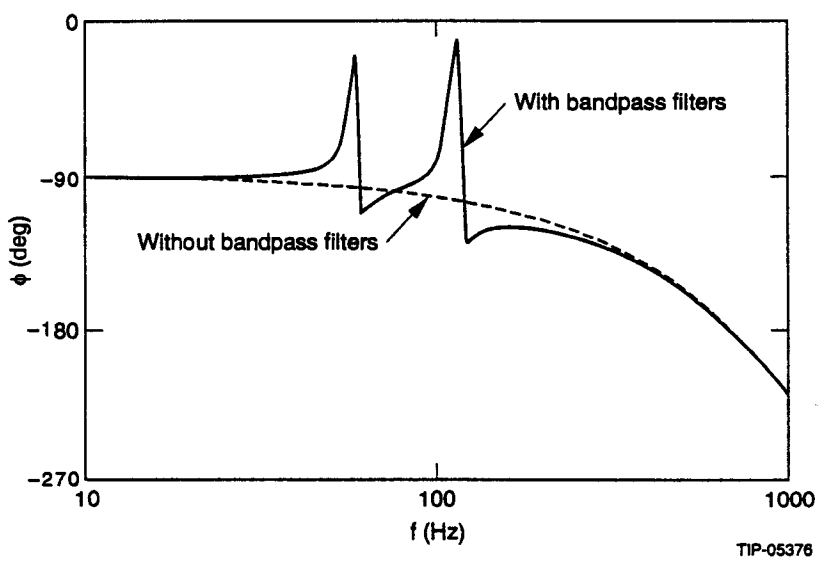

Figure 3.62: Open loop phase/frequency response of the digital voltage loop.

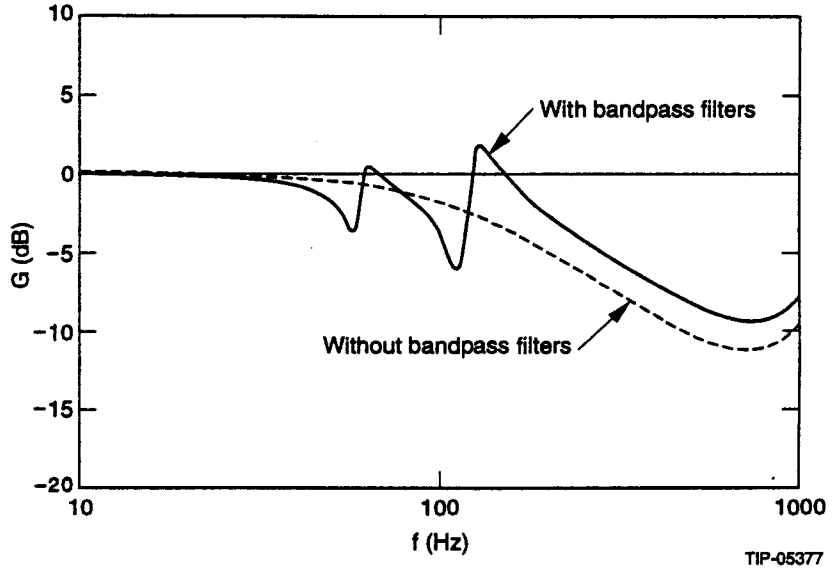

Figure 3.63: Closed loop gain/frequency response of the digital voltage loop.

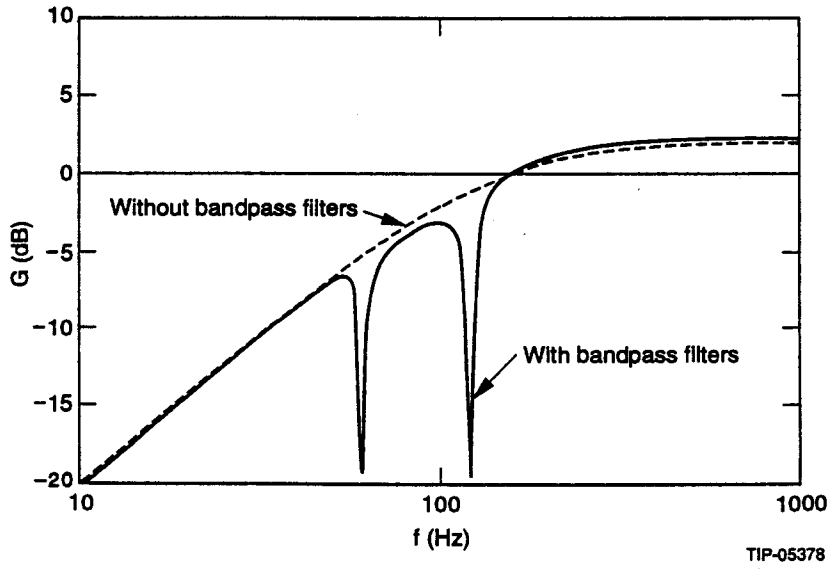

Figure 3.64: Rejection characteristics of the digital voltage loop.

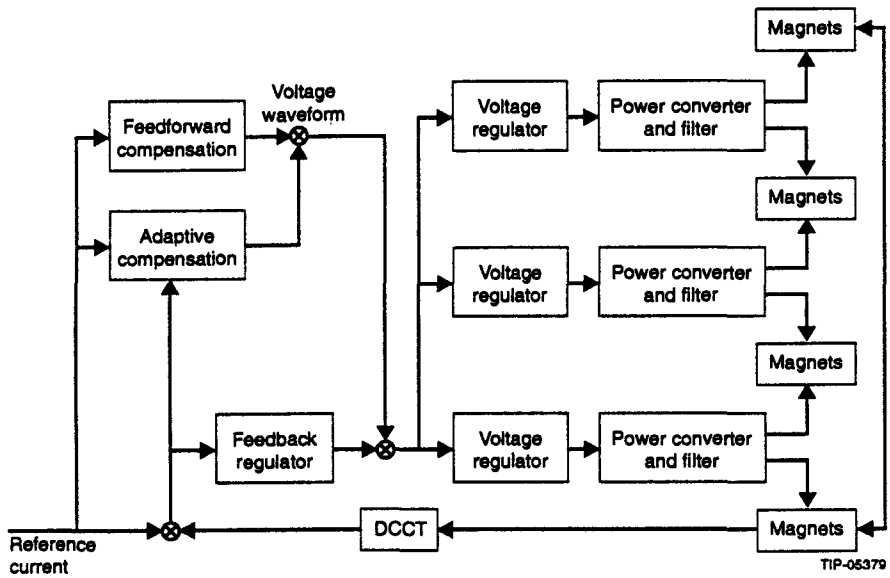

Figure 3.65: Block diagram of the current control loop for the linear ramp mode.

feedback blocks. The three main magnet power supplies are then driven by the same voltage reference.

Feedforward Compensator The feedforward compensator provides the voltage required to drive the current through the magnets and follow the reference current. The feedforward system is an open-loop compensation unable to correct current perturbations and therefore must be complemented with a feedback system.

Feedback Regulator In order to design the feedback loop, the load characteristic must be fully understood. The voltage control loop has a bandwidth of 150 Hz and the output passive filter is basically a second order, critically damped, low-pass filter with a resonant frequency of about 130 Hz. The non-resonant load admittance including the voltage loop and passive filter effects, is represented in the frequency domain in Figure 3.66.

The feedback regulator has been designed with a phase margin of at least 45° at the highest possible frequency. A lag compensator has been selected to fulfill both the stability condition and the dc open loop gain requirement

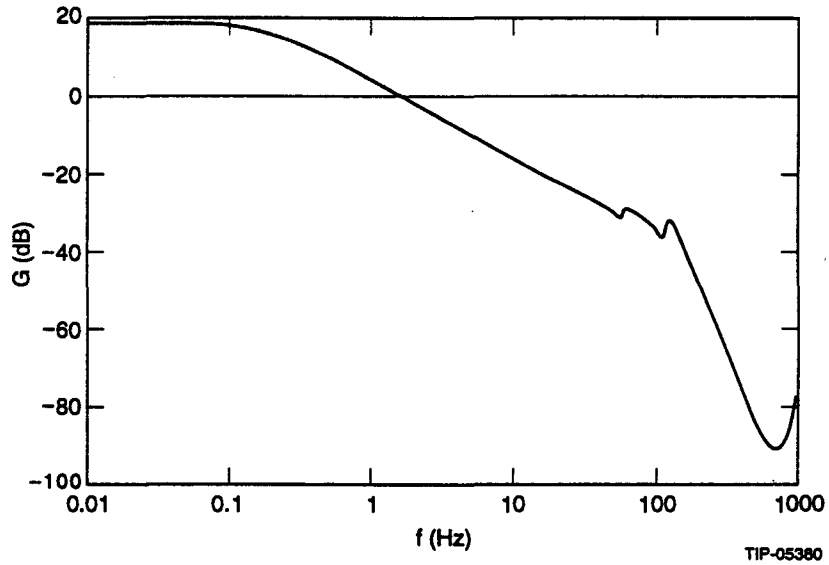

Figure 3.66: Magnitude frequency response of the load admittance including voltage loop and passive filter.

of 80 dB. The current compensator is designed using the equations modeling the voltage regulation loop, output filter and the load, and by taking into account the gain and phase margin requirements. Its transfer function in the Z domain is given by:

$$CI(z) = 70.8\frac{(z-0.99916)(z^2-1.457z+0.6943)}{(z-1)(z^2)} . \tag{3.6}$$

The dc gain is high enough to satisfy the steady-state error specification, and the compensator's zero cancels the pole introduced by the load. The position of the compensator's pole has been determined by stability conditions. The current compensator has been designed using a one-step predictor concept to improve the phase stability margin and has been verified by computer simulations. The open loop gain and frequency responses of the digital current regulation loop are shown in Figures 3.67 and 3.68. It can be seen in these figures that both stability margins are positive. A phase margin of $m = 70°$ is obtained at a phase-margin frequency of $f = 29$ Hz, while the gain margin has a value of $G_m = 10$ dB at a gain-margin frequency of $f_c = 135$ Hz. The closed loop gain/frequency response of the digital current regulation loop has been represented in Figure 3.69.

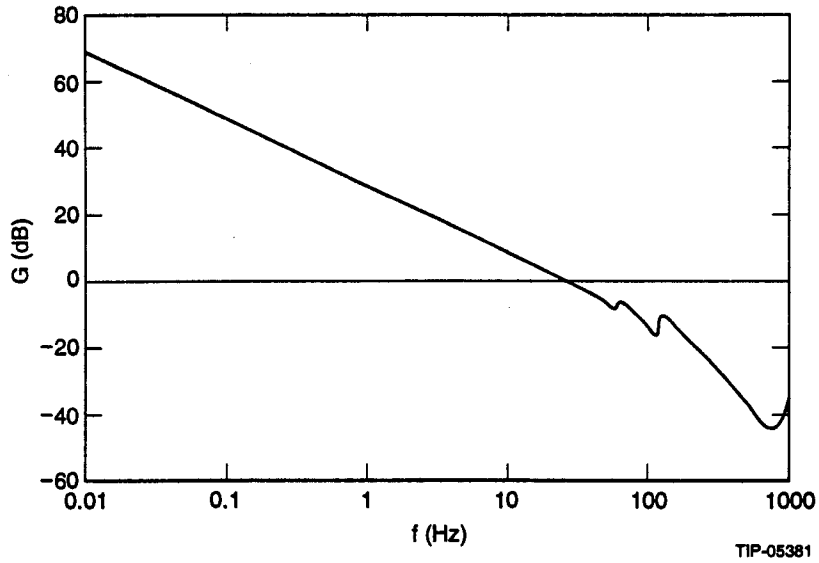

Figure 3.67: Open loop gain/frequency response of the digital current loop.

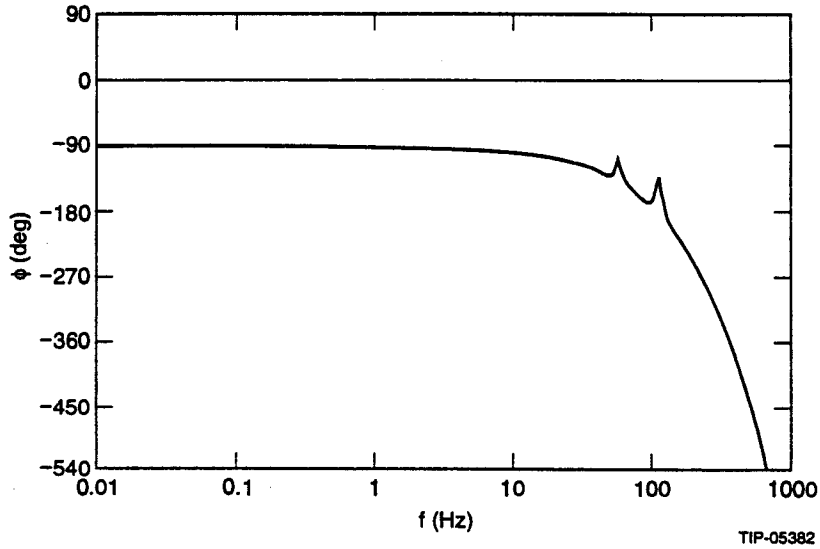

Figure 3.68: Open loop phase/frequency response of the digital current loop.

The feedback loop is stable, having a closed-loop bandwidth of 30 Hz. The rejection characteristics versus frequency of the digital current loop have been plotted in Figure 3.70.

Computer Simulations The digital current loop design has been verified by computer simulations. The current reference and the current flowing through the magnets are represented in Figure 3.71. Due to the action of the feedforward compensation the tracking error is substantially reduced, with the reference and magnet current being macroscopically identical. Nevertheless, the error signal will show the difference between the reference and magnet currents. The current error has been represented in Figure 3.72.

The error shown in Figure 3.72 is due to residual errors in the model used to calculate the feedforward voltage waveform. The regulation requirements are fulfilled in the computer simulations. In addition, the residual current error can be further reduced by using an adaptive feedforward compensator.

Current Regulator Design for the Biased Sinewave Mode In both operational modes, the maximum and minimum current flowing through the magnets has to be regulated to within 100 ppm of the reference current. To satisfy this requirement, a current regulation system with a high open-loop gain at dc and 10 Hz is necessary. High open-loop gain at 10 Hz with adequate closed-loop stability can not be fulfilled with the conventional regulator that was used for the Linear Ramp Mode. The regulation problem has been solved by combining feed-forward compensation and conventional feedback regulation with the frequency conversion techniques of a synchronous regulator. The magnet current is measured with the same DCCT as was used in the ramp mode. The block diagram of the current loop is shown in Figure 3.73. The global control system provides the maximum and minimum current values, while the 10 Hz biased sinewave current reference is locally generated and synchronized with the 60-Hz power supply.

The current regulator is fully digital and operates at a frequency rate of 1440 Hz. It is composed of a feedforward compensator, a feedback regulator and a synchronous $I_{\mathrm{max}}/I_{\mathrm{min}}$ regulator. The voltage reference is generated by adding the outputs of the three regulation blocks. The three ring magnet power supplies are driven by the same voltage reference.

Feedforward Compensator The feedforward compensator provides the voltage required to drive the current through the magnets and follow the

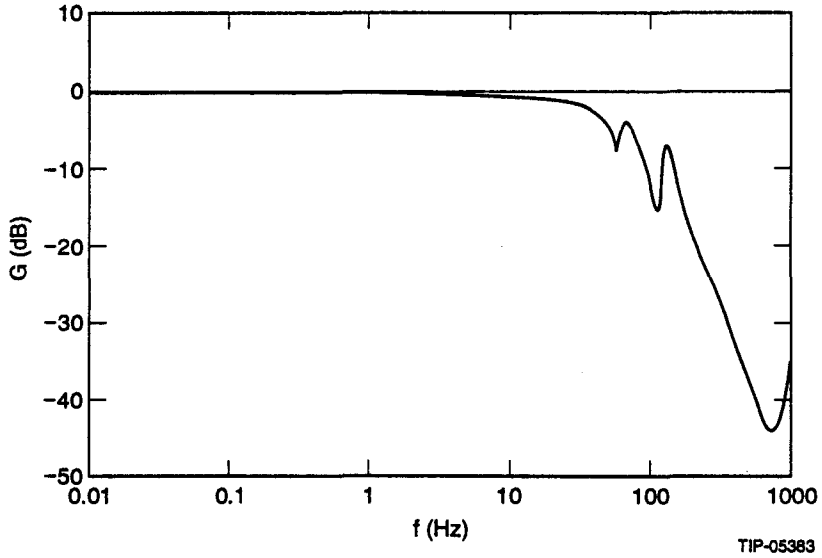

Figure 3.69: Closed loop gain/frequency response of the digital current loop.

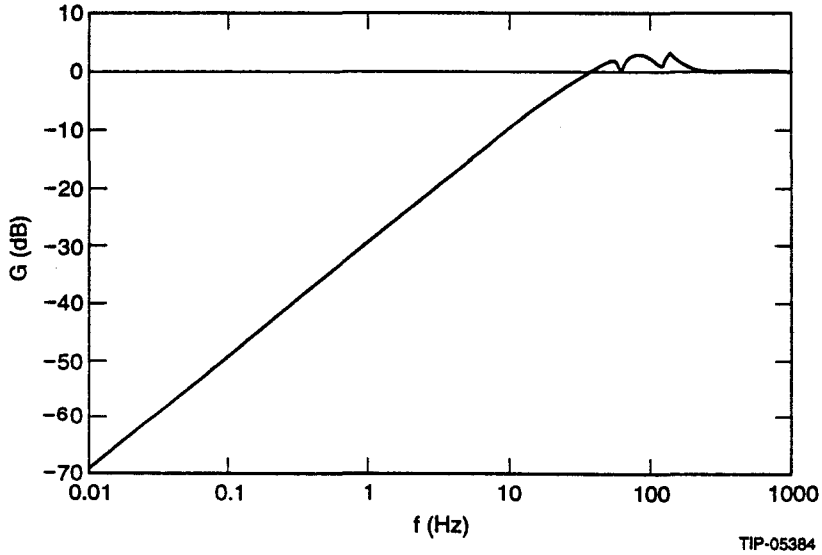

Figure 3.70: Rejection characteristics of the digital current loop.

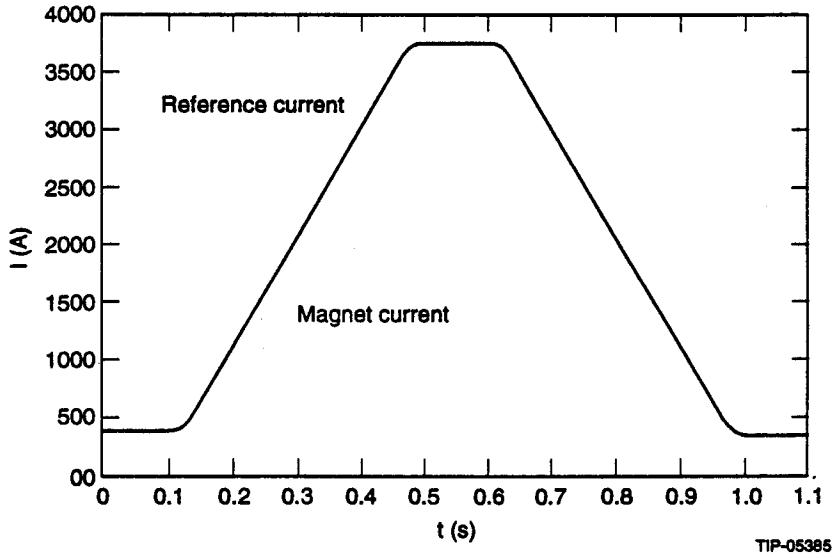

Figure 3.71: Reference and magnet current.

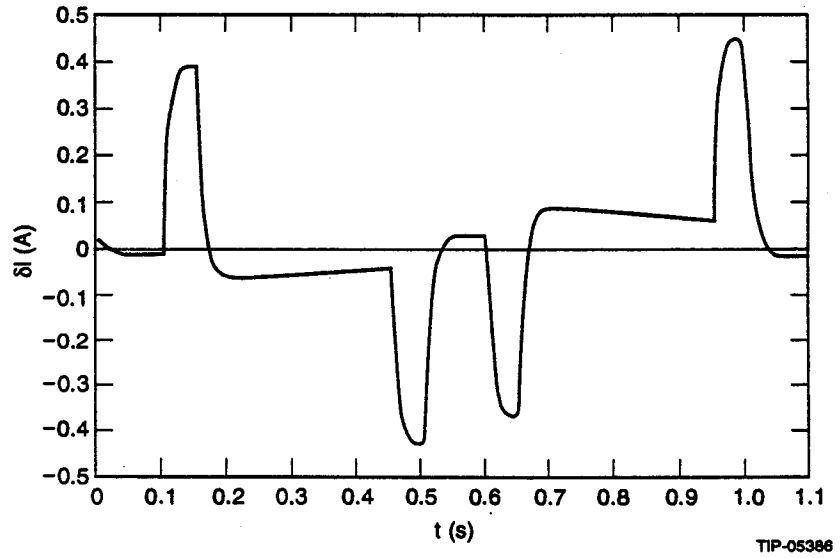

Figure 3.72: Error between reference and magnet currents.

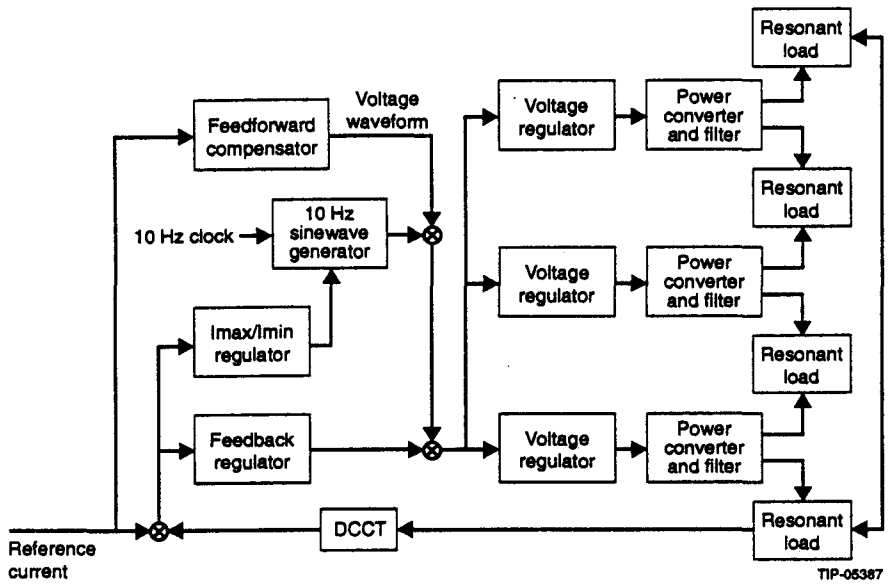

Figure 3.73: Block diagram of the current loop 10 Hz biased sinewave mode.

reference current. The feedforward system is an open-loop compensation unable to correct current perturbations and therefore must be complemented with a feedback system. The output voltage waveform from the feedforward compensator is a calculated biased sine wave that assumes a perfect resonant load.

Feedback Regulator In order to design the feedback loop, the load characteristic must be fully understood. The voltage control loop has a bandwidth of 150 Hz and the output passive filter is basically a second order, critically damped, low-pass filter with a resonant frequency of about 130 Hz. The admittance of the resonant load is represented in frequency domain in Figure 3.74.

The feedback regulator is a proportional cascade compensator with a total gain of 20 dB. The resulting feedback loop is stable, having a closed-loop bandwidth of 20 Hz. A 60° phase margin at 20 Hz is produced by a passive filter in the feedback regulator. The feedback loop has a gain of 30 dB at dc and at 10 Hz, and is not sufficient to satisfy the regulation requirements. The gain at low frequencies can be increased using integral action but the

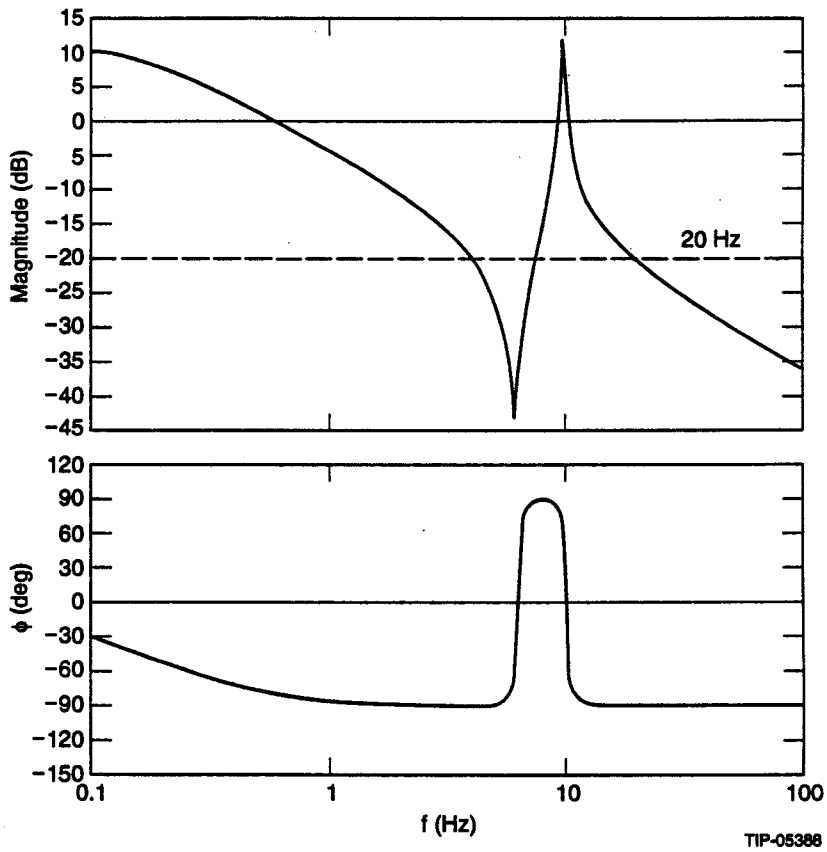

Figure 3.74: Magnitude and phase frequency response of the load admittance.

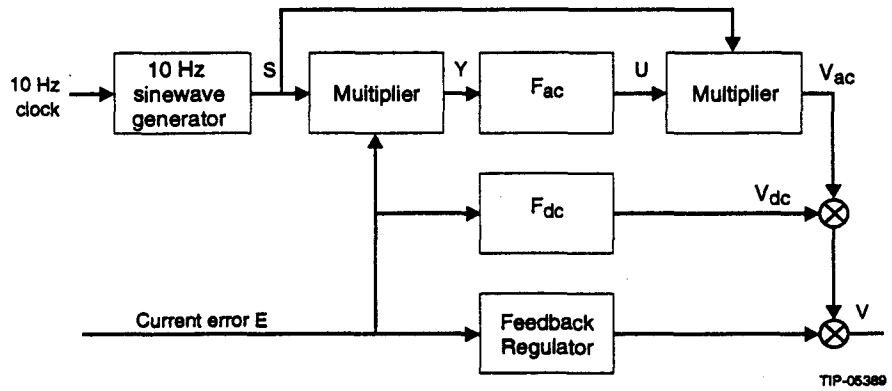

Figure 3.75: Block diagram representing the detection and modulation process.

gain at 10 Hz cannot be substantially increased, using standard techniques, without reducing the phase stability margin.

Synchronous Imax/Imin Regulator The basic idea of the synchronous regulator is to take advantage of the periodicity of the reference current. The current error is measured during one signal period and the correction is synchronously and gradually applied during the following periods. In this way, an equivalent high gain at 10 Hz can be obtained while limiting the closed-loop bandwidth of the synchronous regulator to less than 1 Hz.

The high gain in the low frequency band is easily obtained by integrating the mean value of the error signal (dc). The integrator gain has been calculated for having a correction bandwidth of 0.6 Hz.

Frequency conversion techniques are used to obtain high gain at 10 Hz. The residual 10-Hz sine wave on the error signal is detected in amplitude (ac component only) and integrated. The output of this integrating amplifier modulates the amplitude of a synchronized sine wave. The block diagram in Figure 3.75 shows the model used for the synchronous regulator, the signal demodulation has been implemented with a synchronous detector. The ac and dc components of the error signal are filtered with the integrating amplifiers F_{ac} and F_{dc} respectively.

$$F_{ac} = \frac{K_{ac}}{s} \qquad F_{dc} = \frac{K_{dc}}{s} \,. \tag{3.7}$$

Amplitude modulation and detection are nonlinear processes that can be handled by the Laplace transform using s-plane convolution. The same multiplier is used for implementing both the modulation and the detection process.

Denoting the Laplace transform of $y(t)$ and $u(t)$ by $Y(s)$ and $U(s)$, the transform of both products can be expressed by the following s-plane convolutions.

$$\begin{aligned} Y(s) &= \frac{1}{2\pi j}\int S(\lambda)\cdot E(s-\lambda)\cdot d\lambda \\ V_{ac}(s) &= \frac{1}{2\pi j}\int S(\lambda)\cdot U(s-\lambda)\cdot d\lambda\ . \end{aligned} \tag{3.8}$$

Both convolution integrals are readily evaluated by taking residues at poles of $S(\lambda)$. Neglecting high frequency components, the transfer function of the ac synchronous regulator can be approximated by

$$\frac{V_{ac}(s)}{E(s)} \cong \frac{K_{ac}}{2}\cdot\frac{s}{s^2+\omega_o^2}\ ; \tag{3.9}$$

thus, the transfer function of the equivalent feedback regulator can be expressed by

$$\frac{V(s)}{E(s)} = K_p + \frac{K_{dc}}{s} + \frac{K_{ac}}{2}\cdot\frac{s}{s^2+\omega_o^2}\ , \tag{3.10}$$

where K_p represents the proportional gain of the feedback regulator.

Using the following constant values: $K_p = 10$, $K_{dc} = 40$, $K_{ac} = 160$, the frequency response of the equivalent feedback regulator is shown in Figure 3.76. Using Eq. (3.10), the transfer function of the total open-loop feedback regulation was calculated and the frequency response is shown in Figure 3.77. Comparing Figures 3.76 and 3.77, the improvement of the synchronous regulator is apparent. The 20 Hz closed-loop bandwidth, controlled by the proportional constant K_p, has not been modified. The system is stable, the phase margin has been reduced by only 6° (Eq. (3.10)) and the equivalent open-loop gain at dc and 10 Hz has been dramatically increased. The constant values K_{dc} and K_{ac} have been chosen for having a correction bandwidth of 0.6 Hz for both, dc and 10 Hz components.

Computer Simulations In the computer simulations, the linear phase detection modeled in Figure 3.75 has been replaced by a timing circuit and two sample-and-hold circuits. The timing circuit generates sample pulses

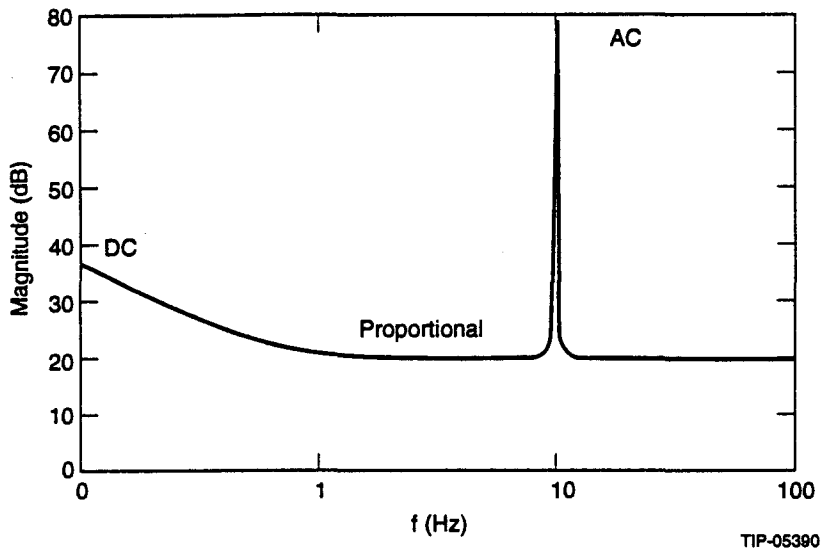

Figure 3.76: Magnitude frequency response of the equivalent feedback regulator.

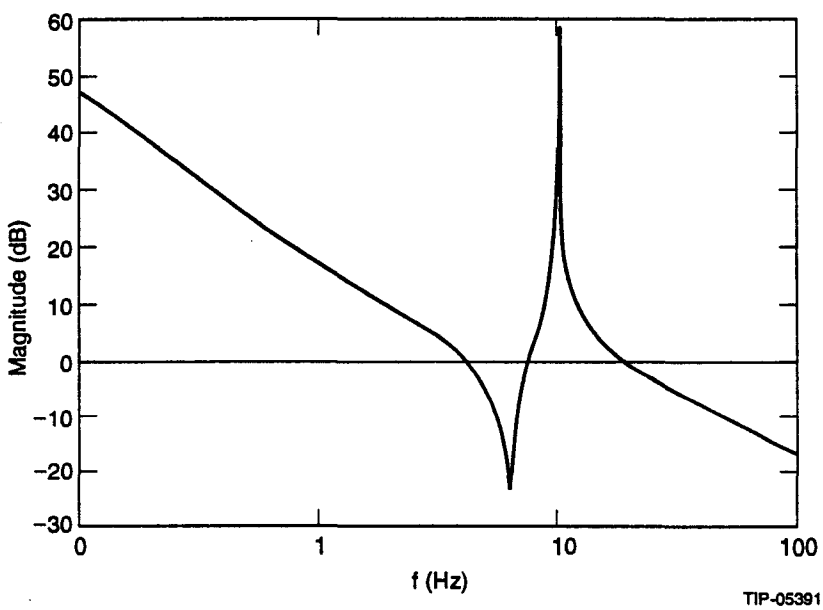

Figure 3.77: Magnitude frequency response of the total open-loop feedback regulation.

synchronized with the maximum and minimum of the magnet current. Two sample-and-hold circuits measure the current error at the maximum and minimum points. This measuring system works in a similar way as a synchronous detector but has a different dc gain. In fact, if the error signal is a non-biased sinusoid with amplitude $\hat{I}$ and the same frequency and phase of the carrier signal $s(t)$, the difference between maximum and minimum sample-and-hold outputs will yield a dc component of amplitude $2\hat{I}$. Under similar conditions, the output of a linear phase detector would be $\hat{I}/2$. The maximum and minimum sample-and-hold output is proportional to the error signal bias and is used to drive the dc regulator. The simulated dynamic behavior of the feedforward compensation and the feedback regulation is shown in Figures 3.78 and 3.79.

In Figure 3.78, the feedforward compensator is connected while the feedback and the synchronous regulator remain disconnected. This figure shows that the feedforward compensator reduces the current error to zero in a few seconds.

In Figure 3.79, the feedforward compensator output has a 10 % error in the dc value as well as in the sinewave amplitude. The feedback regulator has a fast response (20 Hz bandwidth) and reduces the residual dc and ac current errors by a factor of 30.

In the first part of Figure 3.79, the 10 % error feedforward compensator and the feedback regulator are in a steady-state condition. At a time of 1 s, the ac/dc synchronous regulator is connected. The figure shows that the residual current error goes to zero with a time constant, of about 0.25 s, for both ac/dc components, corresponding to a bandwidth of 0.6 Hz.

Power Converters

The power converters which excite the LEB ring magnets consisted of three 24 pulse line commutated thyristor systems.[69] Each system is comprised of two 12-pulse systems offset by 15° and then connected in series to yield 24 pulse operation. The nominal no-load voltage for each supply is 2000 Vdc. The nominal current output is rated for 4100 amps dc. A detailed description of the power converters can be found in the literature.[65]

Harmonic Filtering/Power Factor Correction

The harmonic filter/power correction circuit is connected to each phase of the 12.47 kV ac supply bus and is shown in Figure 3.80. Figures 3.81 and 3.82

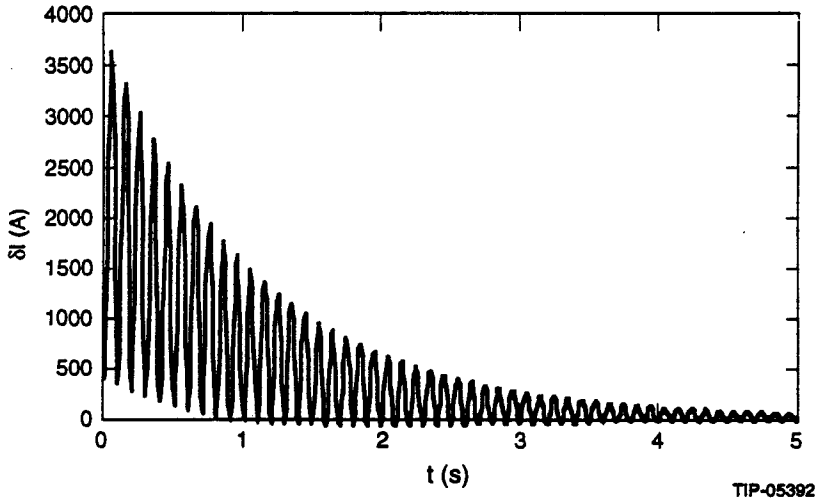

Figure 3.78: Difference between reference and magnet current by using feed-forward compensator.

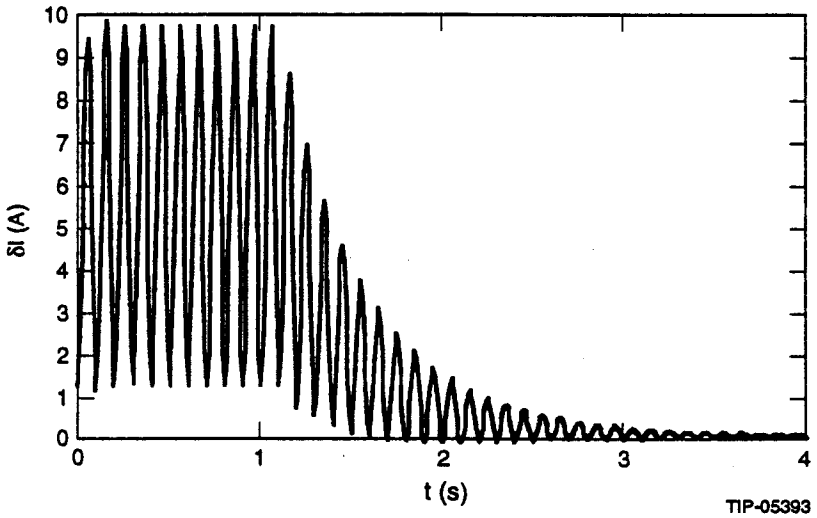

Figure 3.79: Difference between reference and magnet current by using feed-back synchronous regulator.

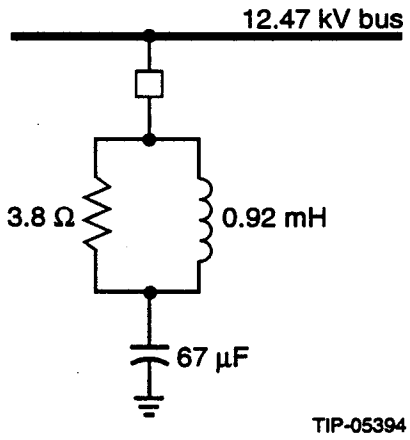

Figure 3.80: Ac harmonic/power factor correction filter.

show both the real and reactive power requirements for the ramp mode and 10-Hz resonant mode respectively.

In order to optimize the cost without compromising the technical requirements, the harmonic filter design is identical for the LEB, MEB and HEB so that industry-standard capacitors can be used and the number and type of spare components can be minimized. The design requirement is to limit the voltage distortion on the 12.47-kV line to less than 5 % total harmonic distortion as recommend by IEEE Standard 519-1992, and to provide a power-factor correction of 0.85. The high pass filter characteristic is designed with a cut-off frequency at 640 Hz to minimize the power dissipation in the filter resistor.

Since 24 pulse converters are used, the individual voltage harmonics on the 12.47-kV bus are less than 3 % of the 60 Hz voltage below the 11th harmonic, so that adequate filtering is achieved with a simple high pass filter. The power-factor correction is achieved by selecting a large capacitance in the filter, producing a power factor of 0.85.

During the normal 10-Hz biased sine wave operation of the LEB, there will be a 10-Hz amplitude modulation of the 12.47-kV line voltage with a 15 % peak-to-peak amplitude variation. This voltage variation has negligible effect on the power converter since its internal voltage regulator compensates for ac input power fluctuations. The resulting voltage variation on the electric power utility's 347-kV bus is expected to be less than 1 %.

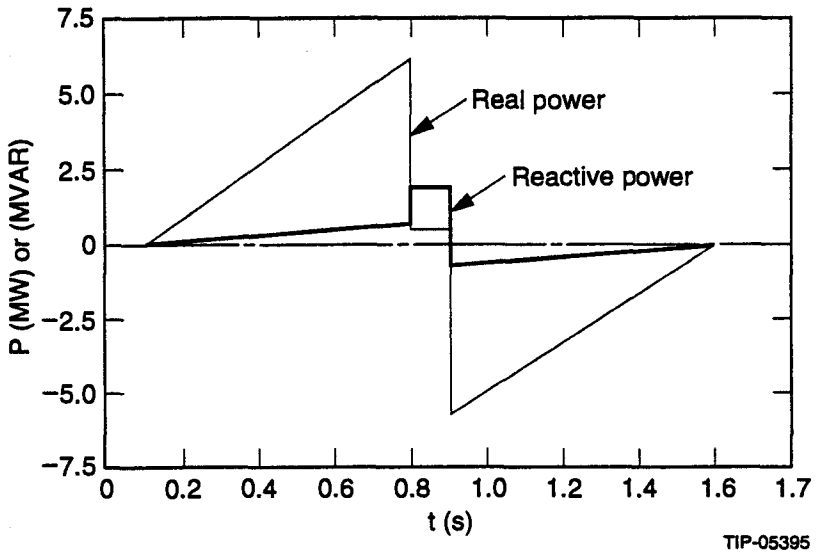

Figure 3.81: Power supply input power in ramp mode.

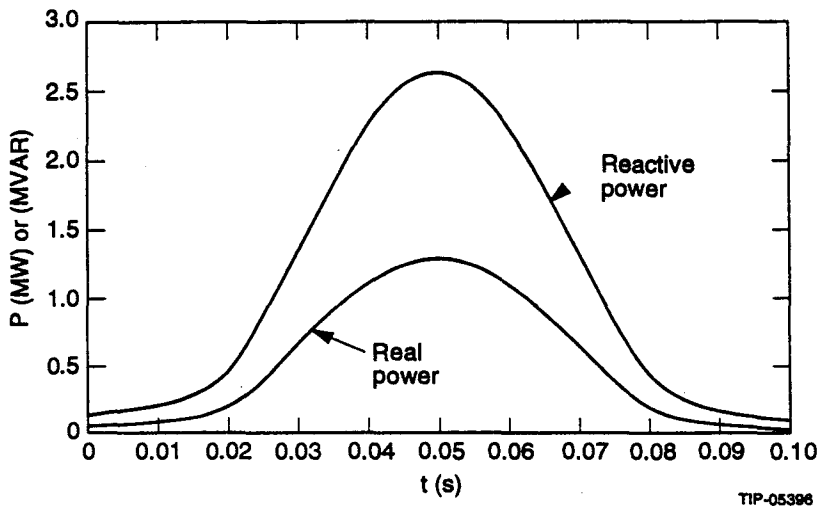

Figure 3.82: Power supply input power in 10 Hz resonant mode.

Harmonic interactions with other components in the ac power system have been studied and it has been determined that the very low impedance of the 12.47-kV bus will preclude the possibility of interactions.

Acknowledgements

The authors would like to thank J. Tool and R. Winje for the key roles they played in the early conceptual development of all the Ring Magnet Power Systems associated with the Super Collider. We thank C. Jach for his work in bringing together the detailed design of the LEB power systems and his role in the success of the collaborative aggreement to build the Energy Storage Inductors in Russia. We also give special thanks to J. Brown, B. Carlisle, C. Christiansen, B. Day, J. Gannon, R. Harold, F. Hooshdaran, J. Huang, A. Medvedko, A. Mendoza, D. Voy, J. Payne, J. Rivera, K. Smedley, R. McConeghy, and R. Nehring for their valuable contributions.

3.2.2 Corrector Power Supply System (W. Merz)

Overview

Functions and Quantities There are 244 individual corrector magnets and power supplies in the LEB corrector system. The power supply output current and consequently the magnet field strength for each element may be independently adjusted. Where groups of elements are to be operated as families, such as with tune quadrupoles, chromaticity sextupoles or high order resonance correction, the elements are grouped via software controls at the application level. Each separate power supply channel is controlled by a waveform generator located in an adjacent controls crate.

Table 3.17 lists the functional elements and quantities by magnet type.

Table 3.17: LEB corrector magnet types.

Element	Dipole	Low Gradient Quads	High Gradient Quads	Chromatic Sextupoles	Harmonic Sextupoles
Quantity	90	72 normal, 4 skew	18	48	12

System Topology The system topology chosen is one that is similar to that used in other accelerator facilities for correction element power supplies. Each individual magnet load current is driven from a dedicated amplifier with the raw voltage for groups of amplifiers being derived from a common dc bulk source. High frequency switchmode power amplifiers are chosen for their efficiency. Bipolar current operation with inductive loads and high dI/dt requirements necessitate the use of four-quadrant supplies. The amplifiers need to act as both source and sink for both current polarities. The amplifiers are grouped in equipment racks based on functionality and location. There are advantages and disadvantages to this choice. With the common input source, the bulk power supply, there is a potential cost savings due to lower cost per kilowatt of power at the higher power levels. Safety interlocking complexity and cost is also reduced. On the other hand, stability of the dc bus, particularly with four-quadrant amplifiers, can be more difficult to achieve and complete independence for each input/output channel is lost. System expandability can be limited as well. In spite of these shortcomings, the common input topology was chosen. Efforts to mitigate the problems mentioned have been addressed in the system design from the beginning.

General Parameters All elements are powered by bipolar current sources. Bipolar operation of the dipoles and tune control quadrupoles is inherently necessary in the LEB design. The chromaticity sextupoles are bipolar for operational flexibility. Other elements maintain bipolar capability for consistency in the hardware system design. Bandwidth requirements are driven by the necessity to track the energy change in the 10-Hz mode of operation. Within reason the electrical magnet parameters have been chosen to optimize power supply output current and voltage operating points and to minimize costs for supplies, cabling and installation. A commonality of design for the supplies is achieved by choosing the current and voltage operating points to be similar. With the exception of the High Field Trim Quadrupoles (HFTQ), all supplies are rated at 25 amps or less. The HFTQ have a maximum current of 100 amps. The total output deviation (TOD), requirement for all supplies is specified at ± 0.1 % of full scale output current.

Table 3.18 lists the requirements for each type of supply. Details of the origin for these requirements are discussed further in Section 3.2.2.

Table 3.18: LEB corrector power supply requirements.

Item	Dipole	Low Field Trim Quad.	High Field Trim Quad.	Chromatic Sext.	Harmonic Sext.	Units
Load current max.	±25	±15	±100	±25	±3.5	A
Output voltage max.	±70	±130	±190	±130	±70	V
Total Output Deviation	±0.1 %	±0.1 %	±0.1 %	±0.1 %	±0.1 %	V
Absolute Accuracy	±0.1 %	±0.1 %	±0.1 %	±0.1 %	±0.1 %	% Full sc. current
dI/dt, max.	±785	±471	±2893	±785	±96	A/s
d^2I/dt^2, max.	±49300	±29600	±181000	±49300	±6000	A/s^2
Power supply bandwidth	5	5	5	5	5	kHz
Cooling	air	air	air (water if necessary)	air	air	
Load power *rms* max.	308	198	1663	289	81	W
Quantity	90	76	18	48	12	

Equipment Layout The three-fold symmetry of the arcs and straight sections of the LEB ring determines the equipment locations. Corrector magnets are situated near the main quadrupole magnets in the lattice. As a consequence most elements are found in the arc regions of the ring, and the three arc service buildings contain the majority of the correction element supplies. The only exception are the HFTQ supplies, which are located in the three straight section service buildings. Figure 3.83 shows the ring layout with the correction element supply locations and the number of supplies per rack. Each rack contains space for additional amplifiers if more elements need to be added. Shielded cable is used to connect the output of each amplifier to its load.

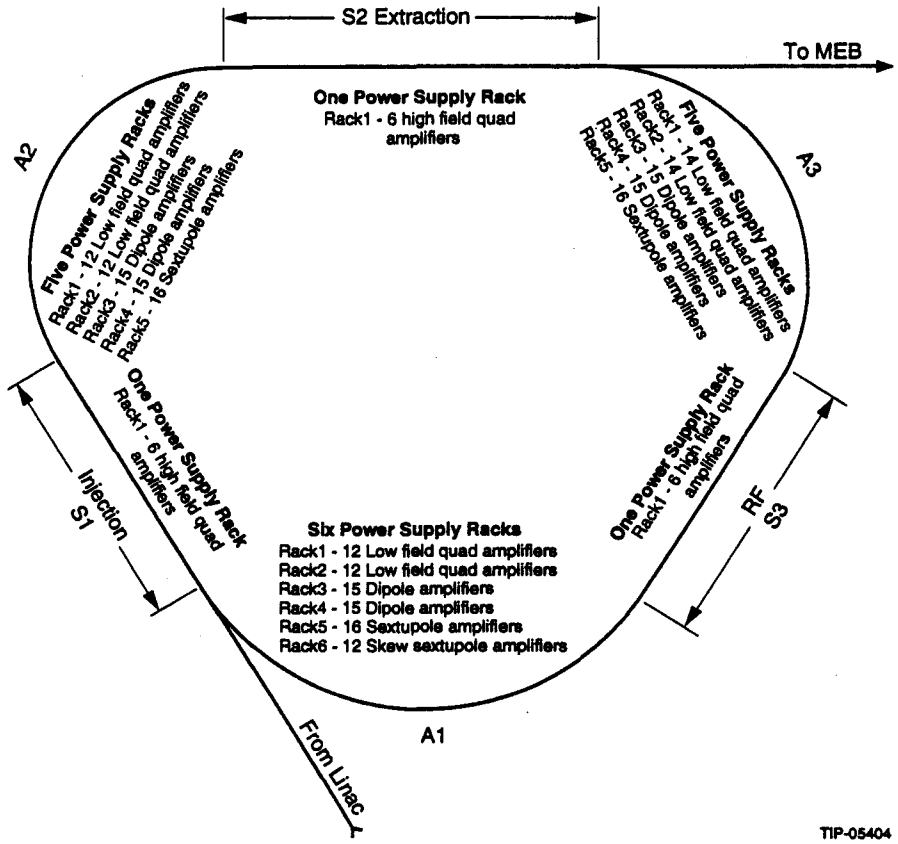

Figure 3.83: General arrangement of the corrector magnet power system.

Operational Modes The fundamental cycling frequency of the LEB is 10 Hz. The current waveform for the main magnets is a fully biased sinewave at that frequency (*i.e.* the main magnet current never goes to zero). For the correctors, this results in the defining waveform also being a 10-Hz sinewave with a peak to peak current not to exceed an absolute value of the maximum current listed in Table 3.18 for each element. Since the waveform has a dynamic component and since the amplifier outputs are bipolar, the current must program smoothly through zero output without violating the TOD requirement.

The other LEB waveform which is reasonably well defined is a 1/3-Hz ramped output. The demands on the corrector supplies in this case are less stringent and can easily be met if the 10-Hz performance is satisfied.

A more general viewpoint of the requirements placed on the correctors is to consider the output to be any arbitrary waveform that does not cause the requirements listed in Table 3.18 to be exceeded. These waveforms and requirements are detailed more fully in Section 3.2.2.

Controls There is a dedicated control channel for each correction element and each bulk power supply. This channel provides for digital control output and status readback as well as analog control input (reference waveform versus time) and analog readback (output current and voltage versus time). The connection from power supply to control system is via fiber optic cable. Waveforms are generated at the application level and downloaded for playback to local control cards residing in controls crates at each service building. Timing information generated by the control system initiates the start of reference playback at the 10-Hz rate (see Section 3.6). The actual waveform is stored as a table locally. Readback and status information are transmitted to the control card for buffering and passed upward on demand. Transmission to and from the power supply is done in serial digital fashion using an SSC devised protocol.[70] Sampling and update rates for information can be as high as 10 kHz.

Acquisition Strategy The power supply system equipment acquisition was broken into two phases. The corrector rack assembly, containing the amplifiers, bulk power supplies and most interconnects, was to be purchased, ready for installation, through competitive bidding. The control module electronics is being developed internally and to be installed either during system installation or provided to the rack assembly vendor as buyer-furnished equipment for incorporation into the rack assembly. Rack assemblies are to be delivered ready for emplacement in the LEB service building.

Technical Requirements

Output Waveforms Since the actual waveforms for the correction magnets have not been explicitly specified, they have been developed based on the LEB main magnet current (or equivalently the momentum profile) waveform. Figure 3.84 defines the requirements for the 10-Hz operation of the corrector supplies. It is assumed that the output waveform will also be a 10-Hz sinewave with a maximum peak to peak current as listed in the requirements

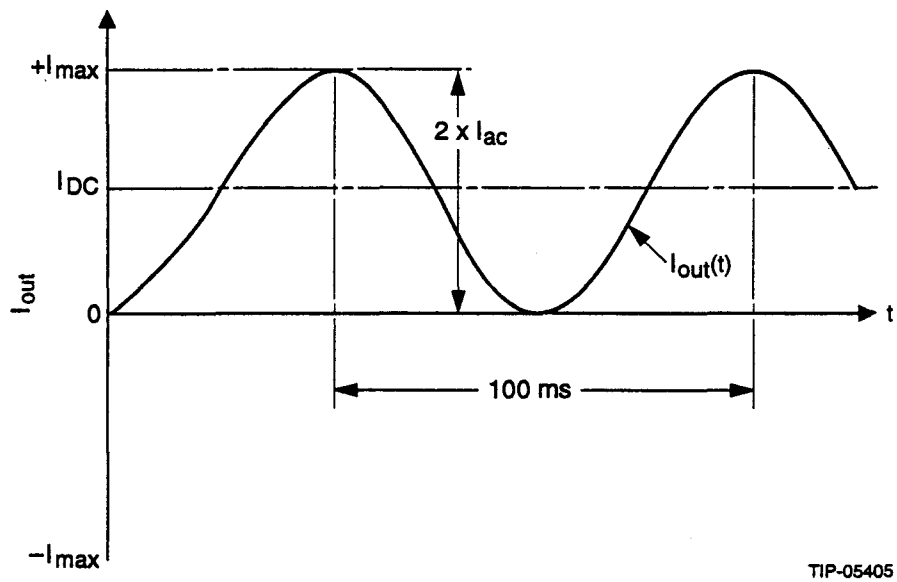

Figure 3.84: Dc offset sinewave.

table for each element. For purposes of deriving the waveform the following equation is used:

$$I_{\text{out}} = I_{\text{dc}} + I_{\text{ac}} \cdot (\cos(\omega t + \phi)) \tag{3.11}$$

where

$$\begin{aligned} I_{\text{dc}} &= -I_{\text{max}}/1 \leq I_{\text{dc}} \leq +I_{\text{max}}/2 \\ I_{\text{ac}} &= \pm I_{\text{max}}/2, \quad I_{\text{max}} \text{ from table} \\ \omega &= 2\pi f, \quad f = 10 \text{ Hz} \\ t &= 0 - 0.1 \text{ seconds} \\ \phi &= \pi \text{ radians} \end{aligned}$$

Figure 3.84 shows the case where $I_{\text{dc}} = I_{\text{ac}} = I_{\text{max}}/2$. Additional power supply requirements, such as dI/dt, d^2I/dt^2 and I_{rms} maximum, can be determined based on the equation for I_{out}. Having thus determined the power supply requirements, other arbitrary waveforms can be supported while still meeting the TOD requirement, as long as the power supply limits are not exceeded.

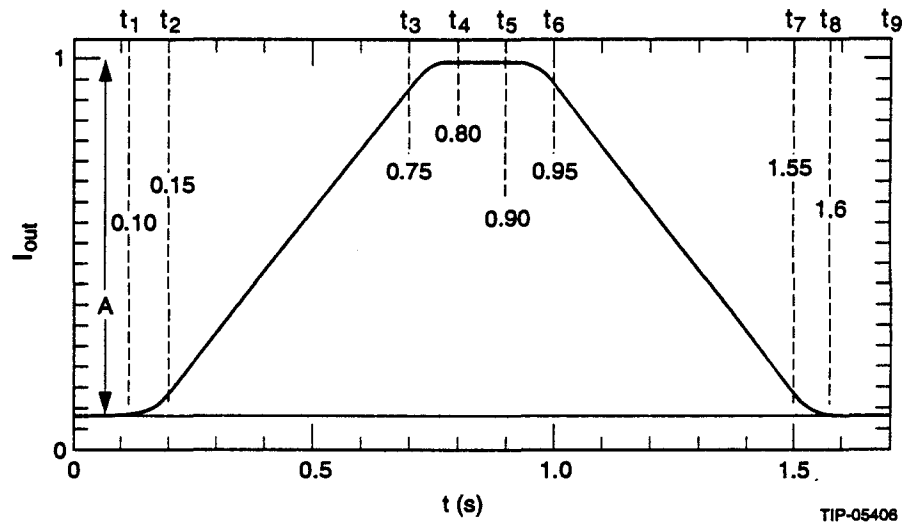

Figure 3.85: 1/3 Hz ramped waveform.

The 1/3-Hz ramped waveform shown in Figure 3.85 is just such an example of another arbitrary waveform. This ramped waveform is less demanding in terms of power supply performance than the 10 Hz operation.

Other Derived Requirements Ampere-turn and TOD requirements for the corrector magnets are derived from the lattice design and tracking studies and can be traced backed to higher level specifications.[71] Maximum current and load impedance values are provided by magnet design choices (see Section 3.1.4 of this book) coupled with power system optimizations. Many other system requirements flow down once the loads are defined. These derived requirements[72] are discussed below.

The first derivative of the current with respect to time—the current slew rate is determined from the waveform equation given in the previous section for each element when $I_{dc} = I_{ac} = I_{max}/2$. The second time derivative of the current, which relates to the amplifier voltage slew rate, is determined from the same equation for the current. The voltage slew rate is dominated by the inductive term and can be approximated by:

$$\frac{dV}{dt} = L \times \frac{d^2I}{dt^2}, \tag{3.12}$$

where L is the magnet inductance.

The voltage slew rate can be important in both the choice of switching frequency and in the design of the voltage regulation loop. Typical current-mode power converter designs for programmable supplies utilize an inner voltage-regulated control loop and an outer current-regulated control loop.

Power supply compliance voltage necessary to satisfy the current requirements has been calculated under worst-case conditions from the load impedance, including cable losses, for each element type, and a safety margin has been added. This voltage requirement becomes the specification for the bulk voltage power supply. Worst-case load power dissipation has been calculated and a somewhat arbitrary amplifier efficiency number of 90 % has been specified as a design goal. Based on the worst-case power dissipation, amplifier efficiency and the number of amplifier units per rack assembly, the bulk supply output power has been specified.

All loads except the HFTQ and harmonic sextupoles are iron core air cooled magnets. The HFTQ are iron-core, water-cooled magnets and the harmonic sextupoles are air-core, air-cooled devices. Each magnet coil has a temperature sensitive switch mounted to it which is connected to an amplifier interlock input. Power supply faults or cooling failures causing excessive temperature rise cause the switch state to change inhibiting the amplifier output. Additional load protection interlocks consist of output overcurrent, overvoltage and ground fault protection; all of which are monitored at the power amplifier. In addition, each amplifier is specified to have input overcurrent and overvoltage protection.

Total Output Deviation The total output deviation (TOD), requirement is used to specify the output current uncertainty due to all error sources. The requirement has been specified in this manner to allow flexibility to the manufacturer in design and cost trade off choices. A graphical representation of the TOD requirement is shown in Figure 3.86. Shown is an error band specified as a plus and minus percent of maximum full scale output current. The vendor is left the freedom of determining what faction of this error band is assigned to each error source. The procurement specification[73] gives the TOD as ±0.1 % as measured from the analog input to the output current of the amplifier. In order to meet this requirement at dc, the loop gain for the feedback system must be in excess of 1000 at low

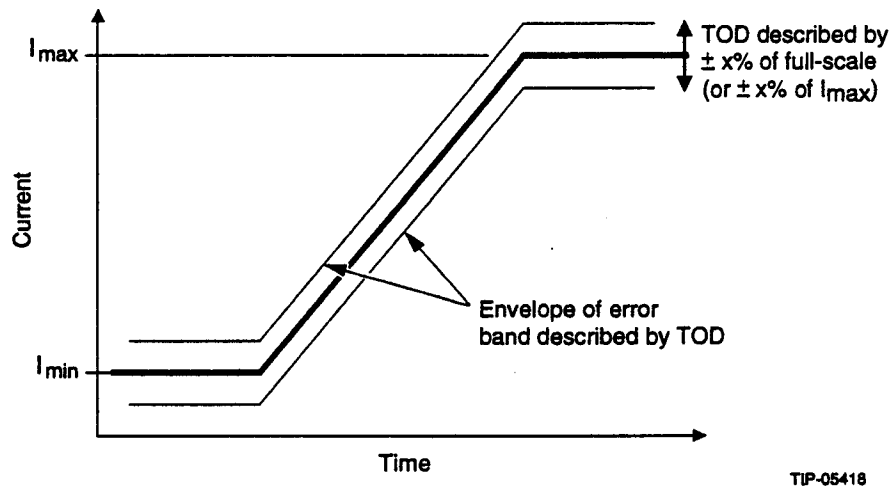

Figure 3.86: Graphical representation of TOD requirement.

frequency. If the loop gain is also in excess of 1000 at 10 Hz, the requirement for the TOD can be met during the dynamic portion of the cycle as well. The small-signal bandwidth required for meeting the TOD due to current lag error can be estimated by:

$$\Delta I = \left(\frac{dI}{dt}\right)(2\pi BW), \tag{3.13}$$

where BW is the bandwidth.

Other factors that must be considered in meeting the TOD requirement include output current ripple, and stability versus time, temperature and line voltage variations. Absolute accuracy in the current measurement is not considered as high a priority as long as the repeatability of setting is maintained. Stability is measured based on any continuous eight-hour period. This is reasonable in light of the empirical nature in which the settings are determined and routinely adjusted during Collider operations. It should be noted that switch-mode amplifiers operating at reasonably high frequencies are easier to filter. In addition the magnets themselves provide a significant filter inductance for reducing current ripple.

Controls Requirements for the control of the LEB correctors in general flow down from higher level machine specifications, Level 3a and 3b.[74] Where explicitly called out and applicable to the power supplies, these requirements

are supported. Additional requirements at Level 4,[75] the system level, have been added to enhance operation of the power supplies. On/off control, load protection, power supply status and output readbacks as well as setting control are called for in the higher level specifications. Details at Level 4 provide additional derived requirements. These requirements are meant to provide a level of operational diagnostics both during normal running and during failures or system check-out. Internal power supply monitoring and controls self-checking also fall into this category. With a fairly large and distributed system of equipment, the ability to do system commissioning and fault diagnostics remotely becomes important. This is particularly important in meeting the corrector system availability requirements.

The interface between the power supply and the control system is done locally via a fiber optic cable connection. The optical, serial, digitally encoded information from the control system is translated into the appropriate format and distributed to the power equipment by a power supply control module. The control module acts as a summing point for all power equipment I/O. The control module resides in the power equipment rack.

Waveform generation and information buffering occur on control cards located in controls equipment crates. A description of the operation of these control cards can be found elsewhere in this document. (See Section 3.6.4 of this document.)

Safety All corrector power supply equipment is classified as requiring personnel safety interlocking[76] due to electrical hazards. The Personnel Access Safety System (PASS, see Section 3.8)[77] provides this by supplying a permit to the bulk dc power supplies when tunnel enclosures are safe for operation. Disabling the bulk supply voltage output prevents dangerous voltages or currents being placed on the loads while personnel are present. In addition, rack enclosures are interlocked such that access to them will also inhibit the bulk power supplies.

Availability The corrector power supply system has been assigned an availability allocation[78] of 0.996 based on a top level analysis of all LEB systems and a comparison to Fermilab Booster operating experience. Equipment mean time between failure (MTBF) numbers have been determined from the availability allocation. The relationship between availability and MTBF is

$$A = 1 - \frac{\text{MDT}}{\text{MTBF}} \tag{3.14}$$

where MDT is mean downtime and is assumed to be 1 hour.

Standard commercial-quality power equipment has demonstrated MTBF values of 20 000 to 100 000 hours. The MTBF values for the subsystem elements are as follows:

244 amplifiers—90 000 hours each
19 bulk power supplies—50 000 hours each
19 control modules—21 000 hours each

Using these values gives a system MTBF of approximately 250 hours and implies a failure causing a one hour interruption would occur about every 10 days.

Loads Table 3.19 lists magnet load values and gives worst-case resistance values for the longest cable runs. The magnet parameters listed correspond to the components in the load model shown in Figure 3.87. The values shown are from measurements made on prototype magnets. Simulations using these values in the model give good agreement with measured frequency response for each magnet except for the sextupole.[79] The expected single resonance characteristic due to the magnet inductance and coil interwinding capacitance is not present in the sextupole, instead a double resonance is found. Figure 3.88 shows this measured double resonance in an impedance versus frequency plot. The origin of this response has not been fully understood at the time of project termination.

Design and Implementation

Topology Figure 3.89 shows a schematic representation of one corrector power supply rack. Expandability has been built in and system modularity has been stressed in order to allow ease of maintenance and repair. Interlocking and fault protection for both amplifiers and bulk power supply are incorporated into the specifications. The specifications[73] define failure modes that might be anticipated to cause cascade-type failures and require protection schemes to avoid them. Commercial equipment of the type specified is currently on the market from several sources. Figure 3.90 shows a typical rack assembly configuration.

Table 3.19: Corrector load parameters.

Parameter	Element	Dipole	Low Field Trim Quads	High Field Trim Quads	Chromatic Sextupole	Harmonic Sextupole	Units
Magnet Inductance	L2	60	213	53	133	100	mH
Magnet dc Resistance	R2	0.24	1.0	0.26	0.56	15.6	Ω
Eff. Magnet Interwinding Capacitance	C3	180	170	1300	300	300	pf
max. Cond. Length	N/A	2× 340	2× 334	2× 116	2× 248	2× 340	ft
Cable Gauge	N/A	10	10	4	10	10	AWG
max. Cable Resistance	R1	0.702	0.690	0.06	0.512	0.702	Ω
max. Cable Self Induct.	L1	32.0	31.3	9.5	23.2	32.0	μH
max. Cable Capacitance Cond. to Cond.	C2	0.018	0.017	0.007	0.013	0.018	μf
max. Cable Capacitance Cond. to Shield	C1	0.032	0.031	0.012	0.023	0.032	μf

Amplifiers In the past, linear amplifiers have been used in implementing such systems. The advent of improved semiconductor devices, especially at higher frequencies and power levels, allows the use of switchmode-type power converters for the amplifiers. The advantages of using switchmode converters are their higher efficiency and smaller packaging requirements. Linear supplies by nature operate away from the saturation point of the active devices and as a consequence, dissipate significant amounts of power. Switching supply devices operate either fully on or fully off; losses occur only during switching transitions. New high-power and high-frequency devices allow cost-effective amplifiers to be designed that operate into the audio range and at high output power. Due to high-frequency and high-efficiency (in

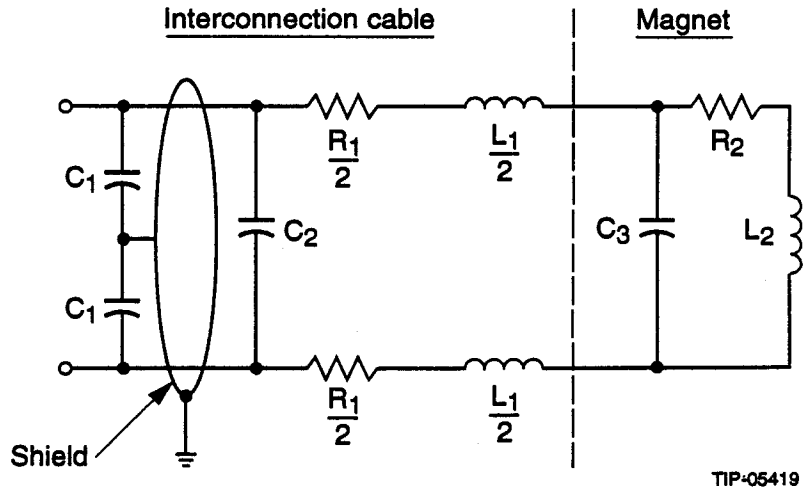

Figure 3.87: LEB power supply load model.

excess of 90 %) operation, heat sink and filtering component sizes are much reduced. Paralleling equipment for increased power output is easily accomplished also. For these reasons, switchmode amplifiers have been chosen for the LEB corrector power supply system. There are five types of amplifiers used for the LEB correctors. The switchmode operating frequency is left for the vendor to choose when doing the detailed design, however, it is expected to be out of the audio range and likely 5–10 times higher than the bandwidth requirement at a minimum. The upper limit will be a function of the switching devices used and the detailed design constraints.

The amplifiers have a dc power input and are capable of dc output. They are, however, also capable of bipolar current output and four-quadrant operation.[80] Figure 3.91 depicts the voltage/current plane and the four quadrants of operation. While in quadrants I and III, power is being supplied to the load. In II and IV energy stored in the inductance is being returned to the supply. Figure 3.92 is a simplified picture of the switch and load arrangement. By the appropriate operation of pairs of switches either polarity of current and/or voltage may be placed across the load. It should be noted that the load is driven differentially by an amplifier, requiring only a single-polarity bulk power source. This is an economy of the topology chosen. However, more switches are needed and it is not possible to ground one side of the load.

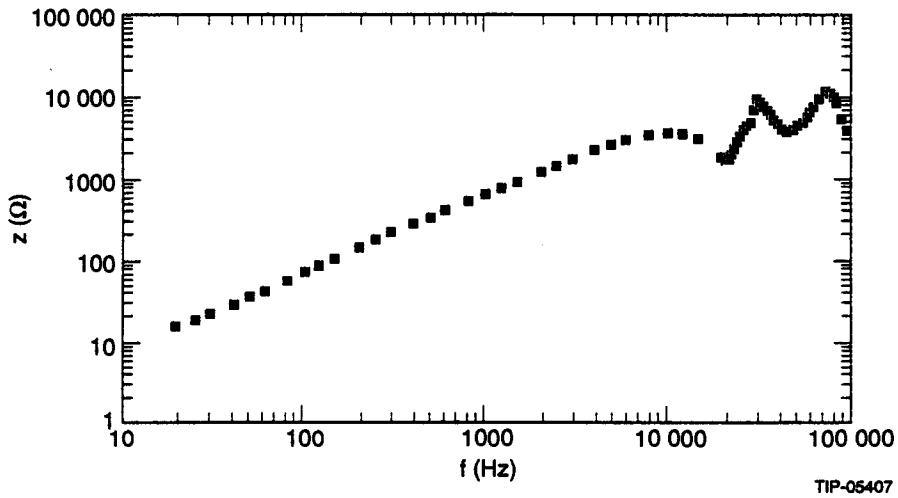

Figure 3.88: LEB sextupole magnet impedance *vs.* frequency.

Control inputs to the amplifier are the reference control signal, an output inhibit signal and an external reset. Control outputs from each amplifier are voltage and current readbacks along with internal fault status monitoring signals. All faults are latching and require fault clearing and assertion of the reset signal before operation can resume.

Bulk Power Supplies There are four types of bulk power supplies, BPS. Table 3.20 lists the BPS by type and their general features. The bulk power supplies utilize ac input from the line and have voltage-regulated, unipolar outputs. The *rms* power rating for each is based on servicing 20 amplifiers except for the HFTQ. HFTQ bulk power supplies are capable of operating 7 amplifiers. The average amplifier population in most rack assemblies is 14 units with the HFTQ being populated with 6 units. The added capacity provides room for additional units and also provides margin for peak output requirements compared to rms output. The output regulation for the BPS is specified at 1 %. Due to the four-quadrant operation of the amplifiers, the BPS will see energy being returned to its output. The specifications for the system prohibit the dissipation of this energy in the rack in order to meet the regulation requirement. It is left to the vendor to chose between storing the returned energy at the BPS output or returning the energy to the ac line.

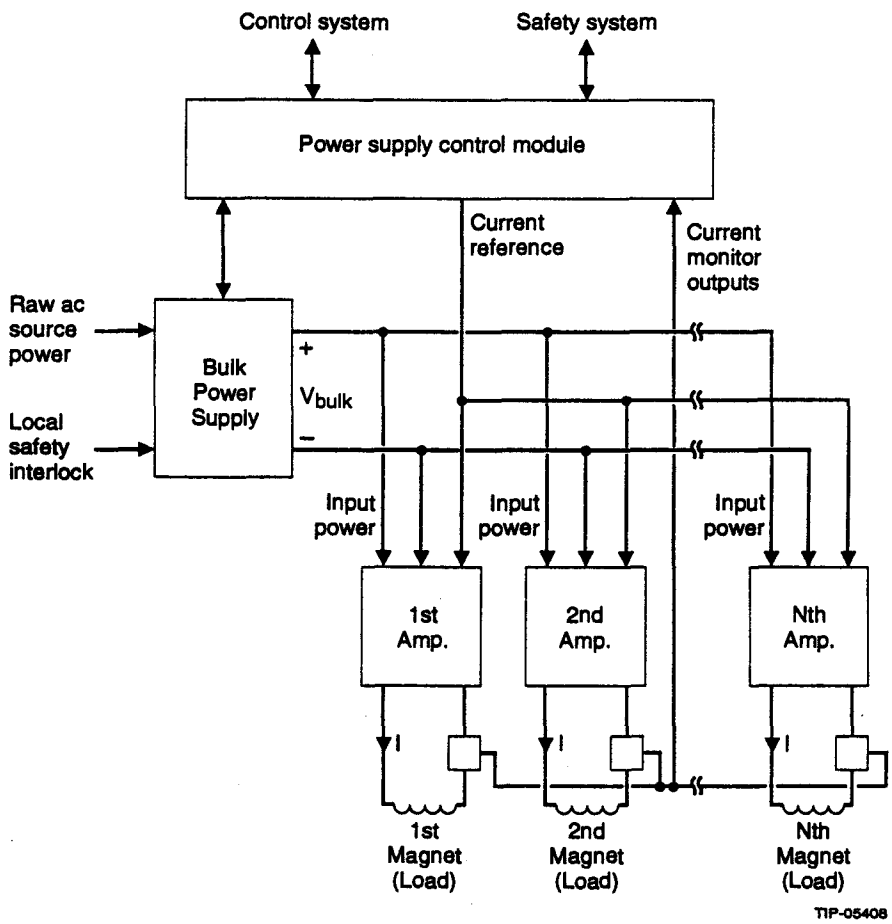

Figure 3.89: Block diagram—LEB corrector power supply system topology.

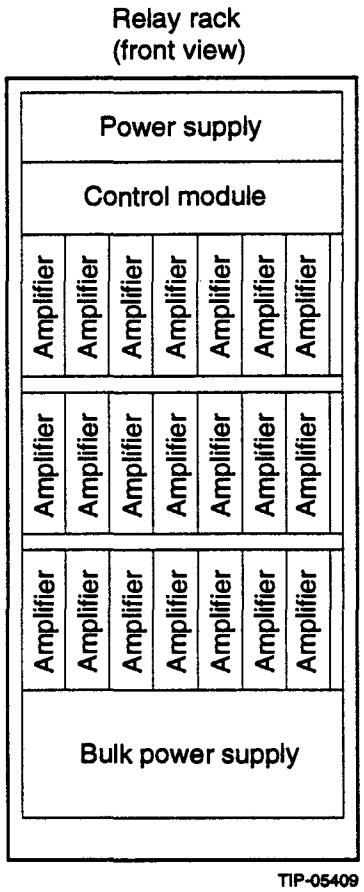

Figure 3.90: Typical LEB corrector power supply rack assembly.

Control inputs to the BPS are on/off/reset, along with the safety interlocks mentioned previously. Status outputs consist of current and voltage monitors and all interlock and power supply protection information. All status lines are latched and require fault clearing and a reset command before operation can resume. Line voltage is specified as 480 VAC, ±10 %, but lower voltage options can be considered by the vendor if justified.

Controls Figure 3.93 depicts the functional control diagram at the power supply end. An identical control channel exists for each amplifier and BPS in

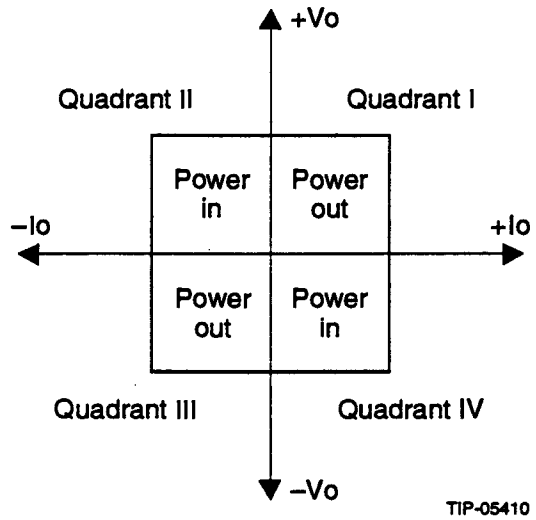

Figure 3.91: Output $V - I$ graph for 4 quadrant power supply operation.

the control module. Pairs of control channels are on individual cards within the control module allowing for easy repair or replacement.

A pair of fiber optic cables from the controls crate waveform generator is connected to the optical transceiver and signals are converted to or from serial digital electrical levels. Following conversion to parallel format, the data and instruction are decoded by the timing generator/logic controller and routed to the appropriate registers. A 16 bit digital to analog converter forms the reference signal to the amplifier. On/off/reset control lines are buffered and sent to the amplifier also. Update rates for the DAC can be as high as 10 kHz. Outputs from the amplifier are buffered, and in the case of analog information, routed through a multiplexer and analog to digital converter under the control of the timing/logic controller. Analog conversion is performed on every DAC update or under direct command from the waveform generator. Digital status information is also returned with each DAC update or on demand. Information is returned to the control system asynchronously with respect to the received data but the waveform

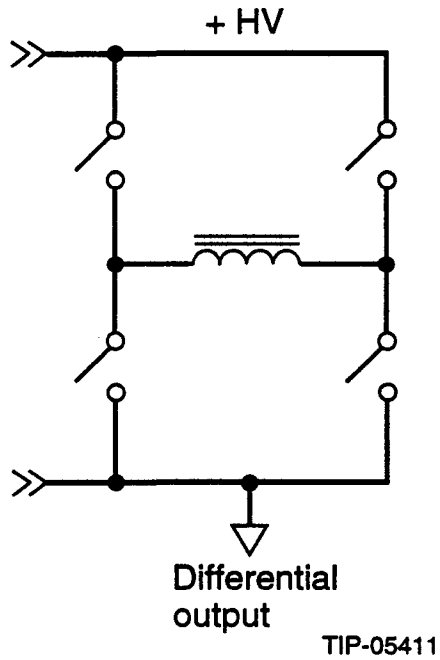

Figure 3.92: Simplified load/switch arrangement.

generator card keeps track of transactions for time-out purposes. All transactions are to be completed in less than 100 μs. Time stamping of the analog and digital information is performed by the waveform generator card as well as supervisory status monitoring for alarms and limit purposes. The waveform generator card filters data and only returns information upward through the control system on demand.

Installation Rack assemblies ready for installation are to be delivered by the vendor. If not already installed by the vendor, the control modules would be installed at the SSCL. Ac input power, load and control cable installation are to follow. System integration and pre-operational testing could then be completed. Power and cable installation are to be completed by the installation contractor. Integration and pre-operational testing is to be performed by SSCL personnel. Cable choice is a compromise between cable costs and voltage drop within the cable. Larger cross-section cable would reduce the losses but cost more. It has also been decided to install electrostatically shielded cable to reduce possible EMI problems related to

Table 3.20: Bulk power supply characteristics.

	Type 1	Type 2	Type 3	Type 4	Units
Output Voltage	70	130	190	130	V
Power, rms, max.	8,000	5,000	15,000	8,000	W
Regulation	±1.0	±1.0	±1.0	±1.0	% p.s.
Maximum Loading	20	20	7	20	Number of amplifiers
Quantity	90	72 + 4 skew	18	48	12

high frequency signal components on the amplifier output from the switching devices. Use of a composite, multiconductor cable, containing not only the power conductors but also the magnet temperature interlock conductors, was being considered as a cost saving since it reduces installation expense.

Design Status All system-level design for the corrector supplies has been completed prior to the initiation of equipment purchase. Procurement specifications and all necessary documentation for bid solicitation has been completed for the power amplifiers, bulk power supplies and the rack assembly. Prototype magnets have been measured and documented. The control module electronics have been designed and a prototype constructed. The communications and logic control portion has been tested. The analog and digital interface to the power equipment has been designed but was not completely tested at the time of the project termination. No equipment was purchased and no vendor responses on the specifications have been obtained.

Acknowledgments

Work summarized here was performed by the members of the Corrector Power Supply Group of the Accelerator System Division's Electrical Engineering Department at the SSCL. The author wishes to thank F. Meyer, S. Heitz, R. Rocamontes, D. Heber, M. Wezensky and D. Sherman for their contributions. J. Payne, of the Beamline Power Supply Group in the ASD/EE Department, and S. Sarkar of the ASD Controls Department contributed to the design of the power supply controls interface and the control module.

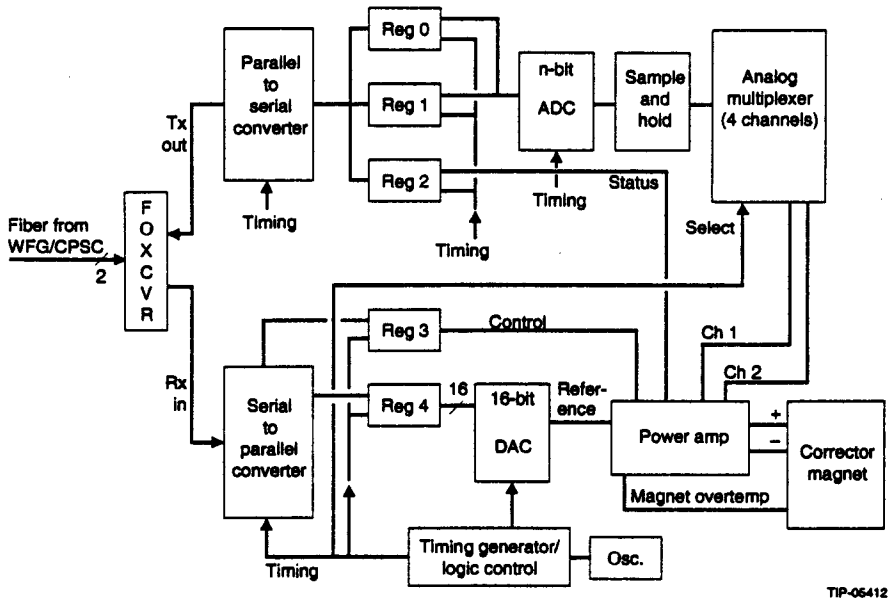

Figure 3.93: LEB corrector P.S. controls.

3.2.3 Injection Power Systems (W. Merz)

Overview

Functions and Quantities The orbit bump magnets in the LEB injection system (Section 2.4.1) are powered in series by a common power supply. A trapezoidal pulse with a max. flattop of 40 μs and a fall time of $\approx$ 11 μs provides the required time dependence of the orbit bump.

The injection septum will be operated in a pulsed mode as well, for reduction of the average power dissipated in the septum current sheet. Only the flattop time is specified (40 μs) and a half-sinewave pulse of 1.5 μs width at base will fulfill the requirement.

Table 3.21 numerates the power supply requirements and load design values. The power supply and magnet design requirements are defined for injection at 1 GeV in anticipation of a Linac upgrade. Nominal operation at commissioning was to be at 600 MeV.

Acquisition and Status Initially, a collaborative effort has been launched with BINP, Novosibirsk under the Interlaboratory Agreement. However, it

Table 3.21: LEB injection power supply parameters.

Item	Septum PS	Bump PS	Units
Quantity	1	1	
I_{max}	12	22.0	kA
I_{out} @ 1 GeV	9.8	20.6	kA
I_{out} @ 600 MeV	7.0	14.8	kA
Flattop Duration, min.	40	40	μs
Output Waveform	Half Sinewave	Trapezoidal	
Total Output Deviation			
Collider Fill	$\pm$0.04 % for 10 μs	$\pm$0.1 % for 10 μs	of I_{max}
Test Beam	$\pm$0.1 % for 40 μs	$\pm$0.2 % for 40 μs	of I_{max}
Rise Time	N/A	N/A	μs
Fall Time, max.	N/A	10.8 (to 87 % of I_{out})	μs
Pulse Length, max.	1500	150	μs
Number of Magnets	1	4	
Magnet Inductance	5	1.3	μH
Magnet Resistance	1	0.1	mΩ
Pulse Repetition Rate, max.	10	10	Hz

has later been decided to design, build and test both the septum and the bump magnet power supply at the SSCL. The magnets have been designed in-house and fabrication of prototypes has been contracted with outside vendors.

The power supply design has only advanced to the early stages of preliminary concepts. Some circuit simulations of design options are completed. The circuit simulations confirm that the chosen design approach can be reasonably expected to meet the design and performance requirements. The detailed requirements are contained in the Linac transfer line Level 3 specification[81] and the power supply Level 4 Technical Requirements[82] documents. No detailed design work has been done.

Requirements

Output Waveforms The septum power supply is not constrained by either rise-time or fall-time requirements; only the output current "flattop" total output deviation (TOD) is critical in defining the waveform. The flat-

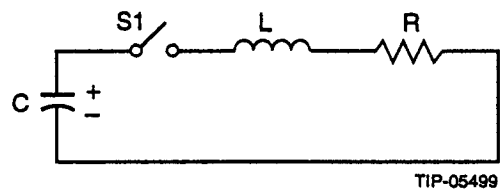

Figure 3.94: Septum power supply RLC circuit.

top duration and TOD requirement can be met by a 1.5 ms half-sinewave current waveform as obtained in a heavily underdamped series RLC resonant circuit like the one shown schematically in Figure 3.94. In this case, L is the magnet and cable inductance and R is the magnet and cable resistance. The charged capacitor is used as an energy storage device. Operation of the switch causes the capacitor energy to be discharged into the magnet. The resonant nature of the circuit provides the pulse duration and the current waveform. The components to implement this circuit are relatively simple and identical approaches have been used at many laboratories. A diode or unidirectional switch is used to terminate the output current pulse after one half period of oscillation. Amplitude control is achieved by adjusting the capacitor voltage. The pulse repetition rate is 10 Hz, the LEB cycling rate. Figure 3.95 shows a graphical representation of the septum power supply output current pulse.

The fall time requirement for the bump power supply coupled with a flattop duration similar to the septum requirement necessitate the use of a different circuit configuration to develop a trapezoidal waveform. Figure 3.96 shows the current waveform for the bump power supply. A lumped element pulse forming network (PFN) is used to develop the waveform, shown in Figure 3.97. The fall time requirement calls for a current decay to 87 % of the nominal flattop value within 10.8 μs after the end of the beam pulse. The rise time is not specified.

Total Output Deviation, TOD The TOD is defined as an envelope of error in the output current due to any error source. This includes output variations due to line or load changes with respect to time, current ripple, pulse to pulse repeatability or other sources. TOD is specified as a plus and minus percentage of the nominal full scale current. Figure 3.98 identifies the TOD measurement and the fall time duration for the Bump power supply

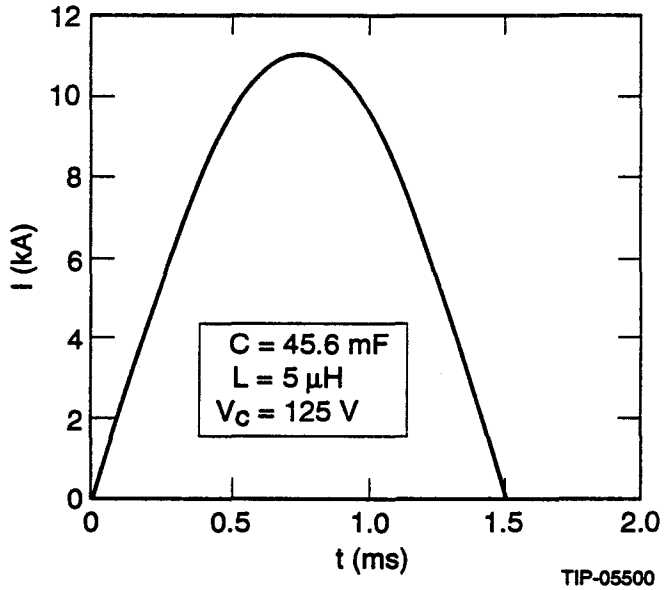

Figure 3.95: Septum power supply output current simulation.

output current. Table 3.21 lists the TOD values. The two values shown correspond to Collider fill operation and to test beam delivery, respectively.

Design

Septum Power Supply The resonant *RLC* circuit has been described above. An energy recovery system utilizing either the load or a recovery reactor and another switch has been planned in order to reduce the charging power supply requirements. This is possible since, after the half-cycle discharge, the capacitor is charged to nearly its initial voltage but with a reversed polarity. The power supply is to be located in the S1 service building in close proximity to the load in the tunnel. Locating the supply close to the load reduces the high-current busing and, thus, losses to a practical minimum. Multiple parallel RG220 coaxial cables are planned for connection as the supply to a cable termination box at the magnet. The high-current switches are going to be assembled using multiple, parallel SCR. If required, a feed-forward technique will be used using the sampled current pulse to correct for pulse-to-pulse variations by adjusting the capacitor voltage on following cycles.

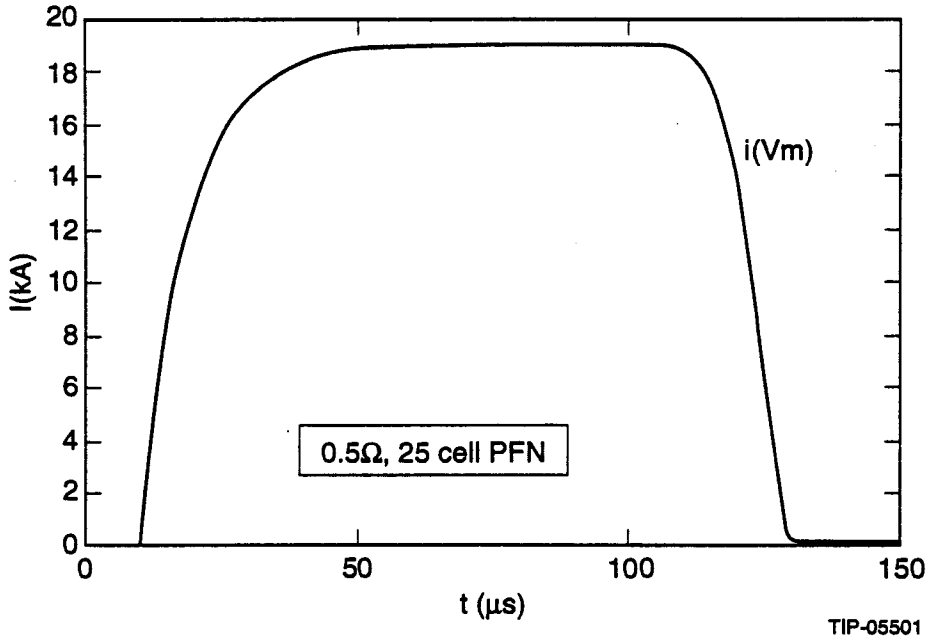

Figure 3.96: Bump power supply output current simulation.

Bump Power Supply Several options have been considered for implementing the bump supply[83] before settling on an approach similar to that chosen for the Fermilab Booster injection power supplies.[84] A 23-25 cell PFN with 0.5 Ω impedance operating at approximately 10 kV is able to meet the flattop and TOD requirements. The PFN impedance is mismatched to the load in order to minimize the voltage necessary. There is however a tradeoff involving the fall time of the circuit in this choice. As the cell inductance in the PFN approaches the load inductance, the circuit response approaches a square wave current output, reducing the fall time. The increased cell inductance, however, drives the impedance higher, and thus the voltage needed to achieve the required current goes up. The simulations confirm that a compromise between voltage, fall time response, flattop duration and TOD can be met with cell inductance of 1 μH and cell capacitances of 4 μF. The simulations also take into account the parasitic inductances and capacitances of all circuit elements. It is necessary, however, to include tunable cell inductors in order to compensate for the uncertainty in the parasitics and the expected tolerances on the circuit devices.

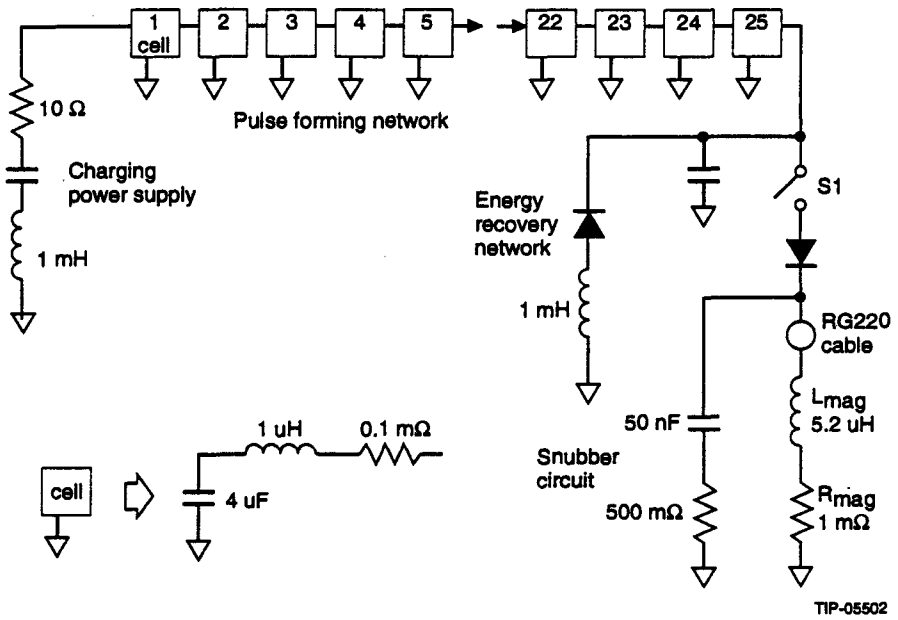

Figure 3.97: LEB bump power supply circuit model.

A charge recovery system is planned for the supply similar to that used on the septum and for the same reasons. The circuit model shown in Figure 3.97 does not show all the elements used generating the simulation shown in Figure 3.96. Reference 3 contains the complete SPICE deck listing for the simulation model. The charging system had not been defined at the time of project cancellation. Under consideration have been resistive, resonant and current controlled systems. The supply is to be located in the S1 service building. Power distribution to the load is to be similar to the configuration for the septum. Interconnection of the series magnets are to be via a stripline-type transmission line. A cable-termination box in the tunnel accommodates the transition from the RG220 cable from the supply to the first magnet in the string of four. The output current switch and regulation scheme are to be similar to the one used in the septum power supply.

Other Options The Russian collaborators from BINP have proposed two other circuit options for use in both the septum and bump power supplies.[85] One option is to use a variation on the resonant approach for both supplies. By combination of a base resonant frequency and several higher harmonics of

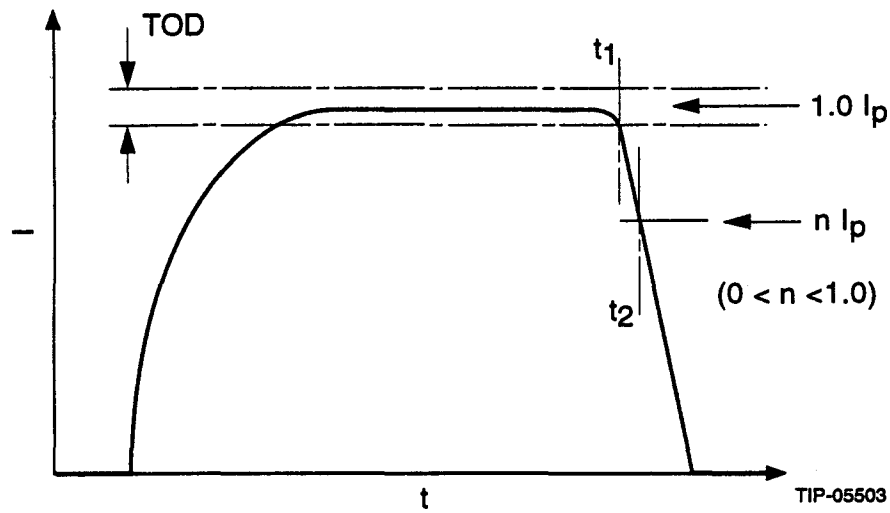

Figure 3.98: Bump output current TOD definition (drawing not to scale).

the base frequency. The base frequency sets the pulse width. The addition of the higher harmonics, with varying amplitudes and timing, defines the pulse shape to meet the fall time and TOD requirements. The second option is to use the resonant approach to set the pulse duration and then add an active circuit network to clip the top of the half-sinewave response to regulate amplitude, TOD and fall time. Both options have been abandoned due to the added complexity for the power circuit and controls.

Acknowledgments

The work summarized here has been performed by the members of the Beamline and Corrector Power Supply Group of the Electrical Engineering Department of the Accelerator Systems Division at the SSC Laboratory. The author wishes to thank F. Meyer for performing the simulations and the majority of the design work. Also deserving thanks are M. Wezensky and D. Sherman for their efforts on developing prototype switch electronics. Many fruitful ideas were obtained from discussions with the members of our BINP collaborators and from their colleagues in Novosibirsk. The incomplete list of BINP personnel consists of A. Chernyakin, N. Dikansky, V. Kiselev, V. Kuper, V. Marusov, A. Medvedko, S. Petrov, E. Trachtenberg, and many others.

3.3 LEB Rf System

(P.D. Coleman, J. Ferrell)

3.3.1 Overview

System Requirements

The LEB rf system is required to provide the voltage and phase program given in Section 2.2. This program facilitates acceleration of the beam from 1.219 GeV/c at injection to 12 GeV/c at extraction. The program requires a maximum peak circumferential voltage of 765 kV and frequency change from 47.51 MHz to 59.78 MHz. Table 3.22 lists the basic LEB rf system requirements.

Table 3.22: LEB rf parameters.

Maximum Voltage	765 kV
Minimum Voltage	25 kV
Injection Voltage	25 kV
Extraction Voltage	80 kV
Frequency Range	47.513 MHz–59.776 MHz
Ramp/Reset Time	50 ms
Maximum Tuning Rate	1.1 GHz/s
Synchronous Phase (Max.)	61.25°
Collider Mode Beam Current (Max.)	100 mA
Test Mode Beam Current (Max.)	500 mA
Rf Power Required for Beam	330 kW maximum
Available Slot Length	25 m

The program calls for a ramp up in 50 ms which repeats every 100 ms (10 Hz) with a resulting duty factor of 50 %. However, since the one-hour duty factor of the LEB during collider-fill operations is only 1.1 % (see Section 1.0.2), a 30 % macro duty factor has been adopted for the rf system. This results in a lower average power handling requirement of approximately 10 % while leaving ample margin to support interleaved beam development cycles and continuous test beam operation.

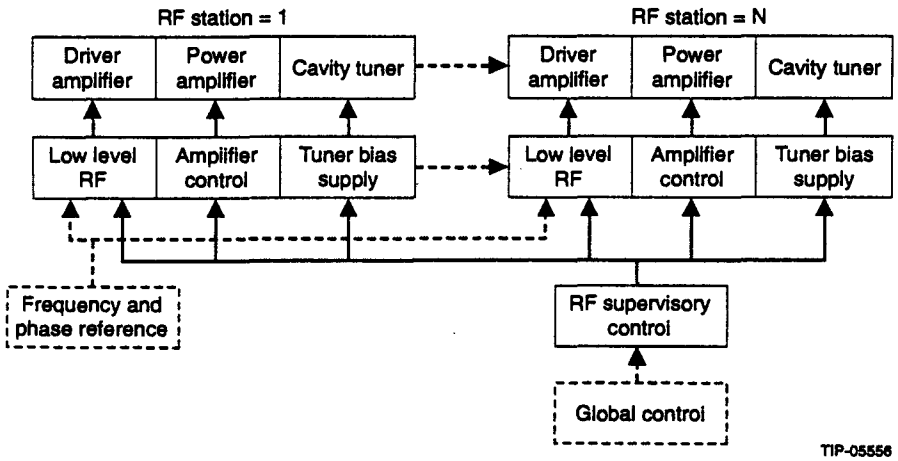

Figure 3.99: LEB rf system block diagram.

System Description

The rf system provides the accelerating voltage using a number of accelerating cavities each driven by a separate power amplifier. The exact number of accelerating cavities will be determined following tests of a prototype cavity. The design goal, driven by cost and impedance considerations, is to provide the voltage using eight cavities for normal operation with sufficient margin to allow operation of the system with six cavities in the event of a failure. Figure 3.99 is a simplified diagram of the rf system. In order to achieve maximum flexibility the rf system is divided into rf stations which are essentially autonomous except for common supervisory controls and frequency and phase reference. This approach allows for operation of each station at its optimum performance.

Rf Station Description

Each accelerator rf station consists of the accelerating cavity, ferrite tuner and associated bias supply, power amplifier and associated power supplies, driver amplifier, low-level rf system and rf supervisory control and monitoring. Figure 3.100 is a block diagram of a rf station. Each station may be operated independently of the supervisory control system for maintenance purposes. All equipment is located in surface buildings except for the cavity and power amplifier.

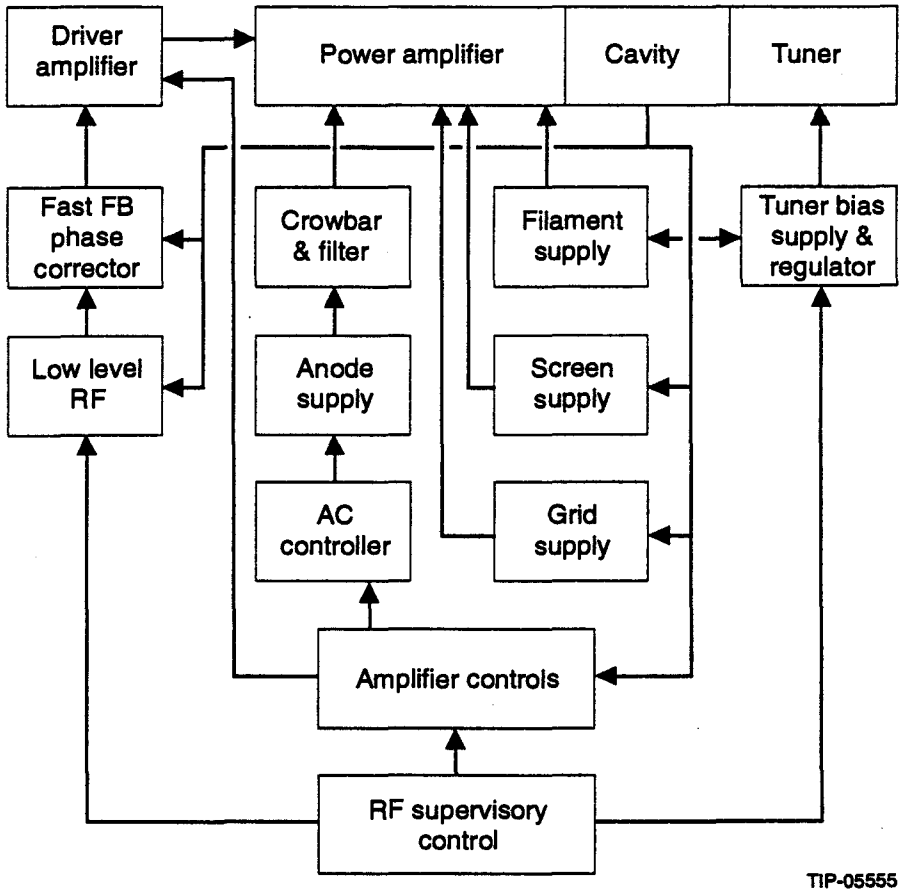

Figure 3.100: Rf station block diagram.

3.3.2 Rf Cavities

Two different cavity designs have been considered for use in the LEB ring: the FNAL booster cavity[86] and the LANL $\lambda/4$ cavity.[87] The FNAL design is a two-gap cavity operated at 30 kV gap voltage and tuned with parallel-biased (bias field parallel to rf magnetic field) NiZn ferrite tuners over a 30 MHz to 53 MHz frequency range. The LANL design is a single-gap cavity and uses lower loss perpendicularly biased (bias field perpendicular to rf magnetic field) yttrium-garnet microwave ferrite in its tuner. The microwave ferrite is advantageous due to its low loss characteristics when perpendicularly biased, and due to its low saturation magnetization and

high electric Q as compared to the NiZn ferrite. The LANL cavity design has been chosen primarily for its potential as a higher accelerating gradient cavity.

Cavity Description

The cavity approach chosen is a $\lambda/4$ coaxial design with the inductive portion of the cavity being a ferrite loaded tuner (cavity $R/Q \cong 37\ \Omega$). To be able to run with as few as 6 cavities each cavity has to be able to operate at a peak voltage of 127.5 kV. This high voltage operation, along with the wide tuning requirement, results in high stored energy and the potential for increased rf losses in the ferrite. Perpendicular magnetic biasing of the ferrite is used to help minimize these losses.[88,6,89]

Figure 3.101 shows a diagram of the cavity. The tetrode amplifier (150 kW) is capacitively coupled into the cavity. The applied magnetic field, provided by the magnet yoke, biases the ferrite to different permeabilities (μ) and hence tunes the cavity. Not shown in the figure is a higher order longitudinal mode (HOM) damper that mounts on the gap end of the cavity. The mode damper is a broadband Smythe-type damper[90,34] and has been analyzed and designed but not constructed. Figure 3.102 shows the calculated performance of the mode damper. The HOM damper is required since use of the low-loss microwave ferrite in the tuner can result in insufficient damping of HOM.

Tuner Concepts

Different ferrite cooling options (conduction, direct liquid, forced air and water-cooled ferrite carrier) have been considered. In the early stage of the project, the conduction and direct liquid-cooled approaches were considered most likely to achieve the high gradient desired, and prototype tuners have been constructed utilizing these cooling methods. The ferrite carrier approach has been analyzed later and substantial design work done but no prototype has been constructed.

Conduction-cooled Tuner The conduction-cooled tuner has been built at the Budker Institute of Nuclear Physics (BINP) and tested at SSCL.[91] It uses BeO discs sandwiched between toroidal ferrite rings to conduct heat from the ferrite rings to a water-cooled copper jacket (see Figure 3.103). BeO

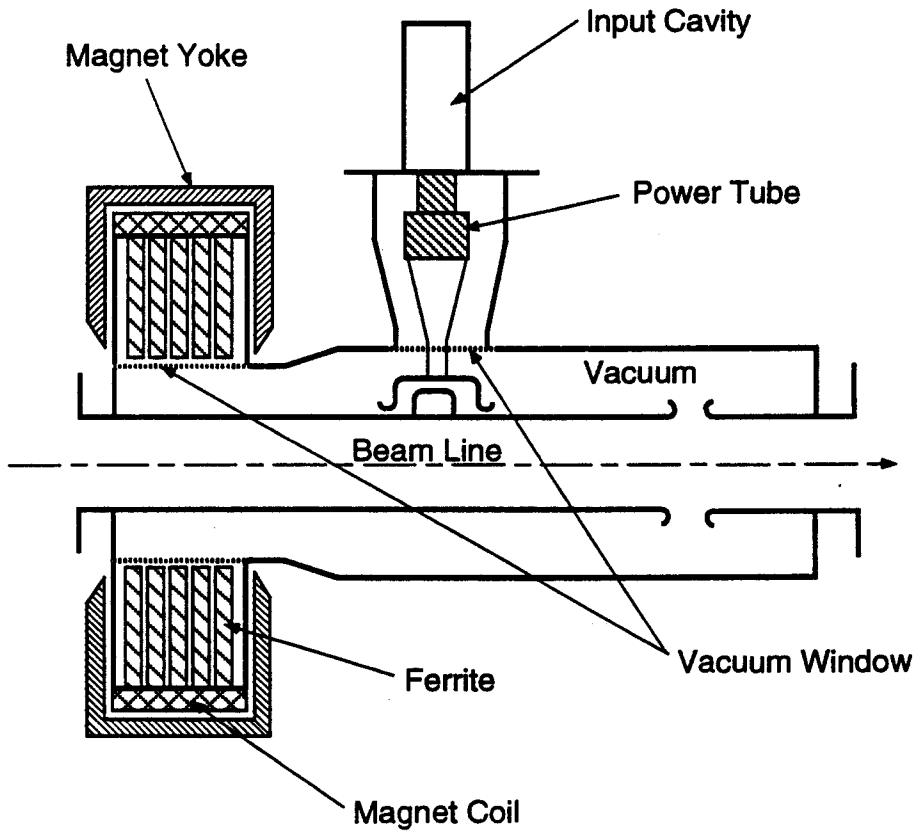

Figure 3.101: LEB cavity diagram.

is chosen because of its high thermal conductivity. The tuner is designed to mate with the same cavity as the directly cooled tuner.

New developments have made the ferrite-carrier approach more attractive and towards the end of the project substantial design work has been done but no prototype constructed.

A thin layer of flexible silicon component known as Elastoseal is used between the ferrite and BeO rings. The ferrite stack is then potted into the tuner housing. The potting is accomplished under vacuum to minimize the possibility of air voids in the glue. The glue serves the purpose of filling air voids as well as providing a flexible layer between the ferrite, BeO and copper. The presence of this layer relieves the mechanical stresses which would occur due to the different thermal expansion coefficients of the materials.

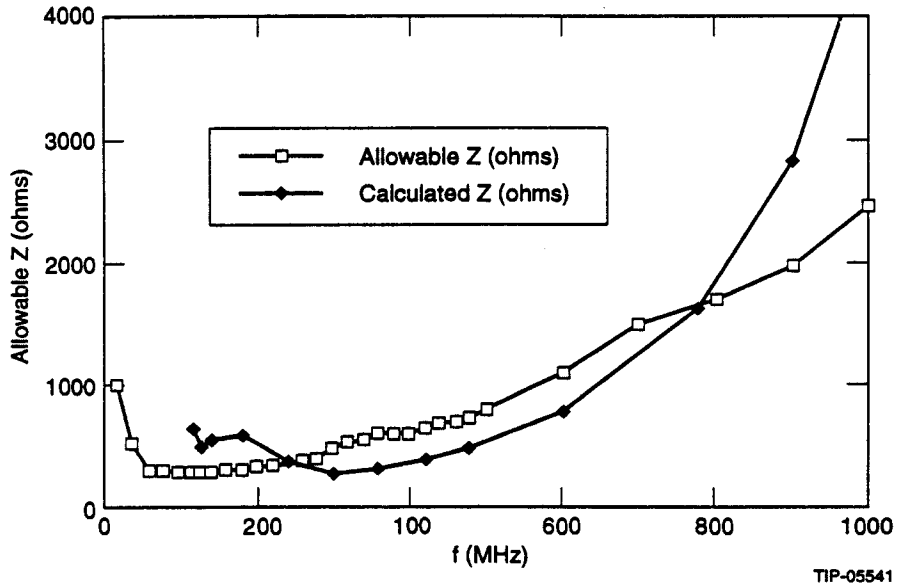

Figure 3.102: Calculated mode damper performance.

Operation at the expected gap voltages and losses could not be achieved without the flexible glue layer. Temperature rise in the ferrite is calculated to be $\sim 25°C$. The Curie temperature of the ferrite is 120°C.

The tuner housing is made of 3-mm thick copper. The housing is fabricated in two sections which are bolted together with the ferrite and BeO inside and then potted. Disassembly is very difficult once the unit is potted. Twenty-four radial slots in the housing reduce eddy currents and promote quick penetration of the bias fields. Stainless steel ribs are brazed to the slotted sections to restore mechanical integrity. The magnet design has been chosen to optimize the ferrite permeability (minimize losses) over the operating frequency range while limiting the maximum coil current to a reasonable value. The ferrite chosen has a saturatization magnetization of 520 Gauss. The permeability varies from 1.4 (59.8 MHz) to 3.27 (47.5 MHz) to provide the impedance required to resonate the cavity. The maximum electric fields in the tuner occur at ~ 53 MHz and are 5.3 kV/cm in air, 3.1 kV/cm in the ferrite and 5.5 kV/cm in the BeO.

Directly Cooled Tuner In the directly cooled tuner design, the toroidal rings of ferrite are separated by 5-mm spacers to allow flow of a cooling fluid

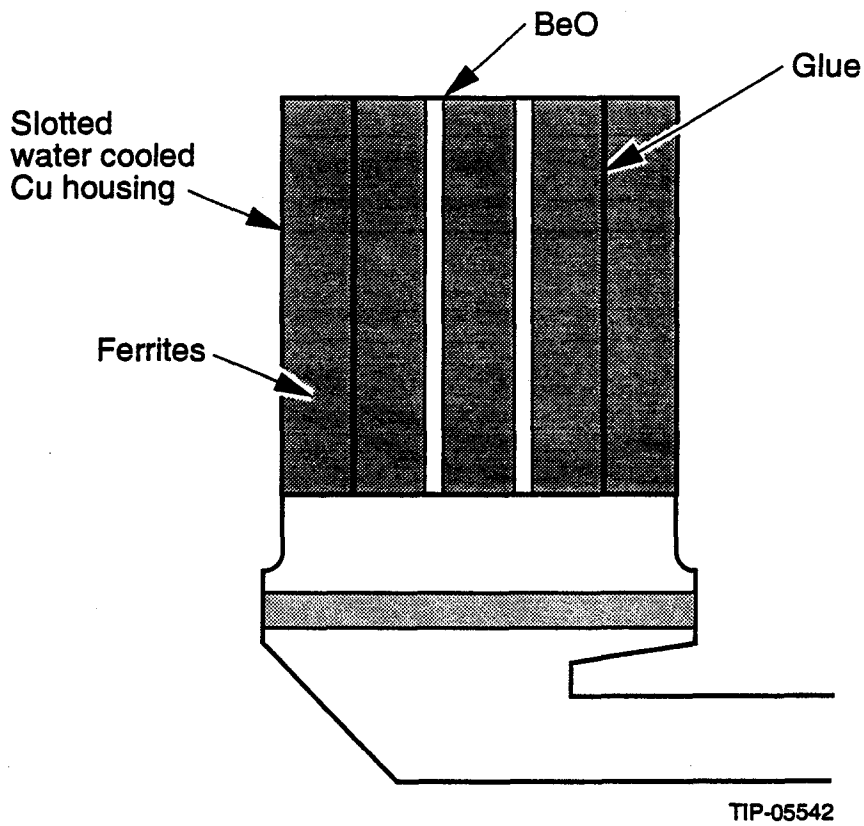

Figure 3.103: Conduction-cooled tuner geometry.

directly over the ferrite surfaces (see Figure 3.104). The liquid is pumped into the bottom of the tuner housing and out at the top allowing the fluid to flow in the same direction as that of natural convection.

Two fluids have been investigated: Fluorinert (FC77), and water (H_2O). Use of the dielectric FC77 has the advantages of high dielectric strength, low rf loss and an inert chemical nature. The disadvantage is that under high temperatures ($> 200°C$) such as might be experienced with an arc, this fluid can produce toxic compounds which could represent an environmental and personnel safety concern.

The use of water as the coolant has the advantages of extremely good heat transfer and it is inherently non-toxic. Water has its disadvantages as well. If a copper tuner shell is used, free oxygen in the water will oxidize the

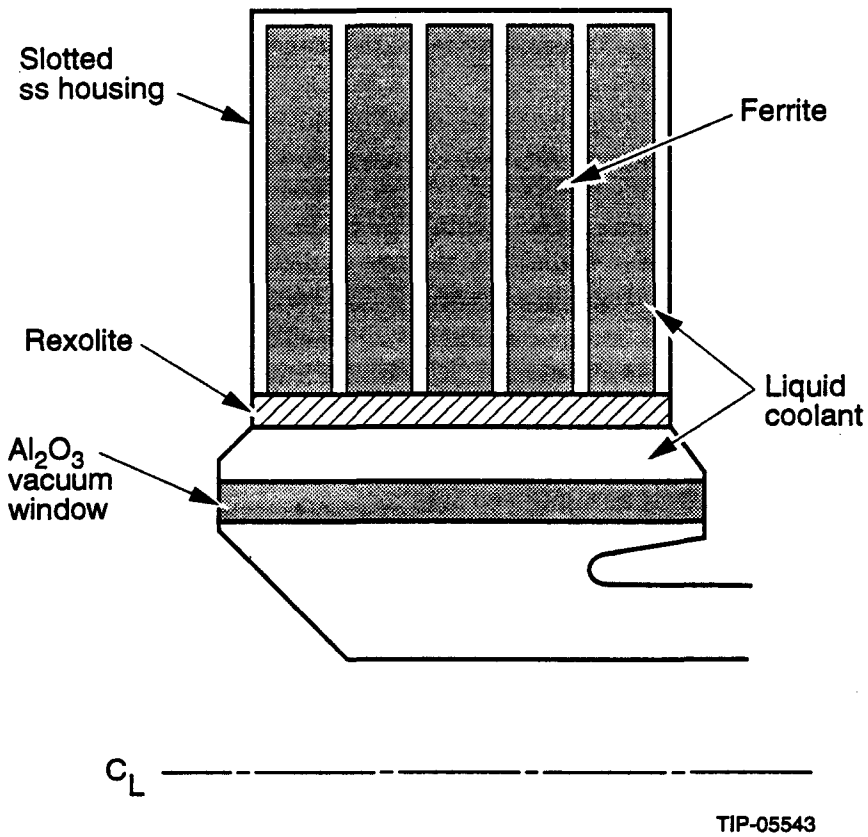

Figure 3.104: Liquid-cooled tuner geometry.

copper surfaces. This oxidation can result in reduced thermal conductivity and it may eventually have an affect on the cavity Q. Another disadvantage is that water has relatively high rf losses.[92] To reduce these losses, special efforts are made to prevent large volumes of water from being exposed to high electric fields.

Bare stainless steel 304 (as opposed to copper plated stainless) is used for the shell material for two reasons. First, its lower conductivity (a factor of 100 below copper at these rf frequencies[93] results in a lower Q cavity. Accurate control (tuning, rf amplitude and phase) is one of the toughest challenges for this rapid-cycling rf system; lowering the Q makes control of the cavity easier. The price paid is increased amplifier power and a higher heat load to the cooling system. The second reason for choosing stainless is

to avoid the copper oxidation problem described earlier when water is used as the coolant fluid. Copper plating of the tuner housing is possible if it turned out to be necessary.

One of the most important regions in the cavity design is around the tuner window. The tuner has been designed to allow testing of both FC77 and water with minimal changes to the hardware. Figure 3.104 shows the tuner geometry while operating with FC77. An alumina window serves as the vacuum barrier and Rexolite is used as a mechanical spacer at the inner radius of the ferrite rings, to prevent a large volume of water in the region between the ferrite inner radius and the vacuum window (undesirable due to the high rf losses in water).

Once the slots have been cut in the tuner shell, it is necessary to find some way to contain the coolant fluid yet not inhibit the bias flux penetration. Figure 3.105 shows the cover that is used. For this purpose, a nonconducting composite material (similar to G-10) is epoxied to the outside of both halves of the stainless shell as shown in Figure 3.105. The shell is designed in such a way as to allow disassembly and reassembly of the tuner. The composite cover also aids in restoring some of the shell strength that was lost by slotting.

Water-cooled Ferrite-carrier Tuner This design, proposed by ANT Telecommunications Inc., incorporates thin ($\approx$ 1-cm thick) tiles of ferrite glued to copper-plated stainless steel cooling plates using a radiation resistant epoxy. Water cooling channels are inside the plates. The cooling plates constitute 16 pie-shaped segments arranged in a disk. They are electrically isolated from each other to suppress eddy currents. Five of these disks are arranged in parallel with high pressure rf contacts between the plates at the outer radius. The end walls are slotted copper plated stainless steel. The glue is carefully chosen to allow for thermal expansion compensation while maintaining good thermal conductivity between the ferrite and the water-cooled carrier. Air gaps between the ferrite surfaces reduce the electric field in the ferrites and hence reduce the electric losses. Figure 3.106 shows the geometry. For a prototype tuner design a limited tuning range has been accepted to be able to use the existing magnet and bias coil of the directly cooled tuner.

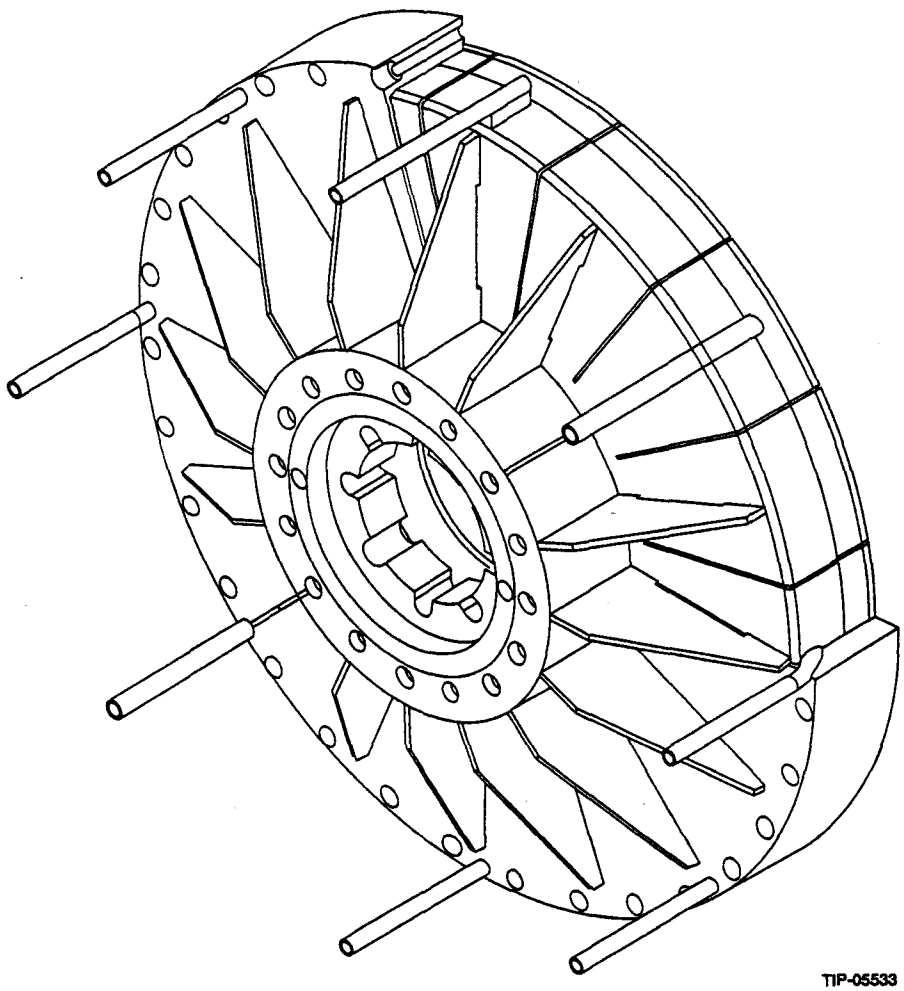

Figure 3.105: Liquid containment approach for liquid tuner.

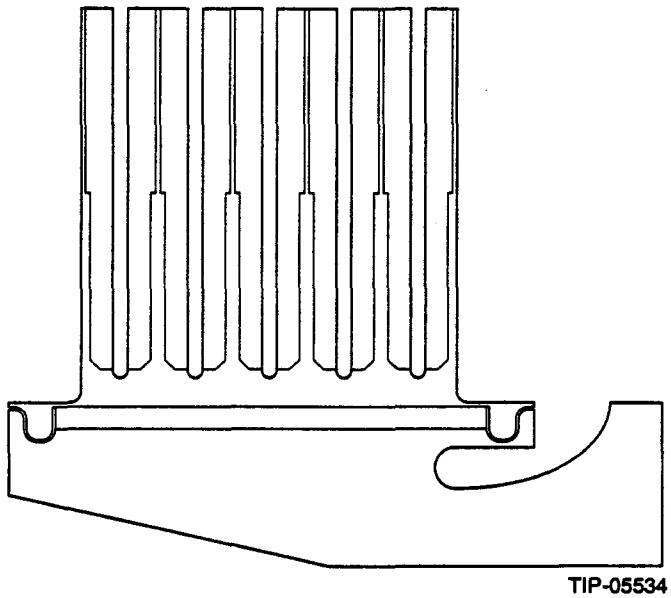

Figure 3.106: Water-cooled ferrite carrier tuner geometry.

Several calculations have been performed to predict the performance of the tuner. Table 3.23 summarizes the results obtained. The design looks very promising, however, termination prevented completion of the prototype design.

Test Results

A prototype cavity and power amplifier have been built which accommodate mounting of both the conduction-cooled and liquid-cooled tuners. A common vacuum window is used. Since the ferrite characteristics are different for the two tuner designs, each tuner uses its own unique biasing magnet.

Conduction-cooled Tuner Test Results

Tuning range

Figure 3.107 shows the cavity's resonant frequency as a function of the applied bias current. As the bias field is increased, the ferrite's μ decreases resulting in a higher resonant frequency. These measurements have been performed at dc bias currents. The frequency range of the cavity with this tuner is more than sufficient.

Table 3.23: Water-cooled ferrite carrier tuner expected performance.

Parameter	Value
tuning range $3.8 > \mu > 1.4$	11 MHz
Maximum electric field in tuner	14.1 kV/cm
tuner bandwidth	> 400 Hz
temperature rise across ferrite	2.5 °C

Cavity Q

The cavity Q has been measured at several resonant frequencies using a network analyzer and verified by ring-down tests during high-power tests. As the bias field is increased (higher resonant frequency), the ferrite has lower magnetic losses, and the Q rises. However, the calculated Q is approximately two times higher than observed. Calorimetry measurements indicate the unexpected losses are located in the tuner.

Temperature effects on tuning

As the ferrite temperature rises, its saturation magnetization M_s falls. This causes a decrease in μ and hence an increase in the cavity's resonant frequency.[94] This effect has been characterized by raising the tuner housing temperature by externally heating the tuner's cooling water. The change in resonant frequency is monitored as the tuner, and hence the ferrite's, temperature is changed. A temperature dependence of $\sim$ 100 kHz/°C has been observed.

Tuner response

The tuner is required to sweep the cavity through the appropriate frequency program during the 50 ms LEB ramp. As the time rate of change in the bias current increases, eddy currents in the magnet yoke and tuner housing will limit the rate of change in resonant frequency.

In order to characterize this effect, the bias power supply is adjusted to a dc level of 281 A (48.6 MHz) and a small amplitude modulation imposed. The resultant frequency swing is then measured as a function of ripple amplitude and frequency. Figure 3.108 shows the tuner response as a function of modulating frequency with the magnitude of the ripple held constant.

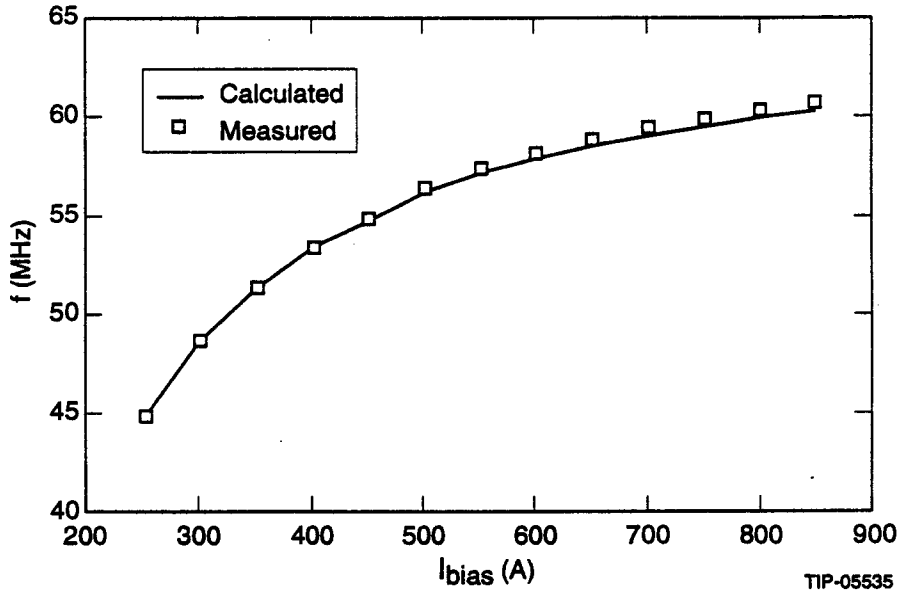

Figure 3.107: Cavity tuning range (conduction-cooled).

The response is seen to roll off by 3 dB at $\sim$ 30 Hz. However the drop in response is relatively slow (-4.5 dB/decade), which indicates that the tuner should have a significant amount of response even at 1 kHz.

High power operation

A variety of tests have been performed to thermally characterize the cavity.[94] The tests have been accomplished with dc bias on the tuner and constant-rf-amplitude pulses. The duty factor of the rf pulses is varied to change the average power level. The average power dissipated in the tuner is measured calorimetrically from the water temperature rise. This measured power includes not only ferrite losses, but also losses in the tuner-housing walls, BeO and Elastoseal.

The dependence of the power dissipated in the tuner has been characterized as a function of voltage and frequency. As expected, the power scales as the square of the gap voltage. It has also been found that, for a given gap voltage, about 1.8 times the power was dissipated at 47 MHz than at 60 MHz. This is a result of a higher percentage of the total cavity energy being stored in the tuner at low frequencies, and the ferrite being more lossy at

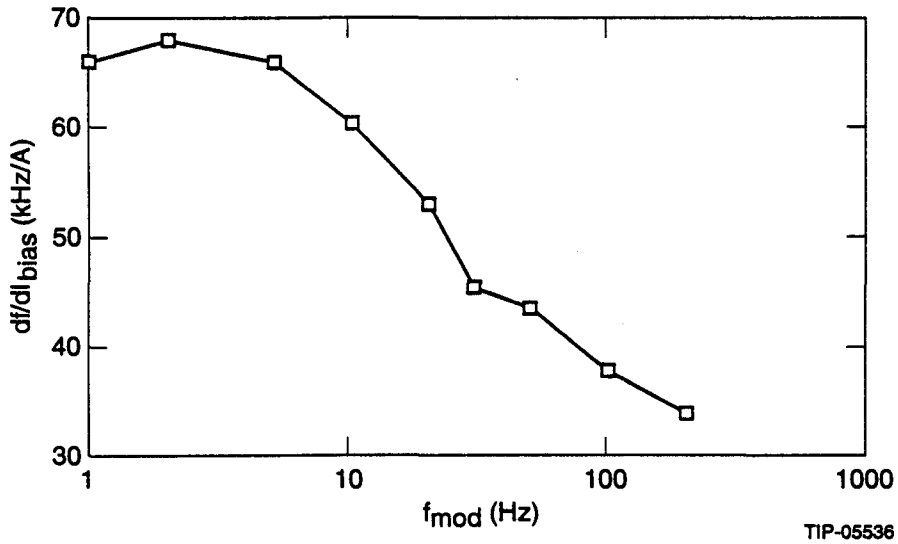

Figure 3.108: Conduction-cooled tuner frequency response.

low bias. The maximum ferrite temperature reached is 80 °C. As expected, the ferrite temperature scales linearly with power dissipated.

In addition to monitoring the tuner temperature rise, numerous other points on the cavity have been monitored to see if any hot spots existed. The only area which has exhibited excessive temperature rise is the flange where the power amplifier connects to the cavity. This flange has been modified to add water cooling.

Tuner performance limits

During the course of testing the cavity with the conduction-cooled tuner, it has been operated over a wide range of voltages and powers. Figure 3.109 shows the various cavity operating points in terms of gap voltage vs. tuner power. The cavity has been operated above 100 kV, but only for short times and at low duty factor. Most high-voltage data has been collected at 80 kV and moderate power (1.7 kW dissipation).

The tuner has failed when operating at 80 kV and higher power dissipation than it has achieved before (2.7 kW data point labeled 3/22/93). Therefore, it has been asked to operate at high voltage and high thermal stress simultaneously in this test. The 80 kV gap voltage corresponds to $\approx$ 30 kV across the tuner at the 58 MHz operating frequency. The ferrite

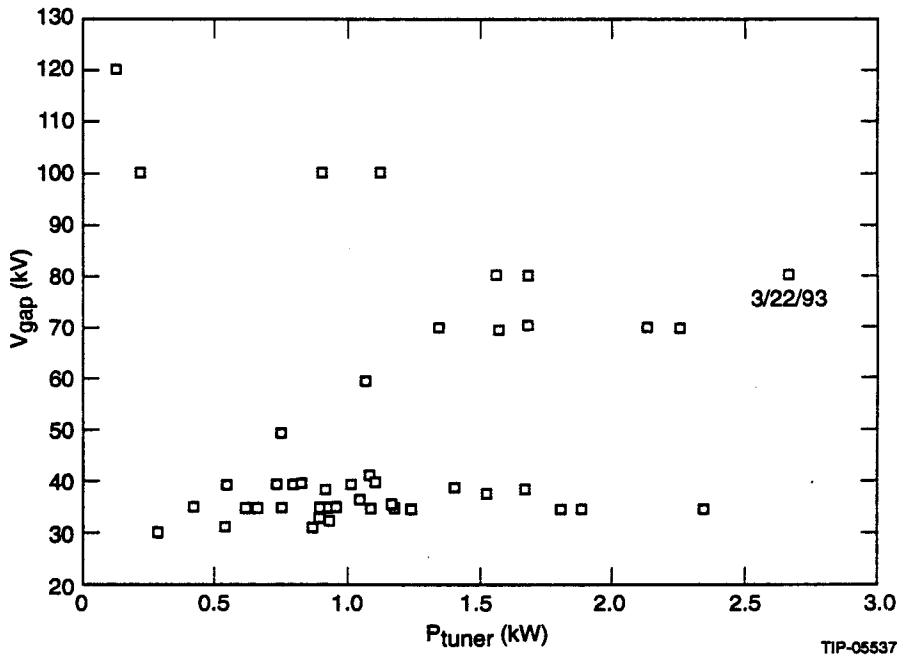

Figure 3.109: Conduction-cooled cavity operating space.

temperature is estimated to have reached 80 °C (30 °C wall temperature). After ≈ 10 minutes operation at this level, the voltage began collapsing ≈ 10 ms into the pulse. Disassembly and inspection of the tuner has revealed that the fault is limited to a localized area in one of the outer ferrite rings at the ferrite/glue/wall interface at the inner ferrite radius. The deposition of power into a small volume has resulted in very high temperatures, melting some ferrite and causing significant cracking due to the high thermal stresses.

The inspection has also revealed an area, away from the damage location, where a small air gap exists between the ferrite and copper wall at the inner radius of the ferrite. It is postulated that such an air gap has existed also at the location of the damage. At this operating voltage, the fields in such a gap are calculated to be 20–25 kV/cm. This could have resulted in the onset of corona and localized heating of ferrite. After some period of time the localized heating would thermally induce a crack in the ferrite which then leads to intense localized heating and catastrophic failure of the ferrite.

Summary

The prototype cavity has been assembled with a conduction-cooled tuner and tested. The tuning range achieved is more than adequate to cover the LEB requirements. The high frequency tuner response starts to roll off at $\sim$ 30 Hz, however the 4.5 dB/decade roll off extrapolates to a significant response at 1 kHz.

The overall cavity Q is lower than expected with the extra losses being located in the tuner. The source of these losses has not been identified. They would limit the high-power operation of the tuner.

The cavity has been successfully run at 80 kV and at moderate powers. The tuner has been critically damaged when pushed to higher powers. The failure is believed to be due to breakdown of air pockets in the Elastoseal between the ferrite and the tuner wall under electric field stress.

Liquid-cooled Tuner Test Results Tests have been performed with both water and FC77 as the coolant. A Rexolite spacer has been initially used to confine the water in the region of the ferrite (thus eliminating high energy densities in large volumes of water). Water leaking past this barrier has proved to be a problem and only limited data is available from that configuration. An alternative approach uses a modified Rexolite spacer, allowing water down to the radius of the vacuum window. The use of the modified Rexolite spacer eliminates a straight line E-field path through the water except in a small region near the vacuum window where high losses are still present. As with the conduction-cooled tuner tests, calorimetric measurements have been used to determine the losses in the tuner. In addition, a fiber optic temperature probe has been used to measure the temperature of the central ferrite ring at its inner radius. Most of the data presented in the following has been taken in this configuration.

Tuning curve

Figure 3.110 shows the tuning curves for FC77 and H_20 operation. Measured and calculated (using a SUPERFISH model) results agree well. The tuning range of the two configurations differs primarily due to the high dielectric constant of water (76 vs. 1.86 for FC77), which significantly changes the impedance of the tuner.

Cavity Q

The cavity Q has been measured with a network analyzer and verified by high power ring-down tests. Table 3.24 summarizes the values obtained.

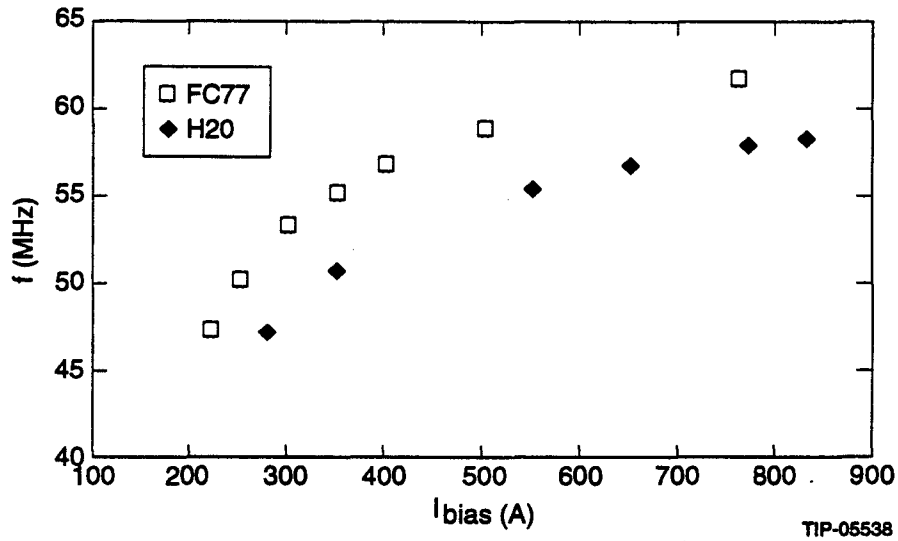

Figure 3.110: Cavity tuning range (liquid-cooled).

Table 3.24: Cavity Q for liquid-cooled tuner at 57 MHz.

	dry tuner	FC77	H_2O
measured Q	1980	1770	1290
calculated Q	2380	2240	1660

Use of the bare stainless steel tuner housing results in relatively low Q. The presence of the water in high-electric-field regions is seen to cause a significant drop in Q. Power amplifier constraints limit the minimum acceptable Q to $\sim$ 1300 for operation with six cavities. The water-cooled tuner is marginal in this respect.

Tuner response

In order to characterize the tuner response, the bias power supply is adjusted to a dc level of 200 A (45.6 MHz), and a small amplitude modulation is imposed. The resultant frequency swing is then measured as a function of ripple amplitude and frequency. Shown in Figure 3.111 is the measured response

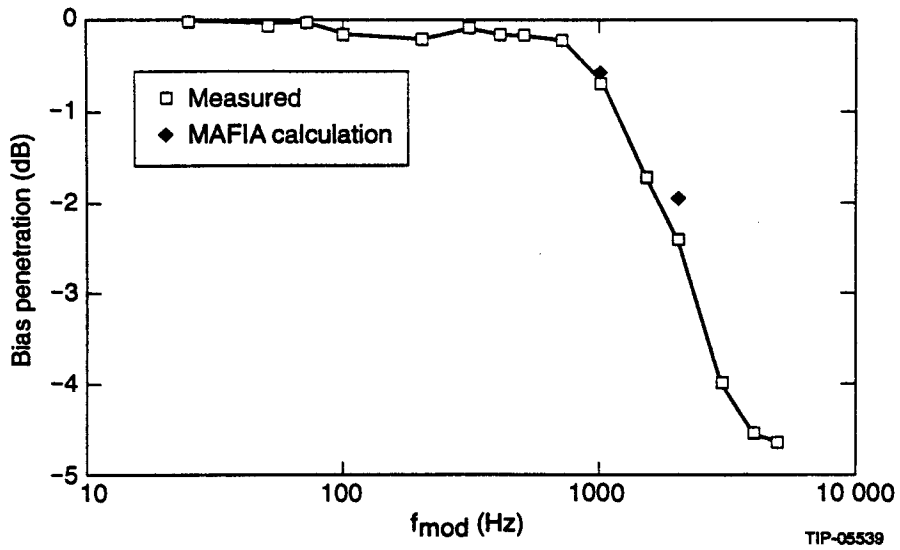

Figure 3.111: Directly cooled tuner frequency response.

along with calculated response using MAFIA.[93] The 3 dB bandwidth is $\sim$ 2 kHz, significantly more than the 600 Hz design goal.

Swept-frequency operation

Initial results of swept-frequency operation have been obtained. An arbitrary function generator (AFG) is used to drive a VCO with the LEB frequency program. Another AFG is used to drive the tuner bias supply with a current program (feed-forward signal) that results in the cavity resonance approximately following the drive frequency. The phase across the tetrode amplifier is then used as an error signal that is added to the feed-forward signal that drives the bias supply.

Figure 3.112 shows the envelope of the rf gap voltage during a 50-ms ramp. Overlaid on this is the frequency program driving the VCO. The gap voltage is seen to stay approximately constant at 19 kV over the entire sweep. The performance during the first 15 ms of the sweep can most likely be improved by damping of a spurious tetrode mode and proper adjustment of the feedback gain in this portion of the sweep.

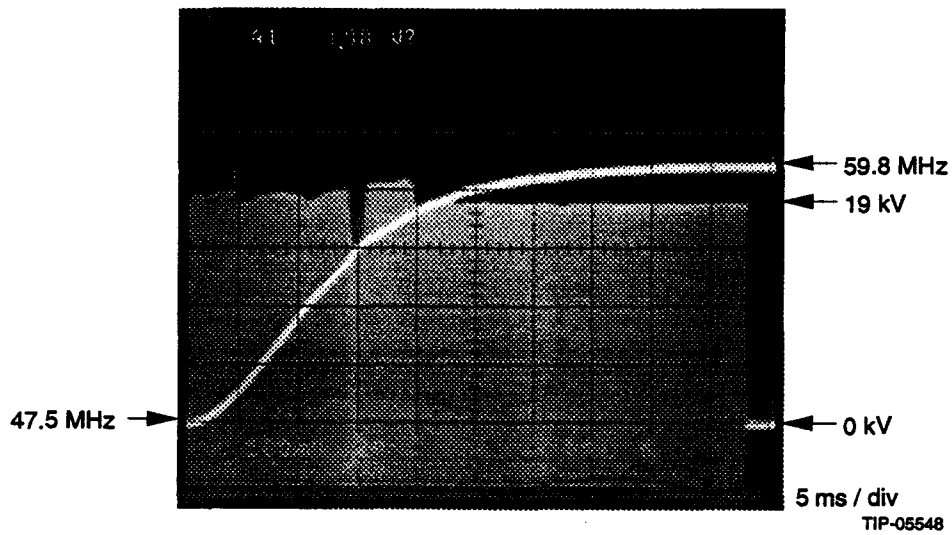

Figure 3.112: Swept frequency operation.

High voltage operation

The LEB voltage program calls for very low cavity voltages at the beginning and end of the ramp (~ 25 kV total ring voltage). As the voltage in the cavity is dropped, multipactoring may occur thereby inhibiting operation of the cavity. For this cavity, typically 1 day of conditioning was required to reach 10–20 kV minimal voltage on the gap. Counter-phasing of the cavities will be necessary to reach the minimum ring voltage required.

Maximum gap voltage

All high-voltage operation on the cavity has been done with dc bias on the tuner and fixed-frequency operation. The cavity is driven by constant-amplitude rf pulses of varying width and duty factor. The cavity has been operated with short pulses (1 ms) up to 140-kV gap voltage.

Operating the cavity at pulse widths larger than 10 ms and at elevated tuner temperatures (~ 35°C), gap voltages of 100 kV were achieved while cooling with FC77 in the tuner. Higher voltage operation may have been possible, however the tuner was reconfigured for water tests before attempt-

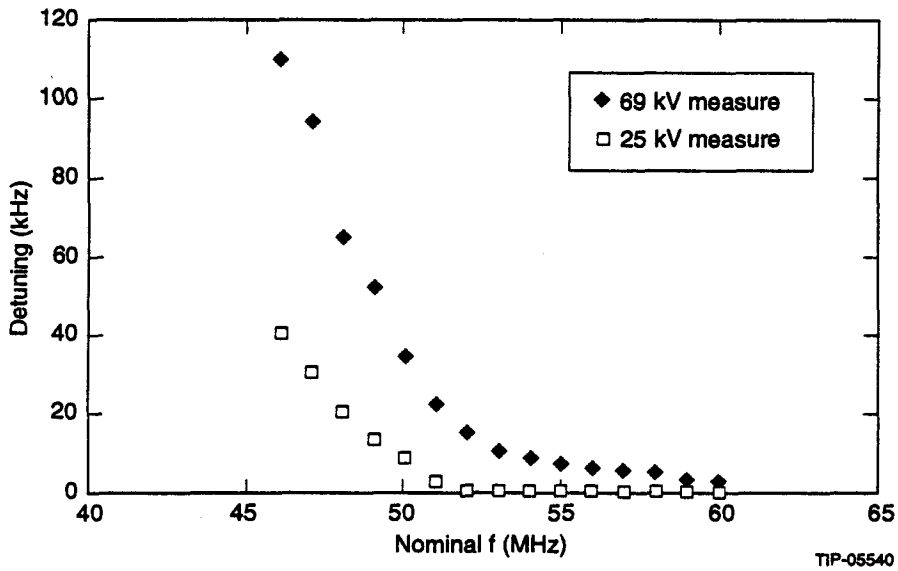

Figure 3.113: Cavity detuning due to non-linearity in ferrite.

ing to operate the cavity above 100 kV. With water, the cavity has been operated up to 130 kV, but arcing occurred after 1 h of operation. The location of the arc corresponds to a region of high loss in the water. It is felt improved flow of water in this region would improve the voltage performance.

Nonlinear effects

Ferrite in high fields is known to exhibit nonlinear effects.[94–96] When the amplitude of the rf field becomes appreciable (> 2 %) compared to the bias field, the effective operating μ changes. This results in a shift of the resonant frequency complicating the control of the cavity.

Figure 3.113 displays measurement data of the frequency shift for this cavity. The detuning is seen to increase with gap voltage. Note also that at high frequencies (high bias field) the effect is reduced.

High power measurements

In order to simplify measurement and interpretation of data, the high-power performance of the cavity has been characterized under fixed single-frequency conditions. The operating frequency has been chosen to be 57 MHz, which represents a power weighted average frequency. The duty factor is adjusted to achieve different average powers for a given gap voltage.

If the cavity is operated at V_o voltage at 57 MHz, an 11 % duty factor should dissipate the same heat in the ferrite as the LEB cycle which peaks at V_o.

The resonant frequency of the cavity is seen to vary with tuner temperature at a rate of 57 kHz/°C for FC77 and 41 kHz/°C for H_2O. This is due to the saturation magnetization of the ferrite and the dielectric permittivity of the water being functions of temperature.[94]

Table 3.25 summarizes the high-power operation data of the cavity.

Table 3.25: High power summary for liquid-cooled tuner.

Configuration	V_{gap} (kV)	df %	$P_{total} = \frac{(V)^2 \cdot df}{(\frac{R}{Q}) \cdot Q}$ (kW)	P_{tuner} (kW)	Coolant temperature rise (°C)	Duration (h)
FC77	70	15	5.8	1.9	6.2	2
	70	11	4.2	1.3	4.3	24
	100	11	8.6	3.3	11.2	3
H_2O	70	17	9.2	5.3	5.1	2
	100	11	12.1	9.2	8.6	2
(tuner arc after 1 h)	130	11	20.4	11.6	10.8	1

Power dissipated in the tuner is monitored with calorimetry of the cooling fluid. From the table it is seen that the use of water results in much more power being dissipated in the tuner. However, it is also seen that water is a much more efficient coolant (*i.e.* less temperature rise per watt deposited in tuner). A temperature rise at $\sim 11°$ is observed during 130 kV operation, which represents an acceptable temperature rise.

Summary

The liquid-cooled tuner has suffered continually from leaks during testing. The combination of liquid cooling and a slotted tuner results in a complex mechanical structure. Significant modifications to the tuner design are necessary in order to solve this problem.

Initial swept-frequency operation of the cavity has been quite encouraging. With minor modifications to the equipment, it is felt that swept frequency operation will be satisfactory.

The cavity has been operated at high voltages and powers. The liquid cooling of the tuner is adequate for handling the powers associated with the LEB program. The cavity has demonstrated 100-kV gap voltages, and with improved circulation of the tuner coolant higher voltages may be possible.

Tests on the cavity have not disclosed any fundamental flaws which will prevent operation at gap voltages of $\approx$ 100 kV. However, finding and demonstrating a long term solution to coolant leaks between the composite shell and tuner housing will not be a trivial task.

3.3.3 Rf Amplifiers

Power Amplifier

The power amplifier utilizes an Eimac 4CW150000E tetrode. The input cavity is a coaxial, fixed-tuned broadband structure to cover the 47 to 60 MHz frequency range. The input cavity is driven at an approximate 12.5 Ω point by four inputs. The output cavity mounts on and is an integral part of the accelerating cavity with the amplifier coupled to the accelerating cavity with a capacitor of about 13 pF. The tube is operated in the grounded grid configuration in class AB. The gap-to-anode voltage transformation ratio is approximately 9 and is flat to 15 % across the frequency range. The amplifier is capable of > 200 kW output. The amplifier has operated without failures during prototype cavity testing. A circumferential spurious mode in the output cavity at $\sim$ 336 MHz has been noted and successfully damped with a lossy microwave absorber material. Another spurious mode exists at $\sim$ 112 MHz and a tuned damper has been added for this mode.

Driver Amplifier

The driver amplifier is a 5 kW, 47 to 60 MHz, solid state amplifier that has four 50 Ω outputs used to drive the tetrode amplifier mounted on the cavity. The unit is complete with power supplies and microprocessor controller and is mounted in two 19 inch racks. The amplifier is water cooled and is comprised of 32 230-W amplifier modules utilizing push-pull FETs, the outputs of which are power-combined. A key feature of this design is the low group delay, less than 50 nanoseconds, which is necessary in order to enable the use of fast rf feedback around the cavity and driver amplifier. The amplifier has performed without problems during prototype testing.

3.3.4 Power Supplies

Nominal ratings of the various power supplies are listed in Table 3.26. Prototypes of these power supplies have been constructed and used in testing of the prototype cavity.

Table 3.26: Nominal power supply ratings.

Power Supply	Voltage (VDC)	Current (amp)
Anode	20,000	20
Screen grid	1,500	1.0
Control grid	1,000	0.5
Filament	15.5	215
Tuner bias	300	1500

Power Amplifier Power Supplies

The design of the power supplies for the power amplifier is driven by the tetrode operating point. In addition, these power supplies are designed to be used on the MEB and HEB as well as the LEB for cost and maintenance reasons.

Anode Power Supply The power supply consists of an outdoor oil-filled transformer/rectifier and an indoor controller. 480 VAC, three-phase, is required for operation. Twelve-phase rectification is used. The controller provides SCR control of the ac feed to the transformer/rectifier and is used for regulation of the dc output voltage to a given value. A vacuum contactor is included in the controller as well.

A crowbar/filter is housed in an indoor unit and consists of a 40 μF capacitor bank and an ignitron crowbar.

Screen Grid Power Supply The power supply is a rack mounted three-phase unregulated dc power supply requiring 208 VAC for operation. The output voltage is adjustable by means of a variable autotransformer on the input.

Control Grid Power Supply The power supply is a rack mounted three-phase unregulated dc power supply requiring 208 VAC for operation. The output voltage is adjustable by means of a variable autotransformer on the input.

Filament Power Supply The power amplifier input cavity design dictates the use of dc filament current. The unit is a three-phase unregulated dc power supply requiring 208 VAC for operation. The rectifiers are water-cooled. The output voltage is adjustable by means of a variable autotransformer on the input.

Tuner Bias Power Supply

The high Q of the cavity and the fast LEB cycling rate make design of this supply one of the most difficult tasks in the LEB rf system. The supply design is driven by the goal of maintaining the power amplifier within 1 dB of resonance over the LEB ramp. A current accuracy of $\sim$ 250 ppm is required to achieve the design goal for a cavity Q of 5000.

The tuner bias power supply consists of an unregulated three-phase power supply followed by a current regulator. Taps are provided on the prototype unit for 150, 200, 250 and 300 VDC at 1500 A. 480 VAC, three-phase, is required for operation. The regulator is a single-quadrant PWM regulator consisting of paralleled 300 A modules. The prototype magnet designs have required three paralleled modules for 900 A capability. The regulator is designed to follow an analog input program in order to provide a current ramp to bias the tuner over the 47.5 to 59.8 MHz frequency range. In addition, a tuning feedback loop is incorporated around the regulator. This loop acts on the cavity input-to-output phase error. The results of prototype tests indicate that addition of a shunt regulator will be necessary to ensure the required tuning accuracy rather than depending solely on the bleed down rate of the supply for negative slope corrections.

3.3.5 Local Low-Level Rf Feedback Loops

The low-level rf system for the LEB provides the local feedback loops which ensure that the rf signal follows the prescribed amplitude and phase program for acceleration of the beam. Due to the small bucket area to bunch area ratio, the requirements for amplitude and phase accuracy are stringent ($\pm$10 kV *rms*, $\pm 1^\circ$ *rms*) in order to avoid excessive beam loss.

The relative beam loading is high, particularly during injection and extraction and exceeds the Robinson criterion during test-beam operation. The test-beam mode, in fact, drives the low-level rf design. The system is stabilized by the use of amplitude and phase feedback loops; however, the loops are strongly coupled by the beam at high currents. The decoupling matrix is therefore beam intensity dependent and varies with time and hence can become quite complex. Fast rf feedback has the effect of lowering the Q by a factor of $(1+H)$, where H is the open loop gain. This raises the Robinson limit and reduces the amplitude/phase loop coupling. The LEB low-level rf design includes the use of fast rf feedback for this reason. It is noted that the use of rf feedback can have an adverse effect on coupled-bunch modes since the feedback increases the real part of the coupling impedance for small machines such as the LEB and any asymmetries in the fundamental response can contribute to coupled bunch instabilities.[97]

General Description

The low-level rf equipment hardware uses a VXI architecture and is based upon a design developed initially by Los Alamos National Laboratory. The system provides a great deal of flexibility, programmability and monitoring capability via the rf supervisory control system. Figure 3.114 is a block diagram of the system.

Description of Local Rf Feedback Loops

There are four feedback loops associated with each rf cavity: amplitude loop, phase loop, fast rf feedback and a tuning loop. The amplitude, phase and tuning loops are VXI based and controlled and monitored by the rf supervisory control system.

Amplitude and Phase Loops Two methods of achieving amplitude and phase stability have been considered. These are conventional amplitude and phase loops and I (in-phase) and Q (quadrature)[98] loops. The I & Q system has the advantage of using circuit boards already developed for use at the SSC and at LANL. Figure 3.115 is a simplified diagram of this system. The system utilizes vector detectors to derive base-band error signals. The detectors are followed by conventional PID controllers which establish the gain and frequency response of the loops. A vector modulator follows the PID controllers. The system utilizes a 20-MHz IF frequency primarily as

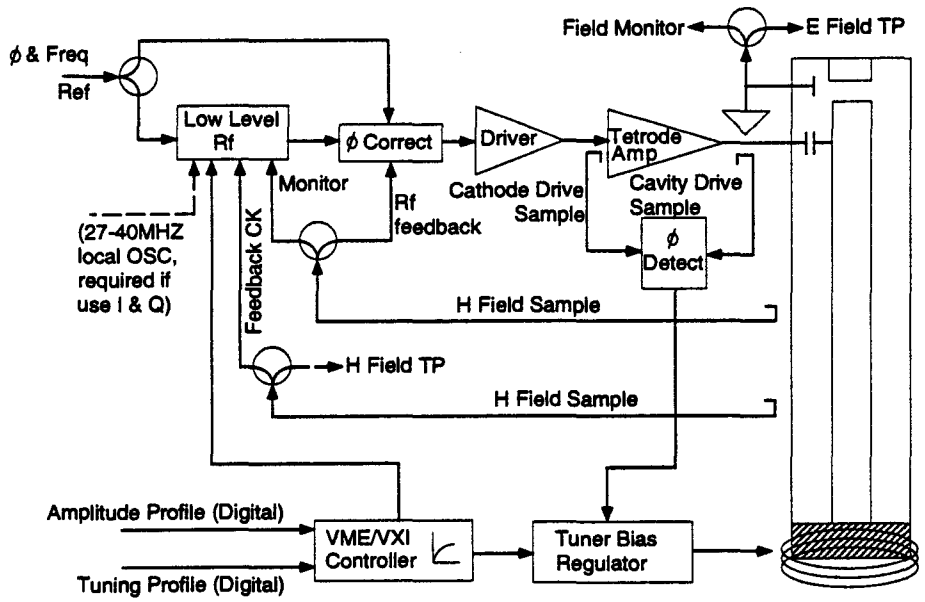

Figure 3.114: Low-level rf simplified block diagram.

a matter of convenience since the previously developed circuit boards used this frequency. A prototype low-level rf system has been constructed with I & Q loops. The system is near completion and has been bench tested but not tested with the prototype cavity.

Tuning Loop The tuning loop acts to maintain the cavity in resonance or close enough to resonance so that the power amplifier can supply the power required for beam acceleration and to overcome cavity losses. The error signal to the tuner bias regulator is derived by comparing the power amplifier cathode drive signal and the cavity field. Figure 3.116 is a simplified diagram of the feed back loop. The key technical issues regarding the tuning loop are the bandwidth of flux penetration into the ferrite, the bandwidth of the tuner regulator and level-insensitive detection of resonance. It is clear that a feedforward system will substantially reduce the gain and bandwidth required of the loop. Preliminary tests of this loop in conjunction with a feedforward system have been encouraging, see Figure 3.112.

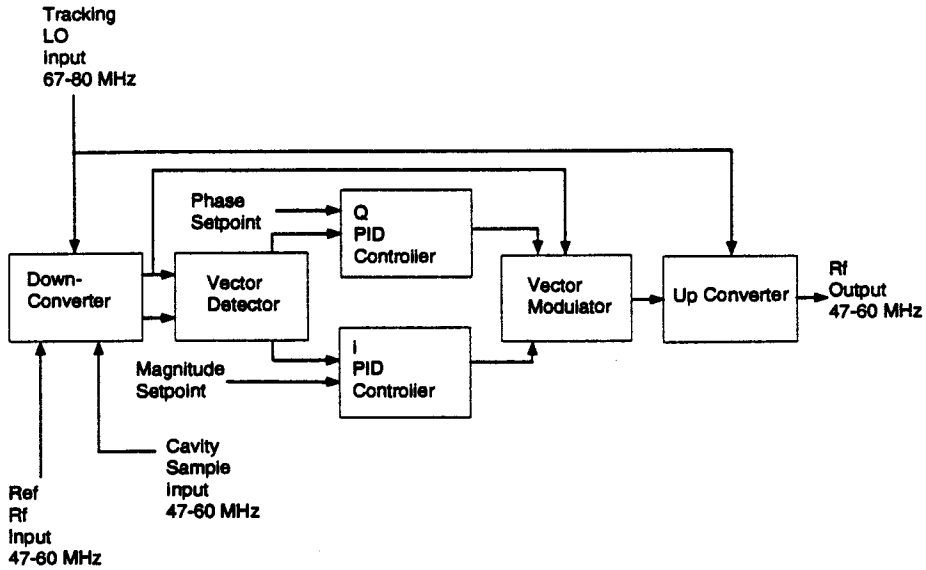

Figure 3.115: I & Q system block diagram.

Fast Rf Feedback Loop The amount of rf feedback which may be applied is limited by the time delay in the system. The maximum delay which maybe tolerated with ±45° phase margin for a given open loop gain is $T = Q/4F_oA$ where Q is the cavity quality factor, F_o is the operating frequency and A is the open loop gain. It is desirable to have A such that $I_B/I_g(1 + A) < 1$ where I_B is the beam induced current and I_g is the generator current. This results in a desired A of $\sim$ 16 and maximum T of $\sim$ 1.3 μs. The LEB rf building layout has been done in a manner to minimize cable lengths. The driver amplifier time delay has already been mentioned. The time delay of an installed station is expected to be < 500 ns.

The large frequency swing in the LEB requires that a phase shifter be incorporated in the feedback loop in order to maintain the proper phase relationship at the feedback loop summing junction. The phase shifter should have low time delay and be reasonably accurate to avoid asymmetries in the cavity frequency response with feedback. Figure 3.117 is a simplified diagram of the phase shifter designed for this purpose. The phase shifter utilizes vector modulators to achieve phase shift. A prototype unit has been constructed and bench tested. Time delay through the phase shifter has been measured as 77 ns. Limited frequency range (52.5–53.5 MHz) tests

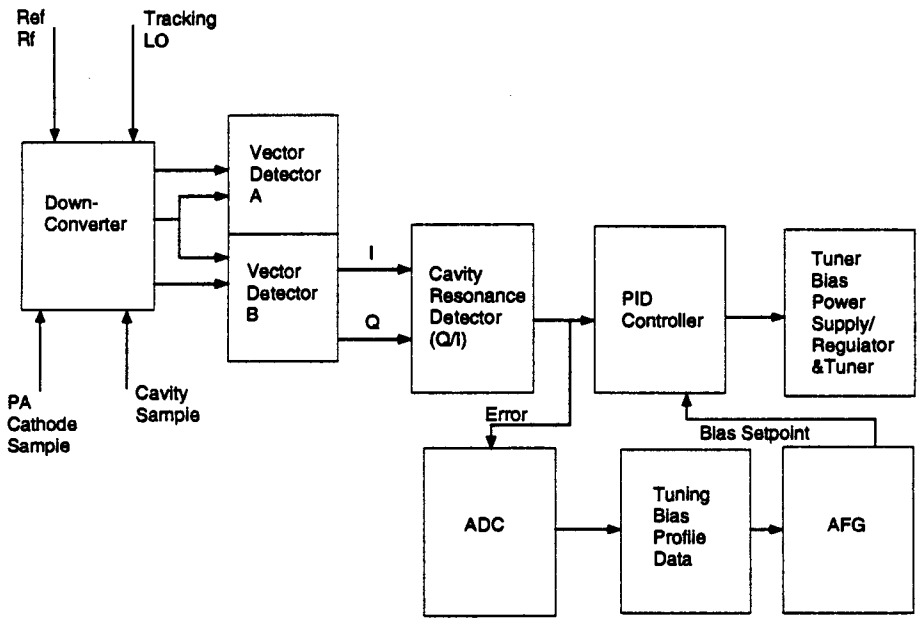

Figure 3.116: Resonance loop block diagram.

have been performed with the cavity and an artificially induced cable time delay of 220 ns. The tests indicate the expected reduction in amplitude and phase error.

3.3.6 Beam Synchronization and Low Level Rf Feedback Loops (L.K. Mestha)

Beam Synchronization and Global Rf Feedback Loops

Feedback Loops Global to the Cavity The global feedback loops control the beam during capture and acceleration and synchronize the LEB and the MEB rf systems for bunch-to-bucket transfer. A schematic of these loops is shown in Figure 3.118.[99] A stable frequency source—in this case a Direct Digital Synthesizer (DDS)—is used to produce a sinusoidal rf signal by reading frequency values from a ramp table. The frequency ramp table is static; corrections to the frequency are needed to minimize errors in beam energy or coherent beam oscillations around the synchronous phase. Beam energy is maintained by the radial loop, where the radial position of the beam at a

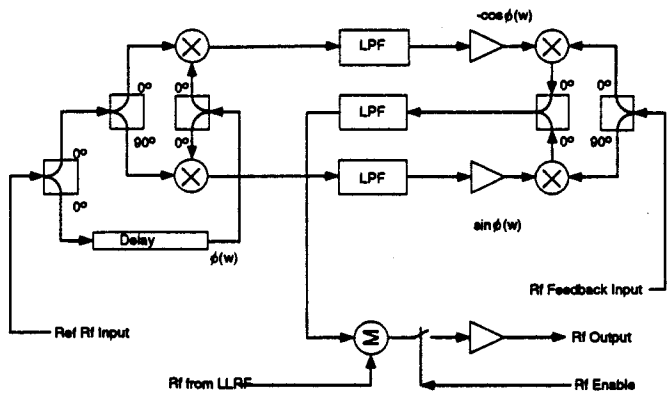

Figure 3.117: Rf feedback and phase corrector diagram.

dispersive location is compared to a reference signal to generate the radial error signal. This signal is processed and added to the frequency ramp values thus varying the rf frequency to maintain the radial beam position within specifications. In the beam phase loop, the longitudinal position of the beam signal from a wall current monitor is compared with the rf signal. It is then processed to convert to appropriate frequency shift through a feedback controller. Here again the frequency shift is added to the frequency ramp values to correct for phase excursions.

While the radial and phase loops are similar to those found at most other synchrotrons, the synchronization loop is unique to the LEB due to its low synchrotron frequency at extraction ($\approx$ 300 Hz, see Section 2.2). Hence, in this section the emphasis is given to the new synchronization scheme,[100] the hardware of the prototype system used to establish 'proof of principle' of the scheme and the results of experiments conducted at Fermilab and CERN PS Booster synchrotrons.

Principle of LEB to MEB Beam Synchronization The purpose behind synchronization is to have both energy and phase of a reference bunch in the LEB match with a target bucket in the MEB, into which the first bunch of protons from the LEB (the reference bunch) is to be transferred. A target marker is generated by selecting the appropriate bucket and dividing the MEB rf signal by the harmonic number. When the phase of the reference bunch in the LEB matches the phase of the target markers in the MEB, the two machines can be phase-locked. Since the proton bunches in the LEB are

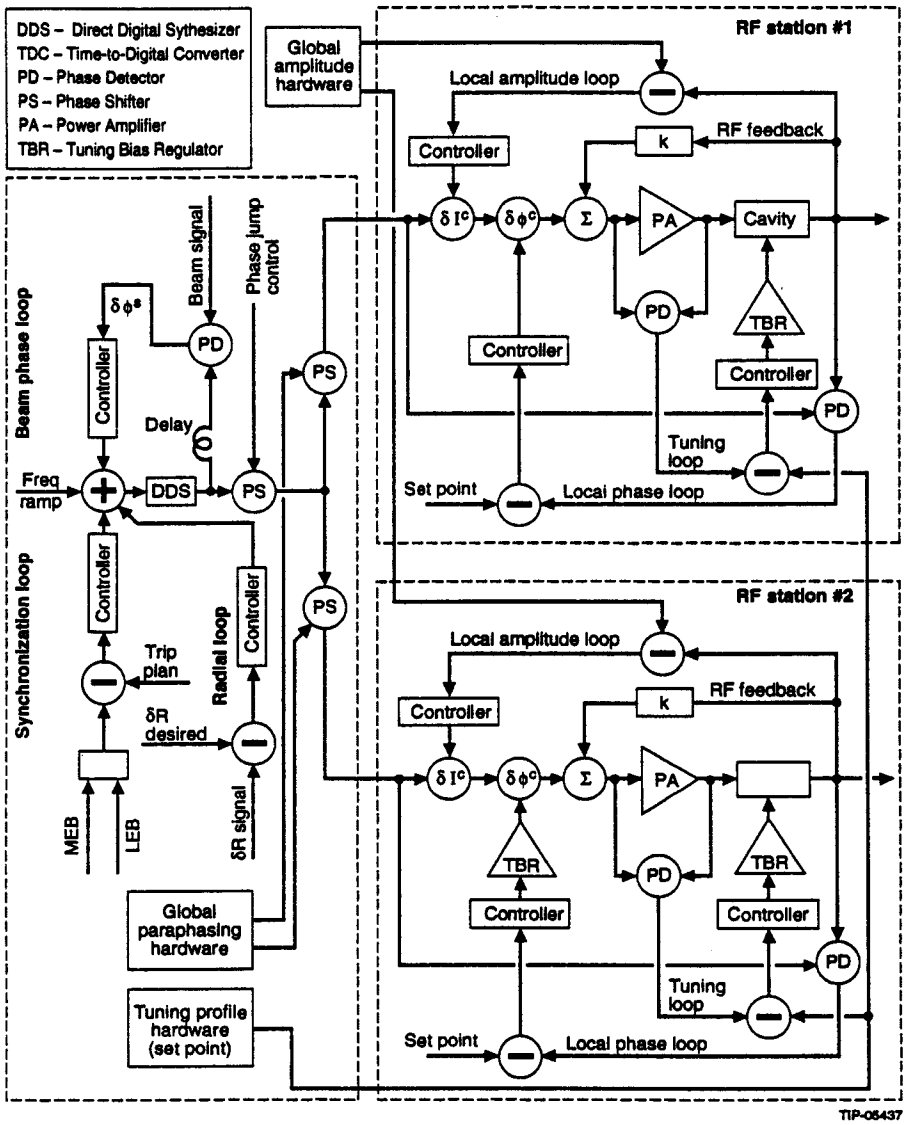

Figure 3.118: Rf beam control loops planned for the SSC Low Energy Booster.

inside the rf bucket, it is considered sufficient to lock the phase and frequency of the LEB rf with that of the MEB rf to achieve synchronization.

The phase and frequency locking can be achieved by either passive or active synchronization schemes. For passive synchronization, the LEB master oscillator is assumed to be very stable and correction is applied to the LEB frequency. At a predetermined time before transfer, the frequency of the LEB master oscillator is offset a few Hz in frequency relative to the nominal frequency at extraction. The phase of the LEB rf slips relative to the MEB rf, and phase coincidence between the LEB and MEB occurs regularly with a frequency equal to the frequency offset.[101] Synchronous transfer of the beam is triggered when phase-coincidence occurs. Active synchronization, on the other hand involves tracking the phase between the LEB reference bunch and the MEB target bucket and adjusting the LEB rf frequency to reach and maintain synchronism a few milliseconds before transfer,[102] thus locking the two rf systems.

Passive synchronization is unreliable and is made impossible for the LEB due to an uncertainty window of 50 μs allowed for synchronous transfer at flat top. In the active synchronization scheme, the time required to phase-lock the LEB rf with the MEB rf depends on the phase-slip factor η of the LEB close to the time of extraction ($f_s \approx 400$ Hz) since radial steering of the LEB beam orbit is done by changing the rf frequency. The time required to correct a longitudinal spatial phase of 5 meters is at least about 10 ms. A simple phase-locking approach of the type used at the Fermilab Booster[103] is difficult to implement since 10 ms before transfer time the phase difference may be very large and difficult to control. Hence a modified and more general approach suitable for fast cycling machines has been developed.[104] The approach is to maintain control of the LEB rf phase by forcing the reference bunch to follow a pre-programmed phase called the "trip-plan," so that close to transfer the phase difference never becomes excessive and the phasing between the LEB reference bunch and the MEB target bucket markers is held constant on a cycle-to-cycle basis. A feedback loop then corrects for only the deviation from the trip-plan. The trip-plan has at least one point in the flat B-field region where the reference markers have the correct phase for the purpose of beam transfer. This technique offers several advantages compared to others discussed above. The greatest advantage would be due to the ability to track a gap in the LEB beam bunch train starting from injection and going all the way up to extraction. By doing such a tracking we not only allow small corrections in the beam radial position for synchronization with the target bucket (due to more time available for synchronization) but

also retain the flexibility to synchronize the gap in the bunch train with the rising edge of the kicker magnets. If we would start to synchronize late in the cycle, generally large radial excursions are required. Synchronizing the gap with the kicker magnet field prevents unwanted radiation at the magnet walls. Also, the predictability feature of the new synchronization scheme due to the same identified bunch matching with the target bucket during extraction on a cycle-to-cycle basis can be used to advantage in day-to-day operation of the machine.

LEB Trip-Plan As mentioned above the trip-plan determines the spatial longitudinal phase between the reference bunch of the LEB with respect to the target marker. During one turn of the target markers in the MEB, the reference bunch in the LEB will have circled several turns depending on the path covered by the reference bunch and the speed at that time. An illustration is shown in Figure 3.119. Let $\tilde{t}_k$ be the time covered by the target markers for the kth turn in the LEB and if t_k is the arrival time of the reference bunch in the LEB, then the trip-plan is given by

$$(S(k))_{\textit{trip-plan}} = v_k(t_k - \tilde{t}_k)\,, \tag{3.15}$$

where the parameter $S(k)$ is the modulo of the longitudinal spatial phase in m for k^{th} turn. The time durations $\tilde{t}_k$ and t_k are measured from a common reference point, *i.e.*, from the start of the LEB cycle. The subscript k indicates the turn number, and v_k represents the velocity of the reference bunch. In Figure 3.120, $S(k)$ is plotted for 3773 turns of the MEB target markers. The MEB to LEB circumference ratio is $(3960/570 = 7 - (1/19))$. Hence, at extraction there will be 19 MEB turns before the LEB reference bunch reaches the same reference point again. This is clearly visible in the trip-plan in Figure 3.120. This will be the trip-plan to which the LEB reference bunches will be locked.

In the presence of field errors the actual path covered by the reference bunch is different from the ideal path. Also, an arbitrary bunch may be selected in the LEB. Then the spatial phase difference we have to reduce to zero in order to lock to the trip-plan is given by[100]

$$\delta S = -v \int \left[\eta\gamma_t \frac{\delta R(t)}{R} - \frac{1}{\gamma^2}\frac{\delta B(t)}{B_0(t)}\right] dt + \delta S_0\,, \tag{3.16}$$

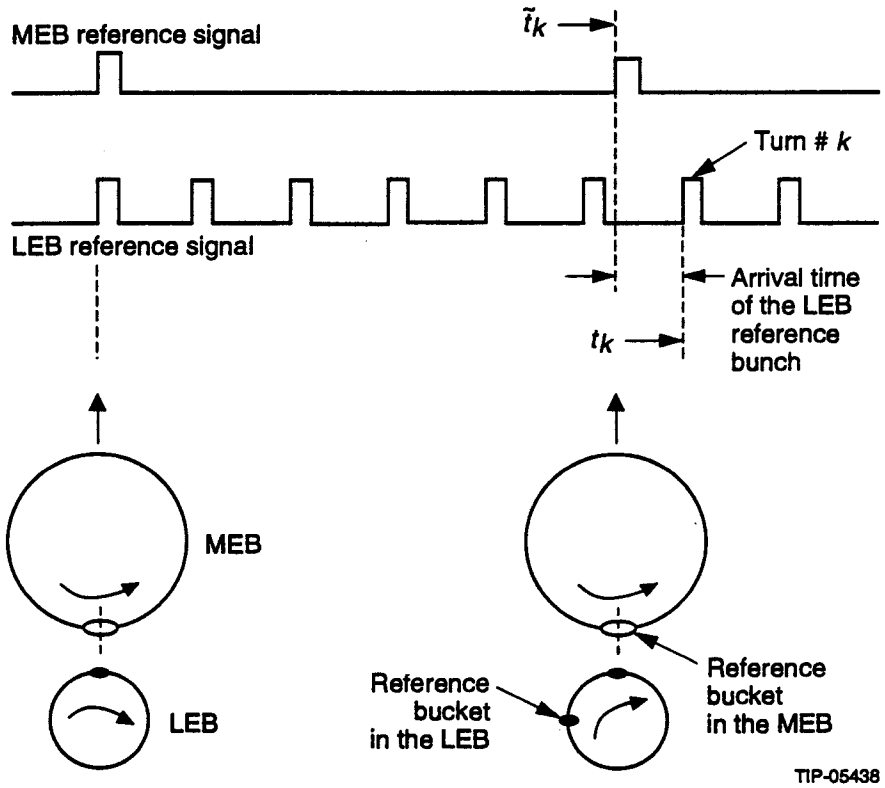

Figure 3.119: Conceptual diagram showing the arrival time of a reference bunch in the LEB.

where $\eta = \frac{1}{\gamma_t^2} - \frac{1}{\gamma^2}$ is the slip factor and δS_0 is the phase deviation created with respect to the MEB target markers by selecting a given reference bunch out of the 114 in the LEB.

Synchronization Loop Hardware (Proof of Principle) The hardware setup used for establishing the 'proof of principle' is shown in Figure 3.121. Two 32-bit floating point Digital Signal Processors (DSP), TMS320C30,[105¶] are used as processing units. The DSP board has 2 Mbyte of dynamic RAM onboard as well as 64 kwords of fast static RAM (SRAM) plus the usual control registers to interface to the VME bus. The Node RAM in each C30

¶Manufactured by Texas Instruments, Inc.

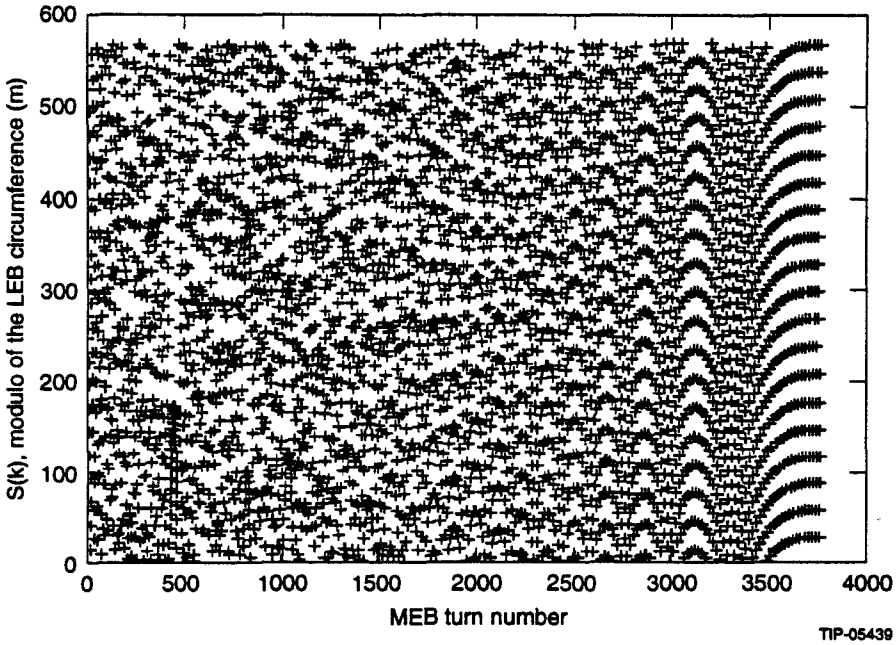

Figure 3.120: LEB trip plan.

processor is 64 Kwords long static memory. The first C30 is used to generate the master frequency by reading the frequency data stored in the SRAM and then launching it to the LEB DDS at time intervals of 960 ns. The MEB DDS is left free running at the MEB injection frequency. Both DDS are driven by a 1 GHz clock to generate the rf frequency. The units used in this experiment are commercial electronic boards.[106][‖]

The target markers are generated by dividing the MEB DDS output by 792 (the MEB harmonic number) and are used to start counting the time with the 32 bit, 20 ps resolution time-to-digital converter[107] (TDC). The reference marker for the LEB is created by dividing the LEB DDS signal by 114 after identifying a particular bunch to track in the bunch-identification circuit (not shown in Figure 3.121) and is used to stop the TDC. The TDC stops when the first LEB marker after the MEB reference marker appears. The start of the time measurement on real time (*i.e.*, each time when the target marker arrives) by marking the bucket from the LEB rf signal is shown in Figure 3.122. The first target marker after the

[‖]Manufactured by Stanford Telecom, Stanford, CA.

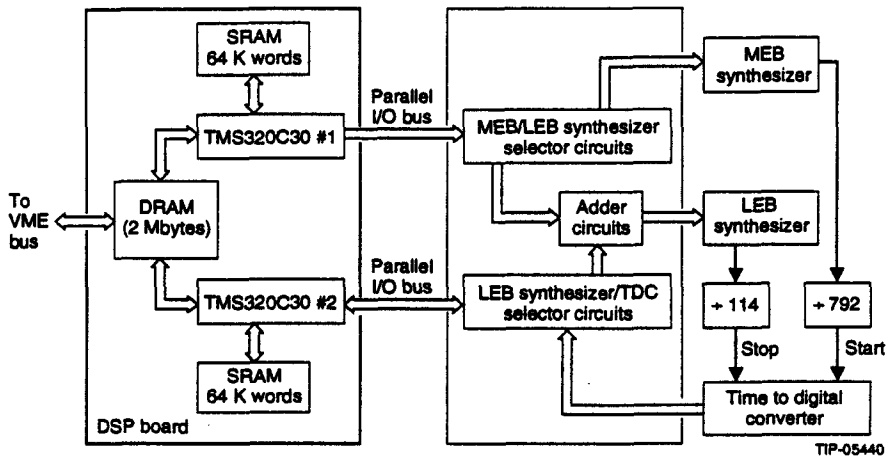

Figure 3.121: Synchronization loop hardware used for bench testing the loop.

'synchronization start' pulse is used to start counting buckets in the LEB by counting the number of rf cycles. After a known number of count (say 10 or any bucket we want to identify) the LEB rf signal is divided by the harmonic number, to generate the revolution marker. In this way, the bucket to be tracked and synchronized as the first bunch with the target markers is being identified. This bucket, as mentioned earlier, then becomes the 'Stop' marker to the TDC. The TDC measures the time interval between two markers every time a 'Start' marker appears. The TDC data is read into the second C30 (see Figure 3.121) and converted to spatial phase by multiplying the stored velocity data in the C30 RAM with the TDC data as described by Eq. (3.17),

$$(S(k))_{measured} = v_k \delta\tau \,, \tag{3.17}$$

where $\delta\tau$ is the TDC data in seconds. To lock to the trip-plan, the difference is obtained by subtracting Eq. (3.17) with Eq. (3.15). Thus,

$$\delta S(k) = (S(k))_{trip\text{-}plan} - (S(k))_{measured} \tag{3.18}$$

which is the phase error. Care has to be taken implementing Eq. (3.18) in the DSP to avoid phase wrap-around problems. For a simple feedback, the phase error of Eq. (3.18) is multiplied by a constant, K, to generate the frequency shift which is given by

$$\delta f_k = -K\delta S(k) \,. \tag{3.19}$$

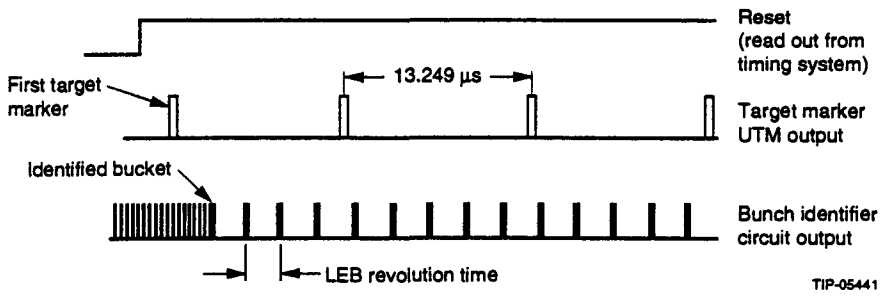

Figure 3.122: Basic timing diagram of the synchronization loop.

This frequency shift is then fed from the second C30 to the adder circuits to change the frequency of the LEB DDS, thereby closing the loop. In Figure 3.123 the decay of the spatial phase error $\delta S(k)$ is shown for different values of the gain K for an initial phase error of 265 meters.

The system as described above has been prototyped at the SSC Laboratory. In addition to the synchronization loop hardware, parts of the beam phase loop have also been bench tested. After this, the complete system has been moved to Fermi National Accelerator Laboratory to conduct further tests with beam. Some parts of the synchronization hardware have also been tested at the CERN PS Booster.

Experimental Beam Studies Aspects of the prototype low-level rf system have been tested at FNAL using the Booster rf system. The ultimate goal of the experiment has been to prove successful operation of the new synchronization feedback system. Initially, parasitic tests have been conducted, *i.e.*, using the beam signal only to test the suitability and operation of the digital hardware, software and loop circuitry. Later it has been planned to control the beam by replacing the existing analog low-level rf system with the digital radial, beam phase and synchronization loops (see Figure 3.124).[108] A formal proposal has been submitted to FNAL requesting access to the[109] Booster facilities at various levels for the following test program.

1. Measure the repeatability of the time-varying phase relationship between Booster beam and the Main Ring injection reference oscillator, during Booster acceleration. The Booster is operating with the existing analog LLRF system. This is essentially the 'trip' measurements for several Booster acceleration cycles at different times during the day. This stage requires only access to a Booster beam phase signal, the

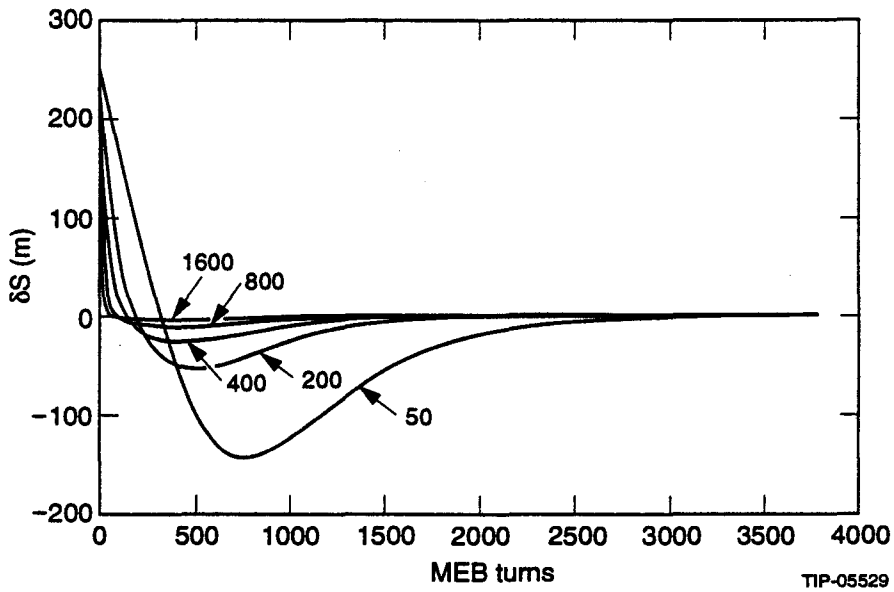

Figure 3.123: Synchronization loop "proof of principle" test results.

Booster VCO signal, and the Main Ring reference signal. The measurements are done parasitically. The information gathered determines the viability of the synchronization system.

2. From the 'trip' measurements, extract the frequency curve and then generate the initial frequency sweep using DSP and DDS. Then test the operation of the frequency program and phase-lock control circuitry, DDS, and the phase detector circuitry in parallel with the analog Booster VCO and beam-phase loop. This stage demonstrates the performance of the digital feedback system subcomponents such as DSP, DDS, TDC, ADC hardware and software to phase-lock to the beam. This stage is also parasitic and requires the measurement of the long delay in the existing beam phase loop.

3. After the success in parasitic tests substitute the analog hardware by the digital system and demonstrate its ability to actually control the beam acceleration (with analog LLRF system disconnected from the Booster). Measure beam parameters such as the beam phase, radial position, intensity *etc.* This stage requires dedicated machine and beam study time.

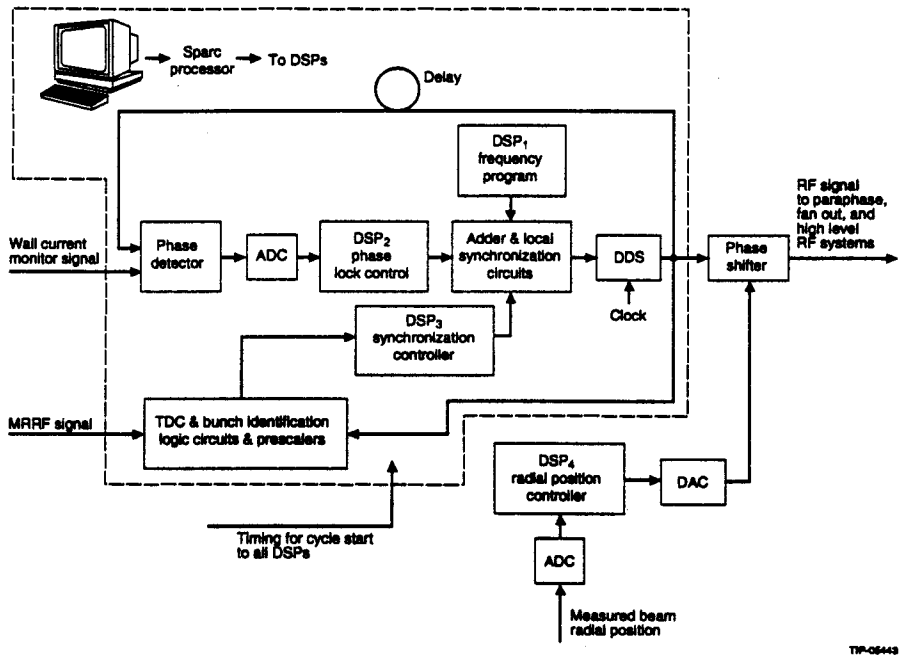

Figure 3.124: Schematic loop diagram of the experimental LLRF beam control system.

4. Close the synchronization feedback loop using the working digital feedback system from stage 3 (with the beam phase loop closed) to demonstrate stable beam acceleration. In this stage the trip-plan is included in the synchronization loop. No beam transfer to the Main Ring will be attempted. During each acceleration cycle perform 'trip' measurements to confirm that the four lobes of Figure 3.125 (described below) appear at the same place on the y-axis. This will not only demonstrate stable beam acceleration with the new synchronization loop in place, but also will give first evidence of synchronization with new scheme.

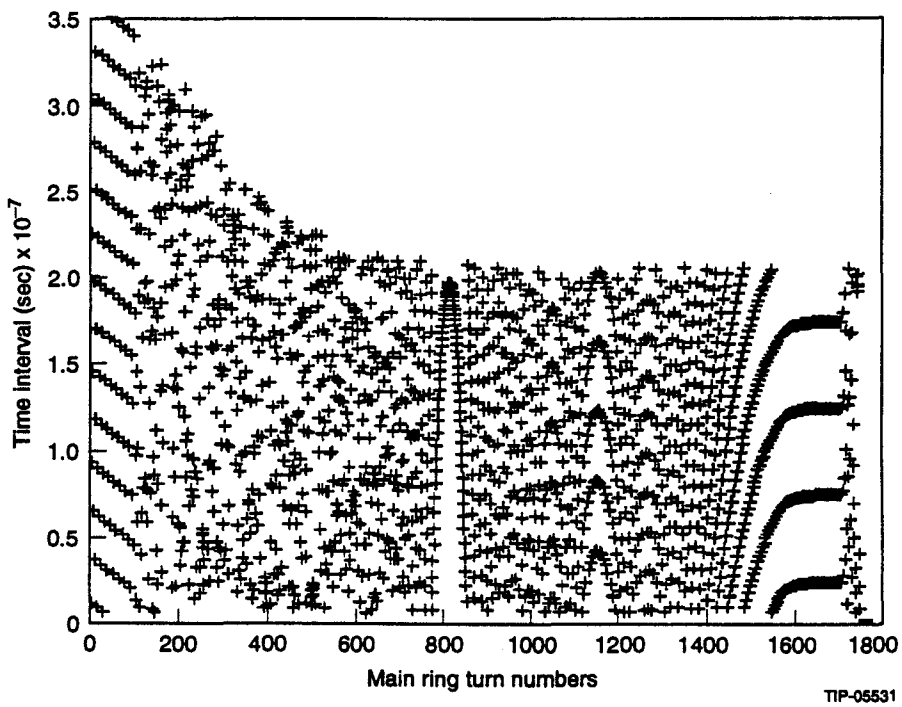

Figure 3.125: Trip measurement with time interval shown in seconds in FNAL booster synchrotron with beam.

5. Transfer beam to the Main Ring using the new LLRF and synchronization feedback system. This final stage, although not essential, would be a proof of the new synchronization idea to herald complete success.

Stages 1 to 3 have been completed successfully. Stages 4 and 5 have not been completed due to the termination of the SSC project. Results of the experiments are discussed below.

A typical time-interval measurement between Booster reference marker and the Main Ring reference marker is shown in Figure 3.125 (also called 'trip' measurement) when the Booster is accelerating beam. The four lobes at the end correspond to the fraction in the ratio of the harmonic numbers ($1113/84 = 13 + (1/4)$) and show that the Booster VCO is locked to the Main Ring oscillator. Several such trip measurements have been done for 25 consecutive cycles and also over a period of 24 days. The fluctuations of integrated phase per Booster cycle appear to be within 8 Booster turns which can be ascertained to a slow drift in the magnetic field. The 'trip' data of Figure 3.125 has been used to extract the frequency curve. The error in frequency measurement depended on the TDC resolution. With the 20 ps resolution TDC, the peak-to-peak measurement error in the frequency is held to within 1 kHz for a sweep from 30 MHz to 53 MHz. This frequency data is stored in DSP #1 for stage 2 experiments.

The delay in the beam phase loop has also been measured with beam in the Booster. It is equal to 1.4 μs. The technique used for such delay measurement is described in a separate report.[108] In stage 2, a long cable with the delay equivalent to the delay measured in the analog beam phase loop has been inserted to parasitically demonstrate the operation of the frequency program, phase-lock DSP, DDS, and the phase detector circuitry in parallel with the Booster VCO. Due to the presence of the DSP in the beam phase loop, the phase detector signal is sampled at 3 μs with a sampling period of 2 μs to generate the frequency ramp. Although the tests have been encouraging with this sampling period, it is believed that a higher sampling rate in the frequency ramp curve and the beam phase loop is appropriate before replacing the VCO. Hence, while controlling the beam in stage 3, a sampling period of 960 ns is used in both the frequency ramp curve and the digital phase loop instead of 2 μs and 3 μs respectively. To accomplish the higher sampling rate the phase loop DSP is removed from the loop. An analog loop filter is used in between the ADC and the phase detector circuitry instead of the IIR filter in the DSP to control the dynamics of the phase loop. The ADC data is directly sent to the 32-bit adders thus bypassing the phase loop DSP.

After the success in parasitic tests of stage 2 with improved sampling rate in the digital beam phase loop the digital hardware has been substituted into the operating machine by opening the VCO. With some adjustments in the

phase loop gain acceleration has been successfully achieved. The beam was however transferred to the main ring during the test runs with the existing Booster synchronization loop closed. All the qualities of the beam expected from a normal Booster run have been preserved during the beam control experiments. In Figure 3.126 the phase detector error, radial position error and the beam intensity curves are plotted for the complete acceleration cycle both for the analog and the digital system. By comparing Figure 3.126(e) with Figure 3.126(f), it can be seen that the phase error between the beam and the rf signal is well under control without additional beam loss (see Figure 3.126(a) and (b) for beam loss).

In parallel with the experiments conducted at FNAL, studies have been undertaken at the CERN PS Booster synchrotron in Geneva to prove the new digital synchronization technique. Similar TDC and DSP hardware have been configured at CERN with the help of the PS Booster rf group. The DSP software has been transported from the SSCL to CERN. As an improvement to the Fermilab experiments, the TDC data is converted to an analog signal using a DAC and then displayed in real time during each machine cycle. In Figure 3.127 the trip measurement is shown for the complete PS Booster cycle. There is only one lobe at the transfer time for this case because of the integer ratio of the harmonic numbers.

When a synchronization loop of the type described above is used in fast cycling machines like the LEB, it may be required to program the gain with respect to time in some or all the loops. A longitudinal beam tracking model[99,100] is used to calculate the time-varying gains by optimizing to a predetermined performance function[110] using new iterative techniques taking into account all the (global and local) feedback loops associated with the LEB rf system.

3.3.7 Acknowledgements

The authors wish to acknowledge the invaluable contributions of I. Averboukh (BINP), C Friedrichs (LANL), Y. Goren, T. Grimm, G. Hulsey, S. Kwiatkowski, V. Petrov (BINP), A. Propp, J. Song, K. Vavra, L. Walling and V. Yakolev (BINP) to the cavity/tuner design; F. Brandeberry, G. Coulter, M. Doub, N. Spayd and K. West for test stand development and prototype testing; E. Marsden and J. Wallace for low-level rf design; H. Rogers for rf feedback phase corrector and amplifier controls hardware design; and E. Bird, S. Blake, M. Gresham and L. Taylor for power supplies design and development.

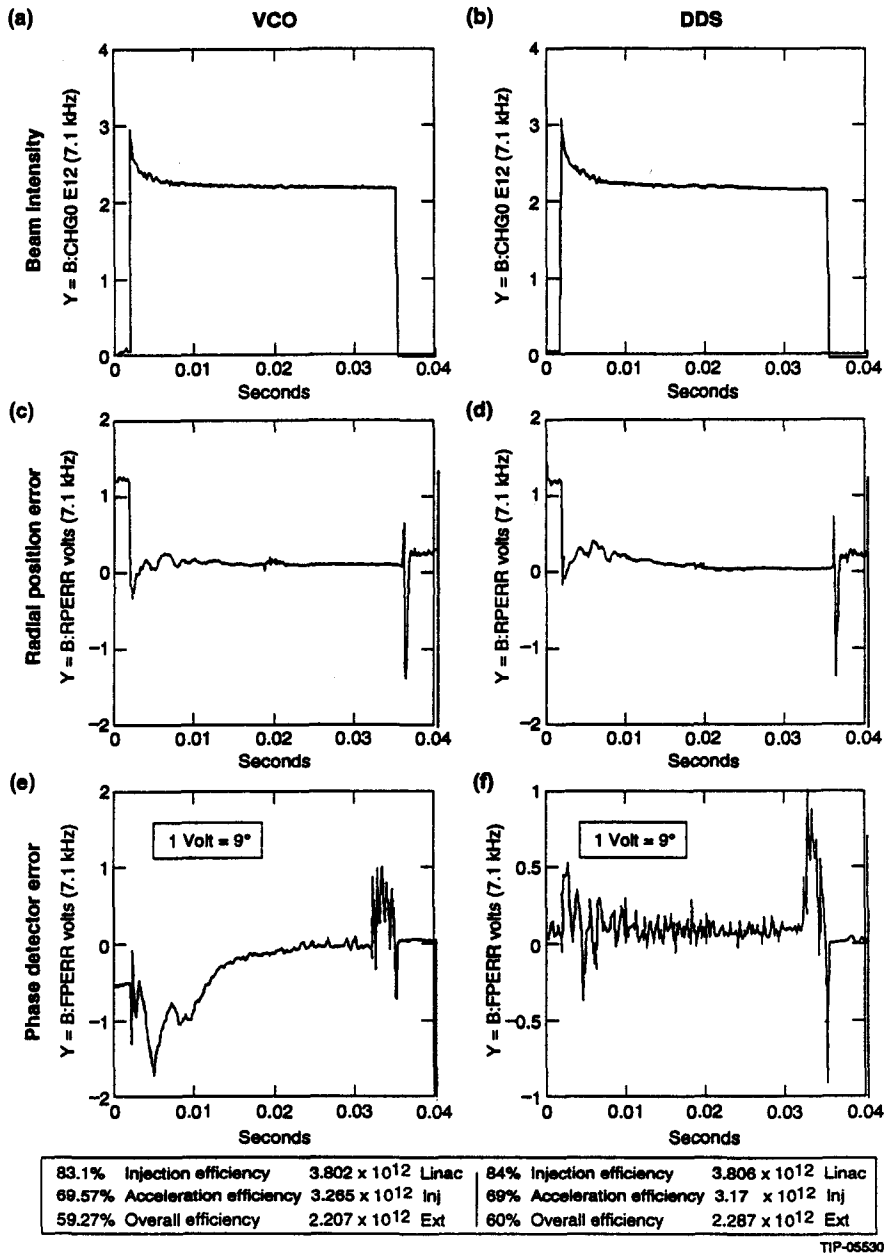

Figure 3.126: Beam control experimental results in the FNAL booster synchrotron.

(a)

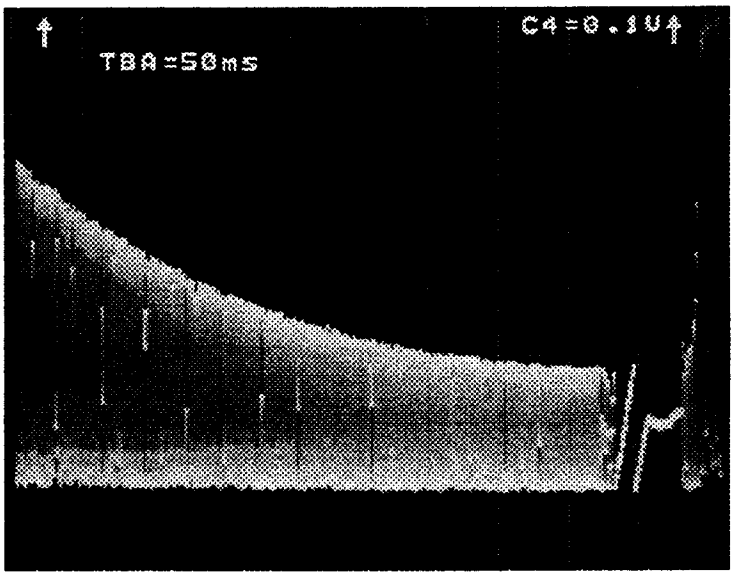

(b)

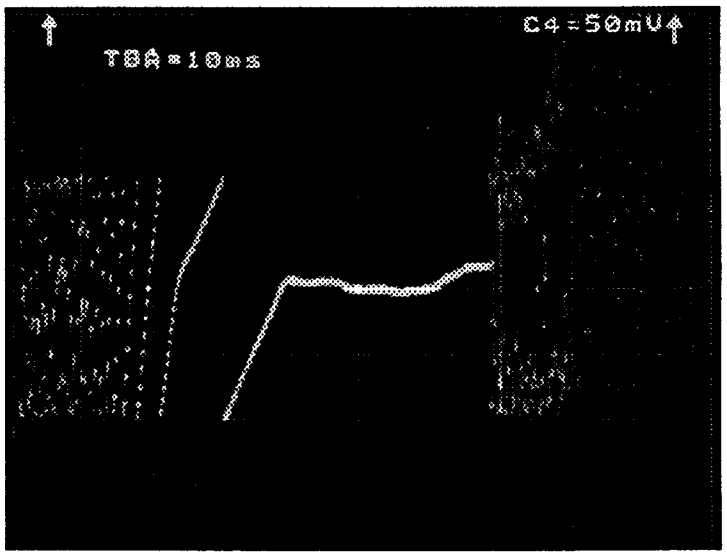

TIP-05532

Figure 3.127: Oscillograms of the trip measurement on the CERN PS booster: (a) for a complete acceleration cycle, and (b) expanded view late in the cycle.

Professor Richard Talman of Cornell University inspired and guided the work on the new type of digital synchronization system in the initial years. After overcoming the critical path with the enthusiastic support and guidance of Bob Webber we were able to prototype a complete system. Later a successful collaboration with FNAL and CERN Laboratories were initiated to test the prototype system.

The prototype hardware is primarily a result of the collective efforts of many team members such as: V. Brouk, J. Mangino, T. Uher, C.M. Kwan and a number of temporary staff members who worked with great care and effort. The author is grateful to D. McGinnis, J. Steimel, J. Lackey, R. Tomlin, and B. Barnes from Fermilab for their cooperation while working on the Fermilab Booster synchrotron. In addition, this author wishes to acknowledge R. Garoby from CERN for his many helpful criticisms, valuable advice and his help to set up the synchronization loop test at the CERN PS Booster synchrotron. While at CERN, the arduous work of J. Evans to interface the prototype system with the CERN beam control system is also acknowledged.

3.4 Vacuum System

(J. Beach)

3.4.1 Overview

The vacuum system includes the beam pipe as well as the pumps and controllers necessary to establish and maintain a suitable high vacuum in the ring. Vacuum requirements in an accelerator arise primarily from the condition that scattering of the beam perticles on the residual gas (air) molecules cause negligible emittance growth. The emittance growth due to residual gas scattering can be estimated using well-known formulae given in, *e.g.* the CERN booklet:[111]

$$\Delta(\beta\gamma\epsilon) = 0.32\lambda P|\ln(1-\eta)|\int_{t_0}^{t_1}\beta^{-2}\gamma^{-1}dt, \tag{3.20}$$

where $\lambda = R/Q$, P is the N_2 equivalent pressure, η is the fraction of the beam particles within in the emittance and β, γ are the relativisticv factors. For a sinusoidal magnet cycle with frequency $f_m = \omega_m/(2\pi)$ to good approximation

$$\int_{t_{inj}}^{t_{extr}}\beta^{-2}\gamma^{-1}dt \approx \pi\frac{\left(\frac{1}{\beta_{inj}}+\frac{1}{\beta_{extr}}\right)}{2\omega_m\left[(\beta_{inj}\gamma_{inj})(\beta_{extr}\gamma_{extr})\right]^{1/2}}. \tag{3.21}$$

For the LEB ring, the relevant machine parameters can be taken from Tables 1.1 and 2.1; $\lambda \approx 7.82$ m, and $\eta \approx 0.95$ (2–σ emittance). Using these parameter values, Eq. (3.20) becomes

$$\Delta(\beta\gamma\epsilon) \approx 0.1 \times P \tag{3.22}$$

and for the emittance growth not to exceed 0.04π mm-mr we get an upper limit of the pressure of about 4×10^{-7} torr. This is well within the range of straightforward vacuum system design.

Besides vacuum containment the vacuum chamber also provides the rf shield for the beam. Care has to be taken not to cause a unnecessary large impedance. This can be caused by transitions in the beam-pipe cross section or gaps at the connection of two segments. Bellows, pumping flanges, sector valves *etc.* can also be cause for extra impedance if not shielded properly.

Those sections of the vacuum chamber located in magnetic elements are subject to rapidly varying magnetic fields, which cause eddy currents. The field distortions created by these currents are not negligible given the fast

cycling rate of the LEB. Steps to reduce the eddy current effects are to reduce the thickness of the material as much as possible and to use material of high resistivity; both of these reduce the amount current generated. The magnetic field generated by the eddy currents can be compensated by correction coils on the vacuum chambers; this approach has been taken at the Brookhaven AGS Booster synchrotron and also been adopted for the LEB dipole chambers.

The LEB magnet lattice has three-fold symmetry: three arcs and three straight sections. Each of the arcs is 143 m in length and consists of four supercells. The length of each straight is 43 m. Each machine superperiod consists of one arc and one straight, and is 190 m in length. The design parameters for the LEB vacuum system are listed in Table 3.27.

Table 3.27: Design parameters of the LEB vacuum system.

Average pressure (no beam)		5×10^{-8}	torr
Average pressure (beam)		1×10^{-7}	torr
Inside aperture	dipole chamber: oval, axes	52×64	mm
	quadrupole chamber: radius	40	mm
	OCD: elliptical, axes	43×80	mm
Temperature rise	max	30	°C
Radiation dose	max	1×10^{8}	rad
Mag. permeability	max	1.02	

The following points require special attention in the design and construction of the vacuum system:

- The contour of the inner wall of the beam chambers and interconnect assemblies should be smooth. Transition pieces should be used whenever necessary.
- Inside welds should be used whenever possible. Outside welds have to be full-penetration welds.
- Thorough cleaning has to be performed before and after machining and before welding and assembly.

- Every part or component has to meet the specific outgassing rates of $< 5 \times 10^{-10}$torr l/s cm^2 at room temperature.
- Leak tightness should be $< 1 \times 10^{-10}$ std cc/s.

3.4.2 Vacuum Chambers

Throughout the ring, there are three different kinds of vacuum chamber—dipole, quadrupole and drift. All the dipole chambers are identical. The quadrupole chambers have 12 different configurations, varying according to the quad packages. There are 15 different lengths of straight drift chambers.

Dipole chamber

The dipole chamber has to meet two electrical requirements:

- The resistivity has to be as high as possible to prevent eddy currents from affecting the beam;
- The walls must be sufficiently conductive to transport the beam image currents smoothly and to contain the bunch wake field.

These requirements can be met by any non-magnetic metal that is suitable for ultra-high vacuum and has relatively high electrical resistance. Based mostly on the experience at the AGS Booster, Inconel 625 has been chosen for the dipole chamber. It has about 75 % greater electrical resistance than 300-series stainless steel, has very low magnetic permeability even after welding, is easy to clean and maintains a low outgassing rate.

Since the beam is bent in the dipoles sagitta has to be taken into account for the dipole chambers. This can be done by using a wide, straight chamber, or using a smaller cross section chamber with the correct bending radius. The second approach has been chosen because wall thickness is reduced thus minimizing the magnet gap.

The cross section is an oval race-track, 66-mm wide and 54-mm high. The tube is built straight initially, and then bent into a radius of 32.709 m. The overall length of the tube is 2.145 m. A cross section of the dipole Chamber is shown in Figure 3.128.

Correction coil Due to the rather large peak $\dot{B}$ ($= dB/dt$) value in the LEB ($\approx$ 38 T/s) field distortions generated by eddy currents in the dipole chamber are sufficiently large to significantly reduce the machine acceptance

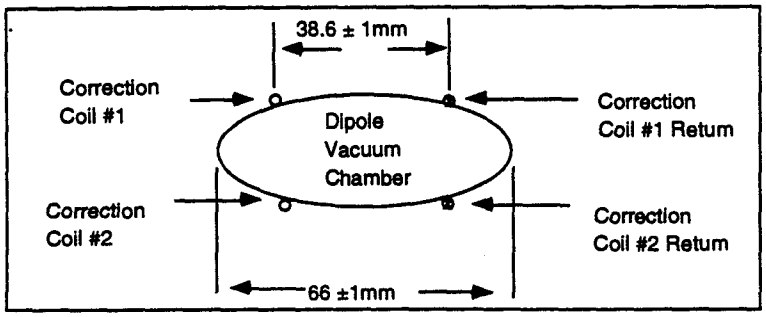

Figure 3.128: Cross section of the dipole vacuum chamber.

and require compensation. The technique pioneered by BNL for the AGS Booster synchrotron uses one or more compensation coils attached over the full length of the vacuum chamber. By mounting the coils to the vacuum chamber, relatively large transverse vacuum chamber movements and chamber to chamber random variation are tolerated as both the field aberrations and their corrections have the same displaced coordinates, thus maintaining correction. The coils are powered by transformer action from a yoke winding of the magnet. In this way, not only the use of a separate power supply is avoided but also the compensation setting becomes independent of the dB/dt value, *i.e.* it is correct at any time during the sinusoidal cycle and also for the slow linear ramp (albeit not required in this mode). Adjustment is provided by variable resistors in the current loop, if required. Even though the peak $\dot{B}$ value of the LEB dipoles exceeds the AGS Booster value by a factor of about four, it has been found that sufficient field correction can be achieved with one coil rather than two. The position of the coils is indicated in Figure 3.128.

The correction coils have to be able to carry about 7 A_{rms} current without degrading, survive the radiation environment and be attachable to the dipole chamber. Since plastic-insulated wire is not, in general, radiation resistant and hard to attach, metallic solid sheathed wire with magnesium oxide insulation between the inner conductor and the sheath has been chosen. For corrosion resistance, a 304 stainless steel sheath is used. A small thickness is desirable for the coil to fit in the magnet gap; the size is specified to be 3-mm outside diameter of the sheath with 20 gauge copper conductor inside. The ends of the coil are to be sealed with epoxy to prevent the MgO from absorbing moisture from air.

Several options have been evaluated for attachment of the correction coils to the dipole chamber: spot welding of metal clamping strips (AGS Booster approach); adhesives; TIG welding of the coil sheath to the chamber; spot welding of the coil sheath to the chamber, and soldering of the coil sheath to the chamber. Soldering has been adopted for production because it is done at a lower temperature than any of the welding techniques, thus preventing possible warping of the tube. Unlike adhesives, the solder strength is not expected to degrade due to radiation.

Prototype A prototype of the chamber has been built. The coils for the prototype are made from off-the-shelf sheathed thermocouple (copper-constantan) wire with 24 gauge inner conductors.** The constantan wire is cut off; only the copper is used. By clamping the coils in place in discrete locations and placing solder patches about 14-mm long every 150 mm the coils are solidly attached to the tube. Eutectic 157 Tin-Silver solder with Eutecsol 682 flux†† have been used for the prototype. Other similar solders are available, but they have not been evaluated. The attachment technique and required size appear to be acceptable.

Quadrupole chamber

For each girder (see Section 3.1.6) one chamber is used. This chamber is welded together from the individual magnet chambers and transition pieces and also incorporates the beam position monitor (BPM). Like the dipole chamber, the quadrupole vacuum chamber is made of Inconel 625. Inside the quadrupoles the chamber cross section is circular with an outer diameter of 83.1 mm; 5-cm long transition pieces are used to connect to the elliptical cross section in the associated orbit corrector dipole. The BPM assembly is keyed to the quadrupole and the connecting pipe has the same diameter as the chamber inside the quadrupole (see Section 3.5.3).

Drift chamber

Since there is no magnetic field in the drift sections, the vacuum chamber in these sections is made of stainless steel with circular cross section.

**Manufactured by Omega Engineering

††Manufactured by Eutectic Corp., Downers Grove, IL

3.4.3 Vacuum Equipment

Pumps

The beam-tube vacuum is maintained by 30 l/s ion pumps; one pump is mounted at one end of each quad chamber for a total of 90. This arrangement assures approximately even spacing about the ring. The system creates an average pressure of 5×10^{-8} torr around the ring after a pumpdown time of 100 h. One controller operates up to 4 ion pumps; the controllers are located and accessible in buildings on the surface.

The pumps are to be Noble Diode Ion pumps or special order standard Diode Pumps with Noble Diode pumping components in the same container. This ensures that adequate pumping capability is available to pump the inert gases, in particular argon.

Bellows Assemblies

Between every two adjacent girders, bellows will be installed. During 10 Hz operation, the beam tube within the dipoles is expected to warm up by 30°C above ambient temperature. In addition, in order to install or remove a girder assembly, there must be some clearance between neighboring flanges to prevent damage to the flanges while lifting or lowering the girder. Each bellows assembly is designed to compress by up to 20 mm in order to satisfy both requirements.

To maintain a low impedance each bellows is shielded by a Be-Cu finger ring that maintains a smooth aperture even through expansion and contraction, as well as lateral offset up to 3 mm. The design of the fingers is based on one that has been used successfully in the LEP collider at CERN.

Four different bellows assembly configurations are used to provide transitions between sections of unlike cross section. Pumping tees of 114.3 mm (4.5″) size are included on two of the bellow configurations as these serve as the 90 locations for ion pumps. Smaller tees are also included on these for attachment of turbomolecular pumps for roughing before starting the ion pumps.

The beam vacuum is protected by sector valves. A fault detected by an ion pump or ion gauge in the same sector causes the valves to close, thus minimizing the loss of vacuum in adjacent sectors. The whole ring will be divided by 101.6 mm (4″) gate valves into 15 vacuum sectors: nine sectors in the arc regions and six sectors in the straights. Five additional gate valves will separate the rf cavity regions, extraction kicker and the injection girder

from other equipment. The valves are air operated with remote position readout. Compressed air is provided in the tunnel for valve operation.

Pumpdown is done through 38 mm (1.5″) hand valves, one per vacuum sector for a total of 20 valves.

Gauges

The vacuum will be monitored from atmospheric pressure down to 10^{-9} torr by pirani gauges, cold cathode gauges and ion pump currents. The pirani gauges, 1 per sector, will be used for rough vacuum. The cold cathode gauges in an "isolated collector inverted magnetron" configuration cover the pressure range from 10^{-2} to 10^{-9} torr. Again, one per sector will be used. The gauge tubes are rugged, have no filament to burn out, and overcome signal losses over the long cable run. A total of 20 tubes will be needed. One gauge controller per vacuum sector will operate 1 pirani and one cold cathode, for a total of 20 controllers.

3.5 Beam Instrumentation and Diagnostics

(R. Webber and R. Aiello)

3.5.1 Background & Overview

The LEB beam, at different times, serves as both a product for delivery to the Collider or the test-beam facility and as a diagnostic probe of the performance of the LEB magnetic lattice, rf systems, and beam tube impedance. It is important that both aspects are considered to determine instrumentation requirements.[112]

Beam instrumentation for the LEB provides for direct measurement of the standard beam parameters: current, loss, position, transverse profile, longitudinal bunch shape, and rf phase. In some instances, these directly measurable parameters serve a useful end in themselves; more often, they provide data from which to derive other properties of the beam and properties of the machine itself. Such beam properties are transverse and longitudinal emittance and momentum spread. Machine parameters include admittance, local apertures, betatron tune, chromaticity, local magnetic lattice functions, and tune and coupling resonances.

During normal LEB operation, as a source of protons for the Collider or test beams, it is primarily the global properties of the beam that are of concern to provide for monitoring and control functions. Sufficient information is typically obtained from only a few monitors in the ring, *e.g.* one current transformer, one or two transverse position pick-ups, one phase monitor, and a small number of loss monitors at critical locations. The local machine properties, deduced by observation of the beam interacting with localized mechanical conditions and electromagnetic fields, are mostly of concern for machine commissioning, performance improvement, troubleshooting and diagnostic purposes. These properties, which are functions of azimuthal position around the ring, include closed-orbit position, betatron amplitude, transverse beam size, and beam loss distribution. Numerous instances of each type of instrument distributed around the ring are required to obtain adequate understanding of the machine.

Beam instrumentation must perform during all phases of machine operation: commissioning, Collider or test-beam operation, and machine troubleshooting and improvement. Commissioning is expected to be characterized by low beam intensity, short injected pulse lengths, the option to vary machine parameters freely, and by somewhat relaxed schedule pressures. During physics operation, the LEB must run at varying intensities

as a reliable, well-oiled machine with suitable instrumentation requiring little dedicated attention. No instrumentation which physically intercepts the beam in any significant way is permitted. Diagnosis of operational problems and machine development and improvement activities may need to be accomplished using dedicated machine cycles interspersed with production cycles and will need to be done over a wide range of beam intensities. Operation with interspersed cycles limits the type of instrumentation allowable for such purposes, *e.g.* slow, destructive scanning wires are not permissible for injection diagnostics if a physics cycle is expected within 100 milliseconds. Diagnosis of serious operational problems will need to be accomplished under conditions of extreme schedule pressure; the ability to quickly and correctly diagnose a source of difficulty is key.

In each operational phase, the machine cycle exhibits one or more of the following uniquely identifiable functional segments: injection, rf capture and bunching, acceleration, transfer synchronization, and extraction. The events and beam characteristics, both static and dynamic, peculiar to each segment define the measurements which must be made and the signals which are available for the purpose.

Injection and extraction are fundamentally single shot events demanding measurements on the time scale of the beam pulse length, a few microseconds. Destructive intercepting monitors are generally allowable, even in the ring under certain conditions, for injection measurements during commissioning, diagnostic, and machine improvement phases. The charge exchange (stripping) process at injection provides free electrons as a signal source and permits independent observation of H^-, neutral, and proton beam trajectories under certain specially arranged circumstances. At injection, the microsecond time-scale macropulse envelope of the beam and the rapidly decaying remnant 428 MHz bunch structure from the Linac are available to produce signals on electromagnetic pick-ups. For extraction, the use of intercepting devices in the ring is severely limited since they may destroy the beam prematurely. The 60 MHz bunch frequency of the beam exists as the prime carrier of information at extraction.

Rf bunching and capture, at the beginning of the LEB cycle, are dynamic phenomena lasting a few milliseconds. During this time 47 MHz beam signals are quickly growing from absence to becoming dominant. Wide-signal-level dynamic range performance of instrumentation is important. Transfer synchronization requires rapid and precise rf phase measurement capability to monitor adiabatic phase matching of the LEB beam to the destination MEB rf buckets.

Table 3.28: Location of beam monitors and value of pertinent lattice parameters.

Function	Device	Slot Length [m]	β_x	β_y	η
Beam Current (fast)	Current Toroid	0.2	24.25	7.76	0
Beam Current (slow)	DC Current Transformer	0.3	9.56	9.97	2.95
Injected Beam Profile	Wire Scanner #1	0.1	10.68	8.92	0
Injected Beam Profile	Wire Scanner #3	0.1	19.18	3.15	0
Bunch Length	Wall Current Monitor	0.2	9.56	9.97	2.95
Rf Feedback (phase)	Wall Current Monitor	0.5	6.46	16.12	0
Rf Feedback (position)	Beam Position Monitor	0.19	12.28	7.97	3.17
Momentum Spread	Residual Gas Monitor	0.5	9.56	9.97	2.95
Vertical Emittance	Residual Gas Monitor	0.5	3.11	31.28	0
Horizontal Emittance	Residual Gas Monitor	0.5	28.46	2.00	0
Horizontal Tune	Pinger Magnet	0.6	25.67	2.00	0
Vertical Tune	Pinger Magnet	0.6	3.09	25.97	0

The acceleration part of the LEB cycle is a continuous and quasi-steady state period. Intercepting instrumentation, other than flying wire devices, are disallowed because of their destructive interaction with the circulating beam. The dominant electromagnetic signals result from the 47–60 MHz bunch frequency. The dynamics during acceleration are associated with the rapid sweeping of the rf frequency through this band during the first tens of milliseconds of the cycle. For constant circulating charge, signals sensitive to beam current grow approximately 30% in amplitude in direct proportion to the increasing particle velocity.

The LEB instrumentation suite, shown in Table 3.28, includes instruments used to measure beam position, loss, current, transverse and longitudinal profile. There are ninety Beam Position Monitors (BPM) and ninety Beam Loss Monitors (BLM), one at each quadrupole location. One BPM provides information also to the rf system for the radial feedback loop. A dc current transformer and one fast current toroid, right after the injection section, are used to measure the beam current on different time scales. Two wire scanners at the injection section provide information on the profile and position of the injected and circulating beam. Two wall current monitors are used to determine beam bunch length during acceleration and to provide phase feedback information to the rf system, respectively. Three residual-gas

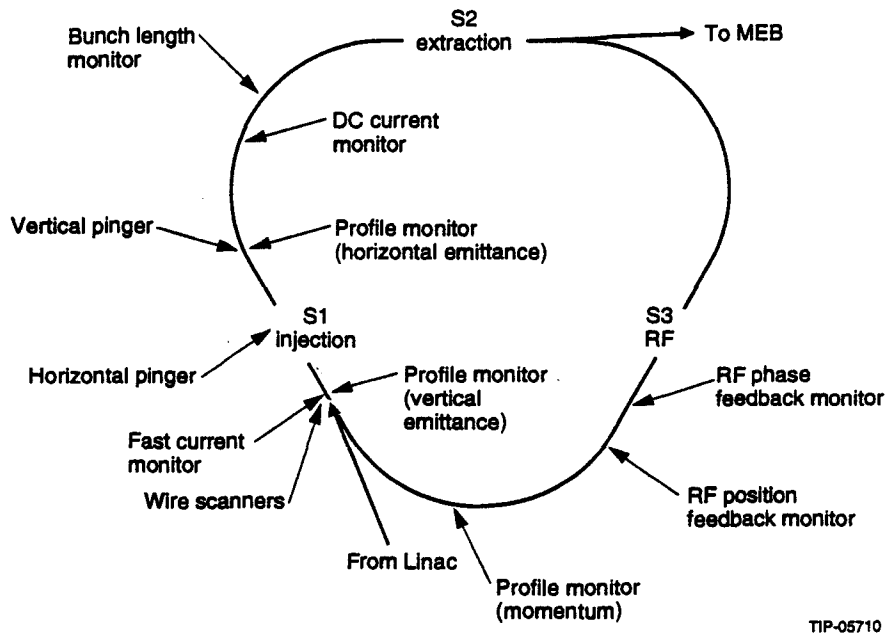

Figure 3.129: Location of beam instrumentation devices in LEB.

profile monitors measure vertical and horizontal emittance and momentum spread. These monitors are non-destructive and provide information during the whole acceleration cycle. Two pinger magnets (small fast kickers), one horizontal and one vertical located at respective high beta locations, are used to perturb the beam during commissioning or machine studies to observe its natural transverse oscillation. Machine parameters such as betatron tune or chromaticity can then be determined.

The monitors' physical lengths and locations in the lattice, with pertinent β function and dispersion values, are shown in Table 3.28 and Figure 3.129.

The numerous implications and demands of the different machine operational modes and acceleration cycle segments require instrumentation with uncomplicated flexibility. Measurement methods and hardware systems to meet these demands for the LEB will be described in some detail. Methods are outlined first assuming certain measurement capabilities; the actual systems planned to satisfy this functionality are then described.

3.5.2 Description of Measurements and Methods

A partial list of the measurements possible with the available set of instruments is here described. Not all measurements can be made during normal operation, since beam perturbation may be needed; and some, like betatron tune or chromaticity, will be made only during commissioning and machine studies.

Closed-Orbit Measurement Knowledge and control of the closed orbit is critical for achievement of maximum beam stability, optimization of acceptance, and minimization of beam loss. The closed-orbit position at any location is calculated by averaging the position as measured with a BPM over numerous passages. In this way, any betatron oscillation of the beam of magnitude A_c can be suppressed. The number of turns required to get resolution Δx at the tune Q is:[113]

$$n \geq \frac{\sin n\pi Q}{\sin \pi Q} \frac{A_c}{\Delta x} \,. \tag{3.23}$$

For example: using the values: $Q = 11.6$, $A_c = 1$ mm, 10 turns are necessary to have 0.1 mm resolution. This is valid as long as the position resolution of any single measurement is not a limiting factor. Such measurements made simultaneously at many locations around the ring provide the required closed-orbit information.

Tune Measurement The machine tune is a measure of the integrated transverse magnetic focusing strength around the ring. Control of the tune value, in a programmatic if not active sense, is essential for stable beam acceleration. For measurement purposes a pinger will be used to impart a transverse impulse to the beam. Observation at one location of the beam's ensuing position oscillation allows determination of the tune. One of the BPMs will digitize and store turn-by-turn position information for analysis. Tune information is calculated from the frequency spectrum.

Emittance Measurement The vertical and horizontal beam emittance are calculated using data from Beam Profile Monitors respectively located at points of large vertical beta, large horizontal beta and zero dispersion. Given the measured beam profile (size) and the expected value of the β functions and dispersion at these points, the emittance value is determined from:

$$\sigma_x = \sqrt{(\beta\epsilon)^2 + \left(\eta\frac{\Delta p}{p}\right)^2} \quad : \tag{3.24}$$

where σ_x = beam size (rms), η = dispersion, ϵ = emittance, β = beta function, and $(\Delta p/p)$ = momentum spread.

Momentum Spread Measurement The Beam Profile Monitor located at a point of small beta and large dispersion, where the transverse beam position is sensitive to energy, provides information useful in determining the momentum spread. The beam size at this location coupled with measurements to determine transverse emittance allow calculation of the momentum spread (see Eq. (3.24)).

Chromaticity Measurement Observing the variation in tune induced by a small change in the radio frequency permits calculation of the chromaticity according to the following equation:

$$\Delta v = \xi\left(\frac{\Delta p}{p}\right) = \frac{\xi}{\eta}\left(\frac{\Delta f}{f}\right) \tag{3.25}$$

with ξ = chromaticity, η is the slip factor, $\eta = \left(\frac{1}{\gamma^2} - \frac{1}{\gamma_t^2}\right)$, p = momentum, f = radio frequency, and v = tune change.

The known relation between variations in momentum and radio frequency makes feasible this method of chromaticity measurement.

Betatron Function Measurement The β function of the magnet lattice along the ring will be measured using the diagnostic pingers and turn-by-turn information from the BPMs. Spectral analysis of the signal from a BPM at any location reveals information about the local amplitude of the induced oscillations. This amplitude is proportional to the square root of the local β function value. The ratio between β functions at two different locations is found by comparing the two spectral measurements.

Phase Advance Measurement The betatron phase advance will be determined using a method similar to the β function measurement. The negative phase difference between the two locations is given by the phase of the two spectrum functions.

Dispersion Measurement Dispersion, the local change in closed-orbit position due to a change in momentum, will be measured by examining the variation of the closed orbit as the radio frequency is varied at a given magnetic bending field value.

Aperture Measurement The Beam Loss Monitor (BLM) system and slow beam-current monitor will be used to measure the machine aperture. A local closed-orbit bump created by corrector magnets is varied in a controlled manner until the amplitude of the perturbation is sufficient to cause a beam loss. Knowing or measuring the amplitude of the perturbation, the local physical aperture can thus be determined.

Local Coupling Parameter The local coupling of horizontal and vertical beam motion will be measured by applying Fast Fourier Transform analysis to digitized BPM information. Knowledge of these coupling parameters can enhance the comprehension and the tuning of the machine.

3.5.3 Instrumentation Systems and Devices

Beam Position Monitors

Overview And Requirements The BPM system is an important tool for beam control.[114] It will:

- Determine the position at injection to steer the injected beam.
- Measure the position after the first turn to close the orbit in the machine.
- Measure the closed orbit during the acceleration cycle.
- Provide information on the turn-by-turn position of the beam to determine certain machine parameters.
- Provide real-time beam position information for the rf feedback system.

The BPM system is specified to have 1 mm *absolute accuracy.* This is the *rms* error between the quadrupole magnetic axis and the reported position of a beam passing on that axis through a BPM. The misalignment between the quadrupole and the BPM mechanical axes is measured in the field by installation alignment survey and can be largely accounted for in reporting

measured beam position. Electronics offset drift and measurement resolution contribute to the absolute accuracy error.

The *resolution* requirement, that is the minimum beam movement that the BPM system is able to detect, is 0.1 mm at 25 mA. The signal-to-noise ratio is the most important parameter limiting resolution.

The processed analog BPM signals are digitized at a turn-by-turn *digitizing rate*. This characterizes the bandwidth required and defines the acquisition system. All BPM channels will have sufficient analog bandwidth to resolve beam position for both injected and circulating beam filling as little as 25% of the LEB circumference. Digitized output data will be available at 10-Hz rate.

The *dynamic range* of the injection and first-turn monitors, since they are useful only for single-turn injection, covers beam currents of 1.5–25 mA. The closed-orbit BPM system dynamic range must extend up to 480 mA, corresponding to the maximum intensity with multiturn injection for test-beam delivery.

The total *linearity error* required is less than 10%. The contribution due to the mechanics shall be corrected by calibrating the monitor on the bench. Electronic nonlinearity will be less than 10% over the center half aperture.

Mechanical Design The BPM pick-ups, 90 in total, are located next to each LEB main quadrupole. Spatial constraints require their placement at the upstream end of the magnet in some locations and at the downstream end in others. A single design, flipped end for end in the two different placements, is used. It is suitable for nestling inside either end of the quadrupole coil overhang with the signal feedthroughs at the outside end for accessibility. A shorted stripline pick-up design satisfies the requirement of electrical non-directionality imposed by this mechanical arrangement. Four electrodes, each 15 cm in length and subtending a 70-degree angle on an 8-cm diameter, are incorporated into each pick-up to allow two-plane observation. Each stripline electrode is designed with 50 Ω characteristic impedance.[115] The signal feedthroughs are radiation resistant and impedance matched. Figure 3.130 shows the BPM assembly.

Alignment fiducials referenced to the mechanical center of the BPM are provided. A field installation survey will measure the displacement between each quadrupole axis and the BPM mechanical center. Displacement between the mechanical and electrical center of each BPM will be measured in the laboratory.

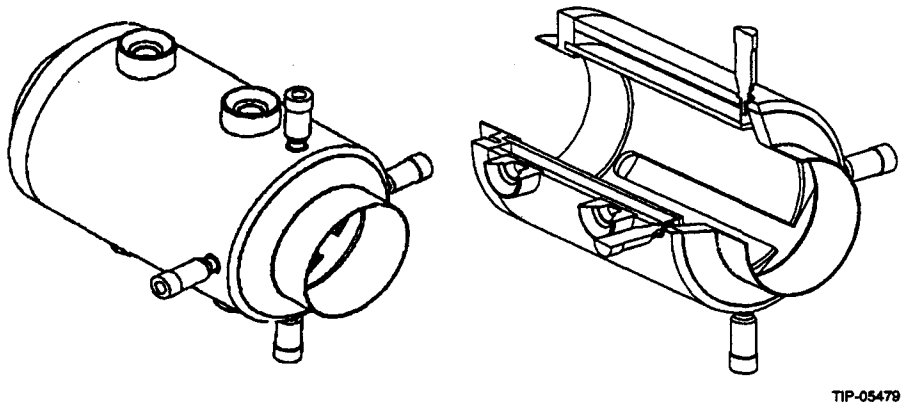

Figure 3.130: BPM mechanical assembly.

Electronics Design The position information is derived by processing the signals from the four striplines of a pick-up. The power ratio of the signals from two opposite striplines is proportional to the beam position in the respective plane.[116,117] The log-ratio technique is used to calculate the beam position, according to Eq. (3.26), where S_x is the position sensitivity of the pick-up expressed in dB/mm, and A and B are the voltages at the opposite striplines.

$$x = \frac{20}{S_x} \log \frac{A}{B} \,. \tag{3.26}$$

The signal processing steps for position measurement are as follows:

- Logarithmically, amplitude demodulate the separate signals.
- Measure the difference and the sum of the signals.
- Digitize the difference and sum, then store the values in local memory.
- Calculate the beam position using the stored difference and sum values.

The log-ratio technique is realized with AD640 demodulating logarithmic amplifiers.[118,119*] A single monolithic device produces a linear response through an input dynamic range of nearly 50 dB; a cascaded pair can extend the dynamic range to over 70 dB. Figure 3.131 is a block diagram of two channels of the position electronics. An rf transformer precedes the logarithmic amplifiers to facilitate impedance matching, supply a differential input

*Manufactured by Analog Devices.

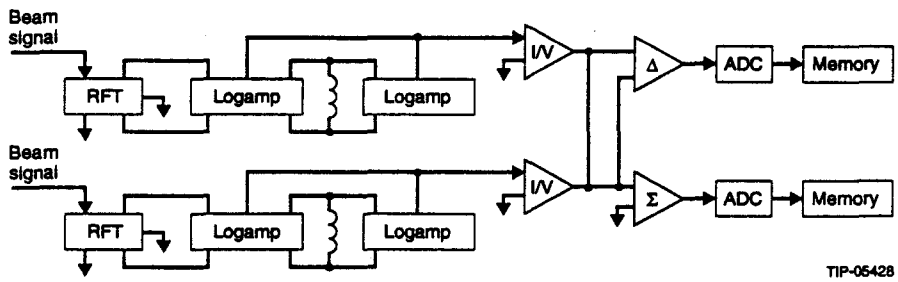

Figure 3.131: Log-ratio position monitor electronics.

to the logarithmic amplifier, and provide a dc ground reference through the center-tapped secondary.

The interstage filter limits the bandwidth of the system, thus lowering the noise floor. The current outputs of the two logarithmic amplifiers are summed at the inverting input of an AD844,† which is optimized for current-to-voltage applications. Two additional op-amp circuits provide the dc sum and difference signals which are then digitized by 12 bit ADCs and stored in local memory for the position calculation. The ADC trigger is provided by the LEB precision timing system and is turn-by-turn synchronous with the beam.

The analog electronics is housed in a shielded enclosure on a VXI digital motherboard.[120] A photograph of the digital module, including the analog front end, is shown in Figure 3.132. Four complete channels, each with an ADC and 64 Kwords of memory, are housed in a single-wide VXI module. For closed-orbit calculation and signal-to-noise improvement, a programmable controller averages a preselected number of digitized turn-by-turn data.

Measurement Strategy The LEB beam presents different signal spectra at different times during the acceleration cycle. During the first 10 turns, groups of nine 428 MHz Linac bunches are captured into individual 47.5 MHz LEB bunches. The proton beam is then accelerated and the LEB rf frequency sweeps to 60 MHz. The beam signal spectrum reflects that of the rf. As the 428 MHz component decreases, the 47.5 MHz increases, reaching full value about 40 turns after injection. This is shown in Figure 3.133a.

†Manufactured by Analog Devices.

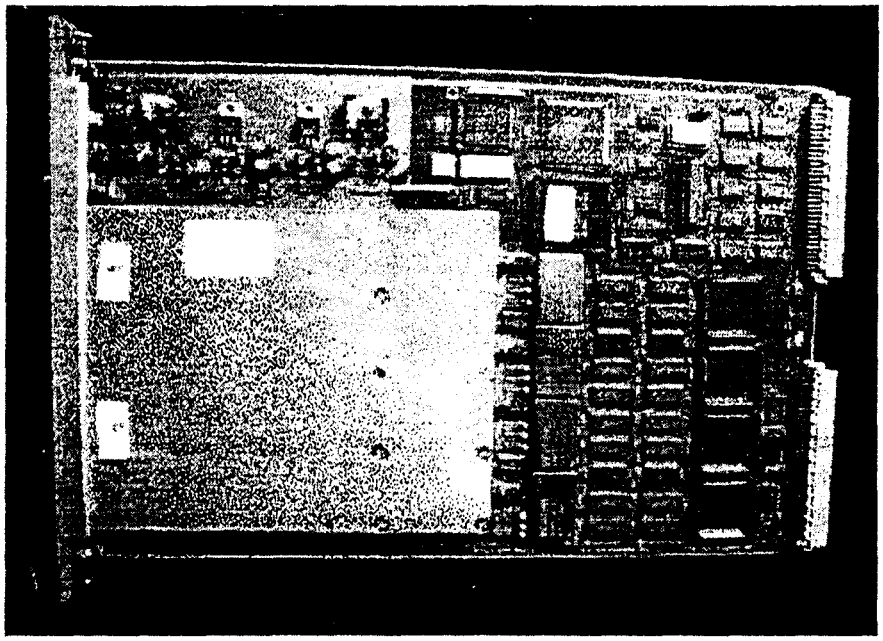

Figure 3.132: VXIbus beam position module.

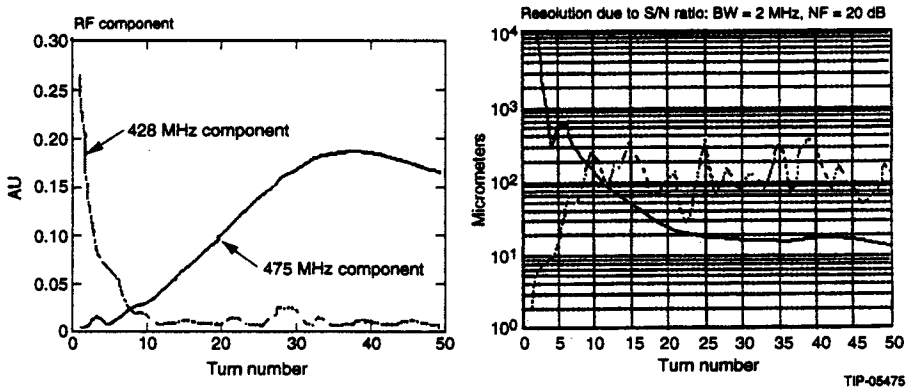

Figure 3.133: BPM system dynamics: a) beam signal spectral amplitudes and b) BPM electronics resolution for first 50 turns after injection.

During the first 10 turns, the 47.5 MHz signal component is too small to be used for beam position measurement purposes. To accommodate this, two different sets of electronics are employed, the injection (or first-turn) electronics and the closed-orbit electronics. Both utilize the circuits described above, but the injection electronics includes a frequency down-converter at the front end to produce a 60-MHz signal proportional to the 428-MHz component. All 90 monitors are equipped with the closed-orbit electronics for both horizontal and vertical planes, only a small number also have the injection measurement capability.

The closed-orbit BPM electronics is sensitive to the fundamental rf component of the beam and must therefore be receptive to different frequencies at different times during the acceleration cycle. The electronics circuit described in the previous section offers sufficient bandwidth to provide satisfactory performance throughout the acceleration cycle, from 47.5 MHz to 60 MHz. The system has been successfully tested at the Fermilab Booster, where the rf frequency spectrum has similar characteristics.

The resolution for each of the two sets of electronics versus the number of turns after injection is shown in Figure 3.133b. It can be seen that as the resolution of the 428-MHz system degrades, that of the 47.5-MHz system improves. The two intercept at about ten turns.

It is important to point out that the "injection BPMs" are useful only for single-turn injection or for the first turn of multiturn injection. The reason for this is not only that the 428-MHz signal decays due to normal debunching

of the beam; the phase of the injected bunches from turn to turn is also not guaranteed. Bunches of any subsequent injected turn may interlace with those of previous turns in any pattern. Therefore, the Linac rf component will be quite dynamic and may be too low to be measured. For this reason the addition of low-frequency electronics sensitive to the revolution frequency component in the beam spectrum has been contemplated.

Prototype Performance Performance of the BPM electronics is shown in Figure 3.134. The horizontal axis signal scales are given in decibel units; 20 dB corresponds to a factor of ten in beam current. These plots have been generated with data obtained from bench tests of prototype electronics using inputs from a test signal generator. Figure 3.134a shows a plot of the position output over the full dynamic range of the circuitry. Different input signal powers and power ratios have been supplied to the electronics to simulate different beam currents and beam displacements. The center vertical trace represents the "beam on center" case and steps between vertical traces correspond to 1 dB changes in the differential input signals. Figure 3.134 shows the expected beam position resolution available through the electronics.[121] The measured resolution of the BPM electronics as a function of input power is shown compared with the ideal case of noiseless electronics. This presentation allows calculation of the electronics' noise figure by measuring the distance, on the horizontal axis, between the ideal and the measured plots.

The prototype has been tested at the Fermilab Booster in April 1993.[118] The signals available in the LEB and in the Fermilab Booster present similar characteristics, the latter sweeping the rf frequency from 30 MHz to 53 MHz in 33 ms.

Measurements have been taken with the test setup shown in Figure 3.135. Signals A and B originated at a set of horizontal beam pickups. Normally these signals are directly connected through coaxial cables to the inputs of the Fermilab rf Beam Position Module which incorporates the AM/PM method of beam detection. For the purpose of this test, each signal is split and sent to both the rf module and the log-ratio circuit to be tested. The outputs of both circuits are digitized by a common ADC module running at a sample frequency synchronized to the Booster revolution frequency. An injection synchronization pulse arrives at the beginning of the Booster cycle and arms the ADC. The Trigger Generator produces a revolution-frequency synchronized pulse train tracking the frequency sweep of the Booster with

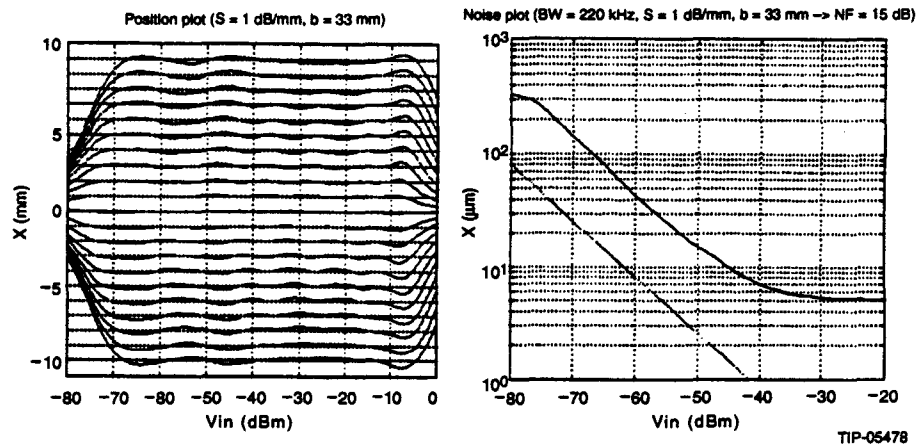

Figure 3.134: BPM electronics performance: a) measured *vs.* ideal position output signal; b) expected resolution *vs.* ideal case of noiseless electronics.

the low-level rf. This signal triggers the Pulse Generator to clock the ADC module for digitization on every fifth revolution, the fastest rate possible for the setup used.

A plot of beam position versus the Booster turn number, as measured using the log-ratio circuit, is shown in Figure 3.136a. Corresponding data from the rf module is used for comparison. The difference between the position values as given by the log-ratio circuit and the rf module is shown in Figure 3.136b.

After the first 4000 turns, agreement is as good as expected given the accuracy of the two systems. The typical error due to electronic offsets in the Booster rf module is approximately 0.5 mm. The uncertainty of the log-ratio circuit, due to ripple caused by saturating gain stages internal to the logarithmic amplifier, is as high as ± 0.1 mm given the Booster pick-up differential sensitivity of 0.52 dB/mm. Twelve bit ADC's are used in the digitizer. With a half bit of noise, ± 16 μm resolution could be realized with the log-ratio electronics and ± 165 μm with the rf module.

During the first 4000 turns several other factors must be considered in order to be able to understand Figure 3.136b. In the early part of the cycle the beam signal intensity increases by about 10 dB and the revolution frequency sweeps from 30 MHz to 47 MHz. Error contributions by the log-ratio electronics are due to both amplitude nonlinearity and nonuniform frequency response. During this time the electronics is processing the beam

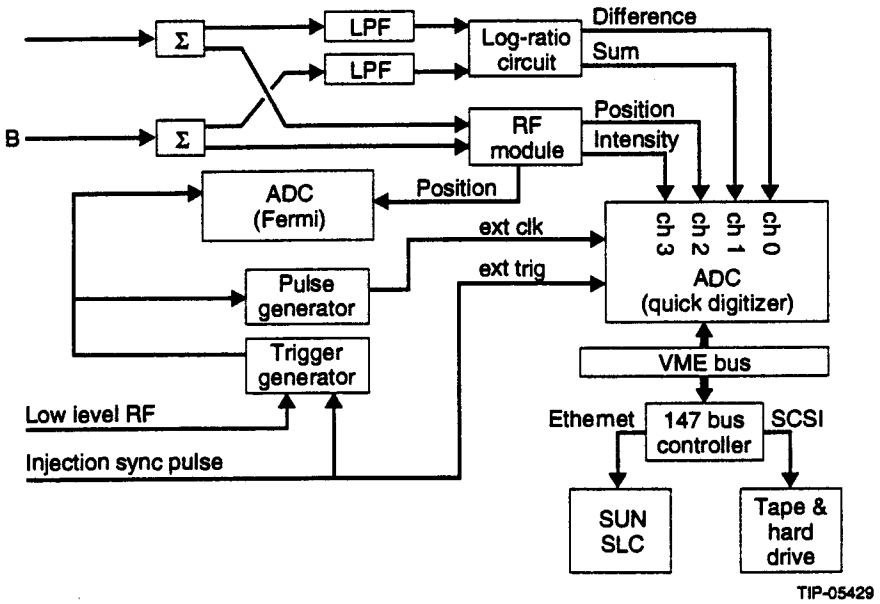

Figure 3.135: Block diagram of the log-ratio, AM/PM position test conducted at Fermilab.

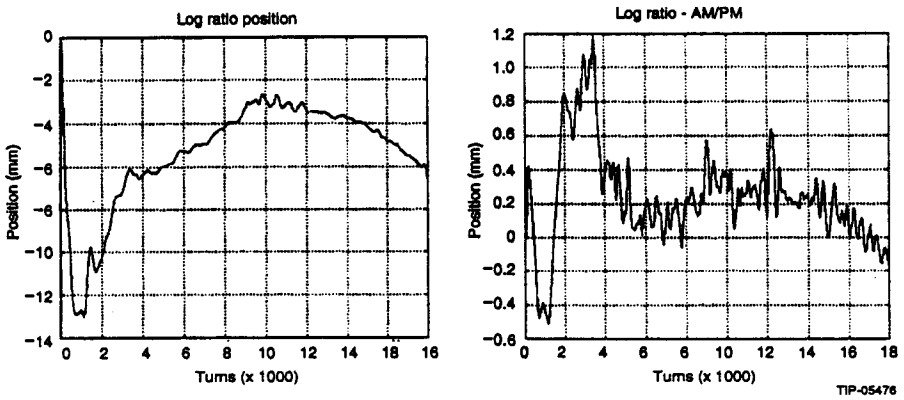

Figure 3.136: Comparison of LEB and Fermilab BPM electronics performance: a) position output through one acceleration cycle. b) difference between outputs of the log-ratio circuit and the AM/PM module.

signal through its maximum dynamic range. Errors due to common mode amplitude sensitivity appear as the ripples in Figure 3.134a, and correspond to ± 0.1 mm. The expected amount of position deviation due to non-flat frequency response is about 0.08 mm. These numbers have been verified by bench testing at the SSC. Errors due to the AM/PM electronics are more difficult to assess because an rf module was not available for lab testing. However, a few known factors can account for at least part of the total error. During the early period of acceleration the beam is between 7 mm and 13 mm off center; considering the Booster pick-up sensitivity, this is in the range where the AM/PM response becomes nonlinear. Although a correction formula is used to calculate position, there is a residual error associated with this non-linearity. Important also is the error due to the frequency response. Down converters and limiters both contribute to the total error band which could be as large as ± 0.4 mm.

The contributions of all these uncertainties amount to about 1 mm, consistent with the data shown in Figure 3.136b.

Beam Loss Monitors

Overview And Requirements The primary purpose of the Beam Loss Monitor (BLM) system is to protect accelerator components from damage due to loss of protons from the beam.[122] Whereas BPMs are sensitive to the beam centroid, loss monitors are sensitive to the beam periphery. Consequently, the BLMs can provide the first indication of large emittance growth, a large beam halo, setting errors of steering and focusing elements, *etc.*

BLM detectors will be placed at each main quadrupole magnet of the LEB ring, *i.e.* where the beam envelope is at maximum size. FNAL Tevatron style ionization detectors or equivalent provide adequate sensitivity for the LEB.[123] With a minimum response of 10 mrad/s, the detectable-loss-rate threshold is approximately 1.0×10^9 protons/s at injection and 1.0×10^8 protons/s at full LEB energy (at 1 m from a point loss at a shallow angle). Signal risetime from the detector is approximately 10 μs.

The BLM requirements are shown in Table 3.29.

Electronic Design A block diagram of the proposed electronics system is shown in Figure 3.137. A prototype of this system has been built and tested for the Linac BLM system.

Operationally, the fast analog integrator provides a times 10 charge gain and stretches the signal so that a sampling ADC of moderate speed can

Table 3.29: Beam loss monitor requirements.

Property	LEB Value
Sensitivity (Injection)	1.0×10^9 protons/s
(Extraction)	1.0×10^8 protons/s
Dynamic Range	10 mrads–100 rad/s
Detector Spacing	$\sim$ 6 m
Pulse Rise Time	$< 10\ \mu$s
Digital Integration Time	100 ms

follow the time development of the beam loss. The fast integrator exhibits a small ($\sim$ 0.1 mV) and stable offset, noise less than 1 mV peak-to-peak, and adequate linearity. Data will be digitized at 10-kHz rate, stored and digitally integrated. Approximately once every LEB machine cycle (0.1 seconds) the digitally integrated data will be sent to the central control system. Locally, the latest 64-K data points are retained for transfer to the central computer upon request. The electronic system for the BLMs will be implemented in a standard format, VXI or VME, the former being preferred because it has been designed to handle analog signals, includes a $\pm$24 V supply, electronic shielding, and larger board space. In fact, the digital portion of the Beam Position Monitor electronics board, already designed and prototyped in the VXI format and shown in Figure 3.132, can serve as the digital portion of a BLM electronics board with very few changes. In addition to the data acquisition board, the BLM detectors require a high-voltage bias supply.

Since economics suggest the wisdom of maintaining common system designs across the several SSC synchrotrons, LEB benefits from BLM system features driven by the critical demands placed those systems in the high energy superconducting machines. It is expected that the control system will monitor the status of the crates containing the BLM electronics. This monitoring includes temperature, air flow, over and under voltage on all the standard power supply voltages, and crate control status. These status parameters are read on a continuous 10-Hz basis. In addition, each BLM board contains a set of status and control registers. These registers hold power up test results, module identification, and default parameters which need to be read only after a restart.

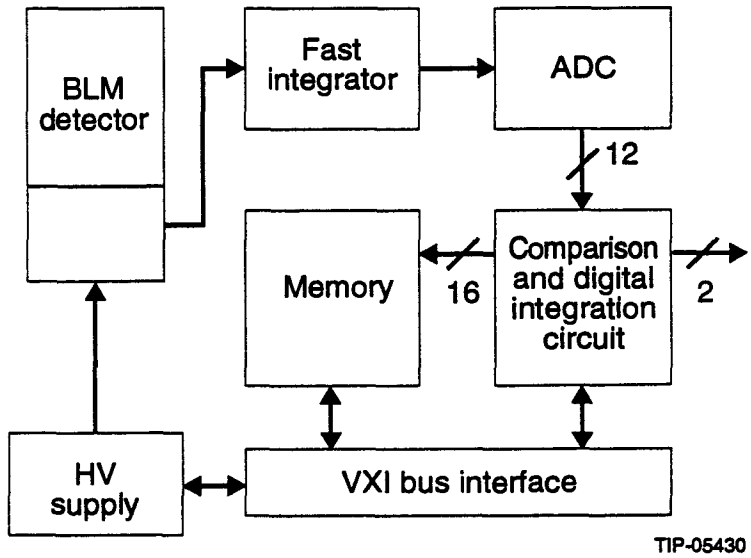

Figure 3.137: BLM electronics block diagram: BLM detector in LEB tunnel, electronics in VXI chassis in surface building.

Beam Profile Monitors

The Beam Profile Monitor system determines the transverse profile of the beam at injection and during acceleration. Thus, the Beam Profile Monitors provide data to determine:

- Emittance at injection (after stripper foil)
- Transverse horizontal emittance (at large β_h, $\eta = 0$ location)
- Transverse vertical emittance (at large β_v location)
- Momentum spread (at large η, small β_h location)

Beam Profile At Injection The beam profile monitor for injection is realized with two horizontally mounted wire scanners. Each scanner has a tungsten wire in the vertical plane to monitor the horizontal profile and position. A stepping motor capable of stepping the wire in submillimeter increments controls the wire position.

One monitor, located between the injection septum magnet and the second orbit bump magnet, will intercept either the injected H^- beam or the

closed-orbit path of any circulating proton beam. The second, located just downstream of the last bump magnet, can intercept the circulating beam in the closed-orbit position. Figure 3.138 is an artist's sketch, based on Fermilab data, showing the turn-by-turn profiles expected to be generated with data from the first monitor at injection. Such a plot is built up from turn-by-turn wire signal data samples as the wire is slowly stepped across the aperture during a number of injections. The negative profiles are of the incoming H^- beam. This beam is stripped to protons, which produce a positive polarity signal and are seen to move off the foil into the closed-orbit position.

For thin wires with thicknesses of a few hundred μm, the losses on a turn-by-turn basis are small and readily calculable. Effective beam profiles can be generated for up to 60 turns before wire distortions significantly alter the beam characteristics.

Foil scattering can be studied with this kind of monitor by comparing 1- and 2-turn injection and varying the number of passes a low-intensity beam makes through the foil. Using the low-intensity results, foil losses can be subtracted from high-intensity, multi-turn injection data, thereby allowing a quantitative look at space-charge blow-up.

A second use of the wire shall be to study intensity and position variations within an injected beam pulse. If the time interval at which the wire readout occurs is set to a fraction of the total time span of the beam pulse, individual profiles can be generated which represent a particular position along the pulse.

Beam Profile During Acceleration To obtain beam profile measurements throughout the acceleration cycle, non-destructive methods must be used. A residual-gas ionization type monitor[124] with a fast data acquisition system will be used for this purpose. The proton beam generates electron-ion pairs by scattering the residual gas in the vacuum chamber; the generated ions are accelerated by an electric field and their signal is amplified by a microchannel plate. The resultant electrons strike an array detector which collects the charge. The read-out electronics convert this charge into a voltage to be digitized and stored in local memory. Observation of fast growth requires the monitor to provide a profile measurement on the time scale of 20 μs. Slow growth mechanisms, on the time scale of 1 ms, relax the timing and allow trade-in of speed for improved accuracy. The system can store

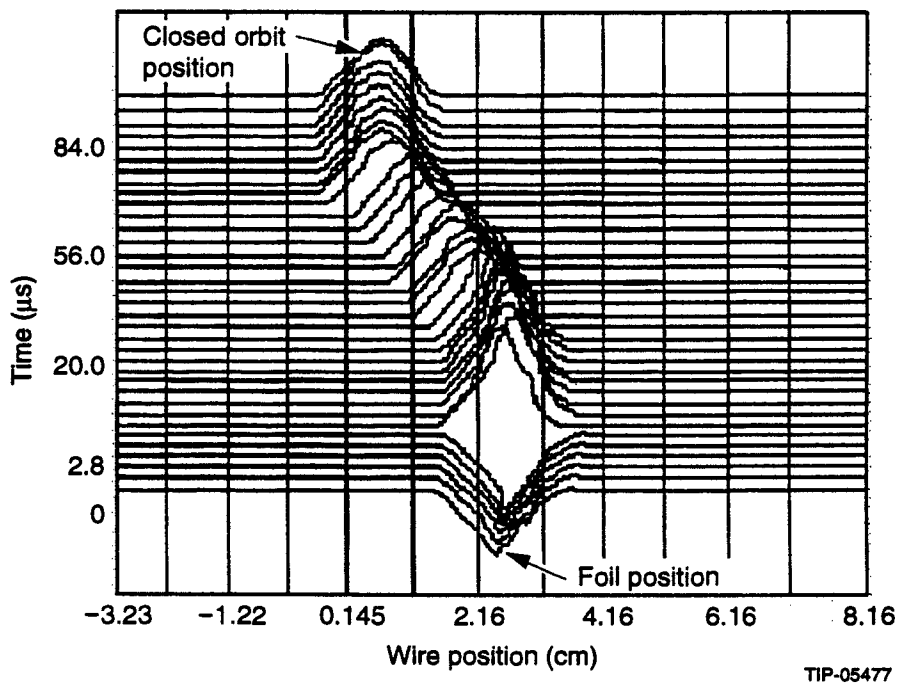

Figure 3.138: Turn-by-turn profile at injection upstream of second orbit bump magnet.

digitized data corresponding to a maximum of 25 measurements per cycle in local memory.

The different modes of operation are here summarized:

- Fast Mode: will measure the emittance growth immediately after injection. The emittance will increase by a factor of two in one synchrotron oscillation (< 20 turns).

- Slow and Cycle Mode: will measure a slow growth at any time during the machine cycle.

Specifications are given in Table 3.30.

Table 3.30: Beam profile measurement requirements.

Parameter	Fast	Slow	Cycle
Integration Time	< 20 μs	< 1 ms	< 1 ms
Repetition	50 μs	2 ms	2 ms
Emittance Resolution	20%	5%	20%
Profile Resolution	10%	2.5%	10%
Number of Measurements/Cycle	> 5	> 5	> 25

Longitudinal Profile and Beam Rf Phase The bunch length (1σ) of the beam, changes from 630 mm to 140 mm during the acceleration cycle. This corresponds to a change from 3 ns to 0.5 ns in the time domain. A high-frequency response device is required for observing such short bunch lengths. The measurement will be made using signals from a wall current monitor,[125] located in the A2 arc sector. This device is realized with a number of resistors bypassing a ceramic break in the beam pipe. The image current flowing through the resistors generates a voltage drop proportional to the beam current. This signal is then transmitted through a coaxial cable to fast electronics. The wall current monitor can provide signals with a bandwidth up to 6 GHz.

A second monitor of the same type, located in the S3 rf straight section, is used to provide information to the rf system for the phase feedback.

Beam Current and H^- Stripping Monitors

A current toroid with a few MHz bandwidth, just downstream of the injection section, will measure the injected beam current pulse and facilitate observation of intensity variations during that pulse.

A dc responding current transformer (DCT) will be used to measure beam current during acceleration.[126] The DCT provides dc measurement stability accompanied by microampere resolution and accuracy. The time-varying velocity of the beam during acceleration must be taken into account when using a beam current measurement to determine the number of particles or charge in the beam. For constant circulating charge, the current increases approximately 30% from injection to extraction energy.

Another tool, useful to monitor the injection process, is the so called e^- catcher, a metallic electrode largely enclosing the H^- stripping foil. Biased with a positive potential, the e^- catcher collects low-energy electrons from the vicinity of the foil. The signal has two components: electrons liberated from the H^- ions by the stripping process and secondary emission electrons due to circulating protons passing through the foil on the 'bumped' injection orbit. A typical signal expected at injection is shown schematically in Figure 3.139. The progression of the injection process can be observed with such a signal. The stripped-electron signal component is present only for the period of time that H^- beam is actually injecting into the LEB. The secondary electron component shows: the turn-by-turn buildup of circulating proton beam in the LEB, the circulating beam while on an orbit that continues to intercept the foil, and a smooth transition to zero as the decaying orbit bump magnitude sweeps the beam off the foil onto the accelerating orbit. This device provides the only direct method to observe the stripping process and numerous other important injection phenomena, including the relative timing of the orbit bump magnet pulse. The signal also permits direct diagnosis of a stripping foil failure.

Consideration is also being given to instrumenting another device to be located just downstream of the third or fourth orbit bump magnet. This device would intercept and detect un-stripped H^- ions to monitor injection stripping efficiency and serve as an additional indicator of foil failure.

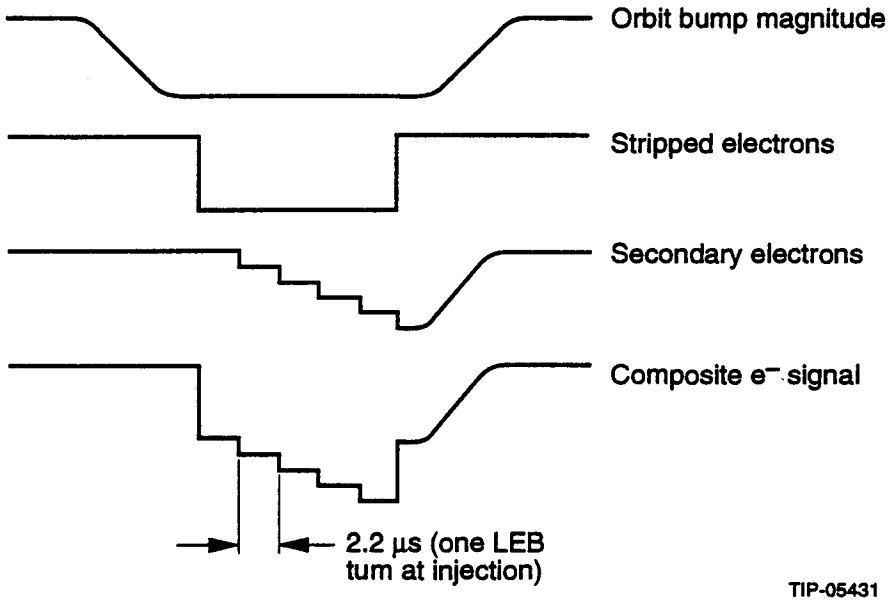

Figure 3.139: Example of e^- catcher signal during 5 turn injection.

Acknowledgements

The authors/editors of this chapter, G. Roberto Aiello and Robert C. Webber wish to acknowledge contributions to the text by Ronald Johnson, Mark Mills, and Alan Jones. The technical designs and accomplishments described herein are a tribute to them as well as to Don Martin, Rudolfo Gonzalez, Pat Evans, Tony Hawkins and the entire SSC Beam Instrumentation Department.

3.6 The LEB Control System

(R. Bork)

3.6.1 Introduction

The general requirements for the LEB Control System (LEBCS) are similar to those for other accelerator control systems. The system must provide supervisory control, an infrastructure for system integration and individual system hardware and application software. Since the LEB is one of the four accelerators making up the SSC injector chain, the LEBCS must also provide close integration with the other injectors and, in particular, the Collider. The LEB also operates at the highest revolution frequency of the injector synchrotrons, and therefore has higher data acquisition and transmission rates which must be dealt with.

This section is intended to cover the general requirements for LEB controls, as well as an overview of the design and philosophy of the control system to meet these requirements. Detailed requirements and design materials can be found in the LEBCS requirements document[127] and the LEB control system preliminary design review materials.[128]

3.6.2 General Requirements

Supervisory Control Requirements

The supervisory control system has to provide the following general functions:

1. Operator consoles with interactive display capabilities. These should provide multi-media capabilities with windowing systems and video display functions.

2. Data archival and retrieval systems. These log and store slow periodic data, such as standard process control data and operator actions, alarm and warning messages, and fast diagnostic data, typically collected as large array sets.

3. Compute servers. They allow for physics analysis software and high-level control software, such as orbit correction algorithms, to be run and interact with the lower levels of the system.

4. Management Information System (MIS). This allows data from the LEBCS to be accessed by other systems to allow viewing at other

sites and data to be combined with other data sources for report and documentation generation.

5. Provisions for local control of equipment during commissioning and maintenance.

Control System Infrastructure Requirements

The controls infrastructure must provide a common environment for interconnection and integration of the LEBCS as a whole. This includes:

1. A communication system, which provides deterministic data transmission within and between individual equipment control systems, with a total bandwidth > 100 Mbits/s.

2. A common software application development package which provides:

   - Operator interface software to meet the requirements listed above for operator systems
   - Realtime capabilities for front end equipment control
   - Network communication capabilities
   - Tools to aid in and accelerate the application development process
   - Application programmer's interface which readily allows data to be read in from/written to the control system.

3. Standard front end interfaces to equipment to be monitored/controlled

4. A beam permit system. The LEB communicates its readiness to accept beam to the Linac beam permit system which allows/disallows injector operation. This requires the LEBCS to verify that all LEB systems are operational and ready for beam from the Linac 20 to 50 ms prior to each LEB cycle and to transmit a ready/not ready for beam signal to the Linac beam permit system at 10 ms (± 5 ms) prior to the begin of an LEB cycle.

Individual System Requirements

Finally, the LEBCS must provide system-specific control hardware and application software. Requirements for this vary by system. The systems involved in the LEB are rf, ring magnet power system (RMPS), corrector

magnet power system (CMPS), beam instrumentation, PASS, low conductivity water (LCW) and vacuum. The number of anticipated I/O channels is shown in Table 3.31, broken down by system.

Table 3.31: LEB discrete I/O channels (approx.).

System	Digital I/O	Analog I/O	Totals
Rf System	2400	640	3040
RMPS	350	30	380
CMPS	4104	912	5016
BI	294	922	1216
Vacuum	336	250	586
LCW	76	48	124
PASS	700	0	700
TOTAL	8260	2802	11062

Corrector Magnet Power Supply The LEBCS must provide controls for 244 correction magnets grouped as shown in Table 3.9 of Section 3.2.2 of this document. The interface to the CMPS power supplies is defined to be at the input of the Digital to Analog Converter (DAC).[129] This puts the task of the CMPS current program onto the LEBCS. In particular, the LEBCS is required to:

- Transmit control and current settings to each power supply at up to 10 KHz;
- Read back power supply status, voltage, and current information from each power supply at up to 10 KHz;
- Operate each power supply in a ramped or dc mode;
- Provide ramp generation software;
- Provide ability to operate magnets individually, by family, or as a machine.

Beam Instrumentation Requirements The LEBCS has to provide all equipment and software between the front-end interface modules and the high-level application code; which are developed by other groups. The instruments to be operated are given in Section 3.5. Primarily, there are 90 Beam Position Monitors (BPM) and 90 Beam Loss Monitors (BLM), plus about 20 other specialized diagnostic devices.

The LEBCS must acquire data from these instruments and provide it to the high-level application codes operating in a compute server at the SSCL Main Control Room (MCR). These codes perform the machine tuning and operating tasks as, outlined in Section 4.2.

Vacuum and LCW System Requirements For the Vacuum and LCW systems, the LEBCS is required to provide all equipment and software down to the sensor level. The LEB contains one LCW plant along with its distribution system to each service building. Total I/O channel count is 132. The vacuum system is distributed throughout the LEB with a total of 536 I/O channels.

3.6.3 Design Approach

The design of the LEBCS has been chosen to be consistent with the Global Control System (GCS) for the SSCL. The LEB is one of five accelerators in the SSCL complex, and based on requirements from all of these machines, a GCS infrastructure has been designed and standards established. The overall design approach has been to establish and verify the requirements and design to them. This appears simple enough, but often requirements are put together piece-meal and drift in from all different groups and factions. Often they can be "desires" rather than requirements, which can place a heavy burden on a system design, both technically and in cost.

It has been attempted not to "reinvent the wheel." Much has been previously developed at other labs and commercially, and this should be drawn on to the extent possible.

Standards have had to be developed early on. Controls for the SSCL accelerators are large, complex systems. Use of standards enhance maintainability and interchangeability, provide for a broader knowledge base for technical support for both hardware and software, and reduce the number of types of spare parts and training required. As much as possible, these standards should be derived from commercial standards. This allows a larger

selection of vendors and products, and would allow SSCL to make use of their technological advances, driven by the market, over the years.

Finally, as much equipment/software as possible should be acquired commercially. This reduces the amount of manpower required to develop a system, as the task becomes more one of system integration.

3.6.4 Infrastructure Design

For the infrastructure of the control system, the LEBCS incorporates the GACS design.[130,131] This design and the design standards are discussed in the following sections.

Front Ends

Front End Crates Front-end equipment provides the I/O channel interfaces into the control system. VME and VXI have been chosen as the bus structures to provide this front end capability. These follow industry and IEEE standards widely accepted at other laboratories, which provide a greater selection of components and new products than typical "lab-only" standards tend to have, plus multi-vendor support for I/O modules. Both VME and VXI provide local, multiple processor capability with various processor boards available having differing process capabilities. Highly reliable I/O modules can be found, which have MTBF figures approximating those of commercial process-control modules.

VME is to be preferred wherever possible over VXI due to the cost difference. VXI should be limited to applications which require either the additional EMI shielding or larger board space which VXI provides over VME.

While VME/VXI provide bus standards, the crate housings, air flow, *etc.* are not specified in the standards. Specifications for these parameters have been developed at SSCL and some units have been delivered and tested. For the LEBCS front ends, about 100 units would be required.

Front End Processors Each VME/VXI crate is to be equipped with its own processor module, known as an Input/Output Controller (IOC). This allows for a distributed processing system. The advantages of this are:

- Independence of systems
- Single processor failure will not cause failure of an entire system or geographical control area
- Local checkout of subsystems during commissioning and maintenance without reliance on a communication system
- Continued subsystem operation if the communication system goes down
- Modular development and commissioning of control application software by subsystem

The processor board chosen as the standard for most applications is a VME 162 module.[‡‡] It comes with a 68040 processor and up to 8 MBytes of RAM and serial interface port. It has been chosen for its processing performance and relatively low cost as compared with other units. Bus adapters have been built to allow this module to be placed in VXI crates. Though this does not allow for full VXI capability, systems within the LEB using VXI are doing so mainly for the shielding and board size attributes of VXI and therefore only require the VME processor capabilities. VXI processors available at this time tend to be limited in performance and cost appreciably more than the VME 162.

Communications

The area of network communications is perhaps where the LEBCS differs most from previous accelerator control systems. It has been decided to use telecommunication industry equipment and standards rather than the typical computer networks of Ethernet, FDDI, *etc.* for backbone services. While this choice has been driven more by the requirements of the Collider and the large distances involved with that machine, it is also to be used on the LEB to keep a single standard for SSCL. A layout of the system is shown in Figure 3.140.

Communication Backbone The network highway which interconnects the processors in the six LEB service buildings and the SSCL main control building is a Synchronous Optical NETwork (SONET).[132] To meet anticipated bandwidth requirements, OC-3 (155 Mbits/sec) has been chosen. At

[‡‡] Manufactured by Motorola, Inc.

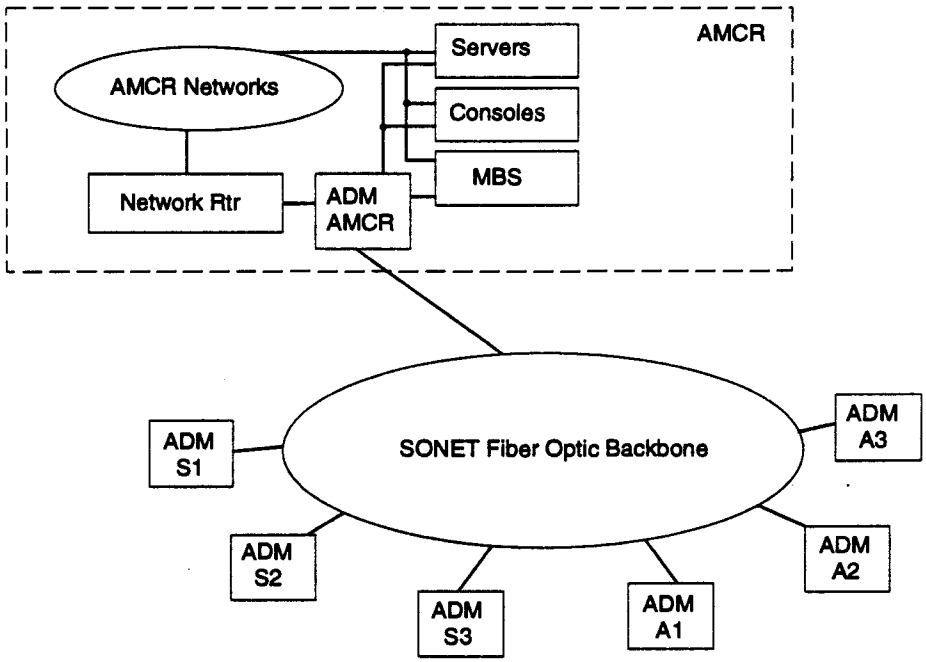

Figure 3.140: LEB control system communications infrastructure.

each service building and the AMCR, an Add Drop Multiplexer (ADM) is to be installed, with OC-3 modules to facilitate connection onto this network and T1 modules for connection to local VME/VXI IOC. Single-mode fibers connect the ADM to complete the backbone. Single-mode fiber has been chosen over multimode because of its higher tolerance to a radiation environment. For redundancy, dual fibers are used. The features of this system as it is laid out are:

- High reliability. Telecommunication equipment typically has a higher Mean Time Between Failure (MTBF) rating and a longer service life than standard LAN systems.
- Point-to-point deterministic communication. Telecommunication equipment runs at a defined 8 KHz rate, which is then "time-division-multiplexed" onto standard higher bandwidth transmission media, such as OC1 or OC3. The deterministic nature is used for both standard inter-processor communication and for transmission of synchronous data to all processors in the system, as described later.

- Private data links and data "grooming." Telecommunication links are based on DS0 (64 Kbit/sec) modules as the basic building block. Higher speed links, such as T1, OC-1, OC-3, *etc.* place more of these DS0 modules within an 8 kHz frame. ADM equipment has the capability to "groom" (add/drop) data down to DS0 (64 Kbit/sec) and any multiple thereof. Therefore, systems with T1 connections to the ADM can have that broken down to multiple DS0, each being individually routed to a different destination. In this way multiple point to point private communication lines to other processor systems are allowed. Once these links are established, they are unaffected by variations in total network backbone traffic, which is not the case is most standard computer networking schemes.

- Upgradeable. The ADM and fiber infrastructure allows for higher performance telecommunications if it becomes required at a later date. This would only require substitution of the backbone OC3 transceivers with higher rate units, such as OC-48 (2.5 Gbits/sec).

Because telecommunications is point to point, use of this equipment alone does not fulfill the requirement of allowing any single processor in the system to communicate with any and all other processors in the LEBCS. To facilitate this, a high-speed router is connected via multiple T1 lines to the ADM at the AMCR. This router has the capability to route up to 300 000 packets per second and can route this data to other T1 lines and/or standard networks, such as an ethernet, in the AMCR.

IOC Communication Interface To provide a T1 communication interface into the VME/VXI IOC, a daughter card compatible with the MVME 162 processor module has been developed commercially to SSCL specifications. The MVME162 module is capable of handling four daughter cards. This could be up to four T1 modules or two OC1 modules, the latter requiring larger board space. The typical configuration at SSCL has two T1 boards, one for standard communications and the second for global synchronous messages. OC1 is reserved for use by data concentrators or other such applications from areas that produce or receive large amounts of data at high rates, such as certain beam instrumentation applications.

Software has been developed for the MVME162 at SSCL such that it accepts standard TCP/IP protocol from the IOC and translates this to PPP (point-to-point protocol) onto the T1 module. This allows the EPICS

software (described later), which uses TCP/IP sockets to communicate, to operate with the T1 system without having to be modified. In effect, the module looks like an ethernet interface to the application software running on the IOC. Further development has been underway at the time of termination to actually make the module appear as multiple ethernet interfaces. Since the T1 line can be broken down to multiple DS0 channels, these could be grouped or singled out as individual internet addresses, thereby allowing TCP/IP to see multiple networks from the IOC. This would allow, for instance, an IOC to communicate directly with another IOC at one address, with alarm and data managers at another address, and perhaps with the AMCR router over yet another.

The baseline design calls for one of these modules to be installed in each VME/VXI crate along with another MVME162 acting as the IOC. Further testing has been planned to determine if a single MVME162 could function as both the IOC and communication module but not completed before termination. Specific concerns in this area are processor performance and limited memory capabilities of this module. However, LEBCS costs could be greatly reduced if the single board configuration could be achieved.

Synchronous Broadcasts Certain information, such as LEB cycle numbers, time of day and machine sequence information, must be transmitted to many or all IOC at the same time. For this purpose, a message broadcast system (MBS) has been developed. The primary components of the MBS are a message transmitter, message resynch router, and MBS receiver.

The MBS transmitter is a VME processor with T1 outputs connected to the SONET backbone. Sequence message/timing pairs are prepared into tables and downloaded to the MBS transmitter. This system is then clocked out by timing signals from the LEB Precision Timing System (PTS). Messages are routed via the LEBCS communication backbone to resynchronization units at each service building, which adjust for ADM jitter and propagation delays and fanout the messages to the T1 MBS receivers on each of the communication modules at each IOC. The MBS receivers decode the messages, determine if the local IOC is interested in a particular message and can provide an interrupt.

This system is capable of delivering messages to an accuracy of 1 ms. In theory, accuracy of 100 μs or less should be achievable, but this requires further development, which has not been completed at the time of termination.

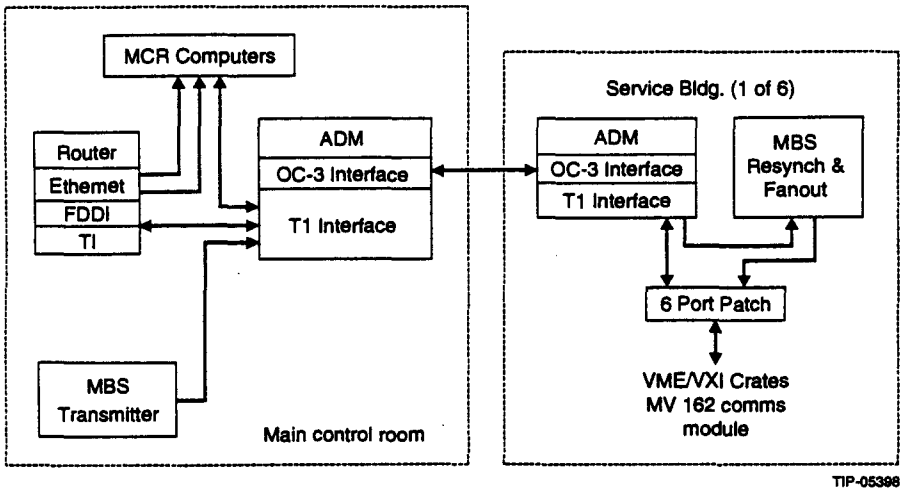

Figure 3.141: LEB control system interconnections.

Integrated Communication System The components of the communication and MBS systems and their interconnections are shown in Figure 3.141. Each service building and the MCR contain an ADM with OC-3 interfaces for fiber connections between buildings and T1 interfaces for twisted-pair connections to local computing equipment. Multi-port patch panels are provided at each ADM and IOC rack to facilitate cable termination. The router at the MCR is configured with FDDI, Ethernet and T1 modules to allow data movement between network types and protocols.

Applications Software Environment

For GCS software development, the Experimental Physics and Industrial Control System (EPICS)[133] has been chosen. EPICS is a set of software tools for the development of realtime control applications. This software has been initially developed at Los Alamos National Laboratory for the Ground Test Accelerator (GTA) project and further enhanced at Argonne National Laboratory for the Advanced Photon Source (APS) project. It has further developed into a collaborative effort, with SSCL, Lawrence Berkeley National Lab, and the Continuous Electron Beam Accelerator Facility (CEBAF) as key contributors.

EPICS has been chosen for use at SSCL for a number of reasons. It meets most of the requirements for LEBCS software. Network communications

protocol via Channel Access which allows any channel in the system to be addressed by any processor in the system. EPICS has software development tools to aid in programming, in particular records, a state notation language and a GUI builder, as well as drivers and a driver-development environment for addressing VME/VXI I/O. It provides data archival and retrieval services and an alarm manager. HP 700 series and Sun Sparc UNIX platforms are supported, and, finally, running on VxWorks in VME processors, it has the real-time capabilities required.

It is felt that time and effort should best be spent on a collaborative effort to advance a common system rather than to start something new. In this way, the SSC will be able to draw on resources from other laboratories for software development through the collaboration. EPICS provides enough capability in its present state for applications to be developed and delivered. Further planned changes and enhancements at SSCL would primarily address the issues of scalability, since the SSC would have more than 300 000 I/O channels.

The changes and extensions to EPICS that have been planned are:

- Development of an EPICS name server. Whenever an EPICS client process needs external data, it must broadcast on the network and each IOC must determine if it has that data and respond to the client. SSC systems would become quite large (100 plus IOC in the LEB, over 2000 SSC site-wide) and constant broadcasting could produce undesirable network traffic and IOC processing in data lookups. Therefore, a scheme of name servers needs to be developed, such that a client calls the name server, which responds with the address of the IOC which has the desired data, and the client then makes a direct connection.

- Enhancement of the capabilities of the alarm manager and data archiver. In EPICS, these facilities are intended to run on an operator workstation, gathering the information desired by the operator at the time. It does currently not allow for central systems which can be accessed remotely by other workstations.

- Saving and restoring. EPICS has limited capabilities to save and restore system setpoints and configurations. Issues to be addressed are sorting of system settings, IOC reboot from saved settings (no control processing until settings are downloaded, *etc.*), IOC sequence of events when reloading settings.

- Enhancement of operator display capabilities. Work in this area is to develop a "parameter page" tool and enhance the GUI capabilities.

- Making EPICS tools more friendly to non-software professionals. EPICS requires a high level of proficiency in C programming and UNIX environments, often unfamiliar to engineering staff which has the knowledge to provide the application. Therefore, graphical software development tools such as a function-block editor for record configuration and a graphical tool to develop sequence-notation language have been under development.

Application Software Development and Documentation

All application software for the LEB provided by ASD/CD is developed according to the ASD/CD Software Development Plan (SDP).[134] This plan details items such as documentation, schedules, development environment, change control, source code control and quality assurance. A Computer Integrated Manufacturing (CIM) model has been developed such that all code-design documentation can be standardized. This model has the following levels:

- 9 - Information exchange: allows access to the LEBCS from other SSCL systems;

- 8 - Machine Integration: Provides information exchange between SSCL machines;

- 7 - Machine Level: Integrates operation of all machine systems;

- 6 - Sector Level: Coordinates control of a machine sector (This level does not apply to the LEB);

- 5 - System Level: Coordinates control of a machine system, such as rf, RMPS, *etc.*;

- 4 - Subsystem Level: Typically that software which oversees all equipment handled by a single IOC;

- 3 - Device Level: operates and controls units such as magnets, compressors, *etc.* as a device;

- 2 - Component Level: Certain devices, such as cryogenic compressors, are composed of rather complex components, therefore this additional level of control;
- 1 - Front End Interface Level: Drivers which interface to VME/VXI modules.

Along with the consistent style of design documentation that this model[128] affords, actual code is also developed modularly for each level. This allows for greater sharing and reuse of code between systems.

Operator and User Interface System Design

Consoles For operator consoles, VME systems are used. A console consists of a VME crate with a Sparc 2 processor board, two dual-graphic-display driver modules, a multi-media video board, Ethernet, and T1 interface. Three 19″ color monitors, keyboard, mouse, and knob box are also provided. VME has been chosen over a commercial UNIX workstation "box" to allow capability to upgrade processors over time and to allow use of the VME T1 module. All consoles in the AMCR have the capability to access data from any of the SSCL machines; there are no consoles specific to the LEB.

File Servers Two fileserver types are to be used in the LEB: one for data archival and retrieval and the other for booting IOC systems. The preliminary design has been for Sun UNIX machines. The archival machine has been selected to be a Sun 640 MP with 10 GBytes of disk space. Two Sun Sparc 10 machines with a 1-GByte disk each is to be used to provide boot services and application code downloading capabilities to the various LEB IOC. Plans have been underway to investigate the possibility of again using VME based single-board processor systems for these applications. This could have the advantage of reduced cost and cleaner installation into 19″ racks instead of floor mount pedestals.

Compute Servers Several single-board VME Sparc processors are to be available as compute servers in the AMCR. These would execute the various physics codes, such as orbit correction *etc.*, and provide access to the LEBCS from other SSCL computing facilities. Additionally, VME162 modules are to be used to act as data concentrators and system controllers for the various LEBCS systems.

Local Operation Operation local to equipment is required for commissioning, checkout and maintenance. For this purpose, lap-top computers are to be used. Operator displays can be downloaded to these computers via the LEBCS networks. Connection of the computers is made via the serial port on the front of each IOC. PPP is the communication protocol and would operate in the same way as the standard T1 connection into the IOC.

System Designs

The LEBCS integrates a number of systems as mentioned in an earlier section. They are interfaced into the LEBCS via the T1 communication links and the channel access capabilities of EPICS. All systems, regardless of responsible group, use VME/VXI IOC. Table 3.32 shows the IOC count by system and location.

Table 3.32: LEBCS IOC by system and location.

Location	BI	rf	CMPS	RMPS	LCW	VAC	TOTAL
S1	6	0	1	0	1	1	9
S2	3	0	1	0	0	1	5
S3	3	50	1	0	0	1	55
A1	4	0	1	2	0	1	8
A2	4	0	1	1	0	1	7
A3	3	0	1	1	0	1	6
MCR	1	0	1	0	0	0	2
TOTAL	24	50	7	4	1	6	92

The individual systems are further described in the following sections. Predominantly, this covers hardware design, which has been in a more final state when the SSC was terminated. Applications software is still in a very preliminary design phase and therefore is not covered. The software which has been detailed can be found in the LEBCS PDR materials.[128]

RMPS Supervisory Control and Protective Systems A block diagram of the RMPS supervisory control system (SCS) is shown in Figure 3.142. The SCS has been designed as a stand-alone system which can operate independently from the LEB control system (LEBCS). An important feature of the system is that a person can use a portable computer to

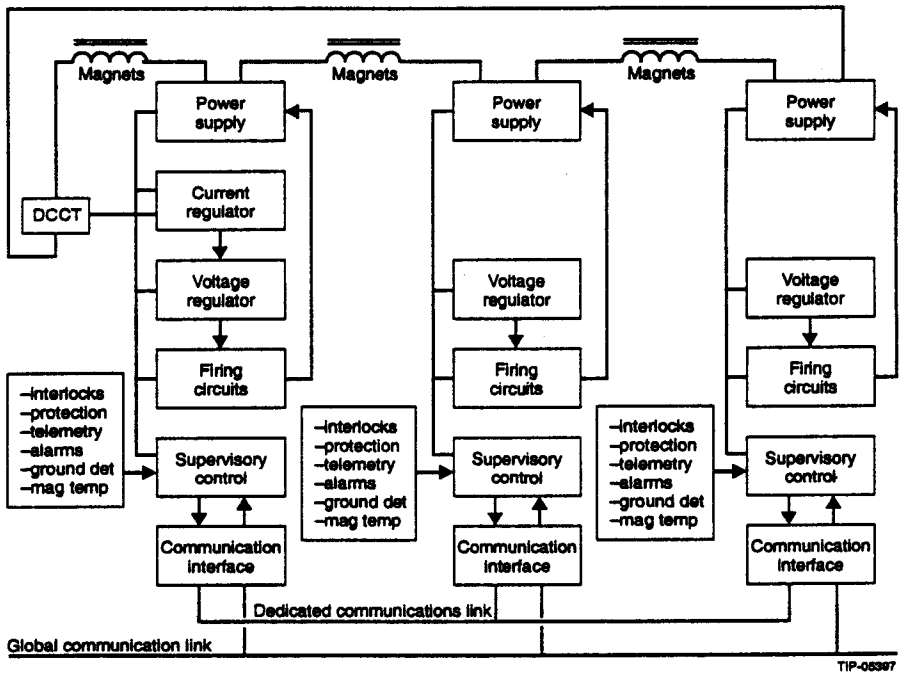

Figure 3.142: Block diagram of the RMPS supervisory control system.

"plug in" to a communications module at any of the three power supply sites and access any function of the SCS. This capability allows for commissioning of the power system independently of the LEB control system and provides for quick troubleshooting during system failures.

To achieve the above requirement, all three supply sites are connected by a dedicated communication link consisting of a shielded twisted-pair cable operating at 23 kbit/s data rate.

Operator requests are transmitted from the central control room to the SCS and the regulation system via the LEBCS. The SCS receives and executes operator commands and acts as a data acquisition system which returns data to the LEBCS.

The functions provided by the SCS are:

- Power supply operating mode control
- Remote control of ac power circuit breakers
- Start-up and shut-down sequences for power converters

- Protective systems monitoring
- Alarm monitoring with time tagging
- First-fault detection
- Sequence-of-events logging
- Remote software diagnostics
- FFT monitoring of analog quantities (implemented in the control room computer or on a portable computer)
- Remote high potential insulation testing
- Magnet over-temperature monitoring
- Remote ground fault detection
- Monitoring of magnet current, power supply terminal voltage, magnet voltage to ground
- Protective interlocks for the complete RMPS, both human safety and equipment protection.

One of the design goals has been to provide sufficient information in the control room so that a failure can be analyzed quickly and a technician be dispatched to the correct site with the required parts and maintenance equipment to repair the failure. This is an essential requirement to achieve the availability of 99.9 % specified for the power system.

The hardware is implemented with standard VME computer modules except for custom designed thyristor firing circuits and regulation modules. The control software has been designed to work on the EPICS software platform.

Corrector Magnet Power System The interface to the CMPS power supplies is a serial fiber link from the power supply to a custom designed VME module.[129] On average, 48 power supplies are to be controlled at each of the six LEB service buildings. The CMPS VME module is designed to handle four power supplies, therefore a single VME crate is required in each service building with 12 of these modules. A diagram of the system is shown in Figure 3.143.

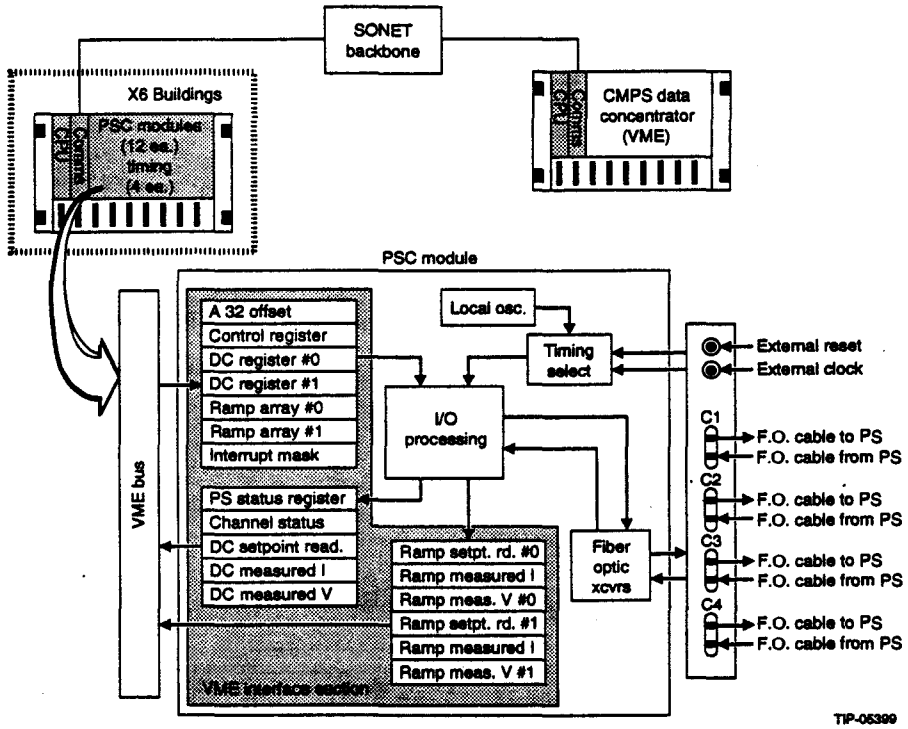

Figure 3.143: Corrector magnet power supply controls.

Front panel connection to this module are trigger (external reset) and external clock connections to the PTS and four fiber pairs to connect the four power supplies. Internal to the board are four identical sections, one for each power supply, with the following capabilities:

- Operate supplies in dc or ramped modes at up to 10 KHz; two registers are supplied for each mode data along with a register select bit in the control register.
- Control register to set up power supply configuration.
- Read-back settings, current, voltage and status. The board has registers to read out the latest values and two array buffer registers which store readings from a full LEB cycle. All settings sent to the power supplies are reflected back to the VME module to allow verification of the link and that the module is sending proper settings.

Software within each IOC sets up the 12 CMPS control modules and provides readouts on request to higher levels of control. The typical sequence is:

- Ramp tables are developed on UNIX workstations and downloaded to the IOC.
- Up to two ramp tables are uploaded to the CMPS modules.
- The IOC receives an MBS message that indicates which ramp is to be executed on the next LEB cycle; this information is passed on to the CMPS module control registers.
- The PTS triggers the CMPS module; the CMPS module sets a pointer to the start of the selected ramp.
- The PTS clocks the CMPS module, and the module sends new settings from the ramp table to the power supply on each clock cycle.
- Upon receipt of a new setting, the power supply returns status, voltage, and current information which the CMPS module stores in VME registers.
- At the end of the LEB cycle, the module informs the IOC where the data from the last cycle resides and that it is ready for readback.
- The IOC reads the data and transmits it to any requesters, such as orbit-correction programs or operator stations.

In addition to the 6 IOC in the service buildings local to the power supplies, an additional IOC resides in a VME crate at the SSCL MCR. The purpose of this IOC is to concentrate data from the other 6 IOC for retrieval by operator stations and compute servers and to provide machine-wide sequencing and operation, such as operation of magnets as families.

For operation of the system, two display windows have been designed: a test control panel and an operations panel. Both panels allow operation of correction magnets either individually, as a family, or as a full machine. The test control panel provides for turn-on and checkout of the system. The operations panel provides for ramp-waveform generation, ramp save and restore and downloading and plotting of data returned from the power supplies.

Injection Power Supply Controls The power supply controls are defined in the Level 3b specifications for the Linac-to-LEB transfer line.[81] This document specifies remote analog and digital status and control. Current and voltage readbacks versus time are necessary for diagnostic purposes. A transient digitizer has been planned for capturing the analog readbacks. Power supply and load protection and safety interlocking are also required. Timing inputs for system charging and discharging are to be provided from the control system.

3.6.5 Rf Supervisory Controls System

The LEB rf supervisory control system provides control and monitoring for the cavity/tuner, amplifiers, tuner bias regulator and low-level rf system (including the frequency and synchronization subsystem). In addition, it provides group control for the entire set of rf stations treated as a single system and interfaces with the global control system to provide a control and data path for accelerator operators. The system will provide four parameters for display to the global control system. 100 points per display per LEB cycle per rf station will be provided with the last seven cycles at any given time being stored. The system also contains diagnostics to aid in trouble shooting and trend identification capability as an aid in preventative maintenance. Each rf station is capable of standalone operation utilizing a UNIX work station as the operator control and monitor point. There is one VME crate and two VXI crates located at each rf station. The VME crate is used for control and monitoring of the amplifier and tuner bias power supply and regulator. One VXI crate is used for control and monitoring of the low-level rf system and the other is used for control of the cavity tuning feedforward system. Figure 3.144 is a block diagram of the rf station control design concept.

The software architecture utilizes the EPICS control software system originated at Los Alamos National Laboratory. EPICS is a distributed controls toolkit built on the UNIX and VxWorks operating systems. Figure 3.145 illustrates the system. The rf controls software is being designed using an Obeject Oriented approach.

VME Controls The VME crate processor provides control and monitoring of the amplifier and power supply systems. This includes on/off logic, interlocks, status monitoring and fault protection and reporting. Fast fault protection such as crowbar triggers and rf inhibits are handled in hardware

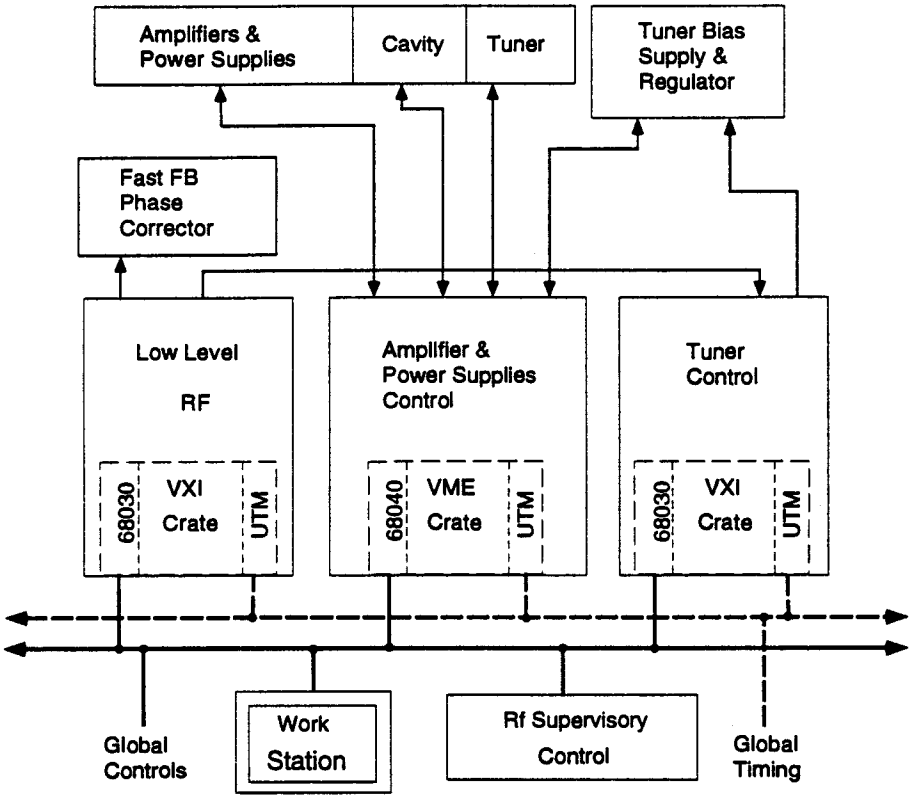

Figure 3.144: Rf station control block diagram.

and reported by the processor. Personnel safety interlocks are also handled in hardware. Slow fault protection such as water flow interlocks is handled by the processor. Amplifier and power supply control and monitoring is resident at each station so that each station may be operated independently of the rf supervisory control system for troubleshooting and maintenance purposes. The prototype software and operator interface has been designed and is in the debugging process.

VXI Controls The two VXI crate processors provide control and monitoring of the low-level rf system and the tuner loop control. Extensive monitoring and programmability is provided. The rf drive level and PID controller gains may be controlled via the VXI processor. The LEB amplitude program is provided as a digital signal to the rf control system and

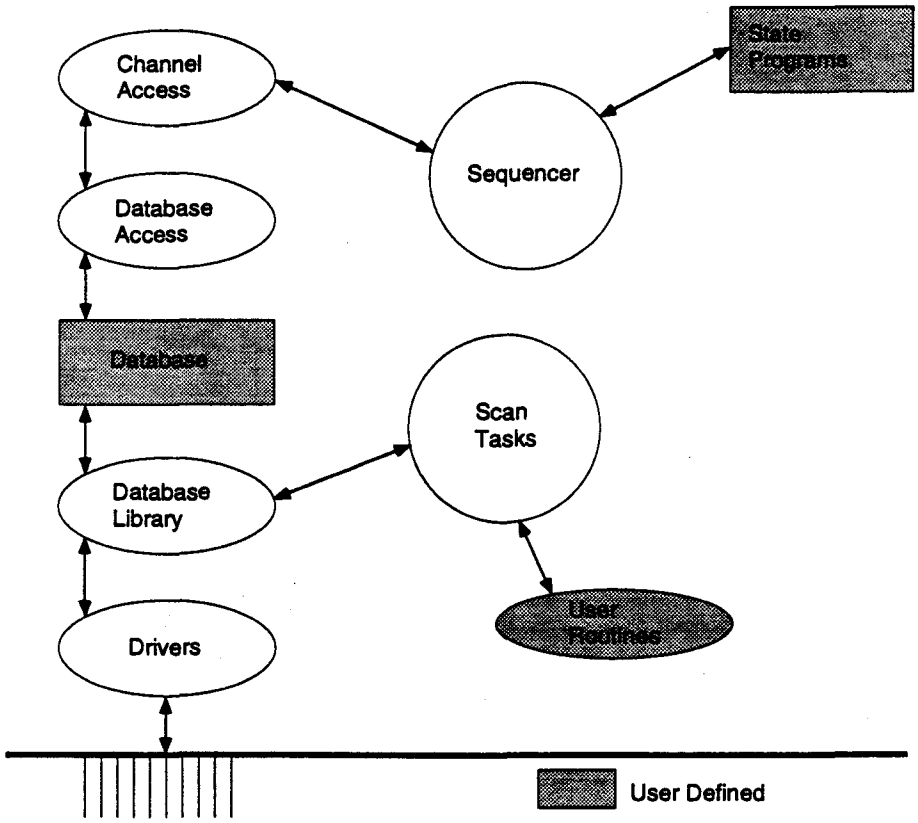

Figure 3.145: EPICS front-end processor internals.

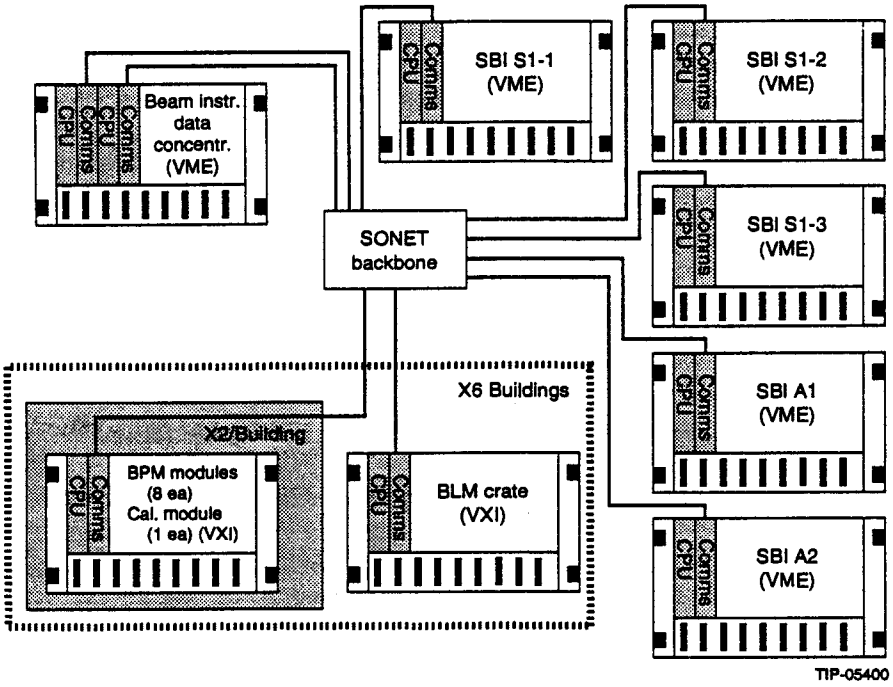

Figure 3.146: Layout of the beam-instrumentation read-out system.

converted to an analog signal by an arbitrary function generator for application to the low-level system.

The control system provides the frequency profile feed forward signal to the tuner bias controller in the form of an analog signal from an arbitrary signal generator. It is planned for this control to be adaptive and correct the feedforward signal in response to the phase error over several LEB cycles.

Beam Instrumentation To incorporate all of the beam instrumentation devices, the LEBCS has to provide 18 VXI crates and 6 VME crates, where the BPM and BLM designs call for VXI modules, requiring two VXI crates for BPM and one for BLM at each service building. All other instruments use VME modules, requiring three crates in service building S1 and one each in A1 and A2. One VME crate resides in the MCR and provides the function of a data concentrator, from which operator stations and other high-level computing systems can request beam-instrumentation data. A layout of this system is shown in Figure 3.146.

All crates have the standard IOC and communications interface, with the exception of the data concentrator. This unit has an IOC, a single-board UNIX processor, and two communication modules, one of which is the standard T1 and the second contains an OC-1 (55 Mbits/sec) interface as a daughter board, instead of the usual T1. This latter module makes the concentrator somewhat different from the others in the LEBCS.

The drive for the bandwidth required by the BI system is the requirement to retrieve turn-by-turn data from up to three BPM (horizontal and vertical position) once per LEB run (LEB run = seven LEB cycles) and deliver this data to the analysis processor within one MEB cycle (6 seconds). Since all three selected BPM could be in the same VXI crate, the bandwidth required is 800 kbits/6 sec or 134 kbits/s per IOC. To allow time for the analysis code to execute prior to the next MEB cycle, this data should actually be available in half the specified time, thus the bandwidth requirement increases to 268 kbits/s per IOC. To accommodate this, six DS0 channels (384 kbits/sec) from each IOC in the system will be groomed by the LEBCS ADM directly to the data concentrator. This requires a data concentrator receiver capable of accepting 8.832 Mbits/sec, thus the need for an OC-1 receiver in the concentrator crate. This special receiver module is also programmed to accept and place it into VME accessible memory space such that it would appear as shared memory to the UNIX processor and IOC in the crate for direct access.

Beam Permit The beam permit system requires reporting of readiness for beam from virtually all LEB systems. The intent is to do this in software. Prior to each LEB cycle, the MBS transmits a message to all IOC to verify their readiness for beam. Each IOC then transmits a beam permit message to an IOC at the AMCR. At 10 ms prior to begin of the LEB cycle, another MBS message is sent to this IOC that sums all of the beam permits transmitted by system IOCs and then passes an LEB ready/not ready message to the Linac. This concept still requires further testing. While dedicated DS0 channels from each IOC would be set up to the beam-permit summation IOC, testing is still required to determine if all IOC can respond across the network within the given time frame.

Vacuum and LCW The vacuum and LCW systems involve slow, industrial-type processes where a commercial process control system, such as Programmable Logic Controllers (PLC), could be employed. EPICS does con-

tain drivers to connect to industrial I/O systems via a VME based scanner module. However, a trade-off study was done, and it was opted to use VME crates and IOC like for the rest of the LEBCS. In this way the consistent structure of LEBCS will be maintained, while the cost is comparable for a system of seven VME crates with IOC or a system of two PLC with five remote crates. An industrial system would require different network cables to be run between service buildings.

The PLC scanner algorithm is not desirable: Typically, the scanner will read in all data from one remote crate, then the next, *etc.*, in a cyclic fashion. If however, an analog input/output module is encountered during a crate scan, data will be read from that module but no other data will be read from that crate until the scan comes back around to that crate on the next cycle.

To implement the system, seven VME crates with IOC will be used. The LCW plant will be controlled with a single IOC with two ADC, one DAC, two digital input and one digital output modules. This VME unit will be local to the LCW equipment at service building S2.

The vacuum system requires crates for control in each of the six LEB service buildings. Along with the vacuum signals, the LCW distribution system sensors in each service building are to be connected to these crates.

Acknowledgements

D. Gurd, S. Hunt, J. Heefner, D. Murray and T. Moore all contributed to the definition of the LEBCS. The rf control system has been designed in a separate effort under D. Dohan's leadership; R. Biggs, J. Bossom, K. Chillara, T. Osberg, R. Richter, H. Rogers and D. Wade all contributed to the design.

3.7 Radiation and Shielding

(J. Bull)

In order to keep the radiological impact of accelerator operation on the work place and to the environment As Low As Reasonably Achievable (ALARA), the SSCL established a stringent set of radiological design guidelines. The LEB was designed to meet all of these design guidelines as stated in Chapter 9 of the SSCL ES&H Manual.[135] Goals and the corresponding legal limits for radiation exposure are presented in Table 3.33.

Table 3.33: Superconducting Super Collider radiation limits and design goals.

	Limit	Design Goal
Member of public off-site (all pathways)	1 mSv/y (100 mrem/y)	0.1 mSv/y (10 mrem/y)
Member of public on-site non-radiation workers *etc.* (all pathways)	1 mSv/y (100 mrem/y)	0.2 mSv/y (20 mrem/y)
Radiation worker (direct "prompt" radiation)	50 mSv/y (5 rem/y) [ACL 5 mSv/y (500 mrem/y)]	2 mSv/y (200 mrem/y)
Air activation (actually immersion) Member of public off-site	0.1 mSv/y (10 mrem/y)	1 μSv/y (0.1 mrem/y)
Water activation Member of public off-site (Water supply)	40 μSv/y (4 mrem/y)	40 μSv/y (4 mrem/y) at 1 m from protected zone

The design limit for the site-boundary dose equivalent from all sources of radiation is 0.1 mSv/y (10 mrem/y), or 10 % of the Department of Energy (DOE) limit specified in DOE Order 5480.11. This limit has been further broken down into air emissions and water activation. For air activation, the SSCL has chosen a limit that is 1 % of the 0.1 mSv (10 mrem) limit specified by the Environmental Protection Agency (EPA). At this level, monitoring of air stack emissions is not as restrictive, giving the laboratory more flexibility in emissions monitoring. The drinking water radiation limit is the same

as the EPA limit of 40 μSv/y (4 mrem/y) for community drinking water systems, often expressed in terms of radionuclide concentrations. A more detailed explanation of the groundwater activation model is discussed later in Section 3.7.5.

On-site criteria used as the basis for shielding at the SSCL arise from a policy set forth by the SSCL Director that most of the SSCL property (site) can be accessed by members of the public without any radiation protection concerns. This policy extends to such areas as shielding berms, which have typically in other installations been fenced off to exclude the public. Thus, for on-site "open areas" *i.e.*, those areas not controlled for radiological protection purposes, the radiation design goal will be less than 0.2 mSv (20 mrem) per working year. This means that average hourly dose rates will not exceed 0.1 μSv (0.01 mrem) in those limited regions close to controlled area boundaries. In the case of a catastrophic beam accident, the maximum allowed dose equivalent is 1 mSv (100 mrem). Thus, apart from personnel such as accelerator operators and technical staff who work in control rooms and other similar places close to controlled areas, and who would normally be badged radiation workers because of their need to work periodically in controlled areas, persons on-site are unlikely to receive any radiation dose above natural background.

The shielding criteria for controlled areas is set at ten times the open-area criteria discussed above. Any area where radiation levels could be elevated above background will be considered a controlled area. The covering of a large portion of the LEB by a thick earth berm results in controlled areas being located at only a few limited places, such as the very top of access shafts and in selected utility buildings. Because of the nature of work inside controlled areas, it is unlikely that any person will be exposed to the highest radiation levels for a whole working year (2 mSv [200 mrem] per work year) so that annual equivalent doses from prompt radiation are unlikely to exceed 1 mSv. However, the Administrative Control Level (ACL) of 5 mSv/y (0.5 rem/y) given in DOE Order N5480.6 could be a challenging goal for some workers, since most of the annual dose equivalent received by radiation workers is through work on activated components. For this reason, the design goal for general shielding is set at a substantially lower annual dose equivalent.

Although accelerators are considered low hazard facilities, the particle beams they produce can be extremely hazardous. Beam losses may occur which will cause, locally, very high levels of radiation. Therefore, it is of the utmost importance to ensure that all areas where accelerator beams are

present are absolutely cleared of personnel before introducing beam. This is done either by a search-and-secure procedure prior to a state-change to exclusion or by a "take-key" system with very strict control over personnel access or a combination of both. For the LEB, a safety interlock system, known as the Personnel Access Safety System (PASS), has been developed, and is described in Section 3.8 of this book. The concepts of "fail-safe" and "redundant" are employed whenever possible, including requiring that two complete programmable logic controllers, programmed independently by two different programmers, be on line at all time, either one of which can cause the system to alarm or turn off the accelerators. SSCL policy requires the use of two independent critical devices to prevent the accelerator beam from entering an occupied area. These devices, such as beam plugs or bending magnets, are constantly monitored by the PASS system. At least one of the two devices must be fail-safe in case of any anticipated problem. If any of these devices fail, the PASS system will disable the accelerator beam earlier in the accelerator chain.

3.7.1 Beam Intensities and Source Terms

The beam parameters used in these calculations are based on the accelerator characteristics listed in the Site Specific Conceptual Design Report (SCDR)[2] and listed in Table 3.34. Initially, the injection energy will be 600 MeV, but an upgrade is planned to increase the Linac beam energy to 1 GeV. The LEB is capable of producing 5×10^{12} protons per machine pulse, at a rate of 10 Hz. The annual beam production, however, is limited by the beam requirements of the Medium Energy Booster (MEB). It takes seven LEB pulses to fill the MEB, which is able to extract beam every 3 seconds. Under these conditions, the average cycle rate of the LEB is 2.33 Hz. Most of the time the boosters will be used to provide test beams to the calibration hall. Based on a 5000 hour operational year for the test beams, the maximum number of protons accelerated by the LEB will not exceed 3×10^{20} protons per year. The beam parameters given here represent upgraded capacities for MEB ramp rates and beam intensities. These optimistic values have been used to ensure adequate shielding is provided.

The beam losses assumed in these calculations were established by the accelerator designers in consultation with the radiation protection group. These assumptions, shown in Table 3.34, represent reasonable, yet conservative estimates of beam loss due to injection, acceleration, collisions, and extraction, based on experience with other proton accelerators and full-scale

Table 3.34: Shielding comparisons for different beam loss conditions.

Design Criteria	Beam Loss	Allowed Dose per Proton	Shielding Thickness
LEB Injection Shielding Requirements (1 GeV)			
High Loss Conditions < 20 mrem/y	5 % point loss @ 2.3 Hz 1.2×10^{19} p/yr	2×10^{-21} rem/p	9 m
Accident Condition < 10 mrem/ event	point loss for 1 hour @ 2.3 Hz 4.4×10^{16} p @ 10 Hz 1.8×10^{17} p	2×10^{-19} rem/p 6×10^{-20} rem/p	6.75 m 7.25 m
LEB Acceleration Shielding Requirements (11 GeV)			
High Loss Conditions < 20 mrem/y	distributed loss @ 2.3 Hz† 1 GeV—10 % loss 4.2×10^{16} p/m/y	5×10^{-19} rem/p	6.75 m
	11 GeV—2 % loss 1.3×10^{17} p/y/15 m	2×10^{-19} rem/p	6.75 m
Accident Condition < 10 mrem/ event	point loss for 1 hour @ 2.3 Hz 4.4×10^{16} p @ 10 Hz 1.8×10^{17} p	2×10^{-19} rem/p 6×10^{-20} rem/p	6.75 m 7.25 m
LEB Extraction Shielding Requirements (11 GeV)			
High Loss Conditions < 20 mrem/y	2 % point loss @ 2.3 Hz 4.8×10^{18} p/y	4×10^{-21} rem/p	8.25 m
Accident Condition < 10 mrem/ event	point loss for 1 hour @ 2.3 Hz 4.4×10^{16} p @ 10 Hz 1.8×10^{17} p	2×10^{-19} rem/p 6×10^{-20} rem/p	6.75 m 7.25 m

† The proton loss is distributed along the length of the LEB, 570 m, in 15 m segments.

Monte Carlo simulations. These estimates were provided at an early stage of the LEB design. Although current operational scenarios have resulted in a reduction of the annual beam intensities, for conservatism, the values given in the table have remained the basis for shielding design.

In a similar manner, the parameters for beam accidents have been defined. For the resistive-magnet accelerators, the definition for a beam accident is controversial. A major beam loss lasting for more than several minutes should be noticed by either the beam instrumentation monitors or the personnel using the beam downstream. Nevertheless, major beam losses have occurred at other laboratories lasting for a large fraction of an hour. Therefore, SSCL has conservatively defined a beam accident in the resistive magnet machines as the full loss of beam for one hour at one spot. This definition has subsequently been incorporated into the DOE Accelerator Safety Order (DOE 5480.25).

3.7.2 Shielding Calculations

When a high-energy particle interacts with a target, a shower of particles is produced, consisting mainly of proton, neutrons and pions. These secondary particles in turn produce more (tertiary) particles and so on, until a large cascade of particles is generated. It is the intensity of this hadronic cascade that determines the lateral shielding dimensions.

Much of the shielding calculations at the SSC Laboratory have been performed with Monte-Carlo computer programs that simulate the hadronic cascade and muon production induced by accelerator beams. These programs generate particles and transport them through a user-defined geometry. Interactions occurring in the geometry are simulated, based on known particle cross sections. The output of these programs consists of tables of star (inelastic interaction) densities and energy densities in specific areas of the modeled geometry, as well as particle fluences. From this information, dose rates, temperature changes, and material activation can be calculated. Most of the shielding designs at the SSC have been simulated with CASIM,[136] and MARS12.[137] Both codes have been used extensively at other accelerator laboratories, and their results have been shown to agree with existing data.[138]

3.7.3 Cover Requirements

One of the first questions asked of the shielding designer is how much shielding is required over the accelerators. For injection, the shielding was de-

termined utilizing a Moyer-type model as described in Thomas and Stevenson.[139] The dose equivalent, H, from a proton beam hitting a target can be expressed as

$$H = H_0 \frac{\exp(-d/\lambda_{\text{eff}})}{(a+d)^2} , \tag{3.27}$$

where d is the shield thickness, a is the accelerator enclosure radius, λ_{eff} is the effective attenuation length, and H_0 is the dose equivalent extrapolated to zero depth in the shield. For 1-GeV protons, H_0 is 7.6×10^{-15} Sv·m^2 and λ_{eff} is 1100 kg/m^3. The average LEB tunnel "radius" is 2 m.

CASIM has been used to determine the shielding requirements for the 11-GeV beam.[140] A typical dipole magnet, (54.3 cm $\times$ 43 cm with a aperture 5.8 cm $\times$ 8.0 cm), has been modeled inside a cylindrical accelerator enclosure. A proton beam with a lateral Gaussian distribution (σ_x, σ_y = 1 mm) is made to hit the magnet 1 mm from the aperture edge. The shielding material is compacted fill material, saved from the excavation of the accelerator tunnels. It has an expected density of 1.85 g/cm^3.

Results of these calculations for compacted fill are shown in Figure 3.147, expressed in terms of dose equivalent per proton lost. As can be seen, the dose equivalent falls off approximately one order of magnitude per meter of shield, a useful rule of thumb used for making shielding estimates. Using this graph, and knowing the expected beam losses, the shielding requirements for each beam loss and design criteria can be determined. These results are presented in Table 3.34. In order to directly compare the shielding requirements for the various scenarios, the allowed dose per proton has been determined by dividing the design criteria by the expected beam loss. The amount of shielding needed can then be read directly from Figure 3.147. In producing the final design specifications, an extra meter of shielding was added as an additional safety factor.

3.7.4 Penetrations

Penetrations for utilities and equipment access to the accelerators provide a path for radiation to leak through the shield. Calculations of the radiation dose through a labyrinth are commonly performed by the use of "universal curves" which graph the attenuation of the dose versus the length of the access, expressed in units of the cross sectional area.[141] To attenuate the radiation, penetrations can be increased in length, shrunk in size, or designed to include right-angle bends.

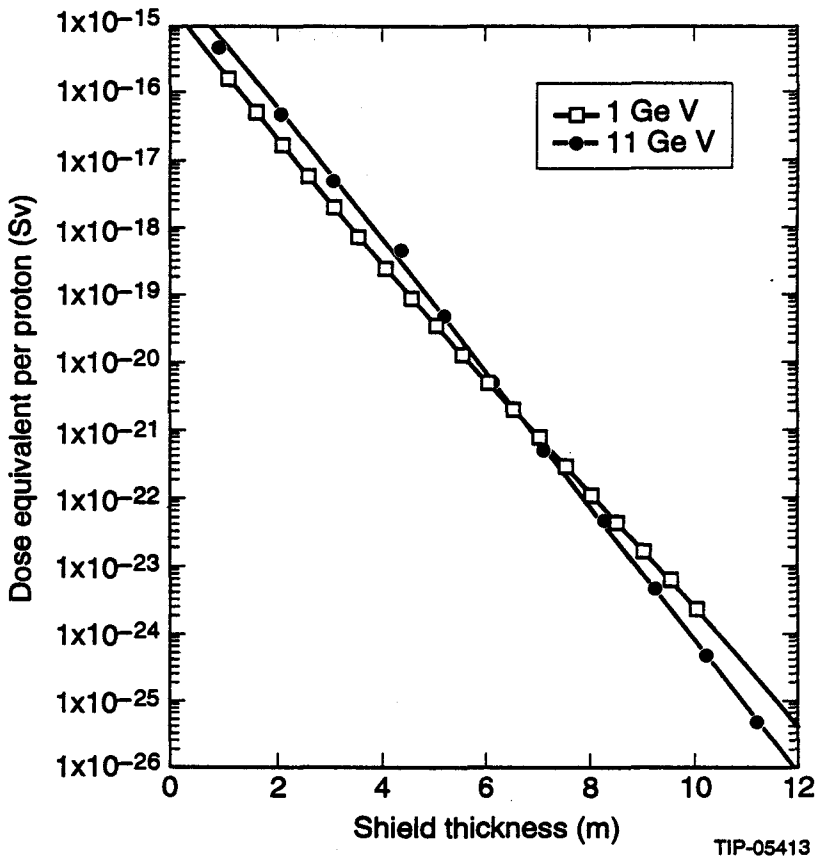

Figure 3.147: Dose equivalent per proton versus shielding thickness for a point loss.

The LEB has two access shafts which are potential pathways for radiation to escape. The main access to the LEB is the elevator and drop shaft at S3. This adit is angled 135° back from the beam direction to reduce the neutron flux up the passageway. The drop shaft located at the end of the adit will be shielded by two foot thick concrete blocks. Personnel access is via the elevator and stairs located to the side of the drop zone. The right-angle bend and two-foot shielding wall separating this area from the drop zone is sufficient to reduce the radiation to acceptable levels. The other access shaft is the emergency exit located at A2. This labyrinth consists of three horizontal sections and one vertical section. Combined, this configuration reduces the radiation levels to meet the design goals.[140]

3.7.5 Groundwater Activation

Due to the unique geology of Ellis County and the public concern for safe drinking water, the SSCL has taken a conservative approach to groundwater activation. The SSCL groundwater activation model requires that the activation concentration in the groundwater one meter outside the accelerator enclosure meets the federal drinking water standards.[142] These standards are expressed in terms of radionuclide concentrations, with the activation of all the nuclides combined resulting in a dose equivalent of less than 4 mrem/y. The concentration limits for these nuclides are 20 pCi/ml for ^{3}H and 0.4 pCi/ml for ^{22}Na. Earlier studies of radionuclide transport in groundwater indicate that ^{3}H and ^{22}Na are the only long lived nuclides (half-live greater than 30 days) with high leachability factors induced in the soil around particle accelerators. Recent experiments completed with samples of Ellis County rocks have confirmed this for the SSCL site, and have provided production and leachability factors specific for this site. Utilizing the radiation transport codes discussed earlier, the radionuclide concentration can be determined. The groundwater model assumes saturation levels of activity. It will take many years of operation before the activation levels build up to these levels.

Groundwater activation has determined the dimensions of the LEB beam absorber shielding.[143] To calculate the absorber shielding, it has been assumed that 20 % of the annual LEB intensity could be sent to the LEB absorber. Thus the annual beam intensity is 6×10^{19} protons. Again, the shielding code CASIM has been used to determine the groundwater activation from this beam intensity. For the LEB beam absorber, the design of the absorber tunnel and the absorber system must keep the average star

production rate at or below 10 stars/cm^3/s taken 1 m from the outer edge of the protected soil around the absorber. This star production rate will result in radionuclide concentrations in the groundwater which meet the federal drinking water standards. To meet this standard, an iron absorber 3.35 m high, 3.35 m wide, and 3.8 m long is required. The maximum contact dose rate after one year of irradiation and one hour of cooling at the side of the absorber will be 25 mrem/h.

3.7.6 Radiation Concerns Associated with Beam Injection

The injection region of the LEB presents some unique radiological problems, and merits special consideration. Details of beam injection are discussed in Section 2.4.1 of this book. Briefly, the H^- beam from the Linac is steered by the injection septum onto a stripper foil, converting most of the beam to H^+ beam for insertion into the LEB. However, a significant fraction of the beam, up to 5 %, will be converted to H^0. This beam will be stopped by a beam absorber located two meters downstream from the stripper foil. In addition, up to 1 % of the beam could be lost in the septum magnet itself.

The size of the H^0 beam absorber has been determined by the groundwater activation criteria. Based on a 1 GeV injection beam energy, calculations indicated that a 1 m^3 block of steel will be needed for the absorber. The maximum dose at the side of the absorber is 4.8 kGy (480 krad) per year and occurs 40 cm down from the front of the absorber. For a quadrupole magnet placed 75 cm downstream from the absorber, the dose per year is 17 kG (1.7 Mrad). None of these dose rates are excessive for radiation areas, and there should be no problem manufacturing equipment for use in the injection region.

The second beam-loss point in the LEB injection girder is the injection septum magnet, where it has been estimated that up to 1 % of the injected beam may be lost. The magnet has been modeled as an iron cylinder with a 3-cm diameter hole for the beam. The beam hits the inside of the magnet at a 50-milliradian angle. The dose rates have been calculated for the inner side of the magnet where the beam hits. The maximum dose on this side of the septum is 90 μGy (9 Grad) per year. The septum magnet is only 5-cm thick, so the dose at the outer edge of the magnet is 1.5 mGy (150 Mrad)/y. This is a high dose rate and additional shielding may be necessary to reduce the groundwater activation levels.

A major concern in the injection region is the residual activation of the beam line components. These have also been calculated by MARS12 and

can be scaled for various irradiation and cool down times. Table 3.35 lists the residual dose rates for several beam elements in the LEB injection girder. For these calculations, it has been assumed that iron is irradiated for one year and then allowed to cool down for one hour. The residual dose rates do not vary greatly with elapsed time for activated iron, decreasing by an additional factor of two after 20 days. As expected, the highest residual levels are associated with the front of the beam absorber and the side of the injection septum. The residual rate at the front of the beam absorber is excessively high, and will still be 5 mSv/h (500 mrem/h) 3 m away from the front face. One way to allow personnel to work on the beam elements near the stripper is to move the H^0 absorber further away from the injection area, such that temporary shielding can be placed over the hot spot of the absorber. For example, 30 cm of iron will attenuate 1-MeV gamma rays by a factor of 10 000. In addition, the absorber can be designed with an reentrant face, to provide additional shielding from the beam hot spot. In any case, special radiation protection procedures need to be developed for personnel working around these components.

Table 3.35: Dose rates due to activated components.

	On Contact	Activation Area	30 cm Away
H^0 absorber (side)	1 mSv/h (100 mrem/h)	1500 cm^2	250 μSv/h (25 mrem/h)
H^0 absorber (front face)	1 kSv/h (10^5 rem/h)	3 cm^2	0.5 Sv/h (50 rem/h)
Downstream Quadrupole	3.5 mSv/h (350 mrem/h)	1500 cm^2	1 mSv/h (100 mrem/h)
Injection Septa (outer surface)	150 mSv/h (15 rem/h)	180 cm^2	5 mSv/h (500 mrem/h)

3.7.7 Radiation Concerns Associated with Beam Extraction

The radiological concerns associated with the LEB extraction focus on the amount of beam lost on the extraction septum. Since in the SSC baseline design no gap is present in the Linac beam pulse, up to three LEB micropulses of 5×10^{10} protons each will be lost on the septum magnet during

each extraction. Calculations with indicate that the septum magnet will receive a dose of 70 mGy (7 Grad) per year. Of greater concern is the residual activity. One foot away from the magnet, the dose equivalent rate is 70 mSv/h (7 rem/h), an unacceptable radiation level for any extended maintenance on the magnet. Special procedures involving localized shielding or remote handling have to be developed to allow for personnel to work in that area. Alternative approach is to create a gap in the circulating LEB beam of at least three empty buckets. Preliminary investigations indicate the feasibility of dropping the Linac beam, but no design has been prepared.

3.7.8 Summary

None of the prompt dose rates are excessively high for beam-loss areas in accelerator enclosures. However, the residual radiation levels are quite large, and special consideration should be made when designing the dose to the extraction septum elements. These estimates have been made assuming that a high-intensity test beam program has been established. For initial operation, the dose rates will be more than a factor of 10 lower than the rates listed above. During this time, measurements will be made to confirm these expected radiation levels. With all of these precautions, the LEB can be operated in a safe and dependable manner.

Acknowledgements

Many members of the SSCL staff were involved in this work. G. Stapleton, L. Coulson, and S. Baker assisted in the development of the design requirements, and together with V. Romero and D. Goss helped to formulate the groundwater activation model. H. Edwards and T. Toohig were invaluable in determining the beam intensities and loss terms. Finally, discussions with J. McGill, N. Mokhov, J. Coyne and also G. Stapleton contributed to the interpretation of the calculational results.

3.8 Personnel Access Safety System

(R. Parry)

3.8.1 Introduction

The Low Energy Booster, like any high-energy accelerator, contains serious personnel hazards with the potential for deleterious results if precautions are not implemented. Hazards for most accelerators include: electrical hazards (high voltage and high current), ionizing and non-ionizing radiation, flammable gases, and high magnetic fields. For the LEB, the predominant hazards of concern are electrical shock and ionizing radiation exposure to the primary beam, both of which can be obviated or mitigated by controlling personnel accesses into the tunnel enclosure. Outside the enclosure radiation levels are much less of a danger due to the radiation shielding. However, radiation interlocks are still used to insure the beam is inhibited at its source in the event of excessively high radiation levels outside the enclosure. The LEB Personnel Access Safety System (PASS) is used to protect personnel from these hazards in underground enclosures by controlling electrically hazardous power supplies and beam safety devices.

Electrical hazards are controlled by a robust fail-safe interface between power supplies and other similar devices. Specifically, the control point is as close as possible to the power source so as to bypass less reliable shut-off mechanisms. In most devices this is the power supply contactor that turns off all power to the device. A contactor acts much like a relay. To further ensure the integrity of the interface, a feedback signal is provided by the contactor to sense that it functioned properly. In the event that devices are inhibited by the system and feedback from the system indicates a malfunction, an alarm is initiated and personnel access into the LEB tunnel is not allowed. The proton beam from the Linac into the LEB is controlled in a similar manner. The devices used to control the beam, typically referred to as radiation-critical devices, are power supplies that control bending of the beam into the LEB. By controlling and monitoring these devices, beam can be inhibited if necessary.

Although the actual design discussed herein has not been implemented in the LEB due to the termination of the SSC project, a very similar system was installed and has been operational for two years in the Accelerator Systems String Test (ASST) facility.[144] The ASST differs from the LEB in being smaller (180 m in length) and not producing radiation; however, for

most other aspects it serves as a testing ground for the LEB PASS and a proof-of-concept.

3.8.2 The Controller

The requirements of a safety system are reasonably well understood due to numerous other accelerators that have been built previously. However, the magnitude of the SSC project places many unique requirements on the design. Each PASS (Linac, LEB, MEB, *etc.*) at the SSC is for the most part independent; however, dependencies exist among the accelerators making communication between the systems necessary. It is therefore imperative that all SSC safety systems work seamlessly together and can be easily integrated. Thus driving the LEB requirements in large part is the worst-case design, namely the Collider system. The Linac, LEB, and MEB are small enough to allow use of conventional technologies such as standard electromechanical relays with their inherent high reliability and fail-safe nature. However, the HEB (7.8 km circumference) and the Collider (87 km) force a different solution. Problems encountered with standard electromechanical relays include excessive voltage drops that are experienced over vast distances that would be prevalent in the enormous machine. In addition, a number of cables are necessary, again making relays an impractical solution.

An electronic implementation of the PASS using digital communication has therefore been adopted. Large computer-based controllers such as CAMAC and VME systems are possible, but generally considered too flexible and difficult to manage for safety applications. Programmable Logic Controllers (PLC) have been available for many years and have advanced to the point where they are being accepted as acceptable solutions in safety applications. The PLC solves many of the problems of relays and has therefore been chosen as the controller for the system.[145–147]

3.8.3 Redundancy

The PASS must provide redundancy.[2] Redundancy takes many forms and varies with the application. In systems where safety is not the prime concern, redundancy typically takes the form of two independent systems with only one being operational at any given time. In the event one system fails, transfer of operation from one system to the other occurs. This type of system is also referred to as a 1-out-of-2 voting system (one controller must function to keep the system running). Redundancy as used in safety critical

applications and as used herein, means 2-out-of-2 voting. Two controllers must function to keep the system running; if either system fails, the operation of the accelerator will shutdown. At one point in the design phase of the LEB PASS, a 2-out-of-3 voting scheme was considered. This type of system has the great advantage of allowing a failure while still remaining operational. Such high-availability schemes are often implemented in systems such as the space shuttle, where the system must continue to run during a failure and possibly multiple failures.[148,149] This approach was eventually dropped due to cost and the questionable need for such a system.

The described redundancy makes the system significantly more reliable from a safety standpoint which is our goal. Speaking strictly from a safety standpoint, reliability is the key issue: one must fail on the side of safety. However, doubling the number of components reduces the availability by doubling the number of components that can fail. In a very large system such as the SSC, reliability is a key issue that must be addressed. Studies have been conducted among various systems to maximize availability (no availability value has been specified specifically for the LEB PASS). The investigation has included obtaining manufacturer's mean-time-before-failure (MTBF) data for various PLC modules and calculating availability.[150,151] Although availability is a key issue, other factors entered into the decision-making process, such as availability of I/O modules, experience, support, software tools *etc.*

Wherever possible, the field devices are also redundant. For example, on each of the personnel access doors that leads into a hazardous area, two door sensing switches are used. One door switch serves as an input for one PLC and the other sensor is connected to the other PLC system. In those cases where two separate field devices are not practical, two signals are derived from a single point (*e.g.* two electrical contacts from a single emergency scram switch are used for control). A block diagram of the system is shown in Figure 3.148.

3.8.4 Software

PLC, like all programmable systems, carry the burden of being software driven. To increase software reliability, two individual programmers are used to program each of the controllers, the advantage being that two individuals are not likely to make the same error. In addition, the system is programmed in a graphical language called Relay Ladder Logic (RLL). The language shows visually the flow of control and therefore allows detection of

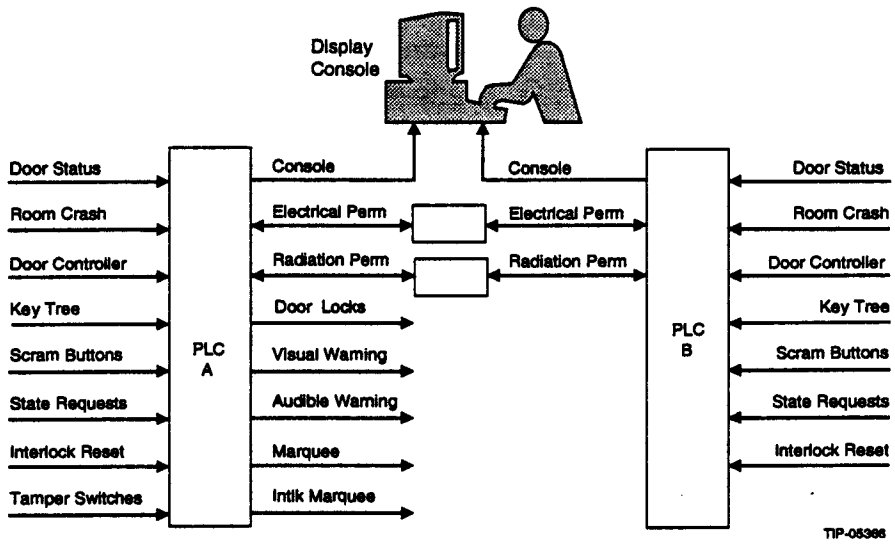

Figure 3.148: System block diagram.

more easily than a conventional text language. Other precautions used to insure software reliability are careful peer reviews, extensive software testing, and strict software configuration management. Configuration management refers to the administrative procedures developed to insure that the system is operating under the correct software.

The console display of information is implemented using Experimental Physics and Industrial Control System software (EPICS),[133] which is also used from the accelerator control system. This software package is powerful and versatile, however, the sole purpose of the display subsystem is to monitor the PASS rather than to control. The safety and integrity of PASS is enforced by insuring that no control communication takes place between the PASS and the console.

3.8.5 Fail-Safe Design

A fail-safe design is another major requirement for the LEB PASS. Designing a fail-safe system using standard electromechanical relays is relatively easy since they are inherently fail-safe. PLC based systems are somewhat more difficult to be fail-safe; however, many of the standard design concepts can be used such as insuring the devices are energized to remain operational. In this way, a loss of power will cause the system to fail in the desired state.

Other precautions implemented are "watchdog timers" or "heart beats" that must be periodically pulsed to insure proper operation.

Further means adopted to ensure that the LEB PASS fails safe include using commercially available devices that were specifically designed for safety and security systems. For example, the door access sensors are fail-safe and tamper proof.

3.8.6 Miscellaneous Safety Requirements

To prevent damage or tampering to the system, all cables are protected in their own dedicated electrical conduit. In addition, all relay racks, cabinets, and enclosures are locked and monitored. Only authorized personnel have access to safety system components.

In the event there is a need to make an emergency exit from the accelerator enclosure, emergency crash buttons located inside the enclosure are used to release locked doors and inhibit radiation and electrical hazards. This emergency switch bypasses the PLC control system completely, so even in the event of a dual PLC fail-to-danger state, emergency egress from the enclosure is possible.

There is a need to display critical information to the user in a clear and unambiguous manner. The LEB PASS design has gone to great lengths in this area. For example, above each of the personnel access doors is a large 10 cm $\times$ 90 cm scrolling marquee display to clearly indicate to personnel the state of the machine (*i.e.*, open access, restricted access, *etc.*).

The operator interface (OPI) or console display uses a graphical user interface (GUI) to clearly display PASS information. Color graphic display screens are used which show the tunnel outlines with doors, indicating their open or closed state graphically and in color.

A chief operator in the control room is responsible for the safety of personnel. All safety-related control of the system requires a unique physical key (*e.g.* door access key), thereby preventing unauthorized control of the safety system. All personnel entering the hazardous area must be accounted for before the system is made operational. Accountability is accomplished by allowing only personnel who have taken a key to enter the area. Once a key is removed, the machine is disabled and cannot be run until all keys have been returned. In addition, only authorized personnel are allowed access. A computer database is scanned to assure that the individual wishing access has had the necessary training and is medically fit to enter the hazardous area. Figure 3.149 shows the LEB tunnel and service buildings. The main

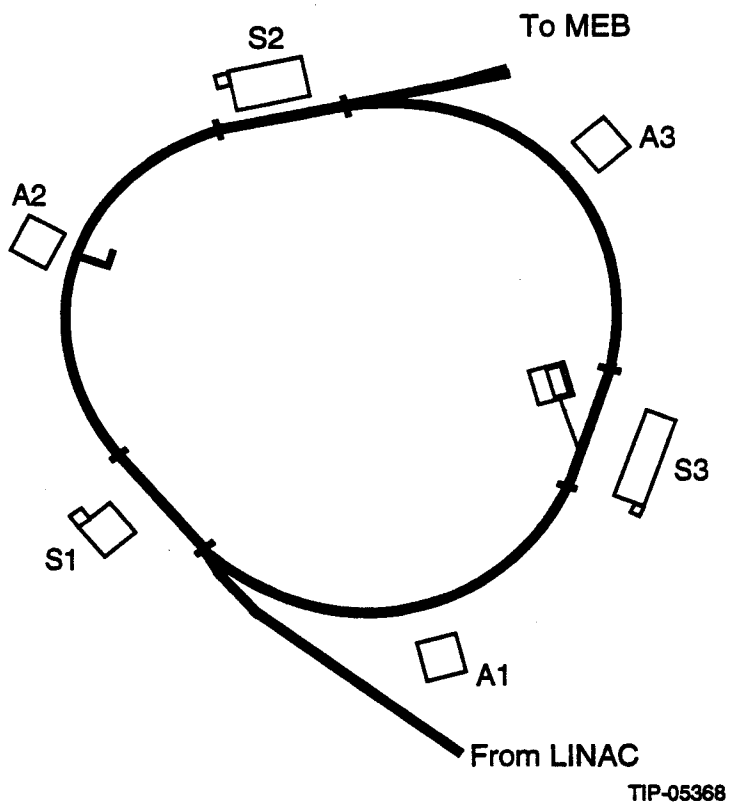

Figure 3.149: LEB service buildings and tunnel.

access point into and out of the LEB is a building S3 where the controlled access booth is located. An emergency egress point is provided at A2.

Testing the system is to be performed routinely every 6 months. All modifications are strictly controlled and all changes result in the re-testing of the system.

3.8.7 Pass Access States

The LEB PASS needs to accommodate various operating scenarios and modes. This is most easily accomplished by specifying several well defined states for the system. The LEB PASS is always in one of five states: open, restricted, search, controlled, and closed access. Each state relates to the type of access that is allowable. Figure 3.150 indicates the LEB PASS states and possible transitions between states.

Open Access

In the open-access state, access into the area is void of electrical and radiation hazards. Thus open access will typically exist only during the very early stages prior to LEB commissioning. Once hazards are introduced into the tunnel, all personnel accesses are restricted.

Restricted Access

Restricted access is available to personnel during periods when the system is "down" with electrical and radiation hazards mitigated. Personnel entering the area must be qualified and have required training. The PASS also provides the mechanism for logging personnel into and out of the tunnel.

Search Access

Before operating the LEB, all persons must be evacuated from the area. This is referred to as searching-and-securing and is accommodated by the PASS in the search state. The search of the area is a combination of administrative and electronically enforced procedures. Administratively a team of two qualified employees search the tunnel moving from point to point resetting interlocks. As the search team proceeds through the area, they carefully inspect under and around all structures to ensure other personnel are not present. Under no circumstances does the team proceed with the search leaving any person behind in the secured area. This team is authorized only

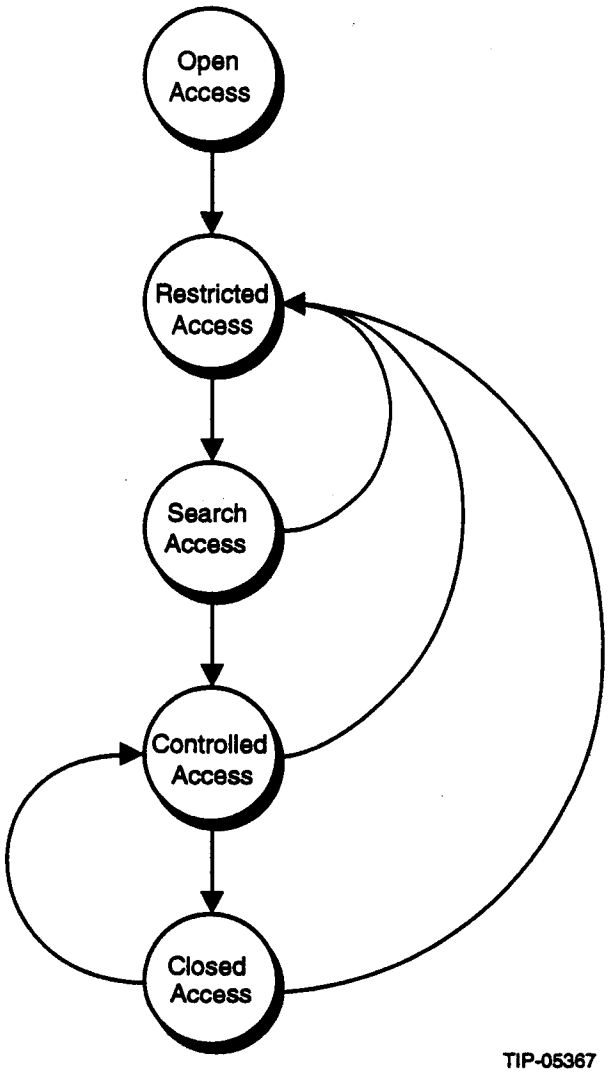

Figure 3.150: PASS state diagram.

after careful training in securing the area. During the time that the two person search-and-secure team evacuates the area of personnel, no further accesses are allowed.

Door-interlock boxes are located at each of the access points. These units sense the door's position via switches affixed to the door. They also serve as a means of forcing the search team to secure the area in a pre-defined sequence. The interlock boxes will not reset if an attempt is made to reset an interlock out of sequence. Any attempt to reset an interlock unit out of sequence will void the search and force the team to begin again.

Controlled Access

Controlled access is permitted for limited time-periods to allow personnel to enter the area in a carefully controlled manner without requiring the area to be secured again by a search-and-secure team. The PASS requirements include strict means of insuring personnel accountability for persons entering the tunnel. The exact controlled access procedure forces personnel to start at the control room where the chief operator on duty is responsible for the safe access of personnel. After being verified for proper training, personnel consisting of a minimum of two persons (buddy system) proceed to the Controlled Access Booth (Figure 3.151), often called a man-trap in the security industry. The procedure for entering and exiting is used extensively at high-security installations. At the SSCL, it is used as a means of assuring personnel accountability and safety. If the personnel wishing to make an access are qualified, the chief operator issues a key to each of the persons. A computer logbook is provided to keep a record of all accesses. The safety control system clearly displays all personnel who have keys along with the date and time the key was taken. This assures that at all times, the chief operator knows who is in the enclosure.

At door D1, personnel call the control room using the intercom and request that the door be opened. While watching the access via closed circuit TV, the chief operator enables the access by remotely unlocking door D1. When personnel are in the booth with door D1 closed, the chief operator releases D2 which automatically locks D1. This technique assures that at all times the access is controlled and that at no time is it possible for unauthorized personnel to have access since the chief operator is always in control. When personnel are ready to exit, they signal the control room via the intercom inside the enclosure at door D2. The operator in the control room remotely opens door D2 which automatically locks D1. Again the chief opera-

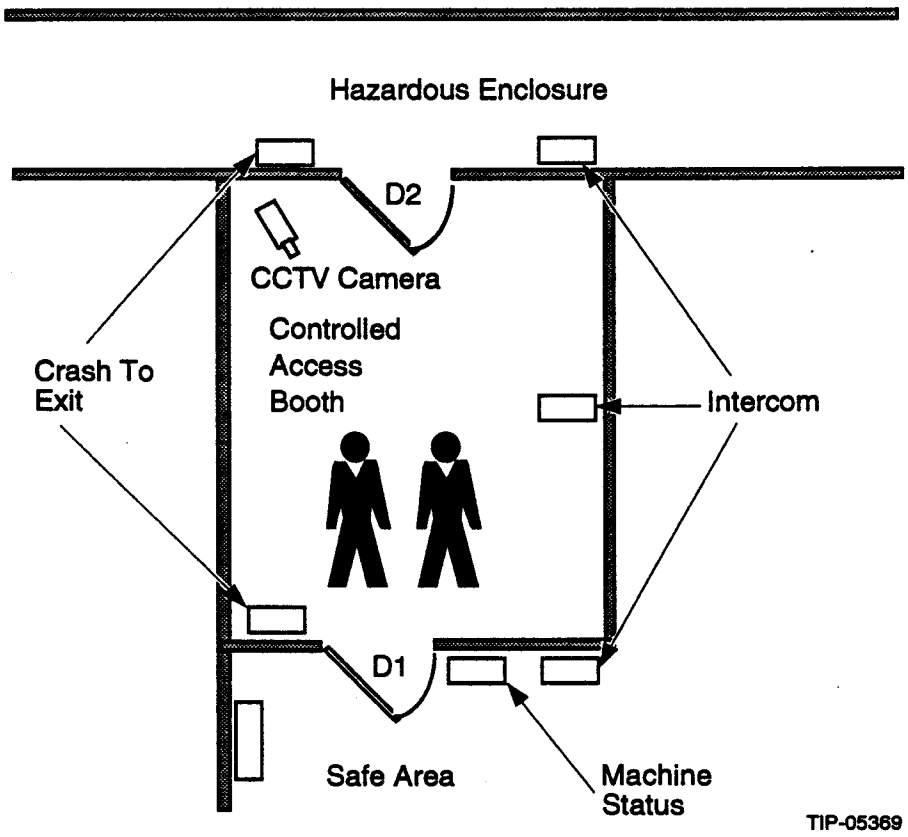

Figure 3.151: Controlled access booth (CAB).

tor must watch the controlled access booth to ensure no additional personnel enter. Exiting personnel return their keys to a key tree. The chief operator completes the controlled access by logging the access complete. Two crash buttons are used to exit the CAB in the event of an emergency.

Closed Access

Resetting the system in preparation for running the machine automatically triggers an audio message throughout the LEB enclosure. Therefore, in the unlikely event personnel are in the tunnel who have been overlooked by the search-and-secure team, they are given ample time to leave the area or actuate one of the numerous scram (crash) buttons located inside the LEB tunnel. After the audio warning time-out, the PASS enables power supplies and other hazardous devices allowing them to be safely energized. At this point the system is considered operational and no further access is allowed into the LEB.

3.8.8 Conclusion

The heart of the LEB PASS consists of the redundant fail-safe programmable electronic controllers, which are used to control and monitor the many aspects of safety relating to electrical and radiation hazards within the enclosures. The system monitors personnel access points, emergency crash buttons, power supplies, radiation-critical devices, and numerous other devices to insure the safety of personnel entering the LEB tunnel. Although Programmable Logic Controllers are new to safety systems they have proven to be viable alternatives to traditional electromechanical relays and adequately meet the requirements of a large distributed safety system. The system permits quick and easy controlled access of personnel into and out of the underground LEB tunnel. Retaining strict and safe control of personnel is enforced by keeping the system in several well-defined states. All the concepts and engineering discussed herein have been proven at the ASST facility which has proved to be an invaluable testing ground for the LEB PASS and all SSCL safety systems.

3.9 Civil Construction and Infrastructure

(J. Jones)

3.9.1 LEB Design and Construction

LEB Design and the Working Group

An LEB Working Group had been formed during the First Quarter of 1991 to develop the design for conventional facilities for the LEB. The Working Group is made up of personnel from Project Management (PMO), Accelerator Systems Division (ASD), Conventional Construction Division (CCD) and the Architect-Engineer/Construction Manager (A-E/CM), PB/MK. The Working Group usually meets on a weekly basis to discuss and resolve design problems during the development and production of the Design Requirements Document (DRD),[152] Title I (Preliminary) Design and Title II (Final) Design.

Schedules

Title II 100 % Design has been completed and the project advertised for bids on July 23, 1992; bids have been received on November 5, 1992; the construction contract awarded to Cajun Contractors, Inc. on December 8, 1992; and a notice to proceed with construction has been issued to Cajun on December 16, 1992. Cajun has continued to work on the conventional facilities into the second week of December 1993 before a stop-work order has been issued.

3.9.2 Site, Geotechnical, Earthwork and Infrastructure

Site

The LEB is located in Parcel 86C with the center of the ring about 275 m south of Old Maypearl Road and 275 m east of Beardon Road.

The most significant natural feature of the site is a small intermittent stream at the west side of the LEB. The tunnel shielding berm would have encroached on approximately 120 m of the stream. The stream has been relocated to the west of the site under a separate contract.

Surface facilities, as described below and as shown on Figure 3.152, are to be constructed at each of the three tunnel arcs and straight sections to house various technical systems. In addition to equipment pads at the surface facilities, 12 sets of choke and capacitor pads are to be located around the

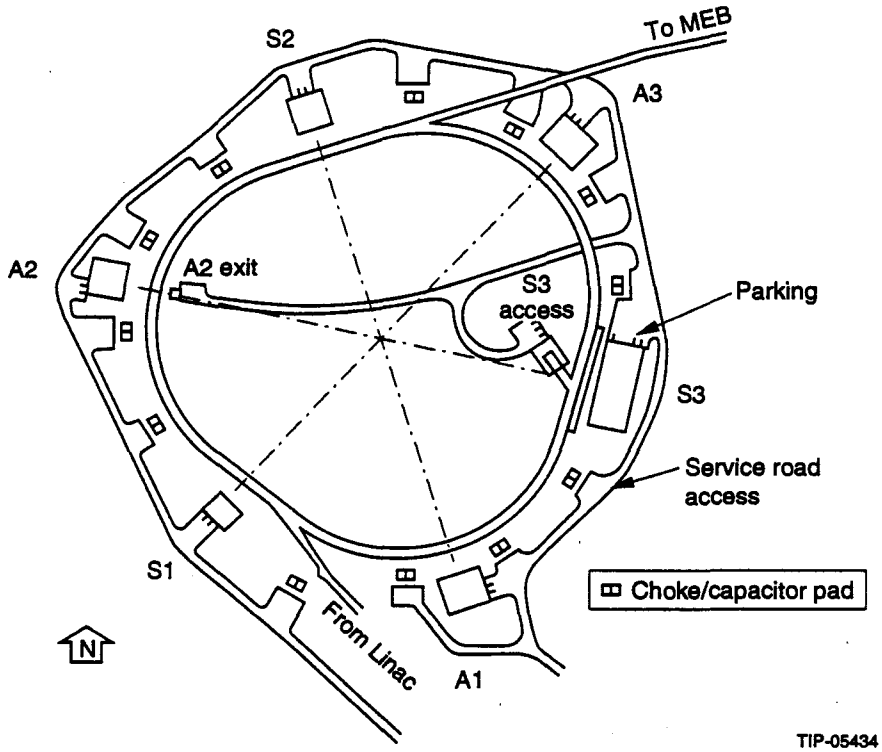

Figure 3.152: LEB site plan.

outside of the ring. The LEB tunnel is connected to the Linac on the south by the Linac-to-LEB transfer tunnel; and it is connected to the MEB on the north by the LEB-to-MEB transfer tunnel. The tunnels are to be covered by a shielding berm as described below.

Electrical service during construction has been obtained from TU Electric. Potable water has been obtained from the Buena Vista Bethel Water Supply Corporation.

Surface runoff water is generally intercepted and diverted away from the LEB complex by channels. Runoff from the interior of the ring is to be channeled to a low point at the southwest side of the ring and conveyed through culverts beneath the berm to the relocated stream.

Geotechnical

There are two major geologic units present at the site: overburden soils and Austin Chalk (AC).

Overburden soils consist principally of residual soils from the AC formation. In some areas, the residual soils are less than one foot thick and contain large amounts of organics; but in most of the areas, the thickness is 0.6–1.5 m. Quaternary deposits are found infrequently near the site along stream channels. Investigations north of the LEB at the Injector Cooling Pond site (inside the MEB ring) have shown the overburden soils to depths up to 6.5 m.

Overburden soils consist basically of two types of moderately to highly plastic clays as follows: the upper, near surface clay is dark brown or very dark brown; and the lower clay is tan and tan-brown. The clays are typically stiff to hard in consistency and contain varying amounts of organic matter.

Below the overburden soils is limestone of the AC formation. The top of the AC weathers to a softer, fractured limestone. The weathered AC has the following characteristics: tan color and large number of fractures; typically contains clay layers and argillaceous interbeds which are soft by rock classification; and the average thickness is approximately 4.25 m.

Below the weathered strata is the fresh, unweathered limestone/AC. The unweathered AC is primarily a gray, microgranular limestone with interbedded calcareous claystone. The AC can be thin to thick bedded, medium to moderately hard and slightly argillaceous. Argillaceuos interbeds in the unweathered AC are typically dark gray.

Existing ground surface varies between approximately elevations 660 and 676. The tunnel floor varies between approximately elevations 640 and 652. Average depths for tunnel excavations are about 6 m with all excavations passing through varying depths of overburden soils and weathered AC for construction of the tunnel floor slabs on unweathered AC.

Earthwork

Topsoil from the site has been stripped and stored in designated stockpiles. Overburden, weathered and unweathered Austin Chalk from tunnel excavation and other LEB construction is stockpiled for reuse as embankment material.

The LEB tunnel, transfer tunnels and access tunnels are constructed by the cut and cover method of construction. The trench is to be backfilled and

covered by an earthen shielding berm. Starting at the surface, the trench is excavated on a 1.5 or 2.0 horizontal to 1.0 vertical slope through the topsoil, alluvium and severely weathered AC. In the moderately to slightly weathered AC, the side slopes have been steepened to 0.5 horizontal to 1.0 vertical. In the unweathered AC, the trench has been cut vertically.

The shielding berm height is to vary up to a maximum height of 8.7 m above the interior of the tunnel roof if the berm density was 125 pounds per cubic foot. Experience at other SSC construction sites with similar materials indicates that a density of 117 pounds per cubic foot can be expected from the design compaction. The amount of shielding to be provided is to be increased proportionally to maintain an equivalent mass which results in a maximum shielding thickness of 9.3 m at injection, 8.5 m at extraction, 7.3 m at other locations around the LEB ring and 8.5 m at the LEB-to-MEB transfer tunnel. Side slopes of the berm are to be 2.0 horizontal to 1.0 vertical.

Areas disturbed by construction are to be seeded with a native grass seed.

Infrastructure

The following infrastructure items are to be provided as part of conventional construction: permanent roads; parking areas; site drainage; sanitary sewer for interior tunnel drain system; potable water for fire protection system; electrical power; communication; cooling pond water; and natural gas.

The Communication System is to have the following features:

- A conduit system is to be constructed to connect all Injector projects.
- At the LEB site, a conduit system is to be constructed around the LEB ring to connect all surface facilities.
- Conduits are to have copper cable for the following: building automation system (BAS) which is to be used to monitor and control heating, ventilation and air conditioning (HVAC); telecommunication system; and fire alarm system. The cables are to enter and exit each of the surface facilities.
- Additional conduit space is to be provided for technical systems and for future growth.

3.9.3 Architectural Systems

Surface Facilities

There are nine surface buildings as follows: A1, A2 and A3 Arc Power Supply Facilities; S1 Injection Facility; S2 Extraction Facility; S3 rf Facility; S3 Installation and Access Facility; A2 Emergency Egress and Access Facility; and S1 LCW Building. Two small rf Buildings (S2 rf a & b) have been planned inside the ring on the S2 Extraction straight for support of additional radio frequency (rf) cavities in S2, but they have been deleted later, because as the rf cavity design nears completion it has become evident that up to 16 cavities will fit into S3.

Building Enclosures

The buildings are to be pre-engineered steel structures with a bright silver metallic exterior finish. Metal panels are to have metal panel liners to provide thermal resistance of R15.

Building Interiors

Interior floors are to be cast-in-place concrete, trowel finished and sealed. Ceilings are to be exposed painted structure and exposed insulation. Interior doors are to be painted hollow metal; and exterior doors are to be painted hollow metal, overhead coiling and overhead sectional.

Code Requirements

The buildings are to be classified as B-4, Industrial Special Usage, in accordance with the Uniform Building Code (UBC); and construction is Type II-N in accordance with the UBC. The exit/egress is to comply with the National Fire Protection Association (NFPA) Code 101; and facilities are to comply with Uniform Accessibility Standards 795.

3.9.4 Structural Systems

Underground Structures

The LEB tunnel is 3.7 m wide $\times$ 3 m high $\times$ approximately 570 m long. The LEB-to-MEB transfer tunnel is 2.4 m wide $\times$ 2.4 m high $\times$ approximately 116.5 m long. A typical cross section of the LEB tunnel is shown in Figure 3.153.

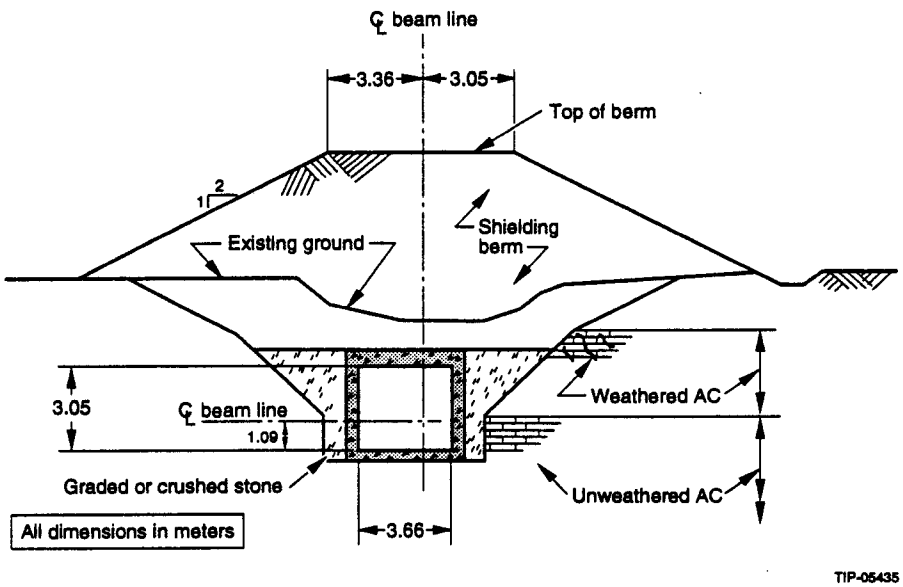

Figure 3.153: Typical tunnel cross section.

The tunnels are designed as cast-in-place reinforced concrete walls and roof slabs bearing on a concrete slab on grade. The tunnel section is designed as a frame with a hinge at the base of each wall. Where the top of the unweathered AC is above the top of the tunnel section, the tunnel walls have been cast against the exposed AC. Where the top of the unweathered AC is below the top of the tunnel section, the trench has been overexcavated and the sidewalls have been formed on both sides. The tunnel is constructed as a series of straight segments (chord construction) around the ring in accordance with the geometry in the Design Requirements Document (DRD).

The tunnel floor slabs have been cast directly on unweathered AC. Slab reinforcement has been placed such that it is continuous across control joints and doweled at construction joints. It is anticipated that the post-construction differential settlement will be less than 1-1/4 mm across adjacent joints.

The frame is designed to be moment-resisting. Where the top of the unweathered AC is below the top of the tunnel section, the frame is designed to support at-rest earth pressure in conjunction with a 50 % hydrostatic force. The structure is designed for a 100 % overburden pressure from the passive radiation shielding. Where the sidewalls have been cast directly against the

unweathered AC, the frame is designed to support full hydrostatic pressure. The structure is designed to support the interior loads from utilities and equipment as presented in the DRD.

The interior utility and equipment loads are to be transmitted to the structure through 41.3 mm (1-5/8 inch) channel inserts (unistrut or equivalent) that have been cast into the concrete walls at 2.44 m on centers.

The S2 Emergency Egress and Access and S3 Installation and Access tunnels are designed and constructed in the same manner as the LEB tunnel. Stairwells and equipment drop areas are cast-in-place reinforced concrete. Steel stairs are to be used. At-grade buildings are to be constructed as described above under Architectural.

Structural concrete is specified to have a 28-day compressive strength of 8 000 pounds per square inch for tunnel roof and walls and 6 000 pounds per square inch for tunnel floor. Grade 60 reinforcing steel is used.

Construction tolerances are as follows: walls, −6.35 mm, +25.4 mm; floor, +0, −12.7 mm; wall flatness, 6.35 mm maximum deviation from a 3.7-m long straight-edge; and floor flatness, Class AX surface finish tolerance, 4.75 mm maximum deviation below a 3-m long straight-edge.

The tunnel floor has a cross slope of 3.2 mm per foot toward a 102 mm × 51 mm deep continuous drain. The continuous drain has been cast into the floor slab adjacent to the interior wall of the tunnel. The structure has been waterproofed on the top and on walls with an elastomeric sheet membrane except where the walls are cast directly against AC. Bentonite waterproofing has been used at contraction joints where the walls are cast directly against the AC. Waterstops have been placed in construction joints.

Tunnel floor slabs have been placed directly on unweathered AC. Waterproofing has not been used under the slabs.

The exterior foundation underdrain system consists of 152 mm (6 inch) diameter PVC perforated pipe enclosed in a 0.6 m × 0.6 m pea-gravel envelope and wrapped in an underdrain fabric wrap. Where the trench is overexcavated and the tunnel sidewalls are formed, the foundation underdrain system has been placed outside each tunnel wall at the bottom of the excavation. The area between the walls and excavation is backfilled with graded or crushed stone to the top of the tunnel. Where the walls have been cast against unweathered AC, the underdrain system has been placed on both sides of the tunnel at roof level.

Building Structures

The foundations for all buildings, except the S3 Installation and Access and A2 Emergency Egress and Access Facilities, are to be stiffened slab-on-grade and grade beams. The foundations for the S3 Installation and Access and A2 Emergency Egress and Access Facilities are to be spread footings under columns and grade beams; and columns resting on shaft walls. The spread footings are to bear on engineered backfill that is placed around the access shafts. All of the slabs are to be placed on compacted granular fill which is to be placed on a vapor barrier over compacted select fill subgrade.

Those buildings that are to have facilities for low conductivity water (LCW), are to have a 38.1-mm deep curb around the perimeter to contain LCW spills. Sumps are to be constructed in the foundations to collect the spills and provide an easier means for pumping the spilled liquid to containment vessels.

Structural concrete is specified to have a 28-day compressive strength of 4 000 pounds per square inch for foundations and grade beams; and 6 000 pounds per square inch for slabs-on-grade.

The framing system for the surface facilities is to be pre-engineered steel buildings. Lateral and vertical stability, bracing and framing systems for the steel buildings is to be as follows: lateral stability systems are to be provided by rigid frames with end-bay framing cross bracing in the other direction; lateral bracing systems are to be used to stabilize the structures against lateral forces created by lateral sway, crane forces and 110 km/h wind forces; vertical framing systems are to consist of steel columns located at exterior grid intersections with the columns extending from the concrete foundations to design framing heights; and roof framing is to consist of gauge metal steel purlins spaced not more than 1.5 m on centers and spanning to the rigid frames with purlins supporting roof loads, dead loads and suspended equipment loads.

Choke and Capacitor Pads

Concrete foundations are required for Energy Storage Inductors (ESIs) and Capacitor Banks that are to be installed at 12 separate locations around the outside of the LEB ring as part of the main magnet power supply. Lightning protection, grounding and fencing are also required.

The choke is 37 m wide × 5.1 m long and weighs about 40 000 kg when filled with oil. The load is distributed uniformly to the foundation by two rails, one on each side.

Environmental regulations require oil and water containment of the 11 340 l of oil in the choke, plus a 50 % safety factor and 110 mm of rainfall per hour (100 year flood). A concrete pad large enough to contain all of the oil and rain water would have been costly and cumbersome to maintain. The preferred alternative is to use a reinforced concrete spread footing surrounded by a two-foot high berm constructed of crushed limestone to contain the oil and channel the oil to a drain. Four 0.61 m (24-inch) diameter pipe drains allow storm water from the 100-year flood to drain from the pad in 2 hours.

Imbiber beads,* are to be used to absorb the oil. The beads are polymer plastic spheres that are approximately 300 μm in diameter. As the beads come in contact with organic fluids, the fluid becomes entrapped by the molecular structure of the polymer. Imbiber beads can absorb as much as 27 times their original volume and, during the absorption process, they will swell to 3.5 to 4 times their original size. Imbiber beads are hydrophobic and will not absorb water or brine solutions.

For a catastrophic spill, an 11-mm thick layer of imbiber beads placed in the drain would absorb the oil spilled and stop the drain so that additional oil cannot escape through the drain. For small oil leaks, a few packets placed on top of the drain will allow the water to run through but absorb the leaked oil so that it can be removed without having to clean the entire drain system.

Lightning protection is to consist of two masts with a static wire strung between the masts. Masts are to be one-piece, tapered steel placed six feet outside of the fence on the centerline of the station. Mast height is 5.5 m so that the midspan of the static wire is at least 4.9 m above the pad. Maximum sag for a 9.5-mm diameter, high strength, copper coated steel aerial ground conductor is less than 0.6 m, even with ice loading. Two electrodes, or ground wells, are required at each mast. The electrodes are spaced 0.6 m from the center of the mast and 1.2 m to each side. Each ground well will require a 3-m long × 19-mm diameter ground rod. Additional ground rods will have to be driven to maintain a 10 Ω maximum resistance to earth for each well. The grounding system is to be constructed to obtain a 5 Ω resistance to ground.

*Manufactured by Dow Chemical.

Each of the 12 capacitor banks is estimated to be 3-m wide × 5-m long and weigh approximately 9000 kg. There are no special foundation requirements for the capacitors; therefore, a spread footing will be used for each capacitor bank.

3.9.5 Mechanical Systems

Heating, Ventilation & Air Conditioning—Surface Facilities

Those areas of surface facilities that are to be air conditioned will have direct expansion, packaged air conditioning units located outside on concrete pads with ductwork extending into the buildings.

Electronics rooms in Buildings A1, A2, A3 and S1 are to have air conditioning capacity of approximately 11 tons each; and electronics rooms in Buildings S2 and S3 rf are to have air conditioning capacity of approximately 18 tons each.

Those surface facility areas that need to be continuously ventilated are to have wall-mounted, belt-driven propeller fans and filtered storm proof louvers with automatic dampers for air intake.

Power supply rooms in all buildings are to have ventilation capacity of approximately 10 000 cubic feet per minute each.

All surface facilities are to be heated with gas fired, suspended unit heaters.

Heating Ventilation & Air Conditioning—Tunnel

The Tunnel HVAC system has the following features:

- Supply air through a packaged air handler with 17 500 cubic feet per minute (CFM) capacity located at the S3 Installation and Access Facility.
- Heating capacity of 1 750 MBH (1,000 BTUs per hour).
- Cooling capacity of 38 tons (tunnel load of 119 kW).
- Exhaust air through an exhaust fan with 17 500 CFM capacity located at the A2 Emergency Egress and Access Facility.

Fire Protection System

- An automatic sprinkler system is to be installed for fire protection at Buildings S2 and S3 rf.

Conveying Systems

The S3 Installation and Access Facility is to have an elevator and crane as follows:

- Personnel and Equipment Elevator: 900 kg capacity.
- Bridge Crane: 15 ton capacity with about 10 m rail span and 8.5 m runway travel distance; and 4.25 m clear hook height above floor and 14 m lift height.

Low Conductivity Water (LCW) Piping System

It has been planned originally to construct a Central Utility Plant (CUP) in the MEB ring and pump LCW to the various injector sites through a stainless steel-pipe distribution system. Because of the possibility of leaks of irradiated water from the overland distribution system, this is not an environmentally acceptable plan. The solution adopted is to construct LCW plants at each of the sites and pipe the LCW into the tunnels through double-walled pipe. At the LEB, the LCW plant is to be housed in an LCW building adjacent to Building S1. LCW is piped into the tunnel and around the ring in a stainless steel pipe system. The stainless steel pipe, from the LCW building through the tunnel wall, is encased in PVC pipe with the PVC pipe opening into the tunnel.

Plumbing

The plumbing system has the following features:

- The foundation underdrain system connects to a sump with a sump pump that is located adjacent to the S3 Installation and Access Facility. Discharge from the sump is to the surface storm drainage system.
- Tunnel slope is such that interior spills and seepage within the tunnel flows to a sump with a sump pump that is located at the low point in the tunnel on the east side of the ring. Discharge from the sump is to a surface station for periodic testing and disposal.

3.9.6 Electrical Systems

Electrical—Tunnel

The tunnel electrical system has the following features:

- Tunnel lighting consists of 100 watt high pressure sodium fixtures spaced at approximately 50 feet on centers. Emergency lighting fixtures and exit lights are fed by remote battery systems located in buildings A1, A2, A3, S1, S2 and S3 rf.
- Power receptacles for 120-volt single-phase equipment are provided at approximately 30 m on centers.
- Power receptacles for 208-volt three-phase and 408-volt three-phase equipment is provided at approximately 45 m on centers.
- Panelboards for 120 volt, 208 volt and 480 volt is located in the tunnel.
- Grounding wire consisting of #4/0 AWG is provided for the entire length of tunnel.
- Fire alarm heat detectors and pull stations with alarm horns are located along the entire length of tunnel.

Electrical—Surface Facilities

The electrical system for the surface facilities has the following features:

- The grounding system consists of a continuous #4/0 AWG exterior loop and interior #4/0 AWG bare conductor.
- Industrial lighting fixtures with emergency lighting and exit signs are to be provided.
- Lightning protection system will be installed to meet the requirements of Underwriters Laboratories, UL-96A, National Fire Protection Association, NFPA 70 and 78, and Lightning Protection Institute Installation Code, LPI 175.
- Convenience receptacles are located at approximately 9 m on centers.
- Panelboards for 120 volt, 208 volt and 480 volt are located at buildings A1, A2, A3, S1, S2 and S3 rf.

- 12.47 kV is to be supplied to harmonic filters at buildings A1, A2 and A3; and also to a substation which is to furnish 480-V feeds to buildings A1 and A3.

3.9.7 Fire Protection Design Analysis (FPDA)

Surface Facilities and Tunnel

Three FPDAs have been prepared, with a final edition being produced in April 1993. The first two editions of the FPDA showed the Maximum Possible Fire Loss (MPFL) to exceed $1 000 000 for Buildings S2 and S3 rf and the Tunnel; therefore, an automatic fire suppression system (automatic sprinklers) would be required at each of those three locations. It has been later determined that fire-loss scenarios that have been used for the tunnel are incorrect. Realistic scenarios have been proposed and estimated, and it has been determined that the MPFL for the tunnel does not exceed $1 000 000; therefore, an automatic sprinkler system is not required in the tunnel. Sprinklers are only required for buildings S2 and S3 rf only.

3.9.8 Acknowledgements

The LEB conventional construction design has been a collaborative effort of many. Participating in the Working Group have been C. Augustin, J. Ballam, R. Dawson, D. Earsom, G. Jackson, T. Morris, L. Norman, D. Silveira and T. Whitaker from the Conventional Construction Division; T. Conley and T. Jimenez from PB/MK; R. Aiello, G. Conway, B. Edwards, J. Ferrell, D. Haenni, R. Harold, W. Merz, M. Wilson, R. Winje and Y. Zhang from the Accelerator Systems Division; J. Bull, J. McGill, G. Tuttle and R. York from the Accelerator Design and Operation Division (later to become the Project Management Office). Additionally and in later stages, J. Clifton, R. Etheridge, J. Ives and R. Molenaar have provided valuable input. T. Conley and J. Rozek have been representing PB/MK during the course of construction, until termination of the project.

Chapter 4

Beam Commissioning

4.1 Overview of Commissioning Task

Commissioning of the LEB beam has been considered to be a challenging task early on in the construction phase. While faster cycling machines have been built and operated as well as machines with more complicated lattices, the combination of rapid-cycling operation and a sectioned lattice—with the matching issues inherent to such designs—poses special operational challenges. Constructively they are attacked at first by ensuring adequate tracking of the ring magnets even under ac conditions, secondly by providing a very flexible set of corrector magnets together with a control system able to handle the computational load of controlling this rather large number of parameters, and thirdly by providing adequate readout bandwidth for the diagnostics to be able to get turn-by-turn data over a whole acceleration cycle. In order to get an understanding of the commissioning issues and also to be able to precisely define the requirements for the beam diagnostics and the control system, a beam commissioning working group was established once the lattice was completely defined. This group has been charged with defining the bandwidth requirements for the control system, producing a list of high-level software to be available for the commissioning task, and establishing a beam commissioning plan. Cancellation of the SSC project prevented the group from producing a final report; this chapter will attempt to summarize the groups findings. The collection of minutes of the group's meetings have become a part of the SSC close-out documentation.[153]

In its early phase the group has developed the beam commissioning scenario presented in the next subsection. From this plan a list of tasks has

been generated, which are subject to further study and simulation. A novel concept used in part for this study is a simulation engine programmed on an iPSC/860 hypercube parallel computer* interfaced to a console workstation using the EPICS system software, which is to be used for the control system (Section 3.6. The simulation engine is based on a modified version of the computer code TEAPOT.[154] Benefits to be obtained from this approach are the ability to perform "dry runs" of the algorithms developed (*e.g.* for orbit correction), testing of the developed software including drivers *etc.* in the control system environment, and the use of the EPICS operator interface in a "semi-realistic" environment.

4.1.1 Beam Commissioning Plan

For the purpose of developing a commissioning plan the beam commissioning of the LEB is divided into five stages:

1. Beam injection and closure of the first turn;
2. Minimization of closed orbit excursions and adjustment of machine tune and section matching;
3. Acceleration of the beam to full energy;
4. Increase of the beam intensity to its design value, and
5. Increase of the beam brightness to its design value.

While it is clearly understood that during the actual commissioning a much more iterative path would be followed, this model has provided useful guidance to define the tasks to be accomplished. In addition, a "top-down" approach for each stage allows to further separate and analyze the issues. In this way, algorithms are refined as more and more "imperfections" are taken into account.

Beam Injection and First-turn Closure

The Linac delivers an H^- beam with an rf structure of 425 MHz and a pulse length between 0.5 and 20 LEB revolutions (at $\beta = 0.78$). The following tasks have been identified to achieve closure of the first turn in the LEB:

*Manufactured by Intel Corp., Sta. Clara, CA

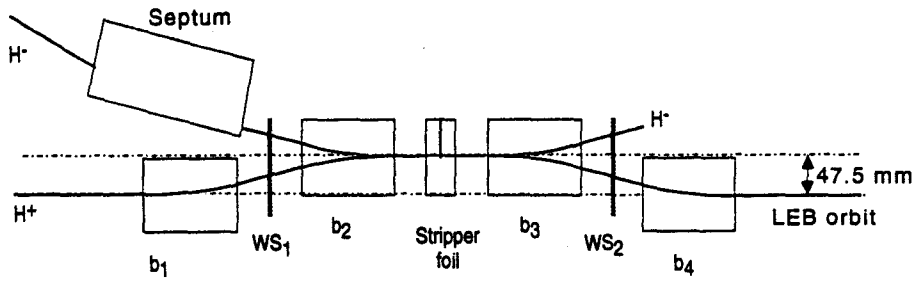

Figure 4.1: Schematic layout of the injection section.

- Tuning of the injection line (which is not within the scope of this document);
- Setting of the injection orbit bumps;
- Measurement of the stripping ratio;
- Threading of the beam around the ring;
- Establishing closure of the first turn.

Injection Orbit Bumps Two wirescanners are foreseen in the injection girder, one before and one after the stripper foil (Figure 4.1). They have sufficient travel to cover both the circulating proton beam and the incoming H^- beam or, in case of the second scanner, any H^- beam leaving the foil location. Together with the position of the beam on the foil (as determined by a viewer screen) they are sufficient to calibrate the orbit bump magnets (which are identical and powered in series). Calibration of the bumps would proceed as follows: With bump magnets at their nominal setting,

- Inject beam with stripper foil removed
- Record beam centroid position at WS_1 and WS_2 (Figure 4.1). By symmetry this gives the angle at the foil:

$$\Theta_{foil} = x_{WS_2} - x_{WS_1}. \tag{4.1}$$

- Insert foil gradually until half of the beam is intercepted (monitor current at H^- dump). This gives beam position at foil location.

- Inset foil completely and measure position at WS_2. This gives the bending angle of the bumps:

$$\Theta_{bump} = \frac{x_{WS_2} - x_{WS_1}}{D_{WS_2-WS_1}}. \tag{4.2}$$

In this way the bump magnets are calibrated and the amplitude of the orbit bump can be found. By adjusting the angle and position of the incoming H^- beam and setting the bump magnets to their nominal angle the stripped proton beam will enter the ring reasonably well centered.

Threading the Beam Around the Ring DIMAD calculations indicate that the beam should circulate in the ring even if alignment tolerances exceed the specifications by a factor of three and no orbit correction is done. The first attempt at closure would therefore involve varying the main magnet setting, assuming that failure of the beam to go around the machine is due to momentum offset. Loss monitor readings and BPM readings at the point of beam loss should aid in finding the direction of the momentum offset. Failing to achieve a first turn in this way, corrector magnets roughly 90° in betatron phase before the point of beam loss would be used to successively thread the beam around the ring.

Closure of the First Turn Bringing the beam once around the ring does not establish existence of a closed orbit within the vacuum chamber. To achieve this the head of the circulated beam has to coincide with the incoming beam in all four transverse coordinates (x, x', y, y'). This can be achieved by varying the last orbit correcting dipoles to ensure that the WS_1 position reading of the circulated beam equals the WS_2 reading of the injecting beam and that both beams hit the foil at the same location.

Closed-orbit Centering and Lattice Tuning

Once successful closure of the orbit is achieved, and the beam circulates at least for a short time, the closed orbit can be centered using the orbit corrector dipoles. This has been successfully tested on the Hypercube simulator; the algorithm used is described in Section 4.2. Definition of this task, however, has uncovered a requirement for at least some of the beam position monitors to be sensitive to the fundamental revolution frequency as the 425 MHz Linac frequency is not guaranteed to give a useful signal

after the first turn, while the bunch-frequency component at 47.5 MHz will not develop until several turns later (and does require a running rf system, which may not be present all the time during the early stage of commissioning). It has also been realized that rf turn-on would be easier in the presence of circulating beam as bunching can be observed. As a result it has been decided to request low-frequency electronics for a subset of 12 of the BPMs to fill in this gap.

The identified tasks in this stage are

- Minimization of orbit excursions using available low-frequency BPMs;
- Activation of the rf system;
- Activation of the radial loop;
- Minimization of orbit excursions using all BPMs (if required);
- Measurement of transverse tunes;
- measurement of the lattice functions (β(s), η(s) and global properties like γ_t).

Before approaching these tasks the expected performance of the LEB without any corrections has been investigated. This has been done to get a feel for the degree of correction actually needed. In a simulation the LEB dynamics including space charge effects have been studied as a function of the residual orbit excursion. Figure 4.2 shows the emittance growth and the beam survival as a function of residual *rms* orbit excursion. The uncorrected *rms* orbit excursion is expected to be about 5 mm (the orbit excursion has been artificially enhanced for some of the simulation runs). This value would not significantly affect the machine acceptance, but it is clear that the emittance goal will not be met. In fact, it will be necessary to center the orbit as precisely as possible to maintain the beam emittance; the expected *rms* orbit excursion after correction is about 1 mm.

Mismatch of the quadrupole and dipole settings—caused by setting errors or by mistracking—will affect γ_t and also cause dispersion in the straight sections. Figure 4.3 presents data for various levels of mismatch. The lattice is seen to be well behaved as long as the quadrupole strength lags behind the dipole strength. The sensitivity seen if the quadrupoles are stronger than they should be has a simple explanation—the tune in the ring approaches 12 and, thus, the main integer resonance. Constructively, the quadrupoles saturate earlier than the dipoles and, thus, a situation where $(\delta Q/Q)/(\delta B/B)$

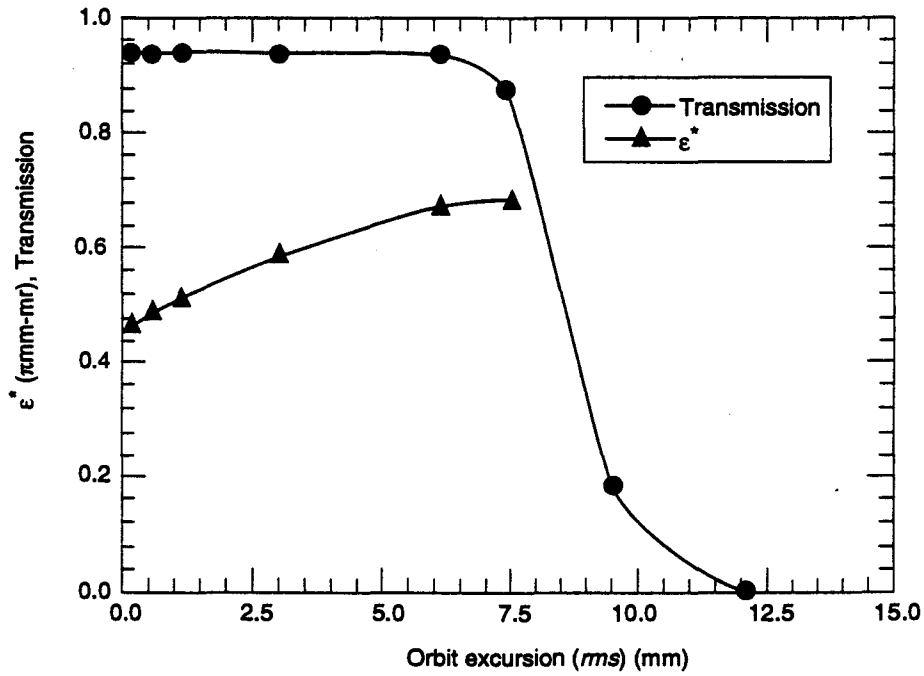

Figure 4.2: Transmission and beam emittance in the LEB for different orbit excursion.

is larger than 1 can be fairly easily avoided. Variation of γ_t does set a lower limit on this ratio, however, as γ_t should not become smaller than about 18 in order to prevent difficulties with the LEB-MEB synchronization.

Data from the prototype magnets show that the deviation from the design tune due to mistracking can be fitted to good accuracy by a third order polynomial, see Figure 4.4. Since the nominal single-particle working point will be (11.85,11.80) to accommodate the space-charge tune shift resonance lines crossed during a ramping cycle will include $\nu_x + 2\nu_y = 35$, $3\nu_x = 35$ and $3\nu_y = 35$.

A simulation study has been done to see the effects of those resonances on the beam emittance using SIMPSONS;[27] 1000 particles are tracked in 6-D phase space with energy ramping according to the sinusoidal LEB cycle. The tune excursion due to magnet saturation differences, which we call tracking error, is included as a systematic quadrupole error, which follows the measurement result of the prototype magnet. Space charge effects are not included so that there is no large tune spread.

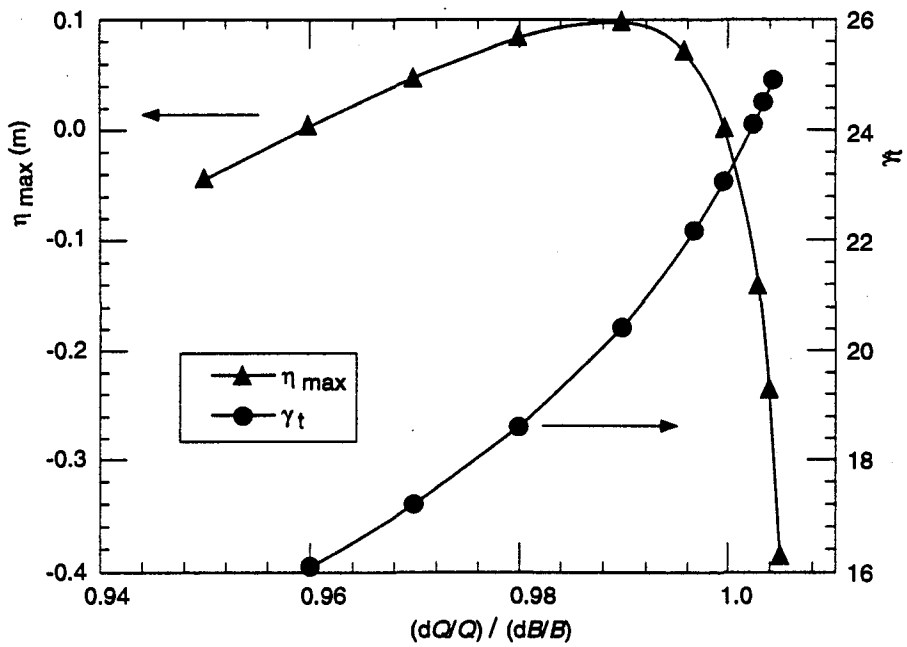

Figure 4.3: Effect of mismatch between quadrupole and dipole strength on straight-section dispersion and transition energy.

Figure 4.5 shows that the *rms* emittance in both transverse planes increases at 18 ms after injection. At that time, the tune satisfies the resonance condition $\nu_x + 2\nu_y = 35$. The initial transverse emittance is 0.4π mm-mrad. Figure 4.6 shows results for the same simulation but for an initial emittance of 4.0π mm-mrad. Because the strength of a nonlinear resonance depends on a particle amplitude, emittance growth due to resonance crossing is enhanced with larger initial emittance.

Orbit Minimization, Unbunched Beam It is expected that right after orbit closure is achieved the beam lifetime will be too short to proceed with rf turn-on. Therefore, the orbit correction algorithm outlined at the end of Section 4.2 will be employed to correct the orbit of the coasting beam as well as possible using data from the low-frequency BPM.

Rf System Initial Turn-on Once the rf system has been activated the correct frequency needs to be found. Straightforward determination by mea-

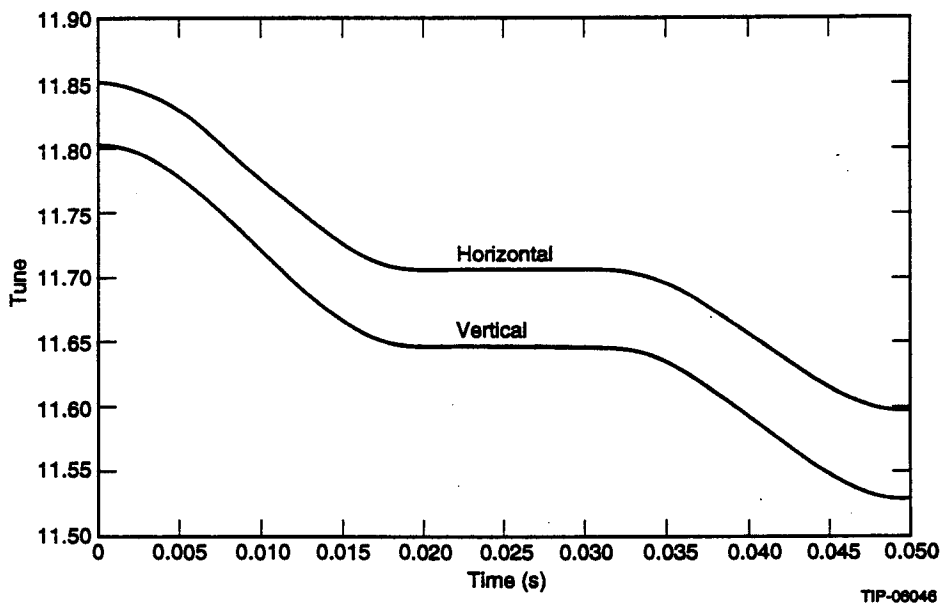

Figure 4.4: Tune variation during the LEB cycle due to mistracking of quadrupoles and dipoles.

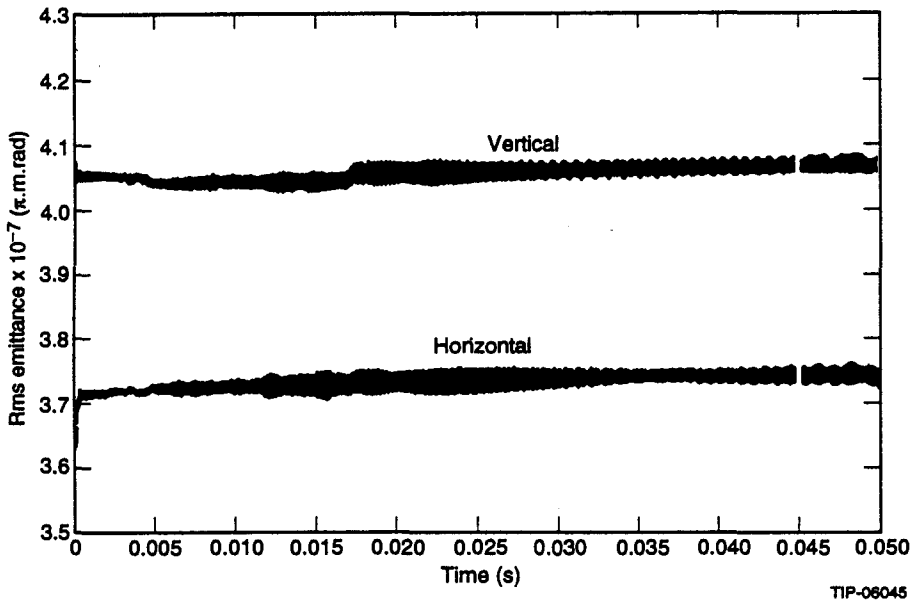

Figure 4.5: Emittance growth in the LEB cycle due to mistracking of quadrupoles and dipoles.

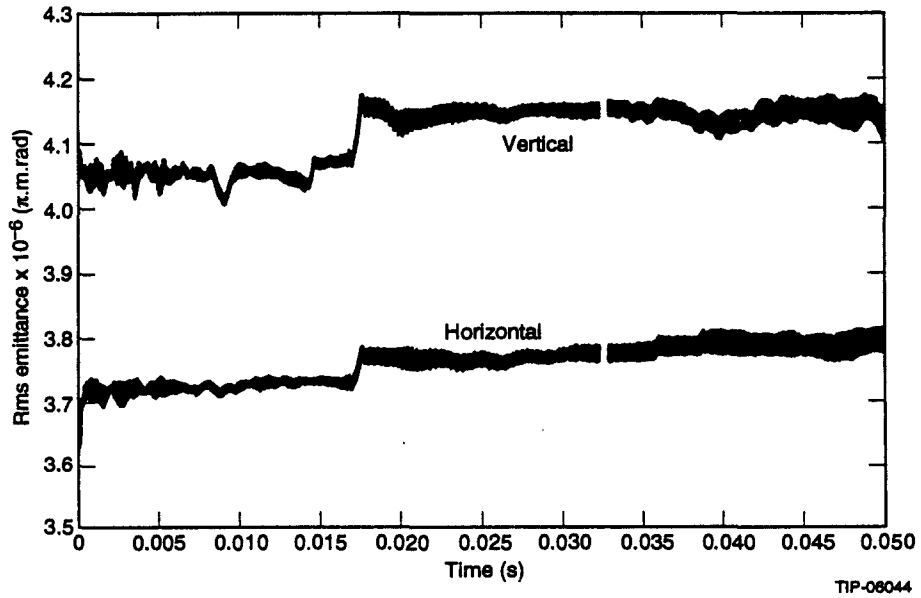

Figure 4.6: Emittance growth in the LEB cycle due to mistracking of quadrupoles and dipoles.

suring the beam revolution time will likely not be accurate enough to set the rf frequency sufficiently close to the nominal frequency (hf_c) that bunching occurs. ESME simulations indicate that at 50 kHz (0.1 %) or more offset from hf_c bunching will not occur, therefore, the frequency has to be scanned. At frequencies close to hf_c partial capture will occur and the resulting tumbling of the bunches will give rise to a momentum offset detectable by the BPMs in the dispersive arc regions as well as a phase oscillation between the beam and the rf. Figures 4.7 and 4.8 shows an ESME result; $\delta p/p$ and δs are plotted against turn number for various frequency offsets and it appears that $\delta\Phi$ is the more sensitive indicator, giving a useful signal down to less than 1 kHz frequency deviation while the sensitivity of the $\delta p/p$ measurement is limited to about 3 kHz deviation ($\approx$0.1 mm offset).

Once the frequency is adjusted the radial loop is closed and its parameters are adjusted to avoid steering of the beam by action of the loop. This is important as it maintains the beam energy and thus allows detection of any energy offset between the Linac beam and the LEB central energy in the next step.

Orbit Centering With the beam bunched, orbit centering will be redone using the complete set of BPMs available. Besides it being important in its own right, any significant difference from zero of the average setting of the BPM would indicate a deviation of the LEB central energy from the beam energy. This would be corrected by an adjustment of the current through the main magnets. The algorithm for this task is described at the end of Section 4.2.

Tune Measurement The machine tune measurement will give the first precise indication of the accuracy of the magnet system settings. It will be important to measure and adjust the tune to ensure a stable operating point and sufficient beam lifetime to proceed with the commissioning tasks.

The integer value of the tune will be determined by finding the dominant spatial frequency around the ring in the closed orbit; this can be done by Fourier analysis. A different approach might be fitting of a sine function to the orbit, but the problem is rather ill-conditioned and an advantage over Fourier analysis is not obvious.

The fractional tune will be obtained by Fourier analysis of the turn-by-turn data from one BPM, of a beam pulse executing coherent transverse oscillations by either injection off-center or excitation by the diagnostic kicker.

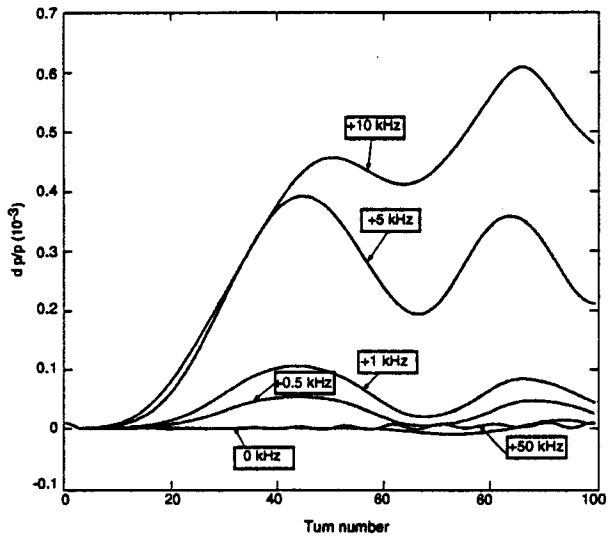

Figure 4.7: Momentum deviation *vs.* number of turns after injection for various deviations of the rf frequency from f_c.

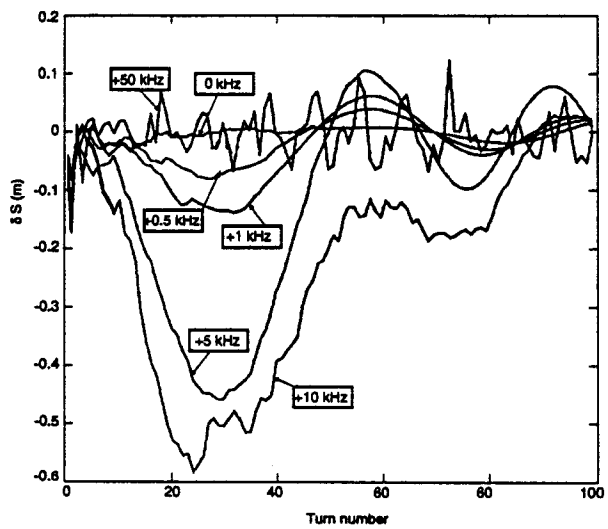

Figure 4.8: Spatial phase deviation *vs.* number of turns after injection for various deviations of the rf frequency from f_c.

Precision of this measurement will be determined largely by the number of turns that the coherent oscillation lasts. Under static conditions a precision of 10^{-3} is being aimed for. Precision can be increased by repeatedly firing the kicker and averaging over several measurements if required; the fast-cycling nature of the LEB makes this method practical. Since turn-by-turn sampling folds the tune spectrum into the interval [0,0.5), the half-integer part will be determined by slight variation of the trim quadrupole strength as an increase in the quadrupole strength will appear to lower the fractional tune when the "true" tune is between 0.5 and 0.999.

Lattice Function Measurement Measurement of the β functions at each trim quadrupole is straightforward by varying the quadrupole strength and determining the tune dependence, using the well known relation

$$\Delta\nu = \frac{1}{4\pi}\int_{quad} \beta\Delta k ds \approx \frac{\beta}{4\pi}\Delta k L_{quad}. \tag{4.3}$$

In a rigorous sense this relation holds true only for vanishing Δk since β itself depends on k. By chosing several values for Δk and keeping the maximum Δk small, < 0.1, accurate determination of β is nevertheless possible. The method is fundamentally limited by the precision of the tune measurement. The procedure has been simulated with the code SIMPSONS to generate tracking data for various values of Δk and Fourier analysis of these. Deviations of the "measured" β functions from the nominal values are in general only a few % (except in one case where a deviation of 12 % has been observed).

The dispersion function η is measured by observing the closed orbit shift as a function of the beam momentum; this is done by varying the rf frequency and using the relation

$$\delta x = \eta\frac{\delta p}{p} = \eta\frac{\gamma^2 - \gamma_t^2}{\gamma^2\gamma_t^2}\frac{\delta f}{f}. \tag{4.4}$$

Although γ_t enters the equation (which will not be known precisely), at injection the relation is dominated by $1/\gamma^2$ of the beam—which will be known to good accuracy—so that the uncertainty introduced is only small. Because $\delta p/p$ variations are typically on the order of 10^{-3}, nonlinearity is not an issue in this measurement (the true nonlinear dispersion in the LEB is very small). On the other hand, care has to be taken to avoid partially scraping the beam thereby skewing the beam distribution that would introduce a deviation in

the beam centroid. This requires one to keep the orbit shifts quite small, a few mm at most, requiring high resolution of the BPM. Again, several data points at various rf frequencies would be taken to ensure linearity. Testing the procedure with tracking data has yielded dispersion values within 15 % of the nominal value of about 3.6 m. In the straight sections a better accuracy will likely be required, depending on the width of the synchro-betatron resonances excited.

Observation of the tune at the same time yields a simultaneous measurement of the machine chromaticity ξ. From the same tracking runs, the chromaticity has been "measured" to within 2 % accuracy (confirming that the somewhat large error seen in the dispersion measurement is not related to an uncertainty in the knowledge of γ_t).

The synchrotron tune will be measured analogous to the betatron tune by applying a longitudinal kick to the beam (*i.e.*, a phase jump in the rf) and observing the transverse oscillation of the beam resulting from the dipole oscillation of the bunches in a dispersive location. The difference lies in the much smaller and variable synchrotron tune, which varies from 0.04 to about 0.002. Using the same Fourier analysis as for the betatron tune the accuracy is greatly reduced because of the limited number of synchrotron periods that can be sampled before the tune changes appreciably. Also, the momentum kick has to be kept small compared to the momentum spread of the beam in order to avoid the nonlinear large-amplitude region of the bucket and possibly beam beam loss; for a given level of BPM introduced noise this further reduces the precision achievable. Nevertheless, for stationary operation and during the early phase in the acceleration cycle a measurement is still possible, and the simulation on the iPSC/860 simulator clearly shows the synchrotron peak in the spectrum allowing determination of ν_s to a precision of 5–15 %. Towards the end of the LEB cycle, however, determination of ν_s will not be practical with this method. An alternative method may be to operate the machine at a rather large chromaticity. This would allow detection of the synchrotron sidebands during measurement of the transverse tune. This has not been further investigated.

Beam Acceleration

Stage III consists mainly of the commissioning of the various rf system components: the rf program generator, cavities cycling at a high voltage, rf loops under dynamic conditions *etc.*; but also the timing system will be required to perform in order to ensure injection at the bottom of the cycle. Since

eddy-current effects may significantly alter the lattice behavior of the machine, slow, ramped operation is foreseen to be used initially until top energy is reached. In this way eddy-current effects are more easily discriminated against as they would be insignificant for the slow cycle. The identified tasks are (assuming the rf system is already commissioned for static operation at injection frequency):

- Activate phase loop
- Activate cycling operation for both rf and magnet system
- Synchronize injection timing with LEB cycle
- Optimize extraction timing
- Tune the extraction line (not within scope of this document).
- Optimize the rf frequency program
- Optimize the rf voltage program

Optimization of the extraction timing and transfer line is important to minimize activation of LEB components. Once this program is successfully completed 10-Hz operation would be attempted, and it is expected to proceed through the same tasks again.

Activate Ramping of Ring In preparation for ramped operation the rf and magnet program would be set to its precalculated functional form using the best available magnetic-field and frequency data obtained from dc operation. Ramping would be activated with the radial loop open for maximum sensitivity; in this way timing of the loss of the beam would indicate at which point in the cycle the frequency program gets to be too far off. The rf frequency would then be piecewise adjusted until the beam survives the full cycle and BPM readings in the dispersive regions are nearly centered. Only late in the cycle would the radial loop be activated and its gain readjusted to cancel any residual momentum errors during the cycle.

Linac-LEB Synchronization The Linac receives a signal from the LEB control system (Section 3.6) that the LEB is ready to receive beam; at which time a Linac pulse is released. Injection timing would be adjusted to minimize losses, the minimum however is expected to be rather shallow

and does depend on the accuracy of the energy match. ESME calculations (Section 2.3.2) indicate that slight advancement of the injection timing may be helpful in relaxing the energy-matching tolerance at the injection.

Extraction Timing Timing of the extraction system early during the commissioning is important to protect the extraction septa from high dose rates. By carefully adjusting the timing of the kicker-firing pulse the number of bunches is minimized, this will be readily detectable on the beam loss monitors adjacent to the extraction-system components. Timing accuracy to a few ns is necessary for this task.

Optimization of the Rf Program Once acceleration and extraction at 12 GeV/c is achieved the rf program is optimized to maximize transmission. Beam loss is expected during capture as well as somewhat later in the cycle where the bunch-to-bucket height ratio is smallest. Using radial position and phase measurements it is expected that the rf program can be adjusted to within a few kV and degrees of the optimal setting.

Increasing the Beam Intensity

At this stage the LEB is able to accelerate beam up to 12 GeV/c extraction momentum at the 10-Hz cycling rate. It is in this stage that a systematic search for the intensity bottlenecks and the causes of losses would be undertaken. Task definition is more difficult in this stage as there will be undoubtedly "surprises" and apparently inconsistent results. However, there are a number of tasks that we expected would be performed sooner or later under almost any circumstance:

- Detuning of the rf cavities;
- Orbit correction as function of time in the cycle (t_{cycle});
- Tune measurement as f(t_{cycle})
- Lattice function measurements as f(t_{cycle});
- Aperture scan of the ring at injection (or a time in the cycle when losses are large);
- Tune space scan.

The group has had only preliminary discussions about this stage.

Increasing Beam Brightness

The likelihood is great that once the design intensity is reached the beam emittance will exceed the requirement of 0.4π mm-mr. In this conceptually last stage the emittance-enlarging would be studied and (hopefully) eliminated. The working group has not reached this stage.

4.2 The Beam Control Simulator

4.2.1 Application Software

Definition of the high-level software required to commission and operate the machine actually serves two purposes: Besides the obvious necessity of software specification, the bandwidth requirement for each package is also determined to a large extent by the software specification. In defining the application software the group has been able to define realistic bandwidth requirements for each subsystem of the LEB beam instrumentation.

The list of application software is shown in Tables 4.1, 4.2 and 4.3, separated into diagnostics software (like display of machine data), transverse beam dynamics and longitudinal beam dynamics. This whole set of software is also referred to as High Level Application Code (HLAC) to discriminate against the routines that perform tasks like instrumentation I/O and transmittal and access of data.

Besides identifying the purpose and parameters for each package, the bandwidth required is also given. It should be noted that these bandwidth values represent the read-out bandwidth for the front-end processors and therefore take into account the frequency at which the operator display is to be updated, which is not always the LEB cycling frequency. In fact, data-intensive operations (like a complete dump of all BPM data over one complete LEB cycle) are restricted to much lower frequencies, often once per MEB cycle. The front-end processors, on the other hand, have local storage and are able in most cases to store data on a turn-by-turn basis, providing comprehensive data if so required. In this approach, the goal has been to avoid one operation that may be only seldomly performed to drive the bandwidth specification for the whole control system.

Table 4.1: Application packages: beam diagnostics.

Name	Parameters	Description	Bandwidth
Closed orbit display	Location in cycle; width of averaging window	Retrieve and display closed orbit at all BPM lcations. Update at 10-Hz rate.	180 BPM × 4 bytes × 10 s^{-1} = 7.2 kB/s
Corrector strength display	Location in cycle	Retrieve and display settings of all correctors. Update once every MEB cycle.	90 correctors × 4 bytes × 1/7 s^{-1} $\leq$ 1 kB/s
Post-mortem dump	Operator request	Retrieve and display BPM data from last 25 000 turns within 2 min.	90 BPM × 2 planes × 4 bytes × 25 000 turns × 1/120 s^{-1} = 150 kB/s
Tune measurement	Timing in cycle	Calculate 1024 turn FFT of selected BPM data at 10 positions on ramp. Optional 4096 turns at 2 points on ramp. Display in 7 s.	1024 × 2 planes × 2 bytes × 10 s^{-1} = 7 kB/s

4.2.2 High Level Beam Control Simulator (G. Bourianoff)

In order to develop and test the commissioning software for the LEB, an interactive simulator as shown in Figure 4.9 has been built to serve as a development platform for High Level Application Code (HLAC). It is built around an Intel iPSC/860 hypercube parallel computer that serves as a particle tracking engine. An intermediate hardware and software layer fully incorporates the EPICS control system as discussed in Section 3.5. Details of the control system are hidden from the HLAC by Application Isolation Code (AIC) which consists of C++ class libraries. By the time of project

Table 4.2: Application packages: transverse beam dynamics.

Name	Parameters	Description	Bandwidth
Closed-orbit smoothing		Smooth closed orbit at 1-Hz rate. Change only 1 scale factor in the ramp.	180 BPM × 4 bytes × 10 s^{-1}+ 90 Correctors × 4 bytes × 1 s^{-1} = 1.1 kB/s.
Set entry correctors		Record BPM readings from first turn and set first two correctors at 1-Hz rate.	180 BPM × 4 bytes × 10 s^{-1}+ 4 Correctors × 4 bytes × 1 $s^{-1} \leq$ 1 kB/s.
Set exit correctors		Record BPM readings after entry correctors set. Set last two correctors ar 1-Hz rate.	180 BPM × 4 bytes × 10 s^{-1}+ 4 Correctors × 4 bytes × 1 $s^{-1} \leq$ 1 kB/s.
Closed three-bump	Midpoint, stride, amplitude	Create a local three-bump in 1 s.	Negligible.
Chromaticity adjustment	Residual chromaticity	Set chromaticity with five rf frequency offsets in 7 s.	1024 points × 2 planes × 4 bytes × 5 points × 1/7 s^{-1} = 6 kB/s.
Poincare plots	Lattice points, cycle number	Display 25 000 turns of 1-D phase space in 2 planes in 7 s.	3 BPM × 2 planes × 4 bytes × 25 000 turns × 1/7 s^{-1} = 172 kB/s.
Global decoupling	Set four skew quadrupoles at operator request	Two minutes response time.	< 1 kB/s.
Injection offset minimization			< 1 kB/s.
Emittance measure-ment, slow	Averaging time—up to 1 ms	Measure and display high-resolution beam emittance data. Display five values per cycle.	

Table 4.2: Application packages: transverse beam dynamics (cont'd).

Name	Parameters	Description	Bandwidth
Emittance measurement, fast	Averaging time—up to 20 μs	Measure and display low-resolution beam emittance data for the first 20 turns.	
Display BLM data	Time in cycle, averaging window	Display output from 90 BLM at 10-Hz rate.	
Beam radius		Display average beam radius obtained from rf feedback system.	

termination, commissioning modules associated with beam threading and closed-orbit correction have been developed using the simulator.

EPICS consists of a set of software tools running on real-time computers known as IOC (Input Output Controllers) for data acquisition and control logic and on UNIX workstations providing operator interface and high-level application code, alarm handling and data archiving. Access by an application program is through a standardized set of subroutine calls that gives access to the data as a named channel. Presence of this layer, called Channel Access (CA), means that the application code does not need information as to the physical location of a channel, just its name. This provides efficient data collection by giving the ability to make asynchronous calls to the data, call-back, and notification upon the change of a value of a channel.

The lower three boxes in Figure 4.9 show the tracking engine and associated VME based modules. The tracking engine consists of one or more (of a maximum of 64) processors of the hypercube. In the VME crate are two Motorola-based Single Board Computers named SBC1 and SBC2, and a memory board containing 8 Mbyte of memory that is addressable from both processors. The memory is used in three sections: a section for passing of control information from the control system to the tracking engine, a section for passing of beam data from the tracking engine to the control system, and a section for transmitting EPICS events (change of state) to the IOC defined

Table 4.3: Application packages: longitudinal beam dynamics.

Name	Parameters	Description	Bandwidth
Beam current	Cycle number, sampling rate	Display beam current from DCCT at 100 points in one cycle in one second.	4 bytes × 100 points × 10 s^{-1} = 4 kB/s.
Beam current at injection		Display beam current from ac toroid throughout the injection process at 25 points during the first five ms, in one second.	< 1 kB/s.
Bunch length		Display bunch length from wall current monitor as mountain range plot.	video monitor of fast oscilloscope
Longitudinal tune	cycle number	Measure ν_s at 10 points during the cycle. Display in one second.	
Longitudinal Poincare		Capture and display $\delta p/p$ *vs.* Φ for 100 synchrotron periods.	
Ramp functions	Up to 10 simultaneous function pairs for display	Display rf voltage, rf phase, 100 points/cycle. Display in one second.	

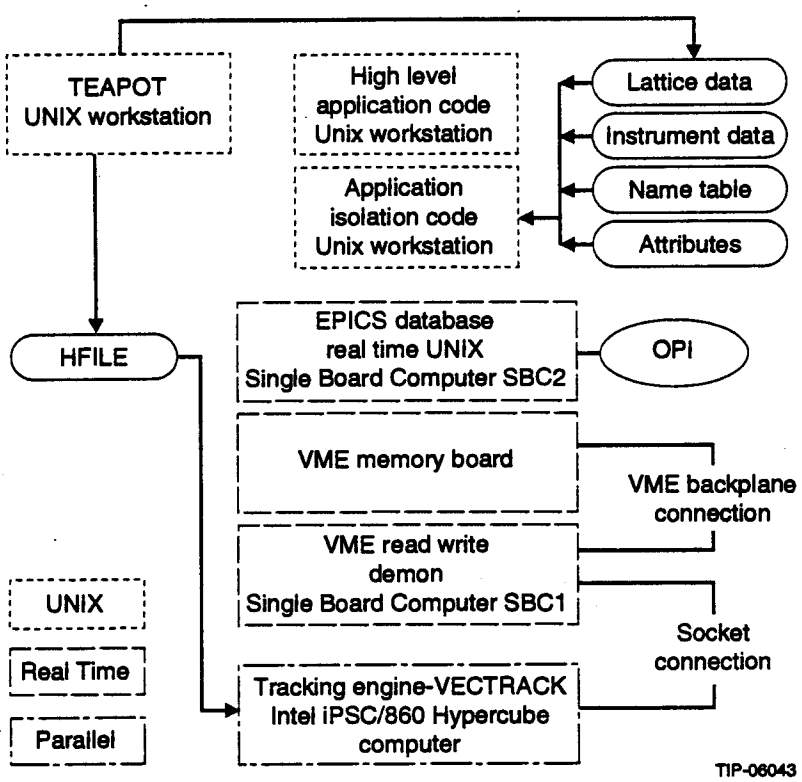

Figure 4.9: Structure of high-level beam control simulator.

below. On SBC1, a Remote VME process (rvmed) is running. SBC2 is operating as an EPICS IOC with process variables corresponding to all control variables and all read-back quantities. Finally, there are a number of panels and other application processes running on one or more UNIX workstations.

At start-up, a TCP/IP socket connection is established between the engine and the rvmed. The tracking engine then reads an "hfile," which contains the description of the lattice to be simulated, an input file containing parameters about the run, and a file containing initial conditions for the particles to be tracked. Once this information has been loaded, the tracking engine tracks the particles through an LEB turn, collects BPM data and passes this information through the socket connection to the demon, which then writes the information to the memory board. Using a semaphore mechanism between the IOC and the tracking engine (TE), new control information is read back to the TE if available, using external VME memory as temporary data storage. The engine then tracks the next turn and keeps repeating this track-check-track cycle until the run is terminated.

The IOC executes standard EPICS code. However, instead of executing an EPICS driver to read new BPM data from VME, EPICS subroutine records are employed. A separate process called Scantask scans (at a rate of 10 Hz) the section of memory containing information about events to be posted and posts the events when necessary.

Operationally, the user makes a set of changes to the control information in the IOC and then sets a flag signifying that the control data has changed. On the next turn, the engine picks up the new information and complies. Only after the beam information has been updated with values corresponding to the new control settings is the flag cleared, telling the operator that the new information is now reflected in the beam read-back values.

The engine employs the TEAPOT[154] algorithm to track particles through the lattice. The total number of particles is distributed over the processors and then tracked until a command is given to stop. At every BPM (beam position monitor), the partial sums of the transverse coordinates are formed and written into array entries. Since the hypercube is a distributed-memory machine, the arrays are globally summed and averaged once per turn to yield the location of the "beam centroid" at each BPM at each turn. The averaging is performed this way in order to condense the inter-processor communication within the hypercube itself as much as possible and improve performance. The top speed of the system is approximately 10 turns tracked per second, and is limited by the actual calculations involved. This is approximately

25 000 times slower than the real accelerator and the implications of this are described shortly.

The Application Isolation Code (AIC) is intended to provide the interface between an application itself and database (EPICS) specific modules. It is designed to provide

- a simple representation of control data in a structured manner;
- independence of high-level applications from hardware-related features;
- portability of control code with respect to different control system software as well as different database packages;
- uniform approach to data retrieval from various sources (EPICS database, text file(s), TEAPOT output).

AIC is realized as a set of C++ base classes which provide basic control of data types and attributes as well as some operations for this data. An application based on the AIC approach consists of some derived classes which include specific data structures and functions to handle these structures. The choice of C++ for this work stems from several advantages offered by this language: 1) Strong type checking is very fruitful in early elimination of syntax errors while designing applications. 2) Operator overloading (allowing the same alphanumeric symbol to perform different operations depending on the class of data being operated upon) results in human-readable control algorithms and a look similar to the handling of native data types in C++. For example, the command to tell the control system the number of turns to average for the BOM data would look like: `avg_turns = 16` where `avg_turns` is an instantiation of a defined data class.

The commissioning software is part of a set of codes referred to as High Level Application Code (HLAC). The set consists of independent modules responsible for beam control, diagnosis and correction. The functions include closed-orbit correction, tune measurement, chromaticity correction, hardware-failure diagnosis, *etc.* The correction modules embody diagnostic and correction procedures that are common to alternating-gradient circular accelerators. The AIC layer allows these modules to be independent of the control system and data-access procedures in use at any particular laboratory.

HLAC modules access data through header files defined in the AIC layer. The variables in the HLAC layer are members of derived data classes and therefore carry the appropriate attributes as defined in the AIC. As is shown

in Figure 4.9, the HLAC does not access any stored resource information directly. It is intended that all HLAC modules conform to this standard in order to make the code more portable.

The EPICS graphical user interface (called OPI) is used to communicate with the HLAC and the machine simulation code running on the hypercube. The OPI executes as a server on the IOC, with a client process running on the UNIX workstation. This enables a user to have easy, intuitive access to channel access variables using the GUI but does not allow for easy communication with other UNIX processes including the HLAC and the simulation code. Communication from an OPI panel is done by posting control flags to the EPICS database and having separate processes in the UNIX machines and hypercube scan these variables through channel access calls.

An example of HLAC is the orbit correction module. It is used to establish and smooth the closed orbit starting from a completely uncorrected lattice. It is realized as a set of following commands:

1. **Set first correctors** - Set the first two pairs of horizontal and vertical correctors to minimize the beam deviations in following two BPM pairs. The strengths $Bl_{xj}/B\rho$ for horizontal correctors $CORR_{xj}$ are determined from the following equations:

$$R_{CORR_{x1}\rightarrow BPM_{x4}}\frac{Bl_{x1}}{B\rho} + R_{CORR_{x2}\rightarrow BPM_{x4}}\frac{Bl_{x2}}{B\rho} = \Delta_{BPM_{x4}}$$
$$R_{CORR_{x1}\rightarrow BPM_{x5}}\frac{Bl_{x1}}{B\rho} + R_{CORR_{x1}\rightarrow BPM_{x5}}\frac{Bl_{x2}}{B\rho} = \Delta_{BPM_{x5}}$$

   where $\Delta_{BPM_{xi}}$ is the beam deviation in i-th horizontal monitor BPM_{xi} and $R_{CORR_{xj}\rightarrow BPM_{xi}}$ is the element $R(1,2)$ of the transfer matrix between j-th horizontal corrector $CORR_{xj}$ and i-th horizontal monitor BPM_{xi} :

$$R_{CORR_{xj}\rightarrow BPM_{xi}} = \frac{\sin(\psi_{CORR_{xj}\rightarrow BPM_{xi}})}{\sqrt{\beta_{CORR_{xj}} * \beta_{BPM_{xi}}}},$$

   where ψ and β are Twiss parameters. The strengths of the vertical correctors are determined from similar expressions.

2. **Adjust main dipole field (coarse)** - correct main dipole field using two horizontal BPMs (#6 and #8) placed before and after first pairs of main dipoles.

3. **Thread the beam through the lattice** - repeat the first command for each superperiod.

4. **Establish closed orbit** - set the last horizontal and vertical corrector pairs (#44 and #45) to minimize the beam deviation in the BPM defined in the first command after the second turn.

5. **Measure closed orbit** - find closed orbit by averaging the beam deviations in all BPM over a fixed number of turns.

6. **Correct the closed orbit** - set all 90 correctors to minimize the deviations of the closed orbit. The strengths of the correctors are determined using a least-square algorithm to minimize the "badness function" F (for the horizontal plane):

$$F(Bl_{x1}/B\rho, ..., Bl_{x45}/B\rho) = \sum_{i=1}^{90} \frac{(\Delta^{after}_{Orbit^i_x})^2}{\beta_{BPM_{xi}}},$$

with

$$\frac{\Delta^{(after)}_{Orbit^i_x}}{\sqrt{\beta_{BPM_{xi}}}} = \frac{\Delta^{(before)}_{Orbit^i_x}}{\sqrt{\beta_{BPM_{xi}}}} - \sum_{j=1}^{45} \frac{\cos(\mu_x/2 - \psi_{CORR_{xj}\to BPM_{xi}})}{2\sin(\mu_x/2)} \sqrt{\beta_{CORR_{xj}}} \frac{Bl_{xj}}{B\rho}$$

where $\Delta^{(before)}_{Orbit^i_x}$ and $\Delta^{(after)}_{Orbit^i_x}$ are the position readings of the i-th BPM before and after correction, ψ and β are Twiss parameters, μ_x is the horizontal phase advance. Similar expressions are used to determine the strengths of the vertical correctors.

7. **Adjust main dipole field (fine)** - correct main dipole field to minimize the average horizontal corrector strength defined in previous command.

8. **Correct injection offset** - set appropriate steering elements in the transfer line Linac-LEB to minimize the beam deviation about closed orbit, defined in first pairs of horizontal and vertical BPMs after first turn.

Because of the nonlinear relationship between Twiss functions and deviation about the reference orbit the whole sequence is repeated twice.

The OPI interface shown in Figure 4.10 is the display produced by the orbit correction module. The upper plot indicates the particle trajectory

generated by the simulation in the present case or from the actual BPM readings when the accelerator would be completed. Modified corrector strengths produced by the HLAC module are sent to the simulator code and reflected in the lower plot. The text windows to the left of the cartesian plot indicate the operation taking place and whether or not it is completed. The column of buttons on the right displays the whole set of the individual correction commands which may be executed from within this module. These commands may be combined in different modules and called independently to produce the desired result.

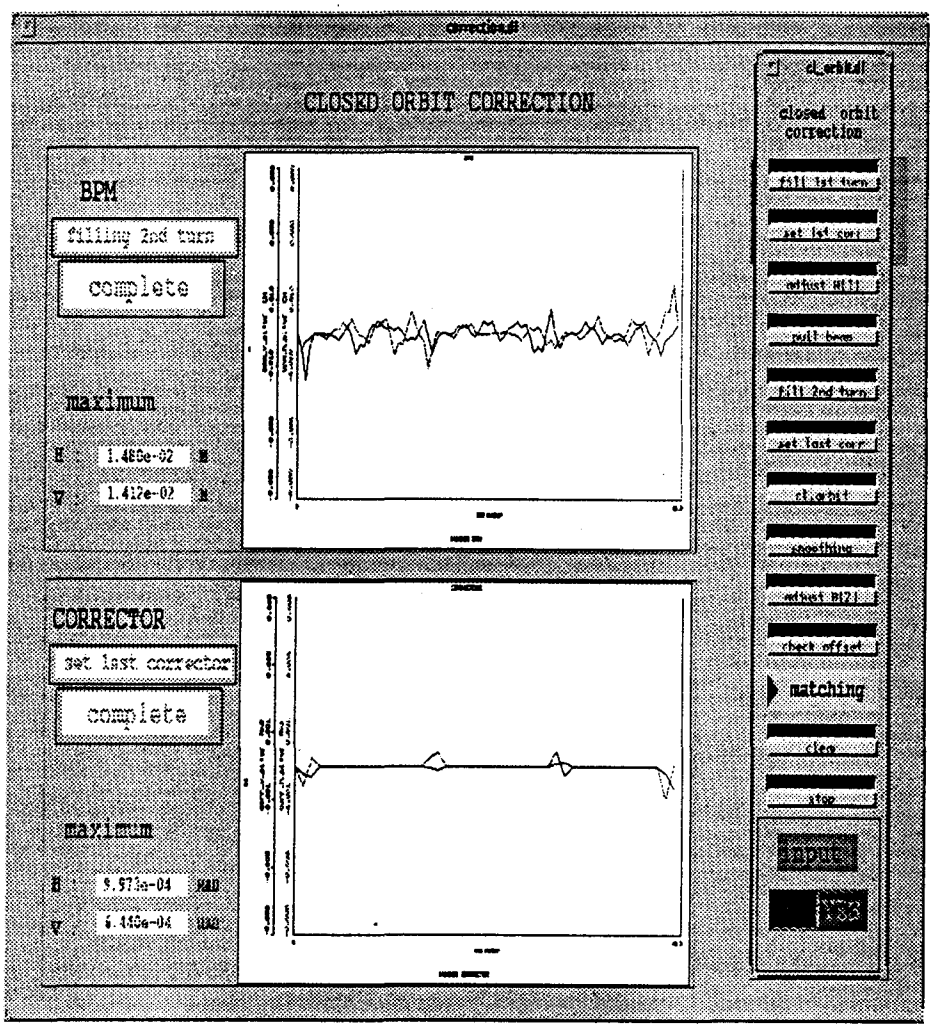

Figure 4.10: Typical screen for closed orbit correction.

Appendix A

Tables and Technical Notes Index

A.1 LEB Parameter Tables

(J. Nonte, T. Webster)

The following tables are reproduced from the latest revision of the LEB Level 3 specifications.[71,74]

Table A.1: General LEB parameters.

Parameter	Symbol	Value
Injection Kinetic Energy	T_{inj}	600 MeV
Extraction Kinetic Energy	T_{ext}	11.1 GeV
Injection Momentum	P_{inj}	1.22 GeV/c
Extraction Momentum	P_{ext}	12.0 GeV/c
Revolution Frequency (injection)	f_{rot}	417 kHz
Revolution Frequency (Extraction)	f_{rot}	524 kHz
Number of Bunches (full)	N_b	114
Bunch Spacing	S_b	5.0 m
Circumference	C	570 m
Transverse Emittance Collider Operations (*rms* normalized)	ϵ^*	0.6π mm-mrad
Transverse Emittance Test Beam Operation (*rms* normalized)	ϵ^*	4.0π mm-mrad

Table A.2: Beam current parameters.

Parameter	Value
Particles per Bunch (collider operation)	1.0×10^{10}
Total number of particles (collider operation)	1.14×10^{12}
Injection Current (collider operation)	76 mA
Extraction Current (collider operation)	96 mA
Particles per Bunch (test beam operation)	5.0×10^{10}
Total number of particles (test beam operation)	5.70×10^{12}
Injection Current (test beam operation)	380 mA
Extraction Current (test beam operation)	478 mA

Table A.3: General lattice parameters.

Parameter	Value
Extraction Kinetic Energy	11.1 GeV
Extraction Momentum	12.0 GeV/c
Extraction Gamma	12.83
Mono-Bipolar	Monopolar
Magnet Type	Resistive
Harmonic Number	114 (2*3*19)
Bunch Spacing	5.0 m
Circumference	570 m
Number of Superperiods	3
Betatron Tune (Horizontal)	11.65 (10.9–11.9)
Betatron Tune (Vertical)	11.60 (10.9–11.9)
Natural Chromaticity (Horizontal)	−15.83 (−14.07 to −16.58)
Natural Chromaticity (Vertical)	−17.59 (−15.07 to −18.22)
Chromaticity Correction Range	+ 20
Transition Gamma (γ_t)	22.10 (21.64–24.64)
Momentum Compaction Factor (α)	0.002047 (0.001647–0.002133)

Table A.4: Arc section lattice parameters.

Parameter	Value
Arc Focusing Structure	$D_2BF_2BD_1OF_1OD_1BF_2BD_2$
Bending Angle per Arc	1200
Arc Length	145.21546 m
Average Arc Radius	69.335 m
Number of Standard Supercells per Arc	2
Standard Supercell Length	36.75 m
Number of Special Supercells per Arc	2
Special Supercell Length	35.85773 m
Supercell Phase Advance (Horizontal)	270°
Supercell Phase Advance (Vertical)	258° (237°–267°)
Bending Angle Per Supercell	30°
Types of Dipole per Arc	1
Number of Dipoles per Arc	32
Dipole Integrated Field Strength	2.62 Tm
Dipole Nominal Effective Length	1.94 m
Dipole Nominal Peak Field	1.35 T
ρ (Dipole Bending Radius)	29.64 m
$B\rho$ (Magnet Rigidity) @ 12 GeV/c	40 Tm
Types of Quadrupole	4
Number of Quadrupoles in Arc	23
Quadrupole Nominal Effective Length	0.5919–0.7564 m
Quadrupole Nominal Peak Gradient	15.355 T/m
Max. Amplitude Function (β) (Hor.)	23.77 m (23.04–24.04)
Max. Amplitude Function (β) (Vert.)	23.26 m (23.17–24.41)
Min. Amplitude Function (β) (Hor.)	3.34 m (3.32–3.38)
Min. Amplitude Function (β) (Vert.)	2.98 m (2.74–3.61)
Max. Dispersion Function (η) (Hor.)	3.58 m (3.56–3.60)
Min. Dispersion Function (η) (Hor.)	−0.40 m (−0.41 to −0.39)

Note: Supercells are typically 3 FODO units.

Table A.5: Straight section lattice parameters.

Parameter	Value
Straight Focusing Structure	$D_2OF_1OD_1OF_2OD_1OF_1OD_2$
Length of Straight Section	44.78454 m
Types of Quadrupole	4
Number of Quadrupoles	7
Quadrupole Nominal Eff. Length	0.5552 m–0.6980 m
Quadrupole Nominal Peak Gradient	15.355 T/m
Max. Amplitude Function β (Hor.)	34.20 m (33.34–34.28)
Max. Amplitude Function β (Vert.)	36.18 m (29.06–37.37)
Min. Amplitude Function β (Hor.)	3.11 m (2.04–4.54)
Min. Amplitude Function β (Vert.)	1.97 m (1.89–2.27)
Max. Dispersion Function (η)	0.0 m
Min. Dispersion Function (η)	0.0 m

Table A.6: Beam acceptance parameters.

Parameter	Value
Dipole Vacuum Chamber Dimension	Oval, 64 mm $\times$ 52 mm
Quadrupole Vacuum Chamber Dimension (ID)	Circular, R 80.5 mm
Ring Acceptance, transverse	36π mm-mrad
Max. Momentum Spread $\delta p/p$	5×10^{-3}
Max. Half Beam Size in Dipole (Hor.)	23.5 mm
Max. Half Beam Size in Dipole (Vert.)	22.5 mm
Max. Half Beam Size in Quad. (Hor.)	32.44 mm
Max. Half Beam Size in Quad. (Vert.)	33.28 mm

Table A.7: Space allocation summary.

Space Allocation	Number per Superperiod	Length (m)	Total Length (m)
Standard Supercell	2	36.75	73.5
Special Supercell*	2	35.85773	71.71546
Arc Section	1	145.21546	145.21546
Straight Section	1	44.78454	44.78454
Superperiod			190
LEB Ring		3×190	570

*Length of a special supercell equals the sum of the length of a half standard cell plus the length of a half special cell.

Table A.8: One-half standard (special) arc cell space allocation.

Space Allocation	Length (m)
Half Quad Defoc. (1/2 QD2)	0.30635
or	or
Nothing*	0.0
Beam Position Monitor (BPM)	0.19
or	or
Nothing*	0.0
Trim Quad QTD2	0.39
or	or
Nothing*	0.0
Drift Space	0.00592
or	or
Nothing*	0.0
Drift Space	0.52848
Dipole	2.163
Dipole	2.163
Drift Space	0.24605
Trim Quad QTF2	0.39
BPM	0.19
Quad QF2	0.5919
Drift Space	0.1
Orbit Correcting Dipole	0.27
Drift Space	0.39605
Dipole	2.163
Dipole	2.163
Drift space	0.25035
Trim Quad QTD1	0.39
BPM	0.19
Quad QD1	0.5983
Drift Space	0.1
Sextupole SD	0.4
Orbit Correcting Dipole	0.27
Drift Space	2.6814
Orbit Correcting Dipole	0.27
Sextupole SF	0.4
BPM	0.19
1/2 Quad QF1	0.3782
Total Half Standard Supercell Length	18.375
Total Half Special Supercell Length	17.48273

* Special half supercell used to connect with straight sections.

Table A.9: Straight section space allocations.

Space Allocation	Length(m)
Trim Quad QTDS2	0.39
BPM	0.19
Quad QDS2	0.6858
Drift Space	0.1
Orbit Correcting Dipole	0.27
Drift Space	6.42307
Trim Quad QTFS1	0.39
BPM	0.19
Quad QFS1	0.6568
Drift Space	0.1
Orbit Correcting Dipole	0.27
Drift Space	2.7976
Trim Quad QTDS1	0.39
BPM	0.19
Quad QDS1	0.698
Drift Space	0.1
Orbit Correcting Dipole	0.27
Drift Space	7.4234
Trim Quad QTFS2	0.39
BPM	0.19
Half Quad QFS2	0.2776
Half Length	22.39227
Total Length	44.78454

Table A.10: Magnet functions.

Function	Magnet	Power Supply
Bending	Main Dipoles	Common Bus
Focusing	Main Quadrupoles	Common Bus
Steering and Orbit Correction	Dipoles	Indep. Powered
Tune Correction and Control ($\Delta\nu = \pm 0.5$)	Trim Quadrupoles	Indep. Powered
Linear Chromaticity Correction (0 Full Cycle)	Sextupoles	Indep. Powered
2nd Order Resonance Correction	Trim Quads Skew Quads	Indep. Powered
3rd Order Resonance Correction	Sextupoles & Skew Sextupoles	Indep. Powered

Table A.11: Magnet count.

Section	Main Dipoles	Main Quads	Orbit Correcting Dipoles	Trim Quads	Skew Quads	Sextu-poles	Skew Sextu-poles
Arc 1	32	23	23	22		16	12
S1		7	7	8	4	0	
Arc 2	32	23	23	22		16	
S2		7	7	8		0	
Arc 3	32	23	23	22		16	
S3		7	7	8		0	
Totals	96	90	90	90	4	48	12

Table A.12: Main dipole magnet parameters.

Parameter	Value
Type	1
Peak Field	1.35 T
Effective Length	1.94 m
Slot Length	2.163 m
Bending Radius	29.64 m
Vertical Full Pole Gap	57.2 mm

Table A.13: Main quadrupole magnet parameters.

Type	Number Required	Effective Length (m)	Slot Length (m)	Aperture Radius (mm)	Peak Gradient (T/m)
QF1	12	0.7564	0.9964	50	15.355
QF2	24	0.5919	0.8319	50	15.355
QD1	24	0.5983	0.8383	50	15.355
QD2	9	0.6127	0.8527	50	15.355
QFS1	6	0.6568	0.9179	50	15.355
QFS2	3	0.5552	0.8326	50	15.355
QDS1	6	0.6980	0.9380	50	15.355
QDS2	6	0.6858	0.9258	50	15.355

Table A.14: Orbit correcting dipole magnet parameters.

Type	Number Required	Effective Length (m)	Slot Length (m)	Full Pole Gap (mm)	Peak Gradient (T/m)
CH	45	0.15	0.27	50	0.17
CV	45	0.15	0.27	50	0.17

Table A.15: Trim quadrupole magnet parameters.

Type	Number Required	Effective Length (m)	Slot Length (m)	Aperture Radius (mm)	Peak Gradient (T/m)
QTF2	24	0.294	0.39	50	0.42
QTD1	24	0.294	0.39	50	0.88
QTD2	18	0.294	0.39	50	1.06
QTFS1	6	0.294	0.39	50	3.14
QTFS2	6	0.294	0.39	50	4.91
QTDS1	6	0.294	0.39	50	0.45
QTDS2	6	0.294	0.39	50	1.92

Table A.16: Skew quadrupole magnet parameters.

Parameter	Value
Type	1
Number Required	4
Effective Length	0.294 m
Slot Length	0.39 m
Aperture Radius	50 mm
Peak Gradient	0.82 T/m

Table A.17: Sextupole magnet parameters.

Type	Number Required	Effective Length (m)	Slot Length (m)	Aperture Radius (mm)	Peak B'' (T/m^2)
SF	24	0.3	0.4	50	44.8
SD	12	0.3	0.4	50	80.16
SD1	12	0.3	0.4	50	86.17

Table A.18: Skew sextupole magnet parameters.

Parameter	Value
Type	1
Number Required	12
Effective Length	0.3 m
Slot Length	0.4 m
Aperture Radius	50 mm
Peak B"	2.67 T/m^2

Table A.19: Resonant mode cycle time parameters.

Parameter	Value
Nominal Cycle Time Collider Operation	0.1 s
Nominal Cycle Time Test Beam Operation	0.1 s
Fill Time Collider Operation	9.6 ms
Fill Time Test Beam Operation	48 ms
Revolution Time (injection)	2.4 ms
Revolution Frequency (injection)	417 kHz
Revolution Frequency (extraction)	524 kHz
Acceleration Time, Up	0.05 s
Filling Scenario	4 to 20 turn injection

Table A.20: Non-resonant mode cycle time parameters.

Parameter	Value
Nominal Cycle Time	3 s
Parabolic Ramp time	0.050 s
Linear Ramp time	1.4 s
dB/dt	0.84335 T/s
d^2B/dt^2	8.4335 T/s^2
Filling Scenario	4 to 20 turn injection

Table A.21: Longitudinal parameters.

Parameter	Value
Maximum Energy Gain Per Turn	0.645 MeV
Maximum Energy Gain Per Second	336 GeV
Rf Frequency at Injection	47.514 MHz
Rf Frequency at Extraction	59.776 MHz
Peak Rf Voltage in Cycle	0.765 MV
Rf Voltage at Injection	0.024 MV
Rf Voltage at Extraction	0.080 MV
Max Synchrotron Frequency (near injection)	21.59 KHz
Min Synchrotron Frequency (at extraction)	0.367 KHz
Max Synchrotron Tune (near injection)	0.0518
Min Synchrotron Tune (at extraction)	0.0007
9595*rms* Bunch Length at Injection	1.43 m
rms Bunch Length at Extraction (unmatched)	0.14 m
rms Bunch Length at Extraction (matched)	.20 m
dp/p at Injection (*rms*)	0.107×10^{-3}
dp/p at Extraction (unmatched) (*rms*)	0.25×10^{-3}
dp/p at Extraction (matched) (*rms*)	0.18×10^{-3}
Bucket Area at Injection	0.016 eVs
Bucket Area at Extraction	0.76 eVs
Bucket Half-Height Injection (dp/p)	0.25×10^{-3}
Bucket Half-Height Max (dp/p)	3.027×10^{-3}
Bucket Half-Height Extraction (dp/p)	3.02×10^{-3}
9595Maximum Synchronous Angle	61.25°

Table A.22: Impedance budget.

Component	Number	$Z_{\parallel}(z)/n$ (Ω)	$Z_{\perp}(y)$ (MΩ/m)
Rf cavities			
(broad band)	16 *	0.48	0.084
Beam position monitor	90	0.36	0.063
Injection Stripper	1	TBD	TBD
Valves (unshielded)	20	0.26	0.6
Transitions	276	TBD	TBD
Flange Welds	732	0.0001	0.0073
Flange Gaps (1mm)	360	0.17	
Pump Ports	90	0.03	0.006
Bellows (shielded)	180	0.40	0.08
Resistive wall		0.06	0.02
Injection Sections			
bellows (unshielded)	7	0.0045	0.0014
bump magnets	4	TBD	TBD
Extraction Section			
bellows (unshielded)	2	0.0002	0.00089
kicker modules	8	0.013	0.25
septa magnets	2	TBD	TBD
bump magnets	5	TBD	TBD
Total		1.778	0.588
Max Allowable	—	3.556	1.176
(Total $\times$ 2)**			

* For Impedance calculation only.

** Factor of 2 is for unknown impedance values.

Table A.23: Tune shift and impedance parameters.

Parameter	Collider Beam	Test Beam
Laslett Tune Shift (maximum)	−0.6	−0.6
Bunching Factor (max tune shift)	3.5	4
Longit. Impedance Budget (Z/n)	3.6 Ω	3.6 Ω
Longitudinal Threshold		
Injection	380 Ω	76 Ω
Extraction	24 Ω	4.8 Ω
Transv. Impedance Budget Z/n (m)	1.2 M Ω/m	1.2 M Ω/m
Z Transverse Threshold		
Injection	83 M Ω/m	16.6 M Ω/m
Extraction	16 M Ω/m	3.2 M Ω/m

A.2 PMTN Technical Notes

(J. Nonte, T. Webster)

Following is a list of all SSC Project Management Technical Notes issued from inception of the SSC Laboratory until the end of May 1994. Some of these notes have been issued originally as Accelerator Design and Operations Department (ADOD) notes.

PMTN-001M	C. Manz, *Impact of Lattice Design on RF Matching Between LEB—MEB.*
PMTN-002P	Y. Yan, A. Sen, A. Chao, G. Bourianoff, *Comment on Round-Off Errors and on One-Turn Taylor Maps.*
PMTN-003P	Y. Yan, *Normalization of the Parameterized Courant-Snyder Matrix.*
PMTN-007C	G. Bourianoff, J. Peterson, *BPM Alignment Issues-Quadrupole vs. Sextupole Centering.*
PMTN-008L	S. Penner, *Injection-By-Stripping Loss Effects.*
PMTN-009L	S. Penner, *LEB Emittance Budget.*
PMTN-010D	R. Shafer, *Beam Loss Monitoring.*
PMTN-013L	S.K. Dutt, *Eddy Current Multipoles during LEB Ramp Cycle.*
PMTN-015B	S. Penner, *Dispersion Due to an Offset Quadrupole.*
PMTN-018M	C. Manz, R. Gerig, *Using the Fermilab Accelerator Applications Software at the SSC.*
PMTN-019L	S. Penner, *Conceptual Design of the LEB Injection Girder.*
PMTN-020B	S. Penner, *Fast Kicker Requirements in the SSC.*
PMTN-021P	S. Penner, *SSC Emittance Budget—A Beginning.*
PMTN-024D	J. Crisp, *Fermilab Damper Experience.*
PMTN-025B	R. Bhandari, *Orthogonal Control of the Position and Slope of the Injected Beam.*
PMTN-026P	S. Penner, *Damper Kinematics.*
PMTN-027L	W. Chou, *Collective Effects in the LEB.*
PMTN-028G	S. Machida, *Modification of TEAPOT to Include Acceleration.*
PMTN-029L	A. Chao, S. Chen, T. Sen, *Estimation Of The Orbit Shift Due To Localized RF Cavities In The LEB.*
PMTN-030M	A. Bogacz, *Transition Crossing—Correction Schemes.*

PMTN-031L	J.F. Knox-Seith, *Calculation of Error Fields Due to Construction Tolerances in the LEB Main Dipole Magnets.*
PMTN-032L	J.F. Knox-Seith, *Calculation of Error Fields Due to Construction Tolerances in the LEB Main Quadrupole Magnets.*
PMTN-034B	J. Bull, *LEB Beam Absorber—Current Status.* November, 1991
PMTN-035L	S. Machida, *Optimizing "Perfect" Lattice of the LEB.*
PMTN-037L	W. Chou, *Requirements for Transfer Damper System in LEB.*
PMTN-038L	S. Penner, *Closed Orbit Errors Due To LEB Extraction Bump.*
PMTN-039L	S. Machida, *Smear and Emittance Growth.*
PMTN-040L	F. Pedersen, *Notes on Low Energy Booster RF Feedback and Controls.*
PMTN-041D	S. Penner, *Injection Damper Driver Design.*
PMTN-042P	G. Stupakov, *Growth of Longitudinal Emmittance Due to Vibration of Magnets.*
PMTN-043R	G. Stapleton, *Radiation Environment in the LEB Extraction Septum Region.*
PMTN-044R	G. Stapleton, *Neutron Attenuation by Simple Labyrinths.*
PMTN-045P	S. Dutt, *Synchotron Radiation from Protons.*
PMTN-048L	S. Penner, *Transverse Dampers for the SSC.*
PMTN-051P	R. Hong, B. Cole, *Vectrack Speedup Summary.*
PMTN-053M	J.A. Palkovic, *How Much Does the Beam Move When We Lose an RF Cavity?*
PMTN-055L	T. Yan, *Suggestion on HOM Damper for LEB Cavity.*
PMTN-0059M	J.A. Palkovic, J.E. Griffin, *A Review of the Status of "Non-Focusing Transition Crossing" Experiments in the Fermilab Main Ring.*
PMTN-0060P	W. Chou, *Comments on Bunch Spacing in the SSC.*
PMTN-0061M	J.A. Palkovic, *Longitudinal Injection Tolerances in the MEB.*
PMTN-0066L	S. Machida, *Resonance Correction for the LEB.*
PMTN-0071M	N. Mao, *Stability Requirements for Magnets of LEB-MEB Transfer Line.*

PMTN-0072M	R. Platt, *Magnetic Field Produced by RMPS Buses.*
PMTN-0077C	V. Thiagarajan, *Increase in bunch spacing in the average number of interactions per bunch crossing.*
PMTN-0083M	N. Mao, *LEB-MEB Transfer Line B Mismatching and Correction.*
PMTN-0084L	V. Thiagarajan, X. Wu, R. York, R. Schlueter, *LEB Dipoles and Quadrupoles.*

REFERENCES

1. J.D. Jackson (ed.). Conceptual Design Report. Technical Report SSC-SR-2020, Superconducting Super Collider CDG, LBL 90/4040, Berkeley, CA 94720, March 1986.
2. J.R. Sanford and D.M. Matthews (eds.). Site-Specific Conceptual Design Report. Technical Report SSCL-SR-1056, SSC Laboratory, Dallas, Tx 75237, July 1990.
3. A. Chao *et al.* Summary of the SSC injector Workshop. unpublished, December 1990.
4. A.A. Garren, E.D. Courant, and U. Wienands. Low Momentum Compaction Lattice Study for the SSC Low Energy Booster. In PAC91[156], page 2829.
5. R.C. York *et al.* The SSC Low Energy Booster: A Status Report. In PAC91[156].
6. W.R. Smythe. Reducing Ferrite Tuner Power Loss by Bias Field Rotation. In *Proc. IEEE Part. Accel. Conf.*, IEEE Trans. Nucl. Sci. IEEE Press, May 1983.
7. R.L. Poirier, T.A. Enegren, and I.B. Enchevich. AC Bias Operation of the Perpendicular Biased Ferrite Tuned Cavity for the TRIUMF KAON Factory Booster Synchrotron. In PAC91[156], page 2943.
8. E.D. Courant and H.A. Snyder. Theory of the Alternating Gradient Synchrotron. *Ann. Phys.*, 3:1, 1958.
9. R.C. Gupta, J.I.M. Botman, and M.K. Craddock. High-γ_t lattices for the TRIUMF KAON Factory. In PAC85[158], page 2308.
10. U. Wienands. Polarization in the New Racetrack Driver Ring of the TRIUMF KAON Factory. In H.A. Thiessen, editor, *Proc. Advanced Hadron Facility Accelerator Design Workshop*, number LA-11432-C, page 245, Los Alamos, NM, February 1988. Los Alamos National Laboratory.
11. N.K. Mahale and A. Maschke. Longitudinal Matching between the LEB and the MEB for the SSC. In PAC91[156], page 389.
12. C.G. Lillequist and K.R. Symon. Deviations from Adiabatic Behavious During Capture of Particles into and Rf Bucket. Technical Report MURA-491, 1959.

13. N.K. Mahale. Capture of a Beam from a Linac into a Resonant Machine. Technical report, SSC Laboratory, Dallas, TX. PMTN, in preparation.

14. N.K. Mahale and M.A. Furman. Debunching and Capture in the LEB for the SSC. In PAC91[156], page 386.

15. X. Wu, R.C. York, R.V. Servranckx, and U. Wienands. Tracking Studies and Machine Performance Simulation of the SSC Low Energy Booster. In PAC93[157], page 255.

16. R.V. Servranckx *et al.* *User's Guide to the Program DIMAD.* SLAC, Stanford, CA, May 1985. Report 285 UC-28.

17. M. Berz *et al.* *User's Guide and Reference Manual for COSY∞.* Michigan State University, December 1991.

18. R.V. Servranckx. New Features in DIMAD. In PAC93[157], page 167.

19. S. Machida. Optimizing "Perfect" Lattice of the LEB. Technical Note PMTN-035L, SSC Laboratory, Dallas, TX, 1991.

20. V. Thiagarajan, X. Wu, R. York, R.D. Schlueter, and K. Halbach. Design of the Main Dipoles and Quadrupoles for the SSC Low Energy Booster. Technical Report SSCL-568, SSC Laboratory, Dallas, TX, March 1992. also issued as PMTN-0084L and LBL-31895.

21. V. Thiagarajan, X. Wu, R.C. York, R. Schlueter, and K. Halbach. Design of Main Dipoles and Quadrupoles for the SSC Low Energy Booster. In J. Rossbach, editor, *Proc. XV. Int. Conf. on High Energy Accelerators*, volume 1, page 626, Hamburg, F.R. Germany, July 1992. Desy, World Scientific.

22. User's Guide for the POISSON/SUPERFISH Group of codes. Technical Report LA-UR-87-115, Los Alamos National Laboratory, Los Alamos, MN, 1987.

23. Reference Manual for the POISSON/SUPERFISH Group of Codes. Technical Report LA-UR-87-126, Los Alamos National Laboratory, Los Alamos, NM, January 1987.

24. Vector Fields Ltd., Oxford, GB. *The PE2D Reference Manual*, July 1990. VF-06-90-24.

25. R.V. Servranckx. Resonance Analysis Program for Circular Machines. private communication.

26. G. Guignard. Selection of Formulae concerning Proton Storage Rings. Technical Report 77-10, CERN, Geneva, CH, June 1977.

27. S. Machida. The Simpsons Program: 6-D Phase Space Tracking with Acceleration. In *Proc. Conf. on Computational Accelerator Physics*, February 1992.

28. J.A. MacLachlan. ESME: Longitudinal Phase Space Tracking–Program Documentation. Technical Report TM-1274, Fermi National Accelerator Laboratory, Batavia, Ill, 1984.

29. J.A. MacLachlan. Longitudinal Phase-Space Tracking with Space Charge and Wall Coupling Impedance. Technical Report FN-446, Fermi National Accelerator Laboratory, Batavia, IL, February 1987.

30. J.D. Jackson. *Classical Electrodynamics.* Wiley & Sons, New York, NY, 1975.

31. N.K. Mahale. Longitudinal Dynamics Issues in the LEB. Technical report, SSC Laboratory, Dallas, TX. PMTN in preparation.

32. S. Machida, G. Bourianoff, Y Haung, and N.K. Mahale. Tracking Study of Hadron Collider Boosters. *Int. Journal of Mod. Phys. A*, page 1058, 1993. Proceedings Supplement.

33. W. Chou. Collective Effects in the LEB. Technical Report PMTN-027L(Rev.), SSC Laboratory, Dallas, TX, 1992.

34. L. Walling, G. Hulsey, and T. Grimm. Broadband Higher-Order Mode (HOM) Damper for SSC LEB Ferrite-Tuned Cavity. In PAC93[157], page 1083.

35. W. Chou. Impact of Cross-sectional Changes in a Beam Tube on Beam Dynamics. In PAC91[156], page 1710.

36. W. Chou. private communication.

37. Y. Goren and T.S. Wang. Voltage Counterphasing in the SSC Low Energy Booster. In PAC93[157], page 883.

38. L.W. Funk. The SSC Linear Accelerator. In PAC93[157], page 1700.

39. R. Bhandari, E. Seppi, and S. Penner. Design Characteristics of the Linac-LEB Transfer Line for the SSC. In PAC91[156].

40. R. Bhandari, J. McGill, F. Wang, and S. Penner. Detailed Studies on the Beam Transfer Lines from Linac to Low Energy Booster of the SSC. In PAC93[157], page 381.

41. S. Penner. Conceptual Design of the LEB Injection Girder. Technical Report PMTN-019L, SSC Laboratory, Dallas, TX, April 1991.

42. M. Syphers. Injection Mismatch and Phase Space Dilution. Technical Report FN-458, Fermi National Accelerator Laboratory, Batavia, Il, June 1987.

43. F.W. Jones, G.H. Mackenzie, and H. Schoenauer. ACCSIM – A Program to Simulate the Accumulation of Intense Proton Beams. In *Proc. XIV. Int. Conf. on High Energy Accelerators*, page 199, Tsukuba, Japan, 1990. KEK, Gordon & Breach.

44. F.W. Jones. User's Guide to ACCSIM. Technical Report TRI-DN-90-17, TRIUMF, Vancouver, BC, Canada, 1990.

45. KAON Factory Study – Accelerator Design Report. TRIUMF, Vancouver, BC, Canada, 1990.

46. H. Schoenauer. On the Use of Predeflectors for Improved Beam Loss Concentration. In EPAC92[155].

47. S. Sheynin and T. Hunter. Preliminary Design Review of the LEB Extraction System. SSCL internal document, December 1992.

48. Design Requirements Document for the Low Energy Booster Extraction Kicker System. SSCL Document AEG-3160060, August 1992.

49. D.E. Anderson and L.X. Schneider. Design and Preliminary Testing of the LEB Extractin Kicker Magnet. In PAC93[157], page 1354.

50. Effect of Radiation on Commonly Used Materials in the Fabrication of Resistive Magnets. Technical Report PMTN-0098, SSC Laboratory, Dallas, TX, March 1994. Compilation of BINP reports on the subject.

51. G.E. Fisher. Iron Dominated Magnets. In M. Month and M. Dienes, editors, *Proc. IEEE Part. Accel. Conf.*, volume 2 of *AIP Conference Proceedings*, page 1120, SLAC, 1985. American Institute of Physics.

52. K. Halbach. First-Order Perturbation Effects in Iron-Dominated Two-Dimensional Symmetric Multipoles. *Nuclear Instrum. Methods*, 74(1):147, 1969.

53. PE2D Training Course: Introduction to PE2D. Vector Fields Ltd., Oxford, GB, October 1989.

54. R.E. Shafer and A. Young. Electrical Characteristics of the SSC Low Energy Booster Magnet System. Technical Report LA-UR-92-3298-01, Los Alamos National Laboratory, Los Alamos, NM, 1992.

55. J.F. Knox-Seith. Calculation of Errors Fields due to Construction Tolerances in the LEB Main Dipole Magnets. Technical Report PMTN-0031L, SSC Laboratory, Dallas, TX, November 1991.

56. Tempel Steel Co. Evaluation of Electrical Steels for use in SSC MAgnet Laminations. Comparison study of magnetic properties, commissioned by the SSC Laboratory from Tempel Steel Co., Chicago, Ill., April 1992.

57. J.F. Knox-Seith. Measurement and Chamfering of the LEB Quadrupole. Technical Report PMTN-0090L, SSC Laboratory, Dallas, TX, May 1993.

58. R. Kurumbailmadam. Analytical and Experimental Study of the Superconducting Super Collider Low Energy Booster Corrector Magnets. Technical Report AMC-2210007, SSC Laboratory, Dallas, TX, 1993.

59. Design Requirements Document for the LEB Extraction Kicker System. Technical Report AEG-3160060, SSC Laboratory, Dallas, TX, 1991.

60. M. Wilson. The Supercollider Filling Sequence. Technical Report PMTN-0091C, SSC Laboratory, Dallas, TX, 1994.

61. D. Fiander. A Review of the Kicker Magnet Systems of the PS Complex. In P. Marin and P. Mandrillon (eds.), editors, *Proc. 2nd European Part. Accel. Conf.*, Nice, France, June 1990. Editions Frontieres.

62. D. Fiander. Collaboration at SSCL. 1991.

63. D.G. Pappas and D.R. Askew. Preliminary Testing of the LEB to MEB Transfer Kicker Modulator Prototype. In PAC93[157], pages 1336–1338.

64. J. Ruemmler. Pilot-Bunch and Long-Pulse Ejection with Stripe Kickers. Technical report, DESY, Germany.

65. J. Reimund. Hierarchical Modelling of Line Commutated Power Systems using SABER. In PAC93[157].

66. E. Tacconi, C. Jach, and R. Winje. 10 Hz Resonant LEB Magnet Power Supply System. In *Proc. IEEE Nuclear Science Symposium.* IEEE, IEEE Press, 1991.

67. E. Tacconi. Low Energy Booster Main Magnet Power Supply System. In EPAC92[155].

68. E. Tacconi. Ring Magnet Power Supply Regulation Loops for the SSC Accelerator Complex. In PAC93[157].

69. C. Jach. 1 Hz/10 Hz Switchable Power Supplies for the LEB. In M. McAshan, editor, *Super Collider 2: Proc. Int. Industrial Symposium on the Super Collider*, Miami Beach, FL, March 1990. Plenum Press.

70. Corrector Power Supply Control System, LEB/MEB. Technical Report AEF-3090004, SSC Laboratory, Dallas, TX.

71. J. Nonte (ed.). SSCL Segment Specification for the Low Energy Booster. Level 3A E10-000004, Rev. A, Superconducting Super Collider Laboratory, Dallas, TX 75237, October 1993.

72. Low Energy Booster, Technical Requirements Document for Correction Element Power Supplies, Level IV. Technical Report AEF-3060002, SSC Laboratory, Dallas, TX.

73. Prime Item Development Specification For Corrector Power Supply Assemblies for the Low Energy Booster at SSCL. Technical Report AEF-3060001, SSC Laboratory, Dallas, TX.

74. Element Specification for the Low Energy Booster Accelerator of the SSC. Level 3B E10-000039, Rev. A, Superconducting Super Collider Laboratory, Dallas, TX 75237, October 1993.

75. Specification for the Corrector Element Power System for the Low Energy Booster at the SSC. Level 4 specification AEF-3060003, SSC Laboratory, Dallas, TX, 1993.

76. Interlocking Areas Containing High Electrical Energy Sources; SSC Laboratory Standard. Technical Report P40-000167, SSC Laboratory, Dallas, TX.

77. Low Energy Booster Personnel Access Safety System. Technical Report AQA-3200605, SSC Laboratory, Dallas, TX.

78. K. Dixon and J. Franciscovich. SSC Accelerator Availability Allocation. Technical Report SSCL-376, SSC Laboratory, Dallas, TX.

79. LEB/MEB Corrector Magnet Characteristics. Technical Report AED-8060006, SSC Laboratory, Dallas, TX.

80. Recommended Practices and Guidelines for Procurement of Magnetic Fusion Electrical Equipment. Technical Report DOE/ER-0133 UC-20-a,B&E, SSC Laboratory, Dallas, TX.

81. Element Specification for the Linac Beam Transfer Line of the Superconducting Super Collider, Level 3B. Technical Report E10-000026, SSC Laboratory, Dallas, TX.

82. Design Requirements Document for the Low Energy Booster Injection Pulsed Power Supply Systems. Technical Report AEF-7150001, SSC Laboratory, Dallas, TX.

83. Design Notes on the LEB Injection Pulsed Power Supplies. Technical Report AEF-7150005, SSC Laboratory, Dallas, TX, April 1994. Compiled by W. Merz.

84. K.R. Bourkland. A 34 kA Rapid Cycling PFN Power Supply for Driving Injection Magnets. page 3974, 1979.

85. N. Dikansky *et al.* Design Notes from the SSCL-BINP Collaboration on the LEB Injection Pulsed Power Supplies. Technical Report AEF-7150006, SSC Laboratory, Dallas, TX, April 1994. Compiled by W. Merz.

86. Q.A. Kerns *et al.* 30-53 MHz Super Cavities for 10-GeV Acceleration in the Fermilab Booster Ring. *IEEE Trans. on Nuc. Sci.*, (NS26):4111, June 1979.

87. C.C. Friedrichs, L. Walling, and B.M. Campbell. Design of an Accelerating Cavity for the Superconducting Super Collider Low Energy Booster. In PAC91[156], page 1020.

88. W.R. Smythe. RF Cavities With Transversely Biased Ferrite Tuning. In PAC85[158].

89. R.L. Poirier. Perpendicular Biased Ferrite-Tuned Cavities. In PAC93[157].

90. W.R. Smythe. Proton Synchrotron RF Cavity Mode Damper Tests. In PAC91[156], page 1020.

91. P.D. Coleman, F. Brandeberry, C. Friedrichs, Y. Goren, T. Grimm, G. Hulsey, S. Kwiatkowski, A. Propp, L. Taylor, L. Walling, J. Averbukh, M. Karliner, V. Petrov, and S. Yakovlev. Status of the SSC LEB RF cavity. In PAC93[157], page 824.

92. C. Friedrichs. Some RF Properties of Water. Technical Report SSCL Tech Note, SSC Laboratory, Dallas, TX, June 1991.

93. L. Walling. 304 Stainless Conductivity Measurement. private communication, September 1993.

94. C. Friedrichs and G. Hulsey. The Effects of Temperature and RF Power Level on the Tuning of the Water Cooled SSC Low-Energy Booster Cavity. In PAC93[157].

95. V.E. Shapiro. Magnetic Loss and Instabilities in Ferrite Garnet Tuned RF Cavities. Technical Report TRIUMF-SSCLR, SSC Laboratory, Dallas, TX.

96. G. Hulsey, V. Petrov, and V. Yakovlev. The Nonlinear Effect in the SSC LEB Test Tuner. Technical Report SSC Tech Note, SSC Laboratory, Dallas, TX, September 1992.

97. F. Pedersen. Notes on Low Energy Booster RF Feedback and Controls. Technical Report PMTN-040L, SSC Laboratory, Dallas, TX, December 1991.

98. S.P. Jachim. Some New Methods of RF Control. 1990.

99. L.K. Mestha *et al.* Interaction of Beam Control Feedback Loops for SSC Low Energy Booster. *Part. Accel.* accepted for puplication.

100. L.K. Mestha *et al.* Instabilities in Beam Control Feedback Loops in Proton Synchrotrons. *Part. Accel.*, 42(1):1, 1993.

101. Y. Kimura *et al.* Synchronous Transfer of Beam from the Booster to the Main Ring in the KEK Proton Synchrotron. In *Proc. IEEE Part. Accel. Conf.*, volume NS-24 of *IEEE Trans. Nucl. Sci.* IEEE Press, May 1977.

102. J.A. Dinkel *et al.* Synchronous Transfer of Beam from the NAL Fast Cycling Booster Synchrotron to the NAL Main Ring System. In *Proc. IEEE Part. Accel. Conf.*, volume NS-20 of *IEEE Trans. Nucl. Sci.* IEEE Press, May 1973.

103. Q.A. Kerns *et al.* New Low-Level Rf System for the Fermilab Booster Synchrotron. In *Proc. IEEE Part. Accel. Conf.* IEEE Press, 1987.

104. L.K. Mestha. Phase-Locked Loop with Controlled Phase Slippage. U.S. Patent No. 5 298 867, March 1994.

105. SKY Computers. *Challenger C30/V User's guide.* SKY Computers, Inc., Chelmsford, MS, July 1990.

106. Stanford Telecommunications. *STEL-2273, The DDS Handbook.* Stanford Telecommunications, July 1990.

107. Highland Technology. *Model M690 Fast Time-to-Digital Converter.* Highland technology, Inc., June 1991.

108. L.K. Mestha. Parasitic Experiments on Fermilab Booster LLRF Systems. Technical Report SSCL-599, SSC Laboratory, Dallas, TX, November 1992.

109. R.C. Webber *et al.* Proposal to Test a new Low Level Rf System on the Fermi National Accelerator Laboratory Booster Synchrotron. Technical Report ADA-3120001, SSC Laboratory, Dallas, TX, November 1991.

110. L.K. Mestha *et al.* Fixed-Structure Suboptimal Feedback Control for Particle Accelerators. *Part. Accel.* accepted for publication.

111. C. Bovet, R. Gouiran, I. Gumowski, and K.H. Reich. A Selection of Formulae and Data Useful for the Design of A.G. Synchrotrons. CERN/MPS-SI/Int. DL/70/4, CERN, Geneva, CH, April 1970.

112. R.C. Webber. Overview and Status of Beam Instrumentation at the SSC. In PAC93[157], pages 2094–2096.

113. J.-P. Koutchouk. *Trajectory and Closed Orbit Correction*, pages 46–64. 1988. M.Month and S. Turner, Springer-Verlag.

114. R.E. Shafer. Beam Position Monitoring. In Beadle and Castillo[159], pages 26–58.

115. D. Meyer and D. Martin. Position Detector Design Using an Electrostatic Application of ANSYS. In AIW93[161]. To be published.

116. G.R. Aiello and M.R. Mills. Log-Ratio Beam Position Monitor. In Hickson and Stover[160], pages 301–310.

117. R.E. Shafer. Log-Ratio Signal Processing Technique for Beam Position Monitors. [160], pages 120–128.

118. G.R. Aiello, M.R. Mills, and R.E. Gonzalez. Test Results of the Log-Ratio Beam Position Monitor Electronics. In PAC93[157], pages 2322–2324.

119. F.D. Wells, J.D. Gilpatrick, and R.E. Shafer. Log-ratio Circuit for Beam Position Monitoring. In PAC93[157], pages 1139–1141.

120. A.A. Jones. VXIbus Beam Position Monitor Module. In Hickson and Stover[160], pages 286–290.

121. G.R. Aiello. Calculated Signal Level from the LEB BPM. Technical Report SSCL-N-754, SSC Laboratory, Dallas, TX, 1991.

122. R.G. Johnson and N.V. Mokhov. Beam Loss Monitor System for the SSC. In AIW93[161]. To be published.

123. R.G. Johnson. Beam-Loss Monitor System Specifications for the SSCL LEB. Technical Report SSCL Tech Report, SSC Laboratory, Dallas, TX, 1994.

124. A.A. Jones. A New VME Based High Voltage Power Supply for Large Experiments. private communication, 1992.

125. R.C. Webber. Longitudinal Emittance: An Introduction to the Concept and Survey of Measurement Techniques Including Design of a Wall Current Monitor. In Beadle and Castillo[159], pages 85–126.

126. K.B. Unser. Beam Current Transformer from DC to 200 MHz range. *IEEE Trans. Nucl. Sci.*, (NS16):934–938, June 1969.

127. SSC Low Energy Booster Level 4 Requirements Specification. Technical Report ABM-3000001, SSC Laboratory, Dallas, TX.

128. R. Bork. SSC Low Energy Booster Control System PDR. Technical Report AMA-3000002, SSC Laboratory, Dallas, TX, 1994.

129. SSC Low Energy Booster Corrector Magnet Power Supply Controller Module Specification. Technical Report ABM-8000007, SSC Laboratory, Dallas, TX.

130. SSC Global Accelerator Control System Level 3 Specifications. Technical Report E10-000043, SSC Laboratory, Dallas, TX.

131. SSC Global Accelerator Control System Level 4 Specifications. Technical Report ABM-8000001, SSC Laboratory, Dallas, TX.

132. SONET90 American National Standard for Telecommunications Digital Hierarchy—Optical Interface Rates and Format Specifications, 1990. ANSI T1.105-1988 and ANSI T1.105-1990.

133. L.R. Dalesio *et al.*. EPICS Architecture. In *Int. Conf. on Accelerator and Large Experimental Physics Control Systems*, page 278, Tsukuba, Japan, 1991.

134. SSC ASD/CD Software Development Plan. Technical Report ABM-8000002, SSC Laboratory, Dallas, TX.

135. SSC Environment, Safety and Health Manual. Technical report, SSC Laboratory, Dallas, TX.

136. A. van Ginneken. Program to Simulate Transport of Hadronic Cascades in Bulk Matter. Technical Report FN-272, Fermi National Accelerator Laboratory, Batavia, IL, 1975.

137. N. Mokhov. MARS12 Code System. In *Proc. SARE Workshop*, Santa Fe, NM, 1993.

138. A. Kalinovsky, N. Mokhov, and Yu. Nikitin. Passage of High Energy Particles through Matter. 1989.

139. R.H. Thomas and G.R. Stevenson. *Radiological Aspects of the Operation of Proton Accelerators.* Int. Atomic Energy Agency, Vienna, Austria, 1989.

140. Radiation Control Review Advisory Group Report and Presentations. Technical Report SSCL-E13-000194, September 1992.

141. K. Gobel *et al.* Evaluating Dose Rates Due to Neutron Leakage Through the Access Tunnels of the SPS. Technical Report LABII-RA/Note/75-10, CERN, Geneva, Switzerland, 1975.

142. V. Romero *et al.* SSCL Groundwater Model. Technical Report SSCL-SR-1233, SSC Laboratory, Dallas, TX, 1994.

143. LEB Beam Absorber Requirements Document. Technical Report AMA-2210004, SSC Laboratory, Dallas, TX, 1992.

144. R. Parry. Personnel Access Safety Systems. In *Proc. Industrial Computing Conf.*, volume 2, page 437, 1992. Paper # 92-0467.

145. P. Gruhn. Risks with Using PLCs for Safety Protection. *C&I*, page 53, September 1990.

146. B. Balls and P. Gruhn. Design Considerations for High-Risk Safety Systems. *Intech*, page 28, March 1991.

147. T. Fisher. Control Systems Safety. *ISA Transactions*, 30(1), 1991.

148. A. Frederikson. Fault Tolerant Programmable Controllers for Safety Systems. *Programmable Controls*, page 109, March 1989.

149. R. Waterbury. Fault-Tolerant/Fail-Safe Systems are Fundamental. *Intech*, page 35, April 1991.

150. Programmable Electronic Systems in Safety-Related Applications. *Health and Safety Executive*, 1985. HMSO, London, UK.

151. R. Parry. Personnel Electronic Safety Systems. In PAC93[157].

152. SSC Low Energy Booster Preliminary Design Requirements. Technical Report C13-00027, SSC Laboratory, Dallas, TX, June 1991.

153. S. Machida. LEB Commissioning Working Group Minutes. Technical Report PCO-000020, SSC Laboratory, Dallas, TX, May 1994. Collection of viewgraphs and notes on the subject.

154. L. Schachinger and R. Talman. Teapot: Thin-Element Accelerator Program for Optics and Tracking. *Part. Accel.*, 22:35, 1987.

155. *Proc. 3. European Part. Accel. Conf.*, Berlin, F.R. Germany, 1992.

156. *Proc. IEEE Part. Accel. Conf.*, San Francisco, CA, May 1991. IEEE Press.

157. *Proc. IEEE Part. Accel. Conf.*, Washington, DC, May 1993. IEEE Press.

158. *Proc. IEEE Part. Accel. Conf.*, volume NS-32 of *IEEE Trans. Nucl. Sci*, Vancouver, BC, May 1985. IEEE Press.

159. R. Beadle and V.J. Castillo, editors. *Proc. First Annual Workshop on Accelerator Instrumentation*, number 212 in AIP Conference Proceedings, New York, NY, 1989. American Institute of Physics.

160. J.A. Hickson and G. Stover, editors. *Proc. Fourth Annual Workshop on Accelerator Instrumentation*, number 281 in AIP Conference Proceedings, New York, NY, 1993. American Institute of Physics.

161. *Proc. Fifth Annual Workshop on Accelerator Instrumentation*, AIP Conference Proceedings, New York, NY, 1994. American Institute of Physics. To be published.